Tailoring the Material Properties of Doped Silicon Nanoparticles

by

Sarah Christine Milliken

A thesis submitted in partial fulfillment of the requirements for the degree of

Doctor of Philosophy

Department of Chemistry

University of Alberta

Abstract

Silicon nanoparticles have sparked researchers' interest as a biologically compatible and abundant quantum dot alternative. Doped silicon nanoparticles (SiNPs) offer unique optical and electronic properties that are not observed for intrinsic Si. These advantageous properties can be applied towards a number of exciting applications such as medical imaging, photovoltaic devices, lighting, and catalysis. In order to fully realize the potential of doped SiNPs it is necessary to precisely control the particle size and surface chemistry, as well as the dopant concentration and distribution within the NP. This thesis focuses on developing synthetic methods to create well-defined and tailorable doped SiNPs.

In Chapter 2 we aim to derivatize the surfaces of doped SiNPs obtained from the thermal processing of HSQ and boric acid. Surface modification of these SiNPs was achieved using a phosphorous pentachloride etching induced reaction with alkoxy ligands of varied chain lengths. Throughout this investigation we assessed the SiNP surface chemistry of as-synthesized B-doped SiNPs through a combination of X-ray photoelectron spectroscopy (XPS), Fourier transform infrared spectroscopy (FTIR) and cross-polarization magic-angle spinning nuclear magnetic resonance spectroscopy (CP MAS NMR). The successful attachment of the alkoxy ligands to the surface of the particle is then assessed by FTIR, XPS and thermogravimetric analysis (TGA) and the change in photoluminescence emission is observed.

With a convenient method for tailoring the surface chemistry of B-doped SiNPs in hand, we turned our attention toward achieving size-controlled preparation of doped particles. This saw the development of a new diffusion-based post-synthesis doping method that drew inspiration from thermally induced diffusion doping of bulk silicon. Chapter 3 describes a thermal diffusion-based

post-synthesis doping method that exploits parent SiNPs with narrow size distributions, boric acid as the dopant source and hydrogen silsesquioxane as a capping agent. The role of annealing atmosphere and structural disorder within the SiNPs were found to strongly influence doping through characterization with TGA, XPS and TGA. The method allows for control of particle size, dopant concentration and surface chemistry.

In Chapter 4 we attempt to provide control of the dopant location through the development of a monolayer doping method. The method sees the design of a molecular dopant precursor scaffold with self-capping properties which forms a monolayer on the precursor intrinsic SiNPs and allows for the shallow thermal-diffusion of dopants. This chapter lays the ground work for precise control over dopant location.

Finally, Chapter 5 summarizes the findings from the previous chapters and further explores relevant future research directions.

Preface

Chapter 1 of this thesis has been published as Milliken, S., Thiessen, A. N., Cheong, I. T., O'Connor, K. M., Li, Z., Hooper, R. W., Robidillo, C. J., & Veinot, J. G. C., "Turning the dials": Controlling synthesis, structure, composition, and surface chemistry to tailor silicon nanoparticle properties. *Nanoscale* **2021**, *13*(39), 16379–16404. I was responsible for developing the scope of the review, delegation and planning of writing, writing the introduction, conclusion, doping section as well as combining and rewriting all other sections of the review for the final submission. A. N. Thiessen was responsible for researching and writing the first draft of the section on nanocrystal structure. I.T. Cheong and Z. Li were responsible for researching and writing the first draft of the section on surface chemistry and optical properties. K.M O'Connor and R.W. Hooper were responsible for researching and writing the first draft of the section on preparation of SiNPs. C. Robidillo assisted with editing and literature review. J.G.C. Veinot was a supervisory author that contributed to the review scope and manuscript preparation.

Chapter 2 of this thesis has been published as Milliken, S., Cui, K., Klein, B. A., Cheong, I. T., Yu, H., Michaelis, V. K., & Veinot, J. G.C., Tailoring B-doped silicon nanocrystal surface chemistry *via* phosphorus pentachloride – mediated surface alkoxylation. *Nanoscale*, **2021**, *13*(43), 18281–18292. I was responsible for the project scope, experimental planning, data collection and analysis, and manuscript preparation. K. Cui assisted with data collection and interpretation of samples using electron energy loss spectroscopy (EELS). B.A. Klein was responsible for data collection and interpretation of samples with solid state nuclear magnetic resonance (NMR) experiments under the supervision of V.K. Michaelis. I.T. Cheong assisted with data collection and interpretation of photoluminescence measurements. H. Yu performed imaging

of samples using transmission electron microscopy (TEM). J.G.C Veinot was a supervisory author and assisted with project scope, data analysis and manuscript preparation.

Chapter 3 of this thesis has been published as preprint as Milliken, S., Cheong, I., Cui, K., & Veinot, J. Post-Synthesis Boron Doping of Silicon Quantum Dots via Hydrosilsesquioxane-Capped Thermal Diffusion. *ChemRxiv*. **2022**. I was responsible for the project scope, experimental planning, data collection and analysis, and manuscript preparation. I.T. Cheong assisted with data collection and interpretation of photoluminescence measurements. K. Cui assisted with data collection and interpretation of samples using TEM and EELS. J.G.C Veinot was a supervisory author and assisted with project scope, data analysis and manuscript preparation.

Chapter 4 of this thesis is an original work. I was responsible for the project scope, experimental planning, data collection and analysis. K. Cui assisted with data collection and interpretation of samples using TEM. J.G.C Veinot was a supervisory author and assisted with project scope and data analysis.

Chapter 5 presents original ideas for future directions developed by me and with input from my supervisor J.G.C. Veinot.

Acknowledgements

First and foremost, I need to thank my parents for their everlasting support and encouragement during my academic studies. You always taught me that through hard work and dedication I could do anything I set my mind to. Even though the path I've chosen has taken me miles away, you've been there every step of the way and I could not have completed this thesis without you.

I would also like to thank my fellow group members, both past and present, for their friendship, insight, and overwhelming kindness. I moved here barely knowing anyone, and now I have a second family that will be incredibly hard to leave behind. I want to especially thank Jay Ho, who has been with me through every step of this program. I'm so thankful we both decided to join this group and I honestly do not think I could have done this without you. I'd also like to thank Riley Hooper, Kevin O'Connor and Emily Cheong for not only being great friends but also for all their advice and help with research. Thank you also to Alyx Thiessen for being a wonderful mentor and always being there when I needed advice or just wanted to vent.

Of course, one of the most important people to thank is my supervisor Dr. Jon Veinot. I'm so incredibly glad that you invited me to join your group. You always encouraged me to think outside of the box, take risks and achieve things I never thought possible. You had unwavering faith in my abilities and never hesitated to support me when I really needed it. I'm so lucky to have had the honor to work with such an intelligent, kind and caring supervisor, and I know that the group will continue to do amazing work with your guidance.

I would also like to thank my collaborators Brittney Klein, Dr. Vladimir Michaelis, Kai Cui, and Emmett Yu for all of their contributions. I'd also like to acknowledge the UofA Analytical

lab, Nanofab and the National Research council for data collection as well as the Chemistry support staff for all of their hard work. Another thank you goes to Prof. Dr. Marc Tornow and Sabrina Artmeier for hosting me during my short research exchange at the Technical University of Munich.

Finally, I want to thank my friends and family in Ontario, as well as the friends I've made during my time in Edmonton. I especially want to thank my best friend Emily Riddell, you made such a positive impact on me and my time here, and I'm so glad we ended up crossing paths. Your unconditional support and friendship over the years means the world to me and I could not have done this without you. Thank you for being a wonderful person and a great friend.

Table of Contents

List of Figures

List of Tables

List of Schemes

Chapter 1:

Introduction

A version of the chapter has been published:

Milliken, S.; Thiessen, A. N.; Cheong, I. T.; O'Connor, K. M.; Li, Z.; Hooper, R. W.; Robidillo, C. J.; Veinot, J. G. C. “Turning the Dials”: Controlling Synthesis, Structure, Composition, and Surface Chemistry to Tailor Silicon Nanoparticle Properties. *Nanoscale* **2021**, *13*, 16379–16404.

1.1 Semiconductor Quantum Dots and Silicon Nanoparticles

Nanoparticles and their unique properties continue to receive wide-spread attention in both fundamental research and commercial applications. A straightforward example of their impact is found in common at-home pregnancy tests that make use of gold nanoparticles with antibodies attached to its surface that selectively bind with early-pregnancy hormones (human chorionic gonadotropin) found in urine.[1] These gold nanoparticles then bind to a strip tagged with anti-bodies that cause the gold to bind and aggregate, causing a pink colour change. This colour change arises from a phenomena known as localized plasmonic resonance (LSPR) which occurs through the collective oscillation of conductance electrons locally about the nanoparticle when illuminated with resonant wavelength of light.[2] Nanoparticles are materials with nano-scale dimensions (1.0 x 10^{-9} m), which are defined as "having dimensions of 1 to 100 nm and enable properties (electronic, optical, magnetic, catalytic, etc.) that are not seen in the bulk".[3] These unique properties are in part due to the large surface area to volume ratio of these materials and quantum confinement effects. [4, 5] Since particle grain sizes are so small, the relative surface area to volume ratio is significantly larger, leading to greater chemical reactivity and stress-induced structural changes.[4] In addition, at these size-scales confinement-effects play a crucial role in defining the properties and characteristics of these materials.

Quantum Dots (QDs) are semiconductor nanoparticles. They were first reported by Brus et al. in 1980, who observed that small semiconductor crystallites exhibited size and shape dependent properties when prepared at dimensions smaller than those of the Bohr radius of a coulombically bound electron-hole pair (exciton) in the corresponding bulk material.[6,7] This results in quantum confinement and sees discrete "atom-like" energy levels emerge that are separated by a forbidden

range of energy levels known as the band gap, and upon excitation they can emit a photon with a very narrow full-width-at-half-maximum. As the size of the semiconductor nanocrystal is decreased the band gap increases, resulting in a higher energy photon with a shorter wavelength being emitted. This size dependence provides a convenient approach toward tailoring optical response.[8] QDs also exhibit high quantum yield, signal brightness and improved photo-stability.[9] These exceptional optical and electronic properties allow researchers to use these QDs for light-emitting diodes,[10] solar cells,[11] fluorescent imaging[12] and sensing applications.[13] The most commonly studied QD systems use toxic/heavy metals (e.g., Pb, Cd) which can pose serious health and environmental issues. Therefore, the practical impact of many QDs is currently limited because of the legislation associated with the controlled use of these materials.[14] Cd and Pb-free QDs have been developed such as InP, however, the natural abundance of its constituent elements can limit their application.

Silicon is the semiconductor that forms the basis for the modern electronics that have revolutionized society; it is bioinert, abundant, and electrochemically stable.[15] The unsurpassed precision with which the properties of silicon can be tailored and the associated processes used to incorporate it into devices are a tour-de-force of 20th Century creativity and ingenuity. In the context of Brus' discovery (vide supra) and the ubiquitous presence of silicon in the electronics industry, it is no surprise that nano-scaled silicon became and continues to be the focus of extensive research efforts. This introduction outlines efforts made to control the optical and electronic properties of silicon nanoparticles (SiNPs) through four key areas: 1) advances in synthesis methods, 2) defining internal structure, 3) incorporation of dopants, and 4) tailoring surface chemistry.

1.2 Preparing Silicon Nanoparticles

One must first have access to materials to fully appreciate their properties, hence it is useful to begin our discussion with SiNP synthesis. Several methods have been developed to produce SiNPs of tailored dimensions including, pyrolysis of silicon precursors,[16-20] nonthermal plasma,[21-24] laser ablation,[25, 26] as well as reduction of metal silicides[27] and silicon halides.[28-32] Each of these diverse (even divergent) procedures comes with associated benefits and challenges while providing varying degrees of control over parameters (e.g., structure/crystallinity, size, composition, surface chemistry) that impact SiNP properties; in fact, SiNPs often appear to exhibit synthetic method-dependant characteristics. To afford the reader with context of the challenges associated with SiNP preparation we begin with a brief historical perspective. Table 1 provides a summary of commonly reported literature procedures used to produce SiNPs that we have chosen to describe in this section.

Table 1. 1 A summary of the methods used to prepare SiNPs and their associate properties.

Method	PL Range (nm)[a]	Diameter (nm)	PL QY (%)[b]	Refs.
Precursor Thermal Decomposition	530 - 1060	1 - 200	5 - 70	17, 19, 33-37, 38, 39, 40-42, 43, 44, 45-50, 51
Nonthermal Plasma	690 - 920	2 - 10	0.5 - 70	52-57
Laser Ablation	400 - 750	2 - 100	10 - 70	25, 26, 58, 59
Etching Bulk Si	300 - 510	2 - 35	12 - 25	60, 61
Solution reactions	320 - 460	1.5 - 10	10 - 25	30, 31, 62-72, 73

[a] PL_{max} reported in literature. Excitation wavelengths vary in the range of 300 - 560 nm as indicated in the listed references.

[b] Absolute PLQY calculated using excitation and emission peak areas.

1.2.1 Thermally-induced Decomposition of Silicon-based Precursors

One of the first successful synthesis routes for producing small quantities (i.e., <500 mg) of SiNPs (i.e., silicon quantum dots) reported by Brus and coworkers involved pyrolysis of disilane.[36] This procedure afforded a narrow size distribution (i.e., d = 1 - 2 nm) of particles that showed photoluminescence maxima (PL_{max}) in the range of 600 - 750 nm and a relative photoluminescent quantum yield (PLQY) of 5.6%.[37] This early work spawned several studies focused on silicon cluster growth.[74] The Swihart group subsequently developed a high-throughput, scalable method (20 - 200 mg/h) that employed a CO_2 laser to induce gas-phase decomposition of a common industrial silicon precursor – silane (i.e., SiH_4). The resulting product contained oxidized SiNPs with crystallite diameters in the 5 – 20 nm range as well as amorphous silicon-based materials. In light of the material complexity the authors suggested the polydispersity was too broad to report accurately. The as synthesized materials showed no detectable PL, however etching with a mixture of hydrofluoric (HF) and nitric (HNO_3) acids reduced the crystalline size, and led to the appearance of PL. The etched products showed PL_{max} in the range of 420 - 855 nm with PLQY of ca. 1%. [50] The Swihart group improved upon the PLQY realizing 2 - 10% for styrene grafted SiNPs and 10 - 20% for those bearing alkyl ligands.[39, 40]

Looking to further improve upon production rates, Swihart and co-workers developed an independent microwave plasma methodology for thermolyzing silane that showcased one of the highest reported rates for generating SiNPs (i.e., 0.1-10 g/h).[35] As synthesized, SiNPs were ca. 13 nm in diameter with a 10.6% polydispersity and showed no PL, however, etching provided a photoluminescent material with a range of PL_{max} (i.e., 456 – 735 nm) that was tuneable by varying the etching time; unfortunately, PLQYs were not reported.[35] One important challenge with these approaches is silane gas can be unpredictable and presents a significant safety hazard. In this

regard, Guruvenket et al. aimed to supplant silane by synthesizing SiNPs via gas-phase pyrolysis of cyclohexasilane. This approach afforded SiNPs 2 nm in diameter with a polydispersity of 10%. Introducing alkyl surface functionalization via hydrosilylation provided a PL_{max} range of 370 - 457 nm with PLQYs 9 - 13%.[41]

In efforts to reduce reliance on costly instrumentation and hazardous precursors, methods that employ solid-state precursors have also been investigated. Nearly four decades ago, researchers discovered nanoscale inclusions of crystalline silicon could be formed within silicon oxide matrices upon annealing of silicon-rich oxides (SRO; SiO_x where x = 1.5) often derived from "silicon monoxide".[33, 34] Under high-temperature heating phase segregation of Si and SiO_2 occurs to yield oxide-embedded SiNPs that can be liberated via etching (Figure 1.1 a).[42]

In 2006, Hessel et al. drew inspiration from these early SiO_x studies and developed a versatile approach using a solution processible SRO polymer, hydrogen silsesquioxane (HSQ; $(HSiO_{1.5})_n$). Others have followed this method using alternative insoluble sol-gel derived polymers as precursors.[16, 51, 75] Heating HSQ induces disproportionation and provides oxide-embedded SiNPs in thin films, as well as bulk powders from which freestanding SiNPs are readily isolated.[20] The SiNPs prepared in this way possessed dimensions in the range of from 3.3 - 8.7 nm that were defined by the thermal processing conditions (i.e., temperature, dwell time, etc.) as well as etching time. These particles show size dependant PL_{max}. As synthesized H-terminated particles have low PLQY of ca. 4%,[43] however like SiNPs prepared using many other procedures presented here, hydrosilylation-based surface passivation provided improved PLQYs (up to ca. 70 %) with an accompanied approximate four-fold increase in brightness.[17, 19, 44, 46, 47, 76] Furthermore, the dimensions of SiNPs prepared in this way could be tuned throughout the range of 1.1 - 90 nm with PL_{max} spanning 530 - 1060 nm (Figure 1.1 b-h). [17, 19, 44, 46, 48, 76]

The Fujii group used a similar method to that reported by Hessel to grow SiNPs with diameters as large as 200 nm and polydispersities of ca. 6%. This was achieved by increasing the temperature range beyond the melting point of bulk Si (i.e., 1414 °C) but below that of bulk silica (i.e., 1710 °C).[49] Although the resulting particles showed no PL, they exhibited Mie scattering with diffuse reflectance peak maxima spanning from 420 to 700 nm.[49] Terada et al. also suggest the HSQ internal structure can also influence SiNP size and crystallinity and showed that decreasing the HSQ cross-linking density provided comparatively large SiNPs with red-shifted PL maxima (700 - 800 nm).[16] The versatility of the HSQ method, has faciliated the synthesis of near-monodisperse SiNPs and superlattices,[19] provided graded structure SiNPs (vide infra), SiNP-based LEDs,[77] narrow band width emission from SiNP/polymer hybrid optical cavities,[78] and even a report claiming a SiNP-based prototype distributed feedback laser.[79]

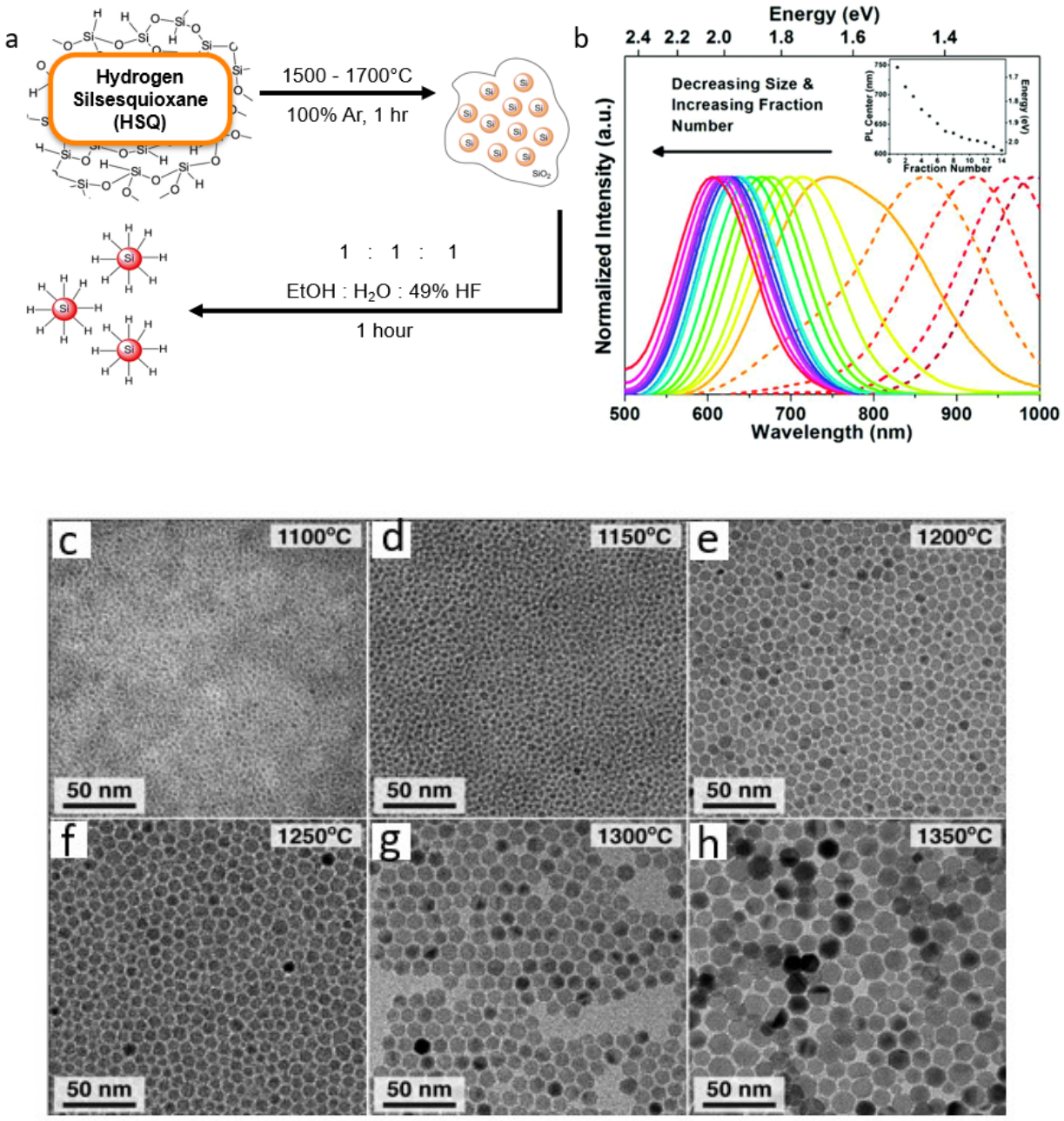

Figure 1. 1 a) Synthesis of SiNPs from thermally-induced disproportionation of HSQ. b) Photoluminescence spectra of allylbenzene-passivated SiNPs showing a blue-shift with decreasing size. c)-h) Bright-field transmission electron microscopy (TEM) images of SiNPs prepared at the indicated temperatures using the procedure in (a). Adapted with permission from ***Nano Lett.*** **2012, 12, 1, 337–342.** Copyright 2012 American Chemical Society.

Producing SiNPs from SRO thermal treatment comes with several advantages: the required infrastructure is straightforward and inexpensive, precursors are safe and readily manipulated, SiNPs are prepared as oxide-embedded (thin film and bulk) and freestanding forms with a broad range of SiNP sizes and PL_{max} are accessible,[34, 42, 49, 50, 51] and particle surfaces are readily designed using solution-phase reactions.[17, 19, 44, 45-47] Despite these favourable aspects, no approach is perfect. For example, it is necessary to prepare/obtain a suitable precursor. HSQ is attractive because it can be manipulated under ambient conditions but must be prepared using literature methods or purchased from a commercial supplier.[20] Other SROs (e.g., "SiO_x") are also attractive but their processability and tailorability are somewhat more limited. It is also necessary to address safety protocols associated with HF etching if freestanding SiNPs are the final target. Finally, the "batch" nature of the various stages of this approach and the low yield of freestanding SiNPs produced (ca. 10%) potentially limits the economically viable large-scale production.[20]

1.2.2 Nonthermal Plasma Precursor Decomposition

An alternative aerosol-phase method for preparing SiNPs employs nonthermal plasma to controllably activate precursors. In these syntheses, a defined mixture of argon carrier gas and silicon precursor (e.g., SiH_4 or $SiCl_4$) is passed through a nonthermal plasma that imparts energy to induce precursor decomposition and nanocrystal formation.[23, 24] Pioneering nonthermal plasma synthesis work of the Kortshagen group provides SiNPs with diameters in the range of 2 - 8 nm with polydispersities of 12 - 17% that show tuneable PL_{max} throughout the 700 - 900 nm range.[53] Consistent with other thermal decomposition methods, functionalization improves PLQY substantially (as high as 60%).[22, 54] Pringle et al. improved upon the PLQY even further by using the liquid precursor, cyclohexasilane, which has the added benefit of being a significantly safer

alternative to silane gas.[56] The researchers then employed density-gradient ultracentrifugation to effectively size-separate alkene-passivated SiNPs and produce PLQYs approaching 70% for PL_{max} in the range of 700-1000 nm.[56] Recently, Li and Kortshagen expanded upon their method and reported a scalable, high-production rate (10 mg/h) aerosol-phase synthesis method for alkene functionalized SiNPs that exhibit 20% PLQY (Figures 1.2 a and b).[52] This latest advance presents an attractive option for rapid mass production of SiNPs, however, unlike materials produced using other methods such as thermolysis, the surface functionalization has only a minor effect on PLQY, making the resulting materials potentially less desirable for applications that require high PLQY.

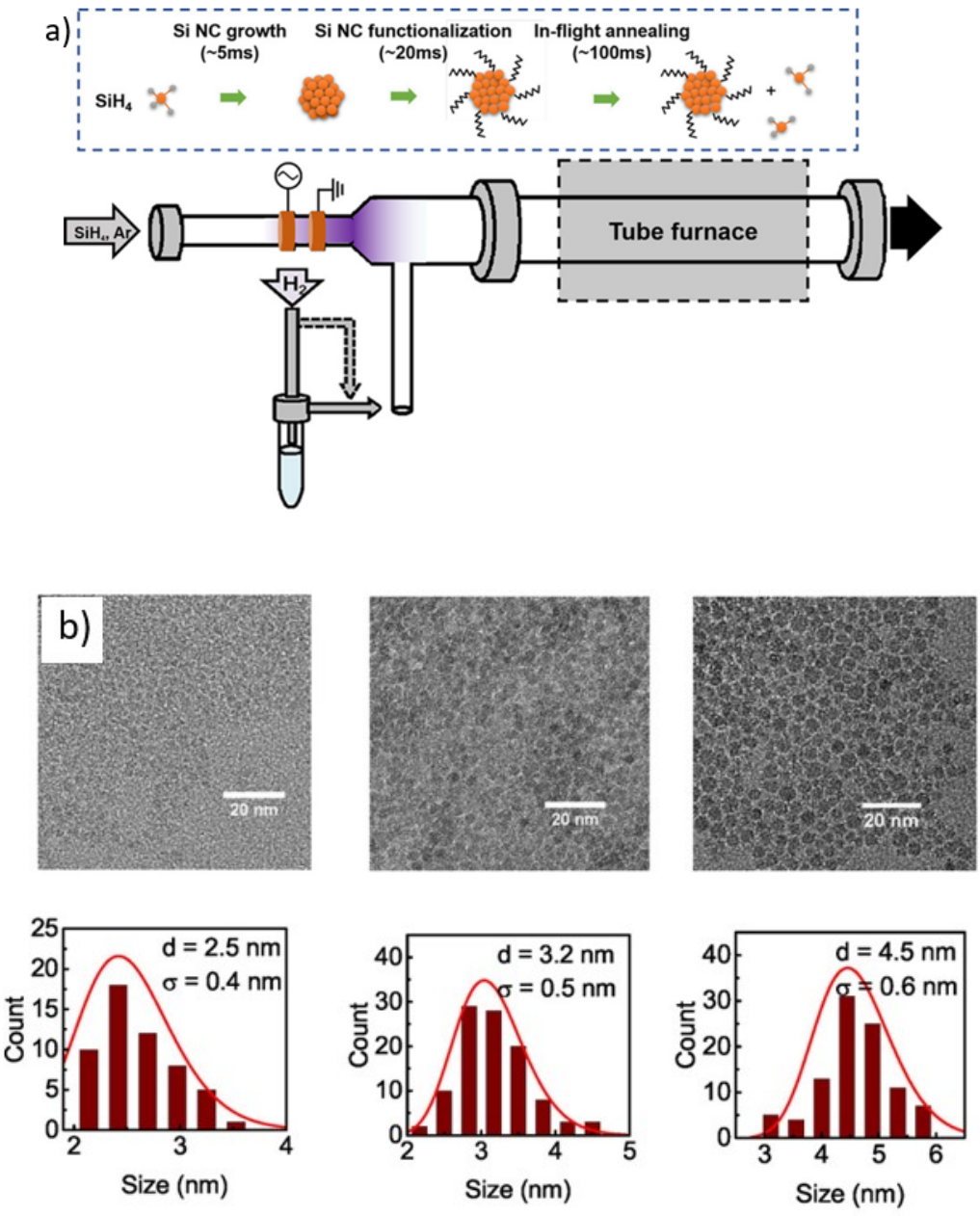

Figure 1. 2 a) Nonthermal plasma synthesis/functionalization of SiNPs. b) Bright-field TEM images of SiNPs produced using non-thermal plasma processing. Reprinted with permission from *Chem. Mater*. **2019**, 31, 20, 8451–8458. Copyright 2019 American Chemistry Society.

Generally, nonthermal plasma preparation of SiNPs brings with it several very attractive attributes. Of particular note, it can provide materials with similar polydispersity and PL_{max} range to those prepared using thermolysis, but at comparatively high production rates (20 - 52 mg/h).[52, 53] Other appealing aspects are: the synthesis occurs entirely in the gas phase and solution-phase processing (i.e., etching, functionalization, etc.) required and the process is amenable with "flow through" preparation and scaling. Still, challenges remain. At present, the accessible NP size range is limited because particles become negatively charged and growth is arrested; this characteristic is both a benefit, because size focusing can be achieve, and a limitation, when larger particles are targeted.[23, 80] Additionally, high PLQYs (i.e., 70%) have only been realized for SiNPs > 4 nm, and PLQY decreases markedly for smaller sizes.[57] Finally, while alternative precursors have been explored, the general procedure employs hazardous precursors (e.g., SiH_4) whose behaviour is often unpredictable.[56, 81]

1.2.3 Laser Ablation and Etching of Bulk Silicon

Broadly, top-down methods involve breaking bulk crystalline Si into smaller pieces with nanoscale dimensions. These methods are generally characterized by less well-defined (i.e., shape/size) products, however, benefit from straightforward infrastructure and scalability. Laser ablation sees bulk Si wafers broken into SiNP fragments using a high-power density light (Figure 1.3 a). Svrcek et al. prepared polydisperse (d = 2 – 100 nm) blue-emitting (PL_{max} ~ 400 - 430 nm) SiNPs using laser ablation in deionized water.[58] Irradiating the SiNPs in an appropriate organic solvent passivates the particle surfaces with alkyl groups and provides PLQYs of 10 - 20%.[26, 59] More recently, Yuan et al. showed irradiation of crystalline Si followed by exposure to pulsed UV light in HF-containing organic solvents produced SiNPs showing PLQY of 50 - 70% and PL_{max} = 750 nm. The particle size ranged from ca 3.1 - 5.5 nm and possessed a bimodal distribution; when

HF was introduced the size was reduced to 2.9 nm with reported improved polydispersity, however it was not quantified (Figure 1.3 b).[25]

Another popular top-down method draws on the original porous silicon preparations and involves electrochemical etching of Si wafers; this approach is well-established for producing mesoporous SiNPs and has been expanded to provide SiNPs.[82] Hwang et al. formed SiNPs by sonicating electrochemically prepared mesoporous and nanoporous silicon.[60] To improve the size distribution, remove surface oxide and introduce Si-H surface reactivity, the particles were exposed to an HF/HNO_3 acid mixture. Following functionalization, using thermal- or photo-induced hydrosilylation small quantities of product (i.e., 0.3 mg NCs per cm^2 of wafer) comprised of SiNPs with an average diameter of 2.7 nm were obtained that showed a blue PL_{max} (i.e., 410 nm) with a QY of 20%.[60] In another study, Liao et al. developed a straightforward one-pot hydrothermal etching procedure that provided particles of 2 - 3 nm diameter and qualitatively appeared to exhibit low polydispersity. The relative PLQY for these SiNPs was ca. 12 % for PL_{max} in the range of 300-480 nm.[61]

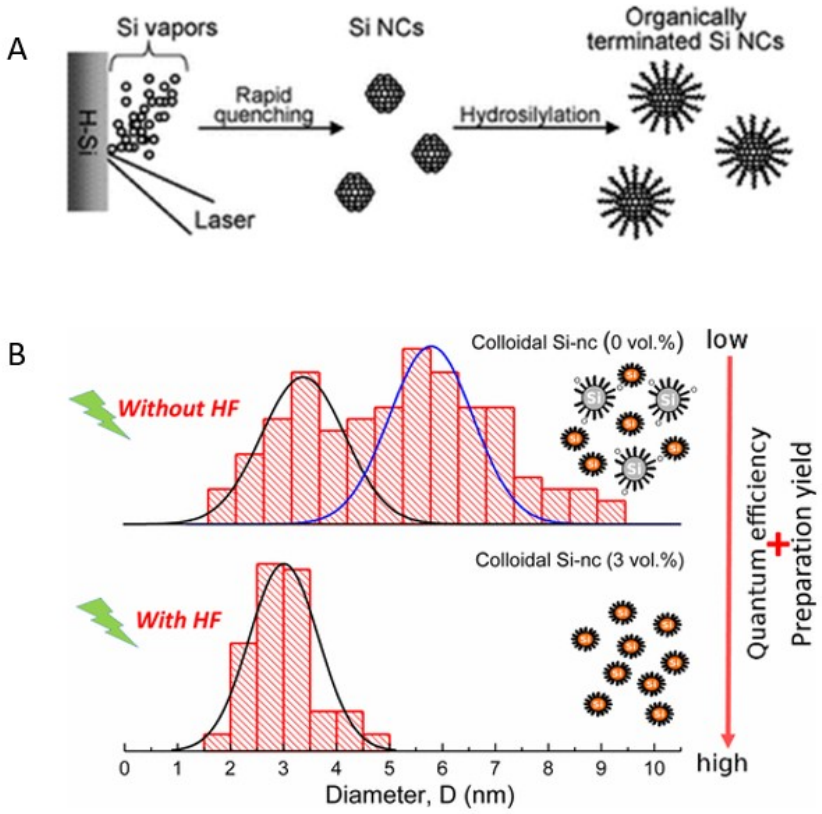

Figure 1. 3 a) Representative top-down approaches for the synthesis of SiNPs by liquid-phase laser ablation. Reprinted with permission from Ghosh, B.; Shirahata, N. *Science and Technology of Advanced Materials* **2014**, *15* (1), 014207. b) Laser ablation by pulsed-UV-laser irradiation in a liquid medium with and without HF. Adapted with permission from *J. Phys. Chem. C* **2017**, 121, 15, 8623–8629. Copyright 2017 American Chemical Society.

Upon first inspection, top-down methods appear very appealing because they employ readily available, safely handled, high purity starting materials (i.e., Si wafers), and offer

straightforward, rapid, and cost-effective approaches that may be amenable with mass-production. Unfortunately, many procedures employ HF etching, provide very small material quantities, and products suffer from large size dispersion and low PLQYs. These factors make them the least-desirable option of those presented here for applications requiring near monodisperse SiNPs that exhibit high luminescence efficiencies; however, this general approach has proven useful in preparing other silicon nanostructures.[83]

1.2.4 Solution-Reduction

Given the versatility and prevalence of solution-phase nanomaterial synthesis, it is not surprising that many "wet-chemical" synthesis methods for producing SiNPs have been reported and some of these approaches even come with substantial controversy.[63, 84, 85, 96] A common and well-established method for synthesizing SiNPs in solution involves the reaction of silicon halides (e.g., SiX_4; X = Cl, Br, I) with a strong reducing agent in the presence of a "capping agent". The liquid/solution phase strategy was originally inspired by work by Heath who used sodium dispersion to simultaneously reduce $SiCl_4$ and octyltrichlorosilane at high temperatures (385 ºC) and pressures (> 100 atm) to produce large polydisperse SiNPs (d = 5 - 3000 nm).[31] Wilcoxon et al. subsequently reduced silicon halides at room temperature and atmospheric pressure by reacting $LiAlH_4$ with $SiCl_4$ to produce SiNPs in the presence of tetraoctylammonium bromide (TOAB).[63] The SiNPs produced ranged from 2 - 10 nm in diameter and exhibited PL_{max} emissions of 350 – 700 nm, however, the polydispersity of the SiNPs was not mentioned. Unfortunately, the reaction as presented comes with the added hazard of producing significant quantities of pyrophoric SiH_4 (incorrectly identified as hydrogen in the original report) as a side product.[86, 87] As such, using

hydride-based reducing agents in comparatively high concentrations is ill-advised for the preparation of SiNPs.

Still, important, and impressive advances using solution-phase reactions employing hydride-based reducing agents have been achieved. The Tilley group improved upon the size distribution and the colloidal stability of the particles reported by Wilcoxon by employing a 1-heptene capping agent that was introduced via Pt-catalysed hydrosilylation. This procedure provided 1.8 nm diameter SiNPs showing a 11% size polydispersity and PL_{max} of 290 nm.[64] As is the case for the products of other syntheses, surface passivation with organic ligands can provide fluorescent SiNPs with improved quantum yield and defining the strength of the reducing agent can offer some control over the NP size.[65] Tilley et al. also showed that particle size could be changed from 1.6 to 2.5 nm using $LiAlH_4$ and $NaBH_4$, with resulting PL_{max} of 347 and 352, respectively.[66] Rosso-Vasic et al. went on to demonstrate this reaction could be scaled to produce 100s of mg quantities.[88]

To circumvent the obvious challenges/hazards associated with hydride-based reductants while embracing the potential benefits of solution-based syntheses, the Kauzlarich group turned to sodium naphthalide and prepared colloidally stable, 5.2 nm (36% polydispersity) diameter particles from $SiCl_4$ in glyme that were surface capped with 1-octanol; the resulting SiNPs showed PL in the range of 410 - 430 nm, however no PLQY data was provided.[30] It was later demonstrated by these researchers that the same general approach could offer some degree of size control by varying the ratio of starting materials. Particle sizes ranged from 3 to 9 nm with polydispersities of 15 - 25% and a range of PL_{max} from 375 - 425 nm with PLQYs of ca. 12%.[62]

Even more gentle reducing agents (e.g., trisodium citrate) used in solution-phase syntheses of non-silicon nanoparticles have been reported to reduce silicon alkoxide precursors (e.g., 3-

aminopropyl trimethoxysilane). Unfortunately, the data provided in these contributions are inconclusive[68, 85] and independent investigations found the luminescent material reported to be SiNPs could be realized even in the absence of any silicon source bringing the identity of the products of these reactions into question.[69]

A unique solution-based strategy for preparing SiNPs involves the reaction of metal silicides (M = Mg, K, or Na) or so-called Zintl phases a variety of reagents. The first report saw the Yang et al. react $SiCl_4$ with Mg_2Si in refluxing glyme followed by functionalization using Grignard reagents to provide alkyl-terminated SiNPs with in the size regime of 2 - 5 nm.[70] Subsequently, Pettigrew et al. reported the preparation of SiNPs upon reaction of magnesium silicide (i.e., Mg_2Si) with bromine, followed by functionalization with n-butyl lithium. The apparent 4.5 nm diameter particles showed blue (340 - 390 nm) PL arising from a short-lived excited state.[71] Highlighting the challenges associated SiNP syntheses, Wilbrink et al. performed the identical reaction without including the Mg_2Si silicon source and observed similar TEM and PL characteristics.[71] Clearly, the approach to preparing SiNPs is complex and should be revisited to elucidate the mechanism and identity of the products. The Kauzlarich group also developed procedures to prepare Mn- and Fe-doped SiNPs upon reaction of doped Zintl phases (i.e., Na_4Si_4) and NH_4Br which were coated with allylamine and dextran that could be used for multimodal (i.e., magnetic resonance and luminescence) biological imaging. Particles prepared using this approach showed diameter of 3 - 4 nm with a polydispersity of 23 – 37% as well as a broad PL ranging peaking at 441 nm, yielding PLQY from 1-18 %.[72, 73]

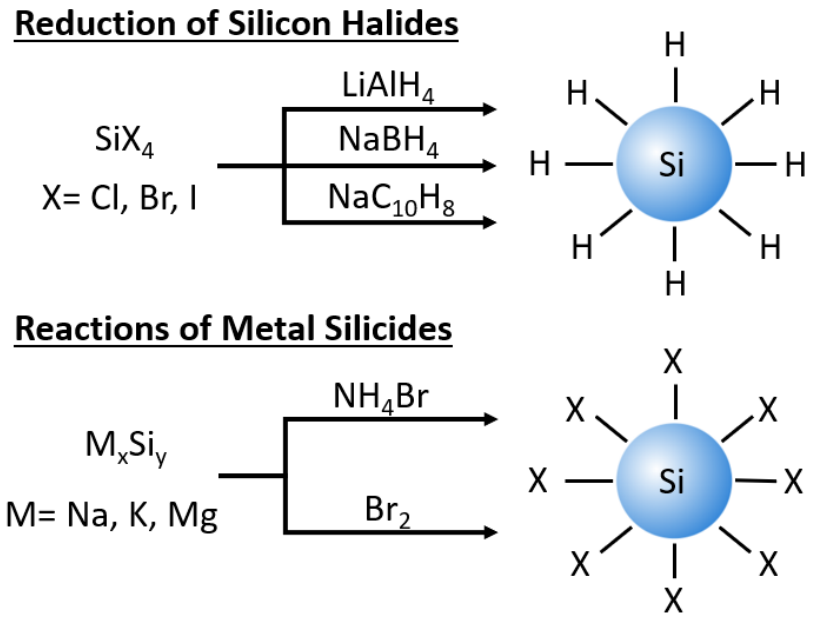

Figure 1. 4 Common solution-based methods for preparing SiNPs.

Preparing SiNPs via solution-phase reduction of silicon halides, as well as reactions of metal silicides coms with common challenges. Currently these approaches provide very small material quantities and can require specialized precursors (e.g., metal silicides). In addition, products often contain unidentified impurities that may, or may not, be nitrogen-based that lead SiNPs that exhibit excitation wavelength dependent blue PL_{max} that arise from a short-lived excited state that resembles the F-band emission of other silicon nanomaterials.[32] While these factors do not preclude using these NPs in a variety of specialized applications, they are not well-suited for those that require tuning throughout the visible spectrum.

1.3.0 The Influence of Nanocrystal Structure

It is no surprise that the nanomaterial structure dictates material properties;[57, 89, 90] this is well illustrated by the observation that the PL_{max} of core@shell SiNPs bearing a shell of graded composition/structure differs from that of NPs bearing an epitaxially grown shell. [123] In this section, SiNP properties are considered in the context of their structure - the nanoparticle core (i.e., composition, degree of crystallinity) as well as the surface groups attached to it (Figure 1.5). The size and crystallinity of, as well as structural strain within the SiNP core, can be controlled by defining the synthesis method/parameters (e.g., plasma power during synthesis, etching protocols during liberation, temperature, etc.)[92-94] as well as applying external pressure through a diamond anvil.[131] While the nature of surface groups is defined by their molecular structure, as well as the method used to tether them to the particle. Oxidation can also influence SiNP surface and core structures and hence plays a crucial role in material properties.

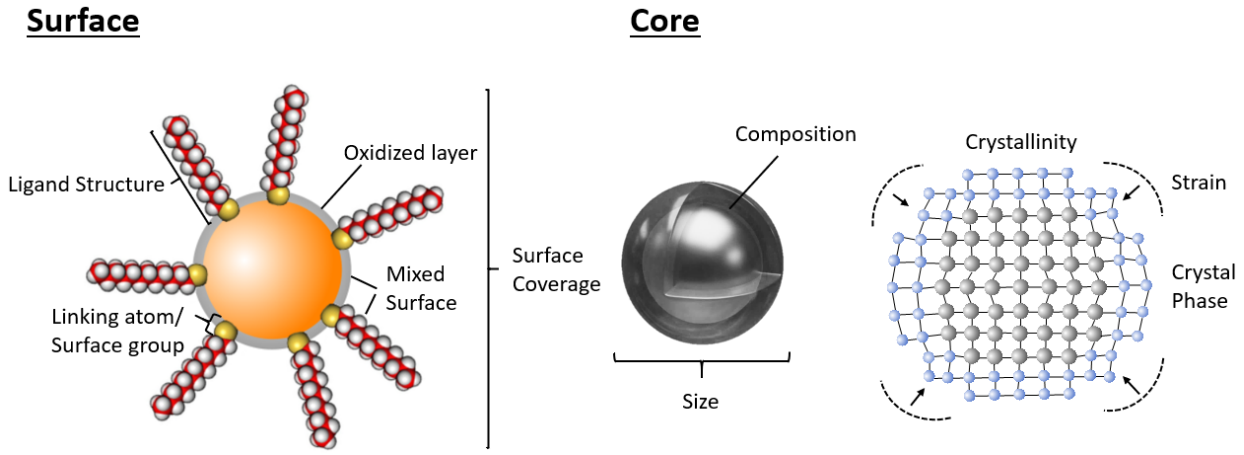

Figure 1. 5 An illustration of the structural components that make up SiNPs and the parameters that can be altered to define properties.

1.3.1 The Influence of Silicon Nanoparticle Core Structure

As is the case for all QDs, the physical dimensions of the semiconductor core influence the optoelectronic response (i.e., PL); tailoring this aspect of SiNPs can be achieved by defining the synthesis conditions[43, 53, 95] as well as through post-synthesis modification.[20, 38, 40, 96] When preparing SiNPs from SROs like SiO_x or HSQ, particle size is defined by peak processing/annealing temperature, particle shape is tied to the heating profile, and crystallinity is impacted by post-synthesis etching.[18, 43, 95, 97] Similarly, plasma syntheses offer considerable control over SiNP morphology and structure; size is defined by controlling precursor concentration and plasma residence time, while crystallinity is dictated by the power applied.[53, 98, 99]

To date, much of the work related to evaluating SiNP structure has focused on size-property relationship; however, some reports have also examined the roles of size uniformity and internal structure. In 2013, pair distribution function (PDF) analysis was used to interrogate Si-Si-Si bond angles and structural coherence within SiNPs; this study showed the internal structure of small particles was disordered and, as the particle sizes increased, the Si atoms became increasingly ordered, as evidenced by more consistent Si-Si-Si bond angles and a Si-Si coordination number closer to 4.[100] Raman spectra combined with structural modelling of plasma synthesized SiNPs revealed a thin (two monolayer) amorphous shell on the outer surface.[98] Together, these studies point to complexities of the SiNP structure that were recently evaluated for HSQ-derived SiNPs using ^{29}Si Solid State NMR (Figure 1.6).[93] This investigation showed these SiNPs consist of a radially graded core structure, with a relatively well-ordered core, semi-ordered subsurface, and disordered surface.[93] While the structure was generally consistent across sizes (Figure 1.6c), only very small (i.e., ca. 1.2 nm) ordered domains were observed in the smallest SiNPs (i.e., d = 3 nm).[93]

This picture of SiNP structure will be invoked in the following discussion regarding the influence of SiNP structure on PL response.

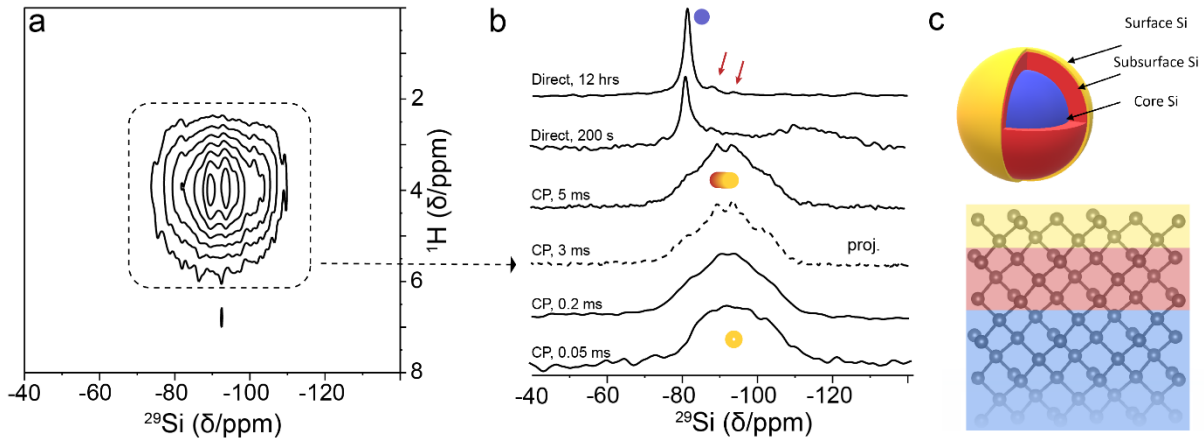

Figure 1. 6 a) A ^{29}Si[^{1}H] HETCOR MAS NMR spectrum of 64 nm H-SiNPs. b) An overlay of ^{29}Si MAS NMR and ^{29}Si[^{1}H] CP MAS NMR of 64 nm H-SiNPs for the indicated mixing times. Arrows in the top spectrum highlight subsurface NMR features in the direct ^{29}Si MAS NMR. c) A representation of the layered H-SiNP structure consisting of an amorphous surface, semi-ordered subsurface, and crystalline core. Adapted with permission from *Chem. Mater.* **2019**, 31, 3, 678–688. Copyright 2019 American Chemical Society.

1.3.2 Impact of Structure on Optical Response

SiNPs often are categorized broadly into two groups: those that exhibit size-dependent PL response and long (i.e., microsecond) excited state lifetimes (so-called S-band emitters) and those that show largely size-independent PL and short (i.e., nanosecond) excited state lifetimes (so-called F-band emitters).[101] As is typical for QDs, the size-dependent emission is often attributed

to carrier quantum confinement.[17, 19, 101, 102] Despite a general trend, the relationship between size and PL_{max} is often not as "clear cut" as for prototypical Cd-based QDs.[102] It has been proposed that this apparent material difference is related, in part, to size-dependent quantum yields that shift in the PL_{max} as a function of the SiNP size distribution.[17]

Despite the established complexities of the SiNP structure noted above, these materials are still typically considered crystalline or amorphous – this is an important distinction because bulk amorphous and bulk crystalline Si exhibit different band structures.[103] In crystalline Si atoms are tetrahedrally coordinated and there is long range order. In the amorphous-phase, some atoms are not four-fold coordinated and this disorder leads to defects. Crystalline Si is an indirect band gap semiconductor with E_g = 1.12 eV; amorphous Si is a direct band gap semiconductor with E_g = 1.75 eV.[104] While quantum confinement of carriers occurs in crystalline and amorphous SiNPs,[105] disordered (i.e., amorphous) systems typically show larger band gaps and smaller Stokes shifts than their ordered (i.e., crystalline) counterparts.[106] Anthony et al. demonstrated PLQYs are impacted by the SiNP core structure - PLQYs are considerably lower for amorphous SiNPs (prepared using low input power plasma) than crystalline systems (prepared using high input power plasma) (Figures 1.7 a and b).[99]

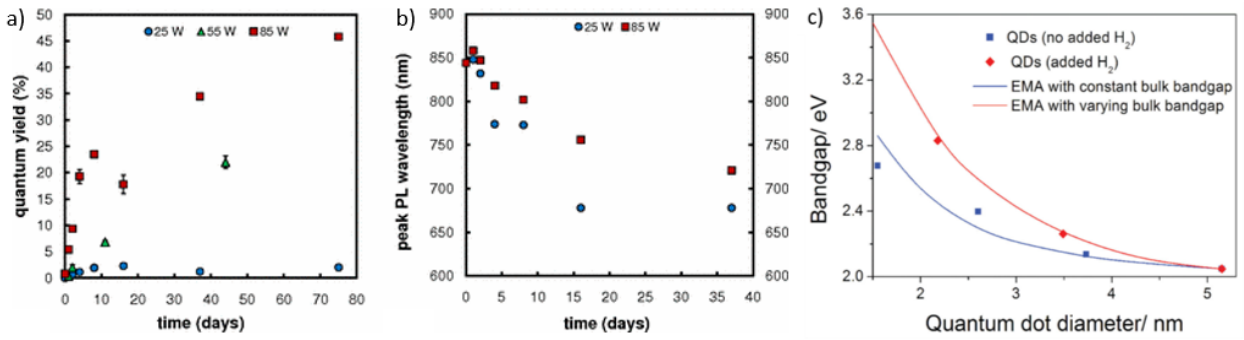

Figure 1. 7 a) The relationship between SiNP PLQY and input power used during plasma synthesis. b) A comparison of the PL spectra of crystalline (red) and amorphous (blue) plasma synthesis prepared SiNPs. c) The relationship between amorphous SiNP diameter and band gap. Images a) and b) reprinted with permission from Anthony, R.; Kortshagen, U., *Phys. Rev. B*, **2009**, *80*, 11540. DOI: 10.1103/PhysRevB.80.115407. Copyright 2009 by the American Physical Society. Image c) reprinted from *Adv. Mater.*, **2015**, *27*, 8011-8016. Licensed under CC BY.

Amorphous SiNPs are attractive because hydrogenation alters their core composition, band gap, and PL response (Figure 1.7 c).[107] Askari et al. demonstrated particle size-dependent hydrogenation and that increased hydrogenation caused band gap widening.[107] The authors did not report the relationship between degree of hydrogenation and PLQY; clearly, this would be an interesting topic for future study, as it has long been proposed that hydrogenation increases SRO PL efficiency and could lead to further tuning of optical response.[108] Like hydrogenation, crystal phase impacts the band gap of bulk silicon and could, in principle, define SiNP PL. In addition, bulk Si allotropes that exhibit direct band gaps in the range of 0.39 - 1.25 eV have been proposed – these energies are in stark contrast to the indirect band gap (1.12 eV) of the ubiquitous diamond-cubic Si that typically comprises SiNPs.[109] Unfortunately, it is currently not possible to access

these Si phases using traditional preparation methods, hence studying their impact on SiNP properties (e.g., PL_{max}, PLQY, etc.) requires a different approach. An indirect and qualitative evaluation of the impact of crystal structure can be performed by monitoring pressure dependence of SiNP PL as reported by Hannah et al. who noted the PL_{max} red-shifted and the PL_{FWHM} broadened with increased pressure.[110] Despite identifying a number of crystal phases within the SiNP samples, the PL of these phases were not reported presumably because the complexities of obtaining phase pure systems. In another independent investigation, tensile strain induced a blue-shift in the PL_{max} that arises from a strain-induced direct band gap.[111] Interestingly, the authors found the impact of tensile strain could be reversed with applied pressure.

The structural uniformity of the SiNP core and its impact on PL_{max} are also intriguing. Many of the aforementioned studies assume uniform internal SiNP structure – this is not necessarily accurate.[112] In the absence of conclusive evidence, one study examining the PL from plasma-synthesized SiNPs suggested an amorphous layer encapsulating the crystalline core could give rise to a high energy fast-PL band (i.e., F-band).[98] It is not clear whether these conclusions could be readily invoked to explain the optical properties of SiNPs prepared using other methods.[153,154] Petkov et al. also reported a correlation between SiNP structure and PL response; in the context of the complex nature of the materials it was broadly attributed to carrier confinement, under-coordinated surface atoms, and local structural variabilities.[100] To gain insight into the structural uniformity of the SiNP core and its influence on PL response, we evaluated SiNP optical properties as a function of crystallite size (determined using X-ray diffraction) and particle diameter (determined using electron microscopy).[92] SiNPs comprised of larger crystallites showed longer-lived, lower energy PL and the effective mass approximation (EMA) provided reasonable predictions of the SiNP PL when using the crystallite size (Figure 1.8).

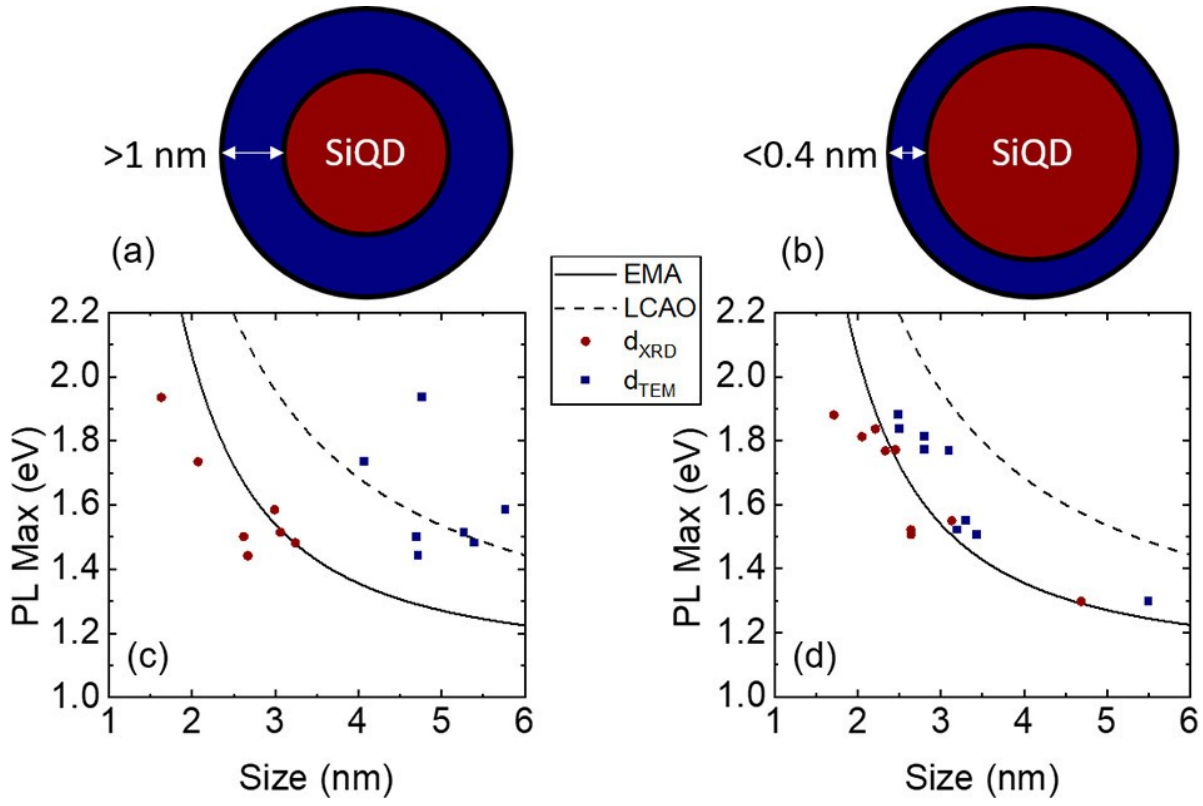

Figure 1. 8 Schematic representations of SiNPs with (a) a significant difference between the overall particle diameter and crystallite size and (b) a similar overall particle diameter and crystallite size. The photoluminescence emission maxima of the two types of SiNPs was plotted as a function of overall particle size (d_{TEM}) and crystalline domain size (d_{XRD}). Adapted with permission from *Chem. Mater.* **2020**, 32, 16, 6838–6846. Copyright 2020 of the American Chemical Society.

The combination of the established low PLQYs noted for amorphous SiNPs,[99] a graded internal structure of SiNPs prepared via thermally processing (e.g., annealing) of SROs, and the etchant-based surface functionalization methods in which reagents remove the outer SiNP surface provide impressive PLQYs provide insight into how careful consideration of structural features

that could improve SiNP optical response.[46, 92, 93, 113] In fact, surface functionalization was achieved upon exposure of hydrogenated SiNPs to PCl_5[46] or XeF_2 [113] in the presence of terminal alkenes. These reagents etch bulk silicon surfaces and remove/minimize surface defects on the SiNP surfaces while providing reactive sites for tethering alkyl surface groups.[114] The resulting materials showed impressive PLQYs of up to 62 and 68%, respectively.[46], 113

1.4. Doping SiNPs

Incorporating low concentrations (e.g., 10^{13} - 10^{18} atoms cm^{-3}) of impurities (i.e., dopants) has provided exquisite tailoring of bulk silicon electronic characteristics.[115] Suffice it to say, it is common knowledge that introducing dopants such as phosphorus (P) or boron (B) can provide desired conductivity (Figure 1.9) and has facilitated the fabrication of fundamental devices such as diodes and transistors.[116] This doping is readily achieved in bulk materials with exceptional precision. It is also important to recall that doping does not always come with positive outcomes, some impurities (e.g., Au) induce "deep defects" that compromise favourable electronic characteristics.[117] Given the benefits afforded by doping in bulk silicon, it is of no surprise that it has been explored as method for tailoring material properties at the nanoscale.

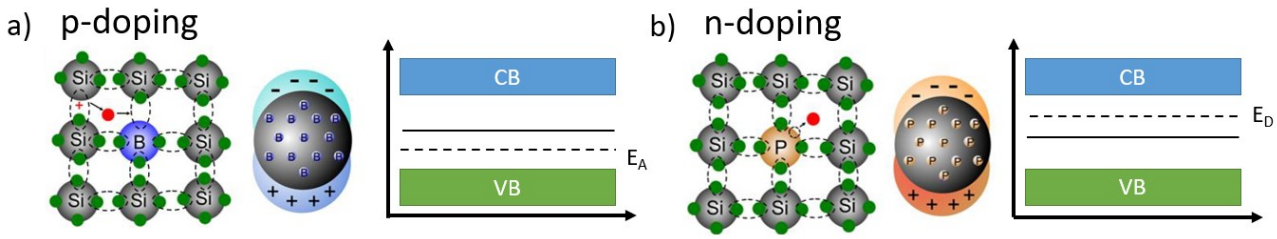

Figure 1. 9 Schematic representation of a) p-type and b) n-type doped silicon. In p-type doping with B used as an example, when substituted into the Si lattice it generates a free hole, resulting in an acceptor energy level (E_A) near the valence band (VB). In n-type doping with P is used as an example, when substituted into the Si lattice it generates a free electron, resulting in a donor energy (E_D) level near the conductance band (CB).

As is the case for bulk Si, nanoscale doping must be done with the greatest possible precision if properties are to be predictably controlled. The key material parameters at play when doping NPs have been summarized elsewhere and include dopant location, synthesis method employed and characterization of the resulting materials.[118] Clearly, establishing methods that allow definition of these characteristics is paramount to understanding, defining, and exploiting the resultant material properties. However, it is important to recall that regardless of how the NP is prepared, physical dimensions play a role in defining the dopant location. For example, doped SiNPs that are strongly confined (i.e., $d < 6$ nm) experience "self-purification" that arises because of stress within the crystalline NP core induced by substitutional dopants causes dopants to migrate to the surface.[119-121] Clearly, doping nanoparticles is challenging and important.

There are some reports describing doping of SiNPs with various species (e.g., B, P, Sb) that are embedded in a matrix (e.g., oxides, oxynitrides, etc.).[106, 122] These important and

foundational contributions point to the potential that doping holds; however, material complexities require use of indirect evaluation (e.g., nuclear magnetic resonance, energy dispersive X-ray spectroscopy, X-ray photoelectron spectroscopy) of dopant species, concentration, and location. While doping freestanding SiNPs comes with some of the same challenges (e.g., accurate determination of dopant concentration, locating low Z elements, material uniformity, etc.) in many cases characterization of these systems can be more definitive and property correlation more straightforward; hence, we have chosen to limit this discussion to doped freestanding SiNPs.

Traditional dopants employed in bulk Si (e.g., P, B), as well as others (e.g., Sb) have been introduced to SiNPs using plasma,[123-126] chemical vapor deposition (CVD),[127] solution,[65, 73] laser pyrolysis,[128] thermal decomposition,[129] electrochemical etching[130] and co-sputtering methods.[130, 131, 132] In 2013, Borowik et al. prepared P-doped SiNPs on the surface of n-type silicon substrates using plasma-enhanced CVD with silane and phosphine precursors.[133] These supported SiNPs were formed in the size regime of 2 – 50 nm and volumetric doping concentrations (N_D) of 10^{20} - 10^{21} cm^{-3} were assumed based upon precursor ratios. Since only limited characterization (i.e., SEM, electrical measurements) was provided it is not possible to comment on the influence of dopant location, crystallinity, hydrogenation, etc. Still, the authors provide a glimpse of the importance of dopant concentration. They found the depletion layer width within the resulting nanocrystal junction that existed between the particle and the underlying substrate varied with SiNP dopant concentration and that the depletion charge increased linearly with NP size.

Almeida et al. employed co-sputtering of Si, SiO_2, and P_2O_5 to fabricate silicon-rich phosphosilicate glass thin films that they annealed to obtain oxide-embedded P-doped SiNPs; freestanding H-terminated SiNPs (d = 5.0±1.2 nm) doped with P (0.4 at. %) were liberated using HF etching.[132] Electron pair resonance (EPR) analysis of the oxide-embedded and freestanding

particles is core to this study. Using fingerprinting methods, the authors concluded P atoms resided in substitutional sites. They also related the magnitude of the hyperfine splitting in the EPR spectra to the NP size. Additionally, they demonstrated the environment/surface of the NP (e.g., oxide-embedded, freestanding in air, freestanding in argon) impacts the doping efficiency and proposed surface water and oxygen molecules could adhere (reversibly) to the NP surface and provide states that trap electrons supplied by the P donors.[119-121]

Reaching beyond the tuning of electronic properties, doping SiNPs provides unique opportunities in tailoring optical response that can benefit advanced photovoltaic devices and plasmonic materials. Computational data suggest doping can offer fine tuning of optical properties to facilitate optimized absorption of the solar spectrum;[119] doping SiNPs also raises the possibility for all-silicon tandem solar cells that require p- and n-type SiNPs.[104, 115, 130, 134, 135] For applications involving the formation of a p/n junctions and conductivity, doping concentration and surface chemistry play important roles. Rocks et al. showed that upon controlled oxidation of p- and n-type SiNPs synthesized by electrochemical etching of doped wafers, dramatic changes in the band gap and Fermi level were observed.[135] For oxidized p-type SiNPs, improvement in fill factor and efficiency were observed for test devices, while oxidized n-type SiNPs showed little improvement to fill factor and a marked decrease in efficiency. The same research group discovered that the electronic structure of doped SiNPs and perovskite $MAPbI_3$ films, ideally aligned to form a Type-I heterojunction, showed dramatic increase in short circuit current density, power conversion efficiencies, and slowed the chemical decomposition of perovskite.[130]

Doping of SiNPs also comes with unique properties not accessible using the bulk material. Using non-thermal plasma methods, Rowe et al. examined how incorporating dopants at concentrations exceeding the bulk solid solubility limit influenced material properties.[125] These

so-called hyperdoped particles can exhibit localized surface plasmon resonance (LSPR) that arises from the collective oscillation of free charge carriers in response to exposure to an external electromagnetic field (Figure 1.10 a). This phenomenon is most commonly associated with noble metals (e.g., gold), and offers the opportunity to overcome the diffraction limit of standard optical fibres concentrating light into exceptionally small areas.[136] Unlike noble metals whose plasmonic response is typically tuned by defining particle size and shape, LSPR of doped QDs can be tuned by controlling dopant distribution and carrier concentration.[136, 137] The usefulness of these materials was demonstrated by Ni et al. who incorporated plasmonic B-doped SiNPs into graphene-based hybrid phototransistors and achieved high-sensitivity ultrabroadband photodetection. The hybridized graphene-SiNP structure allowed absorption of light in the UV-NIR region while the B-doped SiNP LSPR extended the detection range to the MIR (Figure 1.10 b).[138]

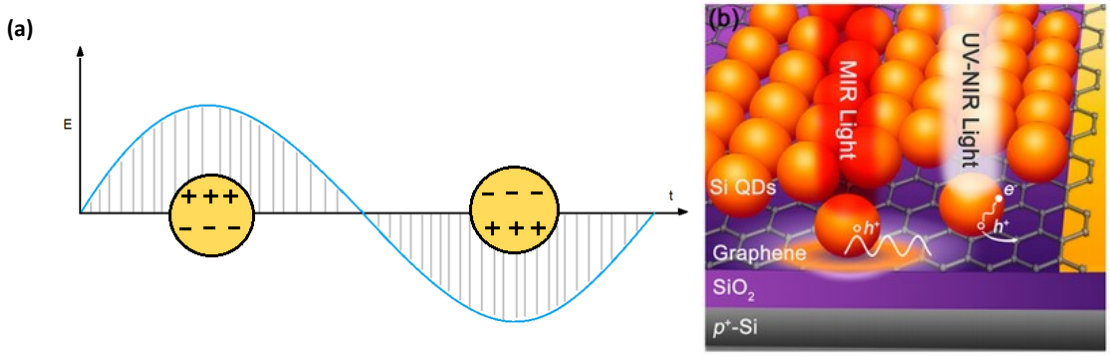

Figure 1. 10 a) Representation of charge carriers oscillating in an electromagnetic field producing LSPR b) Schematic diagram of the structure of the hybrid phototransistor based on B-doped Si QDs and graphene. Adapted with permission from *ACS Nano* **2017**, 11, 10, 9854–9862. Copyright 2017 American Chemistry Society.

Zhou et al. extended the scope of plasmonic SiNPs and demonstrated that n- and p-type doping of SiNPs could provide LSPR response using 13 nm diameter SiNPs containing P (4 – 18 atomic % dopant) and B (7 – 31 atomic % dopant). Interestingly, the authors indicate that full surface oxidation of both types of NPs was necessary to realize an LSPR response and suggested oxidation lowered the surface defect concentration.[123] In a subsequent study, Kramer et al. noted B-doped SiNPs required oxidation to realize LSPR, however, for P-doped SiNPs oxidation was not necessary. This difference in behaviour was attributed to dopant location; P atoms within the SiNPs resided primarily in substitutional sites while B atoms were primarily in surface locations. [165] This proposal was further supported by an independent study by Ni et al.[126] Recently, Rohani et al. used a laser ablation to produce SiNPs hyper-doped with B. This kinetically controlled synthesis method provided high concentrations of B atoms in substitutional sites and as such, these QDs showed LSPR in their native (i.e., non-oxidized) state.[128] This series of reports involving hyperdoped SiNPs prepared using different methods points to the complexities of these systems and the importance of controlling dopant location.

It is not surprising that, in addition to impacting SiNP electronic and plasmonic properties, dopants can also strongly influence the material optical properties, and that the optical response is closely related to identity of the dopant(s) as well as their position and concentration within the particles. Dopant-induced quenching of SiNP PL and/or reduction of PLQY is well established and many studies have aimed to eliminate dopants/impurities to improve PL performance.[139, 140, 141] In some cases, dopant atoms can lead to non-radiative processes such as Auger recombination;[140] strain induced defects arising from differences in the sizes of host silicon and dopant atoms have also been implicated and may act as non-radiative recombination centres.[140, 142, 143] Interstitial defects can also to lead to a loss of PL.[140, 142, 143] While this may paint a picture

that dopants compromise SiNP PL, this is not always the case and typically occurs at comparatively high concentrations (i.e., > 3 at. %).[120, 144] Interestingly, there are reports indicating that introducing low concentrations (<1 atomic %) of B or P atoms leads to increased PLQY while the excited state lifetimes remained in the microsecond region.[118, 144, 145] These observations are consistent with dopants passivating dangling bonds on the SiNP surfaces and suppressing the associated non-radiative recombination pathway.[120, 146] Somewhat surprisingly, even hyperdoped SiNPs can exhibit PL as demonstrated by Limpens and Neale for P-doped SiNPs.[142] The explanation provided by the authors is, for very small SiNPs (d < 6 nm) the large binding energy of dopant-induced carriers in highly confined systems leads to negligible rates of Auger recombination leading to the appearance of PL. In the same study, the authors note that larger SiNPs (i.e., d > 6 nm) show dramatically reduced PL response; the authors suggest the weak luminescence arises from a small subset (i.e., impurity) of non-doped SiNPs.[141, 142] Together, these examples highlight the importance of complications associated with controlling dopant concentration and doping uniformity and underscores the importance of careful and thoughtful material characterization and evaluation.

To this point in our doping discussion, we have focused on SiNPs doped with a single species. Co-doping also offers intriguing possibilities and addresses some of the perceived challenges associated with PL quenching.[147] Co-doped SiNPs are typically prepared with approximately equal concentrations of B and P in each particle. The resulting charge compensation makes it possible to realize substantially higher dopant concentrations than when single dopant species are used and this same charge compensation leads to a significant reduction in the free carriers leading to a reduction in Auger recombination rates to values that approach that of intrinsic Si.[192] The Fujii group used co-sputtering to prepare B and P co-doped SiNPs (d = 1 – 14 nm) that

show size dependent PL (670 - 1350 nm).[148] The PL emission of the co-doped particles were red-shifted as compared to intrinsic silicon. It was observed that the PLQY increased from 1 – 13% for diameters of 1 – 2.8 nm, then decreases dramatically with increasing diameter. The authors attributed this to an increase in the fraction of "not-perfectly compensated" NCs in which Auger recombination becomes the dominant emission pathway.[148] In a subsequent study they define a critical size for carrier delocalization: co-doped SiNPs smaller than 6 nm in diameter show negligible Auger recombination due to localization of the dopant-induced electrons and SiNPs with diameters larger than 6 nm, activation energies are such that dopants induce majority free-carriers leading to altered photophysics and quenched PL.[141]

Realizing near-infrared (NIR) PL is particularly desirable for luminescence-based bioimaging because interference from auto-fluorescence background can be significantly reduced.[149] Nanoscale Si is particularly attractive due to its low toxicity, long-lived excited states that can provide time gated imaging and co-doping now provides access to the NIR spectral region.[150] Fujii et al. demonstrated solvent-induced self-assembly of B/P co-doped SiNPs followed by silica encapsulation that provided supramolecular particles showing PL_{max} in the red-to-NIR (790 nm) with a relative PLQY of 2.3 % and the silica coating presents the opportunity to functionalize the assembly surfaces with a variety of molecules that could facilitate targeted imaging.[151] The authors observed a decrease in PL lifetime, which they attributed to an energy-transfer between the agglomerated SiNPs, where excitons could recombine nonradiatively in "dark" SiNPs. In a complementary study, Limpens et al. produced P and B co-doped SiNPs (d = 2.9-7.3 nm) using non-thermal plasma. Particles larger than 4 nm prepared in this way showed NIR emission and PLQYs similar to the assemblies prepared using the co-sputtering method (~12%).[152]

Moving beyond B and P dopants, Chandra et al. incorporated transition metal dopants (i.e., Co, Mn, and Ni) into oleophilic SiNPs using thermal disproportionation of a hydrosilicate gel preloaded with metal ions. The resulting octadecyl-capped SiNPs exhibited diameters of 3 - 8 nm and contained sub-0.2 atomic % dopant based upon ICP-OES analysis. The particles grown at 1100 °C exhibited only minor red-shifts in PL_{max} upon incorporation of the transition metals as compared to intrinsic SiNPs (Mn = 985 nm, Ni = 992 nm and Co = 1000 nm corresponding to shifts of 67, 74 and 82 nm), however a significant red-shift was seen in particles grown at 900 °C (Mn = 984 nm and Co = 928 nm corresponding to a shift of 278 and 222 nm). The PLQY for the Co-doped system approached 26%, however the PLQY of the Mn and Ni doped systems were only 8 and 5%, respectively, the authors attributed the decrease in PLQYs to nonradiative pathways induced by the doping energy levels.[129] McVey et al. also explored incorporating transition metal doping and introduced Cu into SiNPs using a solution-based method in which Si and Cu precursors were co-reduced using hydride-based reagents in the presence of amine surfactants. The resulting particles were 2.5 nm in diameter with an estimated average of 2-6 dopant atoms per SiNP based upon ICP-MS analyses. The resulting materials showed PL_{max} that varied with dopant concentration (438, 451 and 479 nm for dopant concentrations of 2, 4 and 6 dopants per NP) and exhibited a red-shift compared to undoped equivalents (PL_{max} = 418 nm) and the PLQY approached 22%.[153] It should be noted that dopant concentration in both studies was determined by bulk elemental analysis methods (ICP-OES and ICP-MS respectively) which cannot directly confirm if the dopants are incorporated into the NCs.

1.5.0 Controlling Particle Surface Chemistry

Prototypical tuning of quantum dot PL is achieved by defining the nanoparticle size (i.e., quantum confinement). This is also possible for SiNPs,[17] however, the origin of SiNP PL is complex and surfaces matter. As-synthesized SiNPs are often terminated with hydride (i.e., Si-H), halogen (i.e., Si-X; X=Cl or Br), and/or oxygen containing species (e.g., Si-OH, Si-O-Si, etc.). The established reactivities of these functional groups mean SiNPs are susceptible to oxidation; furthermore, they are not readily compatible with common solvents.[95] As such, surface SiNP modification has been widely explored and methods linking surface groups through Si-C,[113, 154] Si-X,[155-157] Si-N,[32] Si-O,[158, 159] Si-S,[160] and more recently Si-Ge[90] have been reported. Comprehensive reviews of SiNPs surface functionalization have appeared elsewhere;[4, 95, 161] the present discussion focuses on recent advances specifically related to tuning SiNP optical and electronic properties through the direct tailoring of surface species.

1.5.1 Tuning PL Emission Maximum

In 2014 Dasog et al. reported SiNP surface-chemistry dependent PL spanning the visible spectrum.[48] Alkyl-terminated SiNPs (d = 3−4 nm) prepared via hydrosilylation reactions under inert atmosphere exhibited a PL_{max} at 730 nm (red appearance). This emission arose from a long-lived (μs) excited state consistent with reports of so-called slow-band (S-band) emission and was attributed to a band gap transition; this luminescence also did not fade upon prolonged excitation. Equivalent alkyl-functionalized SiNPs prepared in air were partially surface oxidized and a PL_{max} at 630 nm (orange appearance) with a low energy shoulder at 710 nm. This PL emanated from

short-lived excited-states (ns) consistent with so-called fast-band (F-band) emission, did not fade with prolonged constant excitation, and was attributed to unidentified surface states.

In the same study, identical H-SiNPs were functionalized using other protocols to tune the PL_{max} (Figure 1.11 a). Exposure to trioctylphosphine provided trioctylphosphine oxide capped, oxidized SiNPs with a PL_{max}= 590 nm (yellow appearance) and an excited-state lifetime with nano and microsecond components. Reactions with CO_2 yielded blue/green emitting acetal-terminated SiNPs, while N-bonded dodecylamine-SiNPs provide blue PL. In both cases these materials showed excitation wavelength dependant PL_{max} attributed to complex surface chemistry and emission from short-lived excited states. Finally, reaction with diphenylamine provided green-emitting particles PL_{max}= 305 nm, however rapid loss of PL intensity upon excitation precluded acquisition of lifetime data. In all cases the exact emitting species was not identified, however, the authors reasonably attributed long-lived excited states (i.e., S-band) and short-lived excited states (i.e., F-band) to band gap and surface state transitions, respectively. It is also interesting, that in all cases involving surface states alone PL intensity decreased with prolonged excitation while emission from band gap transitions did not.

In 2015 Dasog et al. subsequently showed trace halide (i.e., Br, I, Cl) content impacts SiNP PL inducing red, yellow/orange, and blue emission, respectively (Figures 1.11 b, c).[155] Again, red-emitting SiNPs showed S-band type behaviour while yellow/orange-, and blue-emitting SiNPs showed short-lived excited states that were attributed to surface species. These observations highlight the important role of surfaces in SiNP PL.[155] Interestingly, Matsumoto et al. followed Dasog's investigations and showed that the PL of weakly emitting organic fluorophores could be enhanced via surface adsorption to SiNPs, reinforcing the idea that the surface bonded molecules are a reasonable explanation for the F-band emission.[161]

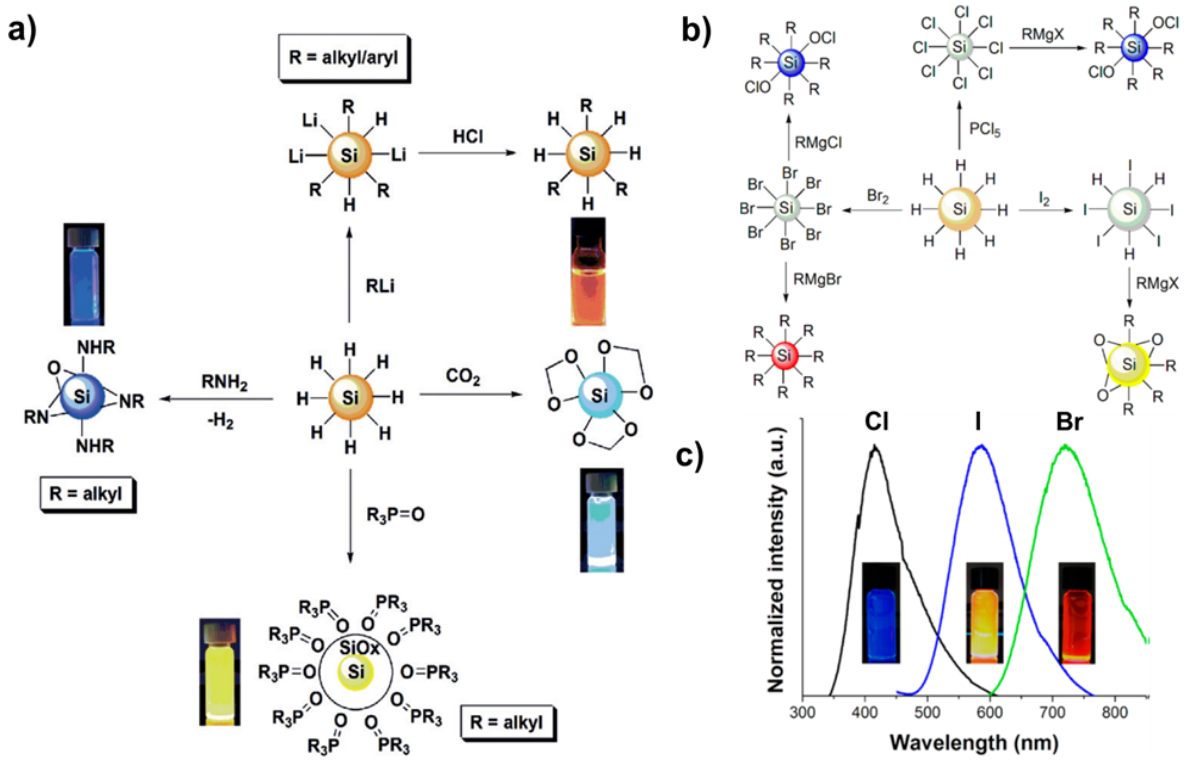

Figure 1. 11 a) Tuning photoluminescence by functionalizing H-SiNPs with alkyl, carbon dioxide, alkylamines, and alkylphosphine oxide. b) Representation of halogenation and alkylation of H-SiNPs and c) PL spectra of alkylated SiNPs bearing Cl, I, and Br surface species. Adapted with permission from *Ange. Chemie* **2015**, 55, 7, 2016 and *Chem. Mater.* **2015**, 27, 4, 1153–1156. Licensed under CC BY and copyright 2015 American Chemical Society.

In 2017, Sinelnikov et al. provided more insights on the influence of surface oxidation and amine moieties on PL response via temperature-dependent PL and time-resolved PL (TRPL; Figure 1.12).[162] Two sizes each (d_{avg} = 3 and 5 nm) of photoluminescent alkyl-terminated SiNPs (R-SiNPs; R = dodecyl; red) with negligible surface oxidation, partially oxidized alkyl-terminated SiNPs (*Ox*R-SiNPs; orange), and alkylamine-terminated SiNPs (RN-SiNPs; R = N-bonded alkyl and oxynitrides; blue) derived from identical Si-H terminated SiNPs were investigated.[162] For R- and *Ox*R-SiNPs the PL maxima red-shifted slightly for larger NPs and the PL blue-shifted upon decreasing the temperature from 377 to 37 K. This size- and temperature-dependent PL response is congruent with band gap-induced transitions and is consistent with the proposal that alkanes do not interfere with intrinsic core emission.[163] An emission mechanism involving exciton splitting (i.e., electrons were trapped in oxide surface states and recombined with holes in the valence band) was proposed for oxidized SiNPs because their PL lifetimes remained in the microsecond regime regardless of the temperature. In contrast, and consistent with other reports, the blue emission from RN-SiNPs was independent of the particle size and did not show substantial temperature dependence (and even red-shifted slightly).[29, 48, 158] Based on these observations, and the nanosecond lifetimes, the authors proposed a charge-transfer (CT) from the excited state of the SiNP to a high-energy silicon oxynitride surface state; subsequently, exciton recombination occurred entirely at the oxynitride surface state and is isolated from the SiNP core.

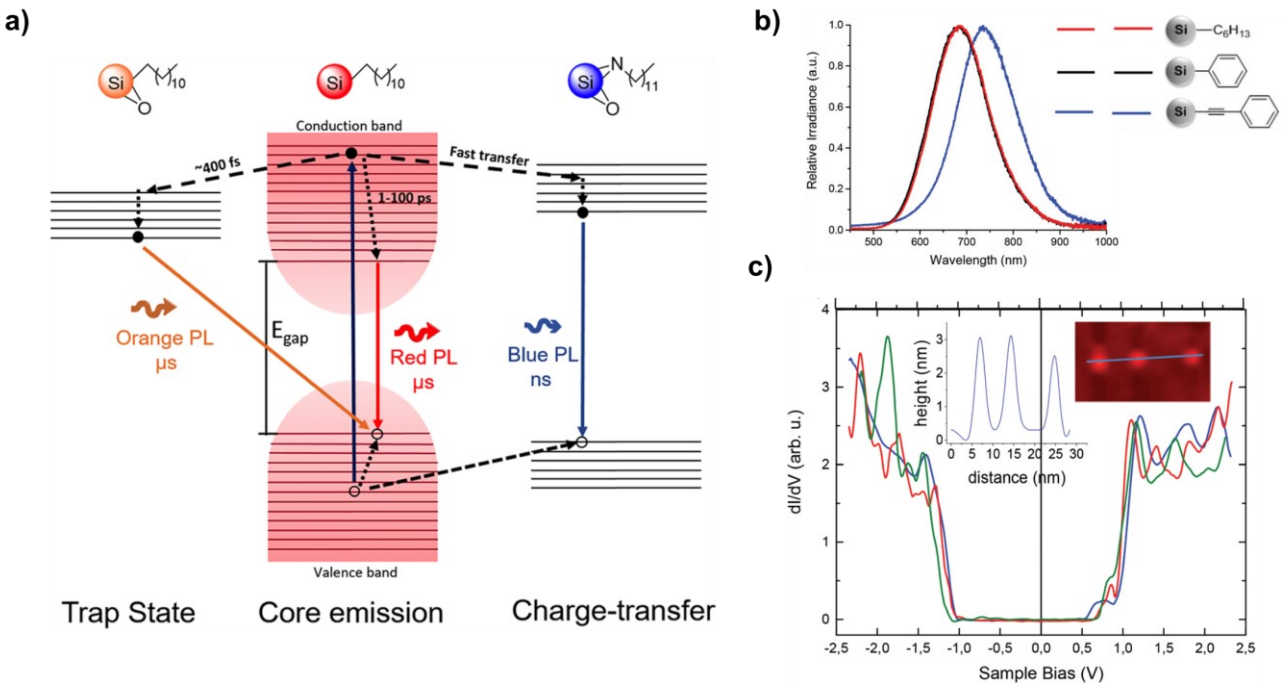

Figure 1. 12 a) Proposed emission mechanisms for SiNPs influenced by surface oxidation and oxynitride moieties. b) PL spectra of SiNPs functionalized with n-hexyllithium, phenyllithium, and lithium phenylacetylide. c) Tunnelling spectra of phenylacetylide-SiNPs. The inset shows the corresponding cross-section of some NCs on which the spectra was acquired. Adapted with permission from *ACS Photonics* **2017**, 4, 8, 1920–1929 and *Nanoscale*, **2016**, 8, 7849-7853. Copyright of 2017 American Chemical Society and 2016 CC BY-NC.

SiNP functionalization via reaction with organolithium reagents provided additional insight into the impact of surface groups and their structure on SiNP optical and electronic properties.[164] Höhlein et al. prepared solution processible SiNPs bearing aryl and alkynyl monolayer passivation and observed phenylacetylene functionalization resulted in red-shifted PL_{max} compared to equivalent SiNPs bearing hexyl or phenyl moieties (Figure 1.12 b), however, no explanation for the observation was provided.[165] Although, π–π stacking of conjugated surface groups (*e.g.,* poly-

3-hexylthiophene (P3HT),[156] styrene,[166, 167] naphthalene,[166] and allylbenzene[168]) led to SiNP aggregation and red-shifted PL_{max}. In a follow up study, Angi et al. investigated the phenylacetylene-functionalized SiNPs using scanning tunnelling spectroscopy and found an in-gap state near the conduction band edge that was attributed to the surface groups and shifts the PL_{max} to a lower energy (Figure 1.11 c).[165] The same authors extended this general approach and used the structure of the surface moiety to define the in-gap state energy and tuned the SiNP PLmax. [229] The selected examples noted here show that through appropriate definition of SiNP surface chemistry tailoring of SiNP PL_{max} may be achieved.

1.6 Thesis Scope

The preceding discussion has introduced the concepts of quantum dots and qualitative aspects of quantum confinement. Readers have also been provided with an overview of recent progress in the tailoring of SiNP optical and electronic properties via methodically designed synthesis methods that afford some control over composition (i.e., doping) and surface modification. This thesis focuses on tailoring the material properties of SiNPs through controlled incorporation of dopants into SiNPs which provides another important degree of freedom in tuning optoelectronic properties through the definition of the material electronic structure. Manipulation of key characteristics can allow tuning of optical and electronic properties of doped SiNPs: 1) surface chemistry, 2) particle dimensions, and 3) dopant concentration and distribution.

In Chapter 2 we aim to derivatize the surfaces of doped SiNPs obtained from the thermal processing of HSQ and boric acid. Surface modification of these SiNPs was achieved using a

phosphorous pentachloride etching induced reaction with alkoxy ligands of varied chain lengths. Throughout this investigation we assessed the SiNP surface chemistry of as-synthesized B-doped SiNPs through a combination of X-ray photoelectron spectroscopy (XPS), Fourier transform infrared spectroscopy (FTIR) and cross-polarization magic-angle spinning nuclear magnetic resonance spectroscopy (CP MAS NMR). The successful attachment of the alkoxy ligands to the surface of the particle is then assessed by FTIR, XPS and thermogravimetric analysis (TGA) and the change in photoluminescence emission is observed.

With a convenient method for tailoring the surface chemistry of B-doped SiNPs in hand, we turned our attention toward achieving size-controlled preparation of doped particles. This saw the development of a new diffusion-based post-synthesis doping method that drew inspiration from thermally-induced diffusion doping of bulk silicon. Chapter 3 describes a thermal diffusion-based post-synthesis doping method that exploits parent SiNPs with narrow size distributions, boric acid as the dopant source and hydrogen silsesquioxane as a capping agent. The role of annealing atmosphere and structural disorder within the SiNPs were found to strongly influence doping as determined by XRD, XPS and TGA. The method allows for control of particle size, dopant concentration and surface chemistry.

In Chapter 4 we attempt to provide control of the dopant location through the development of a monolayer doping method. This is achieved through the design of a molecular dopant precursor scaffold with self-capping properties which forms a monolayer on the precursor intrinsic SiNPs and allows for the shallow thermal-diffusion of dopants.

Finally, Chapter 5 summarizes the findings from the previous chapters and further explores relevant future research directions.

1.7 References

(1) Vidanapathirana, A. K. Use of Nanotechnology in Pregnancy. In *Encyclopedia of Nanotechnology*, Bhushan, B. Ed.; Springer Netherlands, 2014; pp 1-8.
(2) González-Díaz, J. B.; García-Martín, A.; García-Martín, J. M.; Cebollada, A.; Armelles, G.; Sepúlveda, B.; Alaverdyan, Y.; Käll, M. Plasmonic Au/Co/Au Nanosandwiches with Enhanced Magneto-optical Activity. *Small* **2008**, *4* (2), 202-205. DOI: https://doi.org/10.1002/smll.200700594.
(3) Jeevanandam, J.; Barhoum, A.; Chan, Y. S.; Dufresne, A.; Danquah, M. K. Review on nanoparticles and nanostructured materials: history, sources, toxicity and regulations. *Beilstein J Nanotechnol* **2018**, *9*, 1050-1074. DOI: 10.3762/bjnano.9.98 PubMed.
(4) Veinot, J. G. C. Synthesis, surface functionalization, and properties of freestanding silicon nanocrystals. *Chemical Communications* **2006**, (40), 4160-4168, 10.1039/B607476F. DOI: 10.1039/B607476F.
(5) Requejo-Isidro, J.; Coso, R. d.; Solis, J.; Gonzalo, J.; Afonso, C. N. Role of surface-to-volume ratio of metal nanoparticles in optical properties of Cu:Al2O3 nanocomposite films. *Applied Physics Letters* **2005**, *86* (19), 193104. DOI: 10.1063/1.1923198.
(6) Brus, L. E. A simple model for the ionization potential, electron affinity, and aqueous redox potentials of small semiconductor crystallites. *The Journal of Chemical Physics* **1983**, *79* (11), 5566-5571. DOI: 10.1063/1.445676.
(7) Chukwuocha, E. O.; Onyeaju, M. C.; Harry, T. S. T. Theoretical Studies on the Effect of Confinement on Quantum Dots Using the Brus Equation. *World Journal of Condensed Matter Physics* **2012**, *Vol.02No.02*, 5. DOI: 10.4236/wjcmp.2012.22017.
(8) Arquer, F. P. G. d.; Talapin, D. V.; Klimov, V. I.; Arakawa, Y.; Bayer, M.; Sargent, E. H. Semiconductor quantum dots: Technological progress and future challenges. *Science* **2021**, *373* (6555), eaaz8541. DOI: doi:10.1126/science.aaz8541.
(9) Bailes, J. Photostability of Semiconductor Quantum Dots in Response to UV Exposure. *Methods Mol Biol* **2020**, *2118*, 343-349. DOI: 10.1007/978-1-0716-0319-2_25 From NLM.
(10) Lee, T.; Kim, B. J.; Lee, H.; Hahm, D.; Bae, W. K.; Lim, J.; Kwak, J. Bright and Stable Quantum Dot Light-Emitting Diodes. *Advanced Materials* **2022**, *34* (4), 2106276. DOI: https://doi.org/10.1002/adma.202106276. Liu, Z.; Lin, C.-H.; Hyun, B.-R.; Sher, C.-W.; Lv, Z.; Luo, B.; Jiang, F.; Wu, T.; Ho, C.-H.; Kuo, H.-C.; et al. Micro-light-emitting diodes with quantum dots in display technology. *Light: Science & Applications* **2020**, *9* (1), 83. DOI: 10.1038/s41377-020-0268-1. Bang, S. Y.; Suh, Y.-H.; Fan, X.-B.; Shin, D.-W.; Lee, S.; Choi, H. W.; Lee, T. H.; Yang, J.; Zhan, S.; Harden-Chaters, W.; et al. Technology progress on quantum dot light-emitting diodes for next-generation displays. *Nanoscale Horizons* **2021**, *6* (2), 68-77, 10.1039/D0NH00556H. DOI: 10.1039/D0NH00556H.
(11) Song, H.; Lin, Y.; Zhang, Z.; Rao, H.; Wang, W.; Fang, Y.; Pan, Z.; Zhong, X. Improving the Efficiency of Quantum Dot Sensitized Solar Cells beyond 15% via Secondary Deposition. *Journal of the American Chemical Society* **2021**, *143* (12), 4790-4800. DOI: 10.1021/jacs.1c01214. Nozik, A. J. Quantum dot solar cells. *Physica E: Low-dimensional Systems and Nanostructures* **2002**, *14* (1), 115-120. DOI: https://doi.org/10.1016/S1386-9477(02)00374-0. Emin, S.; Singh, S. P.; Han, L.; Satoh, N.; Islam, A. Colloidal quantum dot

solar cells. *Solar Energy* **2011**, *85* (6), 1264-1282. DOI: https://doi.org/10.1016/j.solener.2011.02.005.
(12) Zhang, M.; Yue, J.; Cui, R.; Ma, Z.; Wan, H.; Wang, F.; Zhu, S.; Zhou, Y.; Kuang, Y.; Zhong, Y.; et al. Bright quantum dots emitting at ∼1,600 nm in the NIR-IIb window for deep tissue fluorescence imaging. *Proceedings of the National Academy of Sciences* **2018**, *115* (26), 6590-6595. DOI: doi:10.1073/pnas.1806153115. Kang, Y.-F.; Li, Y.-H.; Fang, Y.-W.; Xu, Y.; Wei, X.-M.; Yin, X.-B. Carbon Quantum Dots for Zebrafish Fluorescence Imaging. *Scientific Reports* **2015**, *5* (1), 11835. DOI: 10.1038/srep11835. Yang, X.; Zhanghao, K.; Wang, H.; Liu, Y.; Wang, F.; Zhang, X.; Shi, K.; Gao, J.; Jin, D.; Xi, P. Versatile Application of Fluorescent Quantum Dot Labels in Super-resolution Fluorescence Microscopy. *ACS Photonics* **2016**, *3* (9), 1611-1618. DOI: 10.1021/acsphotonics.6b00178.
(13) Li, M.; Chen, T.; Gooding, J. J.; Liu, J. Review of Carbon and Graphene Quantum Dots for Sensing. *ACS Sensors* **2019**, *4* (7), 1732-1748. DOI: 10.1021/acssensors.9b00514. Ghosh, S.; Chen, Y.; George, A.; Dutta, M.; Stroscio, M. A. Fluorescence Resonant Energy Transfer-Based Quantum Dot Sensor for the Detection of Calcium Ions. *Frontiers in Chemistry* **2020**, *8*, Original Research. DOI: 10.3389/fchem.2020.00594.
(14) Reiss, P.; Carrière, M.; Lincheneau, C.; Vaure, L.; Tamang, S. Synthesis of Semiconductor Nanocrystals, Focusing on Nontoxic and Earth-Abundant Materials. *Chemical Reviews* **2016**, *116* (18), 10731-10819. DOI: 10.1021/acs.chemrev.6b00116.
(15) Erogbogbo, F.; Yong, K.-T.; Roy, I.; Xu, G.; Prasad, P. N.; Swihart, M. T. Biocompatible Luminescent Silicon Quantum Dots for Imaging of Cancer Cells. *ACS Nano* **2008**, *2* (5), 873-878. DOI: 10.1021/nn700319z. Bhattacharjee, S.; Rietjens, I. M. C. M.; Singh, M. P.; Atkins, T. M.; Purkait, T. K.; Xu, Z.; Regli, S.; Shukaliak, A.; Clark, R. J.; Mitchell, B. S.; et al. Cytotoxicity of surface-functionalized silicon and germanium nanoparticles: the dominant role of surface charges. *Nanoscale* **2013**, *5* (11), 4870-4883, 10.1039/C3NR34266B. DOI: 10.1039/C3NR34266B.
(16) Terada, S.; Xin, Y.; Saitow, K.-i. Cost-Effective Synthesis of Silicon Quantum Dots. *Chemistry of Materials* **2020**, *32* (19), 8382-8392. DOI: 10.1021/acs.chemmater.0c02320.
(17) Yu, Y.; Fan, G.; Fermi, A.; Mazzaro, R.; Morandi, V.; Ceroni, P.; Smilgies, D.-M.; Korgel, B. A. Size-Dependent Photoluminescence Efficiency of Silicon Nanocrystal Quantum Dots. *The Journal of Physical Chemistry C* **2017**, *121* (41), 23240-23248. DOI: 10.1021/acs.jpcc.7b08054.
(18) Yang, Z.; Dobbie, A. R.; Cui, K.; Veinot, J. G. C. A Convenient Method for Preparing Alkyl-Functionalized Silicon Nanocubes. *Journal of the American Chemical Society* **2012**, *134* (34), 13958-13961. DOI: 10.1021/ja3061497.
(19) Hessel, C. M.; Reid, D.; Panthani, M. G.; Rasch, M. R.; Goodfellow, B. W.; Wei, J.; Fujii, H.; Akhavan, V.; Korgel, B. A. Synthesis of ligand-stabilized silicon nanocrystals with size-dependent photoluminescence spanning visible to near-infrared wavelengths. *Chemistry of Materials* **2012**, *24* (2), 393-401. DOI: 10.1021/cm2032866.
(20) Hessel, C. M.; Henderson, E. J.; Veinot, J. G. C. Hydrogen Silsesquioxane: A Molecular Precursor for Nanocrystalline Si−SiO2 Composites and Freestanding Hydride-Surface-Terminated Silicon Nanoparticles. *Chemistry of Materials* **2006**, *18* (26), 6139-6146. DOI: 10.1021/cm0602803.
(21) Kramer, N. J.; Anthony, R. J.; Mamunuru, M.; Aydil, E. S.; Kortshagen, U. R. Plasma-induced crystallization of silicon nanoparticles. *Journal of Physics D: Applied Physics* **2014**, *47* (7), 075202. DOI: 10.1088/0022-3727/47/7/075202.

(22) Jurbergs, D.; Rogojina, E.; Mangolini, L.; Kortshagen, U. Silicon nanocrystals with ensemble quantum yields exceeding 60%. *Applied Physics Letters* **2006**, *88* (23), 233116. DOI: 10.1063/1.2210788.
(23) Yasar-Inceoglu, O.; Lopez, T.; Farshihagro, E.; Mangolini, L. Silicon nanocrystal production through non-thermal plasma synthesis: a comparative study between silicon tetrachloride and silane precursors. *Nanotechnology* **2012**, *23* (25), 255604. DOI: 10.1088/0957-4484/23/25/255604.
(24) Ding, Y.; Yamada, R.; Gresback, R.; Zhou, S.; Pi, X.; Nozaki, T. A parametric study of non-thermal plasma synthesis of silicon nanoparticles from a chlorinated precursor. *Journal of Physics D: Applied Physics* **2014**, *47* (48), 485202. DOI: 10.1088/0022-3727/47/48/485202.
(25) Yuan, Z.; Nakamura, T.; Adachi, S.; Matsuishi, K. Improvement of Laser Processing for Colloidal Silicon Nanocrystal Formation in a Reactive Solvent. *The Journal of Physical Chemistry C* **2017**, *121* (15), 8623-8629. DOI: 10.1021/acs.jpcc.7b00288.
(26) Yu, J.; Hao, H.; Zhang, R.; Zheng, W.; Wu, W. Silicon Nanocrystals Prepared by Femtosecond Laser Ablation in solution under different ablation time. *IOP Conference Series: Materials Science and Engineering* **2018**, *322*, 022049. DOI: 10.1088/1757-899x/322/2/022049.
(27) Beekman, M.; Kauzlarich, S. M.; Doherty, L.; Nolas, G. S. Zintl Phases as Reactive Precursors for Synthesis of Novel Silicon and Germanium-Based Materials. *Materials* **2019**, *12* (7), 1139. Atkins, T. M.; Walton, J. H.; Singh, M. P.; Ganguly, S.; Janka, O.; Louie, A. Y.; Kauzlarich, S. M. EPR and Structural Characterization of Water-Soluble Mn2+-Doped Si Nanoparticles. *The Journal of Physical Chemistry C* **2017**, *121* (3), 1948-1956. DOI: 10.1021/acs.jpcc.6b11000. Zhang, X.; Brynda, M.; Britt, R. D.; Carroll, E. C.; Larsen, D. S.; Louie, A. Y.; Kauzlarich, S. M. Synthesis and Characterization of Manganese-Doped Silicon Nanoparticles: Bifunctional Paramagnetic-Optical Nanomaterial. *Journal of the American Chemical Society* **2007**, *129* (35), 10668-10669. DOI: 10.1021/ja074144q. Neiner, D.; Chiu, H. W.; Kauzlarich, S. M. Low-Temperature Solution Route to Macroscopic Amounts of Hydrogen Terminated Silicon Nanoparticles. *Journal of the American Chemical Society* **2006**, *128* (34), 11016-11017. DOI: 10.1021/ja064177q.
(28) McVey, B. F. P.; Butkus, J.; Halpert, J. E.; Hodgkiss, J. M.; Tilley, R. D. Solution Synthesis and Optical Properties of Transition-Metal-Doped Silicon Nanocrystals. *The Journal of Physical Chemistry Letters* **2015**, *6* (9), 1573-1576. DOI: 10.1021/acs.jpclett.5b00589.
(29) Shiohara, A.; Hanada, S.; Prabakar, S.; Fujioka, K.; Lim, T. H.; Yamamoto, K.; Northcote, P. T.; Tilley, R. D. Chemical Reactions on Surface Molecules Attached to Silicon Quantum Dots. *Journal of the American Chemical Society* **2010**, *132* (1), 248-253. DOI: 10.1021/ja906501v.
(30) Baldwin, R. K.; Pettigrew, K. A.; Ratai, E.; Augustine, M. P.; Kauzlarich, S. M. Solution reduction synthesis of surface stabilized silicon nanoparticles. *Chemical Communications* **2002**, (17), 1822-1823, 10.1039/B205301B. DOI: 10.1039/B205301B.
(31) Heath, J. R. A Liquid-Solution-Phase Synthesis of Crystalline Silicon. *Science* **1992**, *258* (5085), 1131-1133. DOI: doi:10.1126/science.258.5085.1131.
(32) Dasog, M.; Yang, Z.; Regli, S.; Atkins, T. M.; Faramus, A.; Singh, M. P.; Muthuswamy, E.; Kauzlarich, S. M.; Tilley, R. D.; Veinot, J. G. C. Chemical Insight into the Origin of Red and Blue Photoluminescence Arising from Freestanding Silicon Nanocrystals. *ACS Nano* **2013**, *7* (3), 2676-2685. DOI: 10.1021/nn4000644.
(33) Sun, W.; Qian, C.; Cui, X. S.; Wang, L.; Wei, M.; Casillas, G.; Helmy, A. S.; Ozin, G. A. Silicon monoxide – a convenient precursor for large scale synthesis of near infrared emitting

monodisperse silicon nanocrystals. *Nanoscale* **2016**, *8* (6), 3678-3684, 10.1039/C5NR09128D. DOI: 10.1039/C5NR09128D.
(34) Nesbit, L. A. Annealing characteristics of Si-rich SiO2 films. *Applied Physics Letters* **1985**, *46* (1), 38-40. DOI: 10.1063/1.95842.
(35) Gupta, A.; Swihart, M. T.; Wiggers, H. Luminescent Colloidal Dispersion of Silicon Quantum Dots from Microwave Plasma Synthesis: Exploring the Photoluminescence Behavior Across the Visible Spectrum. *Advanced Functional Materials* **2009**, *19* (5), 696-703. DOI: https://doi.org/10.1002/adfm.200801548.
(36) Brus, L. E.; Szajowski, P. F.; Wilson, W. L.; Harris, T. D.; Schuppler, S.; Citrin, P. H. Electronic Spectroscopy and Photophysics of Si Nanocrystals: Relationship to Bulk c-Si and Porous Si. *Journal of the American Chemical Society* **1995**, *117* (10), 2915-2922. DOI: 10.1021/ja00115a025.
(37) Nayfeh, M. H.; Akcakir, O.; Belomoin, G.; Barry, N.; Therrien, J.; Gratton, E. Second harmonic generation in microcrystallite films of ultrasmall Si nanoparticles. *Applied Physics Letters* **2000**, *77* (25), 4086-4088. DOI: 10.1063/1.1334945. Nayfeh, M. H.; Barry, N.; Therrien, J.; Akcakir, O.; Gratton, E.; Belomoin, G. Stimulated blue emission in reconstituted films of ultrasmall silicon nanoparticles. *Applied Physics Letters* **2001**, *78* (8), 1131-1133. DOI: 10.1063/1.1347398.
(38) Li, X.; He, Y.; Talukdar, S. S.; Swihart, M. T. Process for Preparing Macroscopic Quantities of Brightly Photoluminescent Silicon Nanoparticles with Emission Spanning the Visible Spectrum. *Langmuir* **2003**, *19* (20), 8490-8496. DOI: 10.1021/la034487b.
(39) Li, X.; He, Y.; Swihart, M. T. Surface Functionalization of Silicon Nanoparticles Produced by Laser-Driven Pyrolysis of Silane followed by HF−HNO3 Etching. *Langmuir* **2004**, *20* (11), 4720-4727. DOI: 10.1021/la036219j. Hua, F.; Erogbogbo, F.; Swihart, M. T.; Ruckenstein, E. Organically Capped Silicon Nanoparticles with Blue Photoluminescence Prepared by Hydrosilylation Followed by Oxidation. *Langmuir* **2006**, *22* (9), 4363-4370. DOI: 10.1021/la0529106.
(40) Hua, F.; Swihart, M. T.; Ruckenstein, E. Efficient Surface Grafting of Luminescent Silicon Quantum Dots by Photoinitiated Hydrosilylation. *Langmuir* **2005**, *21* (13), 6054-6062. DOI: 10.1021/la0509394.
(41) Guruvenket, S.; Hoey, J. M.; Anderson, K. J.; Frohlich, M. T.; Krishnan, R.; Sivaguru, J.; Sibi, M. P.; Boudjouk, P. Synthesis of silicon quantum dots using cyclohexasilane (Si6H12). *Journal of Materials Chemistry C* **2016**, *4* (35), 8206-8213, 10.1039/C6TC01435F. DOI: 10.1039/C6TC01435F.
(42) Sato, S.; Yao, H.; Kimura, K. Self-Assembly of Si Nanoparticles: Emergence of Two-Dimensional Si Nanoparticle Lattices. *Japanese Journal of Applied Physics* **2004**, *43* (No. 7A), L927-L929. DOI: 10.1143/jjap.43.l927. Withrow, S. P.; White, C. W.; Meldrum, A.; Budai, J. D.; Jr., D. M. H.; Barbour, J. C. Effects of hydrogen in the annealing environment on photoluminescence from Si nanoparticles in SiO2. *Journal of Applied Physics* **1999**, *86* (1), 396-401. DOI: 10.1063/1.370699.
(43) Hessel, C. M.; Henderson, E. J.; Veinot, J. G. C. An Investigation of the Formation and Growth of Oxide-Embedded Silicon Nanocrystals in Hydrogen Silsesquioxane-Derived Nanocomposites. *The Journal of Physical Chemistry C* **2007**, *111* (19), 6956-6961. DOI: 10.1021/jp070908c.
(44) Shirahata, N.; Nakamura, J.; Inoue, J.-i.; Ghosh, B.; Nemoto, K.; Nemoto, Y.; Takeguchi, M.; Masuda, Y.; Tanaka, M.; Ozin, G. A. Emerging Atomic Energy Levels in Zero-Dimensional

Silicon Quantum Dots. *Nano Letters* **2020**, *20* (3), 1491-1498. DOI: 10.1021/acs.nanolett.9b03157. Mastronardi, M. L.; Maier-Flaig, F.; Faulkner, D.; Henderson, E. J.; Kübel, C.; Lemmer, U.; Ozin, G. A. Size-Dependent Absolute Quantum Yields for Size-Separated Colloidally-Stable Silicon Nanocrystals. *Nano Letters* **2012**, *12* (1), 337-342. DOI: 10.1021/nl2036194.
(45) Mastronardi, M. L.; Hennrich, F.; Henderson, E. J.; Maier-Flaig, F.; Blum, C.; Reichenbach, J.; Lemmer, U.; Kübel, C.; Wang, D.; Kappes, M. M.; et al. Preparation of Monodisperse Silicon Nanocrystals Using Density Gradient Ultracentrifugation. *Nano Letters* **2011**, *133*, 11928-11931. DOI: 10.1021/ja204865t.
(46) Islam, M. A.; Mobarok, M. H.; Sinelnikov, R.; Purkait, T. K.; Veinot, J. G. C. Phosphorus Pentachloride Initiated Functionalization of Silicon Nanocrystals. *Langmuir* **2017**, *33* (35), 8766-8773. DOI: 10.1021/acs.langmuir.7b00518.
(47) Sefannaser, M.; Thomas, S. A.; Anderson, K. J.; Petersen, R. J.; Brown, S. L.; Boudjouk, P. R.; Pringle, T. A.; Hobbie, E. K. Radiative Relaxation in Luminescent Silicon Nanocrystal Thiol-Ene Composites. *The Journal of Physical Chemistry C* **2021**, *125* (10), 5824-5831. DOI: 10.1021/acs.jpcc.0c11052.
(48) Dasog, M.; De Los Reyes, G. B.; Titova, L. V.; Hegmann, F. A.; Veinot, J. G. C. Size vs Surface: Tuning the Photoluminescence of Freestanding Silicon Nanocrystals Across the Visible Spectrum via Surface Groups. *ACS Nano* **2014**, *8* (9), 9636-9648. DOI: 10.1021/nn504109a.
(49) Sugimoto, H.; Okazaki, T.; Fujii, M. Mie Resonator Color Inks of Monodispersed and Perfectly Spherical Crystalline Silicon Nanoparticles. *Advanced Optical Materials* **2020**, *8* (12), 2000033. DOI: https://doi.org/10.1002/adom.202000033.
(50) Park, E.; Yoo, H.; Lee, J.; Park, M.-S.; Kim, Y.-J.; Kim, H. Dual-Size Silicon Nanocrystal-Embedded SiOx Nanocomposite as a High-Capacity Lithium Storage Material. *ACS Nano* **2015**, *9* (7), 7690-7696. DOI: 10.1021/acsnano.5b03166. Heitmann, J.; Müller, F.; Zacharias, M.; Gösele, U. Silicon Nanocrystals: Size Matters. *Advanced Materials* **2005**, *17* (7), 795-803. DOI: https://doi.org/10.1002/adma.200401126. Hartel, A. M.; Hiller, D.; Gutsch, S.; Löper, P.; Estradé, S.; Peiró, F.; Garrido, B.; Zacharias, M. Formation of size-controlled silicon nanocrystals in plasma enhanced chemical vapor deposition grown SiOxNy/SiO2 superlattices. *Thin Solid Films* **2011**, *520* (1), 121-125. DOI: https://doi.org/10.1016/j.tsf.2011.06.084. Zacharias, M.; Heitmann, J.; Scholz, R.; Kahler, U.; Schmidt, M.; Bläsing, J. Size-controlled highly luminescent silicon nanocrystals: A SiO/SiO2 superlattice approach. *Applied Physics Letters* **2002**, *80* (4), 661-663. DOI: 10.1063/1.1433906.
(51) Henderson, E. J.; Kelly, J. A.; Veinot, J. G. C. Influence of HSiO1.5 Sol−Gel Polymer Structure and Composition on the Size and Luminescent Properties of Silicon Nanocrystals. *Chemistry of Materials* **2009**, *21* (22), 5426-5434. DOI: 10.1021/cm902028q.
(52) Li, Z.; Kortshagen, U. R. Aerosol-Phase Synthesis and Processing of Luminescent Silicon Nanocrystals. *Chemistry of Materials* **2019**, *31* (20), 8451-8458. DOI: 10.1021/acs.chemmater.9b02743.
(53) Mangolini, L.; Thimsen, E.; Kortshagen, U. High-Yield Plasma Synthesis of Luminescent Silicon Nanocrystals. *Nano Letters* **2005**, *5* (4), 655-659. DOI: 10.1021/nl050066y.
(54) Anthony, R. J.; Cheng, K.-Y.; Holman, Z. C.; Holmes, R. J.; Kortshagen, U. R. An All-Gas-Phase Approach for the Fabrication of Silicon Nanocrystal Light-Emitting Devices. *Nano Letters* **2012**, *12* (6), 2822-2825. DOI: 10.1021/nl300164z.

(55) Jurbergs, D.; Rogojina, E.; Mangolini, L.; Kortshagen, U. Silicon nanocrystals with ensemble quantum yields exceeding 60%. *Appl. Phys. Lett.* **2006**, *88* (1), 233116. DOI: 10.1063/1.2210788.
(56) Pringle, T. A.; Hunter, K. I.; Brumberg, A.; Anderson, K. J.; Fagan, J. A.; Thomas, S. A.; Petersen, R. J.; Sefannaser, M.; Han, Y.; Brown, S. L.; et al. Bright Silicon Nanocrystals from a Liquid Precursor: Quasi-Direct Recombination with High Quantum Yield. *ACS Nano* **2020**, *14* (4), 3858-3867. DOI: 10.1021/acsnano.9b09614.
(57) Kovalenko, M. V.; Manna, L.; Cabot, A.; Hens, Z.; Talapin, D. V.; Kagan, C. R.; Klimov, V. I.; Rogach, A. L.; Reiss, P.; Milliron, D. J.; et al. Prospects of Nanoscience with Nanocrystals. *ACS Nano* **2015**, *9* (2), 1012-1057. DOI: 10.1021/nn506223h.
(58) Švrček, V.; Sasaki, T.; Shimizu, Y.; Koshizaki, N. Blue luminescent silicon nanocrystals prepared by ns pulsed laser ablation in water. *Applied Physics Letters* **2006**, *89* (21), 213113. DOI: 10.1063/1.2397014.
(59) Nakamura, T.; Yuan, Z.; Watanabe, K.; Adachi, S. Bright and multicolor luminescent colloidal Si nanocrystals prepared by pulsed laser irradiation in liquid. *Applied Physics Letters* **2016**, *108* (2), 023105. DOI: 10.1063/1.4939902. Shirahata, N.; Hirakawa, D.; Sakka, Y. Interfacial-related color tuning of colloidal Si nanocrystals. *Green Chemistry* **2010**, *12* (12), 2139-2141, 10.1039/C0GC00502A. DOI: 10.1039/C0GC00502A.
(60) Hwang, J.; Jeong, Y.; Lee, K. H.; Seo, Y.; Kim, J.; Hong, J. W.; Kamaloo, E.; Camesano, T. A.; Choi, J. Simple Preparation of Fluorescent Silicon Nanoparticles from Used Si Wafers. *Industrial & Engineering Chemistry Research* **2015**, *54* (22), 5982-5989. DOI: 10.1021/acs.iecr.5b00446.
(61) Liao, B.; Wang, W.; Deng, X.; He, B.; Zeng, W.; Tang, Z.; Liu, Q. A facile one-step synthesis of fluorescent silicon quantum dots and their application for detecting Cu2+. *RSC Advances* **2016**, *6* (18), 14465-14467, 10.1039/C5RA25563E. DOI: 10.1039/C5RA25563E.
(62) Zou, J.; Sanelle, P.; Pettigrew, K. A.; Kauzlarich, S. M. Size and Spectroscopy of Silicon Nanoparticles Prepared via Reduction of SiCl4. *Journal of Cluster Science* **2006**, *17* (4), 565-578. DOI: 10.1007/s10876-006-0082-9.
(63) Wilcoxon, J. P.; Samara, G. A.; Provencio, P. N. Optical and electronic properties of Si nanoclusters synthesized in inverse micelles. *Physical Review B* **1999**, *60* (4), 2704-2714. DOI: 10.1103/PhysRevB.60.2704.
(64) Tilley, R. D.; Warner, J. H.; Yamamoto, K.; Matsui, I.; Fujimori, H. Micro-emulsion synthesis of monodisperse surface stabilized silicon nanocrystals. *Chemical Communications* **2005**, (14), 1833-1835, 10.1039/B416069J. DOI: 10.1039/B416069J.
(65) McVey, B. F. P.; Tilley, R. D. Solution Synthesis, Optical Properties, and Bioimaging Applications of Silicon Nanocrystals. *Accounts of Chemical Research* **2014**, *47* (10), 3045-3051. DOI: 10.1021/ar500215v.
(66) Shiohara, A.; Prabakar, S.; Faramus, A.; Hsu, C.-Y.; Lai, P.-S.; Northcote, P. T.; Tilley, R. D. Sized controlled synthesis, purification, and cell studies with silicon quantum dots. *Nanoscale* **2011**, *3* (8), 3364-3370, 10.1039/C1NR10458F. DOI: 10.1039/C1NR10458F.
(67) Rosso-Vasic, M.; Spruijt, E.; van Lagen, B.; De Cola, L.; Zuilhof, H. Alkyl-Functionalized Oxide-Free Silicon Nanoparticles: Synthesis and Optical Properties. *Small* **2008**, *4*, 1835-1841. DOI: 10.1002/smll.200800066.
(68) Zhong, Y.; Peng, F.; Bao, F.; Wang, S.; Ji, X.; Yang, L.; Su, Y.; Lee, S.-T.; He, Y. Large-Scale Aqueous Synthesis of Fluorescent and Biocompatible Silicon Nanoparticles and Their Use

as Highly Photostable Biological Probes. *Journal of the American Chemical Society* **2013**, *135* (22), 8350-8356. DOI: 10.1021/ja4026227.
(69) Ddungu, John L. Z.; Silvestrini, S.; Tassoni, A.; De Cola, L. Shedding light on the aqueous synthesis of silicon nanoparticles by reduction of silanes with citrates. *Faraday Discussions* **2020**, *222* (0), 350-361, 10.1039/C9FD00127A. DOI: 10.1039/C9FD00127A.
(70) Yang, C.-S.; Bley, R. A.; Kauzlarich, S. M.; Lee, H. W. H.; Delgado, G. R. Synthesis of Alkyl-Terminated Silicon Nanoclusters by a Solution Route. *Journal of the American Chemical Society* **1999**, *121* (22), 5191-5195. DOI: 10.1021/ja9828509.
(71) Wilbrink, Jonathan L.; Huang, C.-C.; Dohnalova, K.; Paulusse, J. M. J. Critical assessment of wet-chemical oxidation synthesis of silicon quantum dots. *Faraday Discussions* **2020**, *222* (0), 149-165, 10.1039/C9FD00099B. DOI: 10.1039/C9FD00099B.
(72) Ma, X.; Xu, F.; Atkins, T. M.; Goforth, A. M.; Neiner, D.; Navrotsky, A.; Kauzlarich, S. M. A versatile low temperature synthetic route to Zintl phase precursors: Na4Si4, Na4Ge4 and K4Ge4 as examples. *Dalton Transactions* **2009**, (46), 10250-10255, 10.1039/B913320H. DOI: 10.1039/B913320H. Tu, C.; Ma, X.; Pantazis, P.; Kauzlarich, S. M.; Louie, A. Y. Paramagnetic, Silicon Quantum Dots for Magnetic Resonance and Two-Photon Imaging of Macrophages. *Journal of the American Chemical Society* **2010**, *132* (6), 2016-2023. DOI: 10.1021/ja909303g.
(73) Singh, M. P.; Atkins, T. M.; Muthuswamy, E.; Kamali, S.; Tu, C.; Louie, A. Y.; Kauzlarich, S. M. Development of Iron-Doped Silicon Nanoparticles As Bimodal Imaging Agents. *ACS Nano* **2012**, *6* (6), 5596-5604. DOI: 10.1021/nn301536n.
(74) Swihart, M. T.; Girshick, S. L. Thermochemistry and Kinetics of Silicon Hydride Cluster Formation during Thermal Decomposition of Silane. *The Journal of Physical Chemistry B* **1999**, *103* (1), 64-76. DOI: 10.1021/jp983358e. Swihart, M. T.; Girshick, S. L. Ab initio structures and energetics of selected hydrogenated silicon clusters containing six to ten silicon atoms. *Chemical Physics Letters* **1999**, *307* (5), 527-532. DOI: https://doi.org/10.1016/S0009-2614(99)00545-X. Onischuk, A. A.; Strunin, V. P.; Ushakova, M. A.; Panfilov, V. N. On the pathways of aerosol formation by thermal decomposition of silane. *Journal of Aerosol Science* **1997**, *28* (2), 207-222. DOI: https://doi.org/10.1016/S0021-8502(96)00061-4. Onischuk, A. A.; Strunin, V. P.; Ushakova, M. A.; Panfilov, V. N. Studying of silane thermal decomposition mechanism. *International Journal of Chemical Kinetics* **1998**, *30* (2), 99-110. DOI: https://doi.org/10.1002/(SICI)1097-4601(1998)30:2<99::AID-KIN1>3.0.CO;2-O.
(75) Liao, Y.; Xu, Y.; Chan, Y. Semiconductor nanocrystals in sol–gel derived matrices. *Physical Chemistry Chemical Physics* **2013**, *15* (33), 13694-13704, 10.1039/C3CP51351C. DOI: 10.1039/C3CP51351C.
(76) Mastronardi, M. L.; Hennrich, F.; Henderson, E. J.; Maier-Flaig, F.; Blum, C.; Reichenbach, J.; Lemmer, U.; Kübel, C.; Wang, D.; Kappes, M. M.; et al. Preparation of Monodisperse Silicon Nanocrystals Using Density Gradient Ultracentrifugation. *Journal of the American Chemical Society* **2011**, *133* (31), 11928-11931. DOI: 10.1021/ja204865t.
(77) Angı, A.; Loch, M.; Sinelnikov, R.; Veinot, J. G. C.; Becherer, M.; Lugli, P.; Rieger, B. The influence of surface functionalization methods on the performance of silicon nanocrystal LEDs. *Nanoscale* **2018**, *10* (22), 10337-10342, 10.1039/C7NR09525B. DOI: 10.1039/C7NR09525B. Maier-Flaig, F.; Rinck, J.; Stephan, M.; Bocksrocker, T.; Bruns, M.; Kübel, C.; Powell, A. K.; Ozin, G. A.; Lemmer, U. Multicolor Silicon Light-Emitting Diodes (SiLEDs). *Nano Letters* **2013**, *13* (2), 475-480. DOI: 10.1021/nl3038689.
(78) Cheong, I. T.; Morrish, W.; Sheard, W.; Yu, H.; Tavares Luppi, B.; Milburn, L.; Meldrum, A.; Veinot, J. G. C. Silicon Quantum Dot–Polymer Fabry–Pérot Resonators with Narrowed and

Tunable Emissions. *ACS Applied Materials & Interfaces* **2021**, *13* (23), 27149-27158. DOI: 10.1021/acsami.1c01825.
(79) Zeng, P.; Wang, F.; Zhang, Y.; Zhou, W.; Guo, Z.; Wu, X.; Lu, M.; Zhang, S. Edge-Emitting Silicon Nanocrystal Distributed Feedback Laser with Extremely Low Exciton Threshold. *ACS Photonics* **2021**, *8* (5), 1353-1363. DOI: 10.1021/acsphotonics.0c01846.
(80) Bhandarkar, U. V.; Swihart, M. T.; Girshick, S. L.; Kortshagen, U. R. Modelling of silicon hydride clustering in a low-pressure silane plasma. *Journal of Physics D: Applied Physics* **2000**, *33* (21), 2731-2746. DOI: 10.1088/0022-3727/33/21/311.
(81) Schulte, P. A.; McKernan, L. T.; Heidel, D. S.; Okun, A. H.; Dotson, G. S.; Lentz, T. J.; Geraci, C. L.; Heckel, P. E.; Branche, C. M. Occupational safety and health, green chemistry, and sustainability: a review of areas of convergence. *Environmental Health* **2013**, *12* (1), 31. DOI: 10.1186/1476-069X-12-31. Ruby, D. S. Safety considerations for high-efficiency crystalline-silicon solar cell fabrication. In *Conference Record of the Twentieth IEEE Photovoltaic Specialists Conference*, 26-30 Sept. 1988, 1988; pp 523-528 vol.521. DOI: 10.1109/PVSC.1988.105757.
(82) He, Y.; Su, Y.; Yang, X.; Kang, Z.; Xu, T.; Zhang, R.; Fan, C.; Lee, S.-T. Photo and pH Stable, Highly-Luminescent Silicon Nanospheres and Their Bioconjugates for Immunofluorescent Cell Imaging. *Journal of the American Chemical Society* **2009**, *131* (12), 4434-4438. DOI: 10.1021/ja808827g. Cullis, A. G.; Canham, L. T. Visible light emission due to quantum size effects in highly porous crystalline silicon. *Nature* **1991**, *353* (6342), 335-338. DOI: 10.1038/353335a0. Cullis, A. G.; Canham, L. T.; Calcott, P. D. J. The structural and luminescence properties of porous silicon. *Journal of Applied Physics* **1997**, *82* (3), 909-965. DOI: 10.1063/1.366536. Heinrich, J. L.; Curtis, C. L.; Credo, G. M.; Sailor, M. J.; Kavanagh, K. L. Luminescent Colloidal Silicon Suspensions from Porous Silicon. *Science* **1992**, *255* (5040), 66-68. DOI: doi:10.1126/science.255.5040.66.
(83) Park, J.-H.; Gu, L.; von Maltzahn, G.; Ruoslahti, E.; Bhatia, S. N.; Sailor, M. J. Biodegradable luminescent porous silicon nanoparticles for in vivo applications. *Nature Materials* **2009**, *8* (4), 331-336. DOI: 10.1038/nmat2398. Lin, V. S.-Y.; Motesharei, K.; Dancil, K.-P. S.; Sailor, M. J.; Ghadiri, M. R. A Porous Silicon-Based Optical Interferometric Biosensor. *Science* **1997**, *278* (5339), 840-843. DOI: doi:10.1126/science.278.5339.840. Niccolai, L.; Bassetto, M.; Quarta, A. A.; Mengali, G. A review of Smart Dust architecture, dynamics, and mission applications. *Progress in Aerospace Sciences* **2019**, *106*, 1-14. DOI: https://doi.org/10.1016/j.paerosci.2019.01.003.
(84) Li, Q.; Luo, T.-Y.; Zhou, M.; Abroshan, H.; Huang, J.; Kim, H. J.; Rosi, N. L.; Shao, Z.; Jin, R. Silicon Nanoparticles with Surface Nitrogen: 90% Quantum Yield with Narrow Luminescence Bandwidth and the Ligand Structure Based Energy Law. *ACS Nano* **2016**, *10* (9), 8385-8393. DOI: 10.1021/acsnano.6b03113. Zhong, Y.; Sun, X.; Wang, S.; Peng, F.; Bao, F.; Su, Y.; Li, Y.; Lee, S.-T.; He, Y. Facile, Large-Quantity Synthesis of Stable, Tunable-Color Silicon Nanoparticles and Their Application for Long-Term Cellular Imaging. *ACS Nano* **2015**, *9* (6), 5958-5967. DOI: 10.1021/acsnano.5b00683. Gong, T.; Li, Y.; Lei, B.; Zhang, X.; Liu, Y.; Zhang, H. Solid-state silicon nanoparticles with color-tunable photoluminescence and multifunctional applications. *Journal of Materials Chemistry C* **2019**, *7* (20), 5962-5969, 10.1039/C9TC00938H. DOI: 10.1039/C9TC00938H.
(85) Pujari, S. P.; Driss, H.; Bannani, F.; van Lagen, B.; Zuilhof, H. One-Pot Gram-Scale Synthesis of Hydrogen-Terminated Silicon Nanoparticles. *Chemistry of Materials* **2018**, *30* (18), 6503-6512. DOI: 10.1021/acs.chemmater.8b03113.

(86) Hu, G.; Sun, Y.; Xie, Y.; Wu, S.; Zhang, X.; Zhuang, J.; Hu, C.; Lei, B.; Liu, Y. Synthesis of Silicon Quantum Dots with Highly Efficient Full-Band UV Absorption and Their Applications in Antiyellowing and Resistance of Photodegradation. *ACS Applied Materials & Interfaces* **2019**, *11* (6), 6634-6643. DOI: 10.1021/acsami.8b20138.
(87) Wells, A. S. On the Perils of Unexpected Silane Generation. *Organic Process Research & Development* **2010**, *14* (3), 484-484. DOI: 10.1021/op100080v.
(88) Rosso-Vasic, M.; Spruijt, E.; van Lagen, B.; De Cola, L.; Zuilhof, H. Alkyl-Functionalized Oxide-Free Silicon Nanoparticles: Synthesis and Optical Properties. *Small* **2008**, *4* (10), 1835-1841. DOI: https://doi.org/10.1002/smll.200800066.
(89) Wang, X.; Zhuang, J.; Peng, Q.; Li, Y. A general strategy for nanocrystal synthesis. *Nature* **2005**, *437* (7055), 121-124. DOI: 10.1038/nature03968.
(90) Albanese, A.; Tang, P. S.; Chan, W. C. W. The Effect of Nanoparticle Size, Shape, and Surface Chemistry on Biological Systems. *Annual Review of Biomedical Engineering* **2012**, *14* (1), 1-16. DOI: 10.1146/annurev-bioeng-071811-150124.
(91) Reiss, P.; Protière, M.; Li, L. Core/Shell Semiconductor Nanocrystals. *Small* **2009**, *5* (2), 154-168. DOI: https://doi.org/10.1002/smll.200800841.
(92) Thiessen, A. N.; Zhang, L.; Oliynyk, A. O.; Yu, H.; O'Connor, K. M.; Meldrum, A.; Veinot, J. G. C. A Tale of Seemingly "Identical" Silicon Quantum Dot Families: Structural Insight into Silicon Quantum Dot Photoluminescence. *Chemistry of Materials* **2020**, *32* (16), 6838-6846. DOI: 10.1021/acs.chemmater.0c00650.
(93) Thiessen, A. N.; Ha, M.; Hooper, R. W.; Yu, H.; Oliynyk, A. O.; Veinot, J. G. C.; Michaelis, V. K. Silicon Nanoparticles: Are They Crystalline from the Core to the Surface? *Chemistry of Materials* **2019**, *31* (3), 678-688. DOI: 10.1021/acs.chemmater.8b03074.
(94) Shu, Y.; Kortshagen, U. R.; Levine, B. G.; Anthony, R. J. Surface Structure and Silicon Nanocrystal Photoluminescence: The Role of Hypervalent Silyl Groups. *The Journal of Physical Chemistry C* **2015**, *119* (47), 26683-26691. DOI: 10.1021/acs.jpcc.5b08578. Rowland, C. E.; Hannah, D. C.; Demortière, A.; Yang, J.; Cook, R. E.; Prakapenka, V. B.; Kortshagen, U.; Schaller, R. D. Silicon Nanocrystals at Elevated Temperatures: Retention of Photoluminescence and Diamond Silicon to β-Silicon Carbide Phase Transition. *ACS Nano* **2014**, *8* (9), 9219-9223. DOI: 10.1021/nn5029967.
(95) Clark, R. J.; Aghajamali, M.; Gonzalez, C. M.; Hadidi, L.; Islam, M. A.; Javadi, M.; Mobarok, M. H.; Purkait, T. K.; Robidillo, C. J. T.; Sinelnikov, R.; et al. From hydrogen silsesquioxane to functionalized silicon nanocrystals. *Chemistry of Materials* **2017**, *29* (1), 80-89. DOI: 10.1021/acs.chemmater.6b02667.
(96) Pi, X. D.; Mangolini, L.; Campbell, S. A.; Kortshagen, U. Room-temperature atmospheric oxidation of Si nanocrystals after HF etching. *Physical Review B* **2007**, *75* (8), 085423. DOI: 10.1103/PhysRevB.75.085423.
(97) Yu, Y.; Lu, X.; Guillaussier, A.; Voggu, V. R.; Pineros, W.; de la Mata, M.; Arbiol, J.; Smilgies, D.-M.; Truskett, T. M.; Korgel, B. A. Orientationally Ordered Silicon Nanocrystal Cuboctahedra in Superlattices. *Nano Letters* **2016**, *16* (12), 7814-7821. DOI: 10.1021/acs.nanolett.6b04006.
(98) Hannah, D. C.; Yang, J.; Kramer, N. J.; Schatz, G. C.; Kortshagen, U. R.; Schaller, R. D. Ultrafast Photoluminescence in Quantum-Confined Silicon Nanocrystals Arises from an Amorphous Surface Layer. *ACS Photonics* **2014**, *1* (10), 960-967. DOI: 10.1021/ph500145p.

(99) Anthony, R.; Kortshagen, U. Photoluminescence quantum yields of amorphous and crystalline silicon nanoparticles. *Physical Review B* **2009**, *80* (11), 115407. DOI: 10.1103/PhysRevB.80.115407.
(100) Petkov, V.; Hessel, C. M.; Ovtchinnikoff, J.; Guillaussier, A.; Korgel, B. A.; Liu, X.; Giordano, C. Structure–Properties Correlation in Si Nanoparticles by Total Scattering and Computer Simulations. *Chemistry of Materials* **2013**, *25* (11), 2365-2371. DOI: 10.1021/cm401099q.
(101) Mazzaro, R.; Romano, F.; Ceroni, P. Long-lived luminescence of silicon nanocrystals: from principles to applications. *Physical Chemistry Chemical Physics* **2017**, *19* (39), 26507-26526, 10.1039/C7CP05208A. DOI: 10.1039/C7CP05208A.
(102) Wheeler, L. M.; Anderson, N. C.; Palomaki, P. K. B.; Blackburn, J. L.; Johnson, J. C.; Neale, N. R. Silyl Radical Abstraction in the Functionalization of Plasma-Synthesized Silicon Nanocrystals. *Chemistry of Materials* **2015**, *27* (19), 6869-6878. DOI: 10.1021/acs.chemmater.5b03309.
(103) Jarolimek, K.; Hazrati, E.; de Groot, R. A.; de Wijs, G. A. Band Offsets at the Interface between Crystalline and Amorphous Silicon from First Principles. *Physical Review Applied* **2017**, *8* (1), 014026. DOI: 10.1103/PhysRevApplied.8.014026. Vatan Meidanshahi, R.; Bowden, S.; Goodnick, S. M. Electronic structure and localized states in amorphous Si and hydrogenated amorphous Si. *Physical Chemistry Chemical Physics* **2019**, *21* (24), 13248-13257, 10.1039/C9CP01121H. DOI: 10.1039/C9CP01121H.
(104) Guha, S.; Yang, J.; Yan, B. Amorphous and Nanocrystalline Silicon Solar Cells and Modules. In *Reference Module in Materials Science and Materials Engineering*, Elsevier, 2016.
(105) Park, N.-M.; Kim, T.-S.; Park, S.-J. Band gap engineering of amorphous silicon quantum dots for light-emitting diodes. *Applied Physics Letters* **2001**, *78* (17), 2575-2577. DOI: 10.1063/1.1367277.
(106) Park, N.-M.; Choi, C.-J.; Seong, T.-Y.; Park, S.-J. Quantum Confinement in Amorphous Silicon Quantum Dots Embedded in Silicon Nitride. *Physical Review Letters* **2001**, *86* (7), 1355-1357. DOI: 10.1103/PhysRevLett.86.1355.
(107) Askari, S.; Svrcek, V.; Maguire, P.; Mariotti, D. The Interplay of Quantum Confinement and Hydrogenation in Amorphous Silicon Quantum Dots. *Advanced Materials* **2015**, *27* (48), 8011-8016. DOI: https://doi.org/10.1002/adma.201503013.
(108) Lisovskyy, I.; Voitovych, M.; Litovchenko, V.; Voitovych, V.; Nasieka, I.; Bratus, V. Radiation Induced Enhancement of Hydrogen Influence on Luminescent Properties of nc-Si/SiO2 Structures. *Nanoscale Research Letters* **2016**, *11* (1), 545. DOI: 10.1186/s11671-016-1744-7. Cheylan, S.; Elliman, R. G. Effect of hydrogen on the photoluminescence of Si nanocrystals embedded in a SiO2 matrix. *Applied Physics Letters* **2001**, *78* (9), 1225-1227. DOI: 10.1063/1.1338492.
(109) Wang, Q.; Xu, B.; Sun, J.; Liu, H.; Zhao, Z.; Yu, D.; Fan, C.; He, J. Direct Band Gap Silicon Allotropes. *Journal of the American Chemical Society* **2014**, *136* (28), 9826-9829. DOI: 10.1021/ja5035792. Guo, Y.; Wang, Q.; Kawazoe, Y.; Jena, P. A New Silicon Phase with Direct Band Gap and Novel Optoelectronic Properties. *Scientific Reports* **2015**, *5* (1), 14342. DOI: 10.1038/srep14342.
(110) Hannah, D. C.; Yang, J.; Podsiadlo, P.; Chan, M. K. Y.; Demortière, A.; Gosztola, D. J.; Prakapenka, V. B.; Schatz, G. C.; Kortshagen, U.; Schaller, R. D. On the Origin of Photoluminescence in Silicon Nanocrystals: Pressure-Dependent Structural and Optical Studies. *Nano Letters* **2012**, *12* (8), 4200-4205. DOI: 10.1021/nl301787g.

(111) Kůsová, K.; Hapala, P.; Valenta, J.; Jelínek, P.; Cibulka, O.; Ondič, L.; Pelant, I. Direct Bandgap Silicon: Tensile-Strained Silicon Nanocrystals. *Advanced Materials Interfaces* **2014**, *1* (2), 1300042. DOI: https://doi.org/10.1002/admi.201300042.
(112) Hannah, D. C.; Yang, J.; Kramer, N. J.; Schatz, G. C.; Kortshagen, U. R.; Schaller, R. D. Reply to "Comment on 'Ultrafast Photoluminescence in Quantum-Confined Silicon Nanocrystals Arises from an Amorphous Surface Layer'". *ACS Photonics* **2015**, *2* (3), 456-458. DOI: 10.1021/ph500490a. Kůsová, K.; Ondič, L.; Pelant, I. Comment on "Ultrafast Photoluminescence in Quantum-Confined Silicon Nanocrystals Arises from an Amorphous Surface Layer". *ACS Photonics* **2015**, *2* (3), 454-455. DOI: 10.1021/ph500403j.
(113) Mobarok, M. H.; Purkait, T. K.; Islam, M. A.; Miskolzie, M.; Veinot, J. G. C. Instantaneous Functionalization of Chemically Etched Silicon Nanocrystal Surfaces. *Angewandte Chemie International Edition* **2016**, *56* (22), 6073-6077. DOI: 10.1002/anie.201609651.
(114) Kovacs, G. T. A.; Maluf, N. I.; Petersen, K. E. Bulk micromachining of silicon. *Proceedings of the IEEE* **1998**, *86* (8), 1536-1551. DOI: 10.1109/5.704259. Bansal, A.; Li, X.; Lauermann, I.; Lewis, N. S.; Yi, S. I.; Weinberg, W. H. Alkylation of Si Surfaces Using a Two-Step Halogenation/Grignard Route. *Journal of the American Chemical Society* **1996**, *118* (30), 7225-7226. DOI: 10.1021/ja960348n. Rivillon, S.; Chabal, Y. J.; Webb, L. J.; Michalak, D. J.; Lewis, N. S.; Halls, M. D.; Raghavachari, K. Chlorination of hydrogen-terminated silicon (111) surfaces. *Journal of Vacuum Science & Technology A* **2005**, *23* (4), 1100-1106. DOI: 10.1116/1.1861941.
(115) Satpathy, R.; Pamuru, V. Chapter 4 - Making of crystalline silicon solar cells. In *Solar PV Power*, Satpathy, R., Pamuru, V. Eds.; Academic Press, 2021; pp 71-134.
(116) Johnson, N. M. Mechanism for hydrogen compensation of shallow-acceptor impurities in single-crystal silicon. *Physical Review B* **1985**, *31* (8), 5525-5528. DOI: 10.1103/PhysRevB.31.5525. Caldas, M. J.; Fazzio, A.; Zunger, A. A universal trend in the binding energies of deep impurities in semiconductors. *Applied Physics Letters* **1984**, *45* (6), 671-673. DOI: 10.1063/1.95351.
(117) Bullis, W. M. Properties of gold in silicon. *Solid-State Electronics* **1966**, *9* (2), 143-168. DOI: https://doi.org/10.1016/0038-1101(66)90085-2.
(118) Oliva-Chatelain, B. L.; Ticich, T. M.; Barron, A. R. Doping silicon nanocrystals and quantum dots. *Nanoscale* **2016**, *8* (4), 1733-1745. DOI: 10.1039/c5nr04978d.
(119) Chan, T.-L.; Zhang, S. B.; Chelikowsky, J. R. An effective one-particle theory for formation energies in doping Si nanostructures. *Applied Physics Letters* **2011**, *98* (13), 133116. DOI: 10.1063/1.3571552.
(120) Hiller, D.; López-Vidrier, J.; Gutsch, S.; Zacharias, M.; Wahl, M.; Bock, W.; Brodyanski, A.; Kopnarski, M.; Nomoto, K.; Valenta, J.; et al. Boron-Incorporating Silicon Nanocrystals Embedded in SiO2: Absence of Free Carriers vs. B-Induced Defects. *Scientific Reports* **2017**, *7* (1), 8337. DOI: 10.1038/s41598-017-08814-0.
(121) Dalpian, G. M.; Chelikowsky, J. R. Self-Purification in Semiconductor Nanocrystals. *Physical Review Letters* **2006**, *96* (22), 226802. DOI: 10.1103/PhysRevLett.96.226802.
(122) Gutsch, S.; Laube, J.; Hiller, D.; Bock, W.; Wahl, M.; Kopnarski, M.; Gnaser, H.; Puthen-Veettil, B.; Zacharias, M. Electronic properties of phosphorus doped silicon nanocrystals embedded in SiO2. *Applied Physics Letters* **2015**, *106* (11), 113103. DOI: 10.1063/1.4915307.
Huang, S.; So, Y. H.; Conibeer, G.; Green, M. Doping of Silicon Quantum Dots Embedded in

Nitride Matrix for All-Silicon Tandem Cells. *Japanese Journal of Applied Physics* **2012**, *51*, 10NE10. DOI: 10.1143/jjap.51.10ne10.
(123) Zhou, S.; Pi, X.; Ni, Z.; Ding, Y.; Jiang, Y.; Jin, C.; Delerue, C.; Yang, D.; Nozaki, T. Comparative Study on the Localized Surface Plasmon Resonance of Boron- and Phosphorus-Doped Silicon Nanocrystals. *ACS Nano* **2015**, *9* (1), 378-386. DOI: 10.1021/nn505416r.
(124) Kramer, N. J.; Schramke, K. S.; Kortshagen, U. R. Plasmonic Properties of Silicon Nanocrystals Doped with Boron and Phosphorus. *Nano Letters* **2015**, *15* (8), 5597-5603. DOI: 10.1021/acs.nanolett.5b02287.
(125) Rowe, D. J.; Jeong, J. S.; Mkhoyan, K. A.; Kortshagen, U. R. Phosphorus-Doped Silicon Nanocrystals Exhibiting Mid-Infrared Localized Surface Plasmon Resonance. *Nano Letters* **2013**, *13* (3), 1317-1322. DOI: 10.1021/nl4001184.
(126) Ni, Z.; Pi, X.; Zhou, S.; Nozaki, T.; Grandidier, B.; Yang, D. Size-Dependent Structures and Optical Absorption of Boron-Hyperdoped Silicon Nanocrystals. *Advanced Optical Materials* **2016**, *4* (5), 700-707. DOI: https://doi.org/10.1002/adom.201500706.
(127) Borowik, Ł.; Nguyen-Tran, T.; Cabarrocas, P. R. i.; Mélin, T. Doped semiconductor nanocrystal junctions. *Journal of Applied Physics* **2013**, *114* (20), 204305. DOI: 10.1063/1.4834516.
(128) Rohani, P.; Banerjee, S.; Sharifi-Asl, S.; Malekzadeh, M.; Shahbazian-Yassar, R.; Billinge, S. J. L.; Swihart, M. T. Synthesis and Properties of Plasmonic Boron-Hyperdoped Silicon Nanoparticles. *Advanced Functional Materials* **2019**, *29* (8), 1807788. DOI: https://doi.org/10.1002/adfm.201807788.
(129) Chandra, S.; Masuda, Y.; Shirahata, N.; Winnik, F. M. Transition-Metal-Doped NIR-Emitting Silicon Nanocrystals. *Angewandte Chemie International Edition* **2017**, *56* (22), 6157-6160. DOI: https://doi.org/10.1002/anie.201700436.
(130) Rocks, C.; Svrcek, V.; Velusamy, T.; Macias-Montero, M.; Maguire, P.; Mariotti, D. Type-I alignment in MAPbI3 based solar devices with doped-silicon nanocrystals. *Nano Energy* **2018**, *50*, 245-255. DOI: https://doi.org/10.1016/j.nanoen.2018.05.036.
(131) Fujii, M.; Fujii, R.; Takada, M.; Sugimoto, H. Silicon Quantum Dot Supraparticles for Fluorescence Bioimaging. *ACS Applied Nano Materials* **2020**, *3* (6), 6099-6107. DOI: 10.1021/acsanm.0c01295. Sugimoto, H.; Fujii, M.; Imakita, K.; Hayashi, S.; Akamatsu, K. All-Inorganic Near-Infrared Luminescent Colloidal Silicon Nanocrystals: High Dispersibility in Polar Liquid by Phosphorus and Boron Codoping. *The Journal of Physical Chemistry C* **2012**, *116* (33), 17969-17974. DOI: 10.1021/jp305832x.
(132) Almeida, A. J.; Sugimoto, H.; Fujii, M.; Brandt, M. S.; Stutzmann, M.; Pereira, R. N. Doping efficiency and confinement of donors in embedded and free standing Si nanocrystals. *Physical Review B* **2016**, *93* (11), 115425. DOI: 10.1103/PhysRevB.93.115425.
(133) Borowik, Ł.; Nguyen-Tran, T.; Roca i Cabarrocas, P.; Mélin, T. Doped semiconductor nanocrystal junctions. *Journal of Applied Physics* **2013**, *114* (20), 204305. DOI: 10.1063/1.4834516.
(134) Nayak, P. K.; Mahesh, S.; Snaith, H. J.; Cahen, D. Photovoltaic solar cell technologies: analysing the state of the art. *Nature Reviews Materials* **2019**, *4* (4), 269-285. DOI: 10.1038/s41578-019-0097-0. Mazzaro, R.; Gradone, A.; Angeloni, S.; Morselli, G.; Cozzi, P. G.; Romano, F.; Vomiero, A.; Ceroni, P. Hybrid Silicon Nanocrystals for Color-Neutral and Transparent Luminescent Solar Concentrators. *ACS Photonics* **2019**, *6* (9), 2303-2311. DOI: 10.1021/acsphotonics.9b00802. Meinardi, F.; Ehrenberg, S.; Dhamo, L.; Carulli, F.; Mauri, M.; Bruni, F.; Simonutti, R.; Kortshagen, U.; Brovelli, S. Highly efficient luminescent solar

concentrators based on earth-abundant indirect-bandgap silicon quantum dots. *Nature Photonics* **2017**, *11* (3), 177-185. DOI: 10.1038/nphoton.2017.5.
(135) Velusamy, T.; Mitra, S.; Macias-Montero, M.; Svrcek, V.; Mariotti, D. Varying Surface Chemistries for p-Doped and n-Doped Silicon Nanocrystals and Impact on Photovoltaic Devices. *ACS Applied Materials & Interfaces* **2015**, *7* (51), 28207-28214. DOI: 10.1021/acsami.5b06577.
(136) Brongersma, M. L.; Shalaev, V. M. The Case for Plasmonics. *Science* **2010**, *328* (5977), 440-441. DOI: doi:10.1126/science.1186905.
(137) Zhong, Y.; Malagari, S. D.; Hamilton, T.; Wasserman, D. Review of mid-infrared plasmonic materials. *Journal of Nanophotonics* **2015**, *9* (1), 093791. Baldassarre, L.; Sakat, E.; Frigerio, J.; Samarelli, A.; Gallacher, K.; Calandrini, E.; Isella, G.; Paul, D. J.; Ortolani, M.; Biagioni, P. Midinfrared Plasmon-Enhanced Spectroscopy with Germanium Antennas on Silicon Substrates. *Nano Letters* **2015**, *15* (11), 7225-7231. DOI: 10.1021/acs.nanolett.5b03247.
(138) Ni, Z.; Ma, L.; Du, S.; Xu, Y.; Yuan, M.; Fang, H.; Wang, Z.; Xu, M.; Li, D.; Yang, J.; et al. Plasmonic Silicon Quantum Dots Enabled High-Sensitivity Ultrabroadband Photodetection of Graphene-Based Hybrid Phototransistors. *ACS Nano* **2017**, *11* (10), 9854-9862. DOI: 10.1021/acsnano.7b03569.
(139) Podhorodecki, A.; Zatryb, G.; Golacki, L. W.; Misiewicz, J.; Wojcik, J.; Mascher, P. On the origin of emission and thermal quenching of SRSO:Er3+ films grown by ECR-PECVD. *Nanoscale Research Letters* **2013**, *8* (1), 98. DOI: 10.1186/1556-276X-8-98. Hiller, D.; López-Vidrier, J.; Gutsch, S.; Zacharias, M.; Nomoto, K.; König, D. Defect-Induced Luminescence Quenching vs. Charge Carrier Generation of Phosphorus Incorporated in Silicon Nanocrystals as Function of Size. *Scientific Reports* **2017**, *7* (1), 863. DOI: 10.1038/s41598-017-01001-1. Tchebotareva, A. L.; de Dood, M. J. A.; Biteen, J. S.; Atwater, H. A.; Polman, A. Quenching of Si nanocrystal photoluminescence by doping with gold or phosphorous. *Journal of Luminescence* **2005**, *114* (2), 137-144. DOI: https://doi.org/10.1016/j.jlumin.2004.12.014.
(140) Limpens, R.; Fujii, M.; Neale, N. R.; Gregorkiewicz, T. Negligible Electronic Interaction between Photoexcited Electron–Hole Pairs and Free Electrons in Phosphorus–Boron Co-Doped Silicon Nanocrystals. *The Journal of Physical Chemistry C* **2018**, *122* (11), 6397-6404. DOI: 10.1021/acs.jpcc.7b12313.
(141) Limpens, R.; Sugimoto, H.; Neale, N. R.; Fujii, M. Critical Size for Carrier Delocalization in Doped Silicon Nanocrystals: A Study by Ultrafast Spectroscopy. *ACS Photonics* **2018**, *5* (10), 4037-4045. DOI: 10.1021/acsphotonics.8b00671.
(142) Limpens, R.; Neale, N. R. Free electron-driven photophysics in n-type doped silicon nanocrystals. *Nanoscale* **2018**, *10* (25), 12068-12077, 10.1039/C8NR02173B. DOI: 10.1039/C8NR02173B.
(143) Newman, R. C. Defects in silicon. *Reports on Progress in Physics* **1982**, *45* (10), 1163-1210. DOI: 10.1088/0034-4885/45/10/003.
(144) Lu, P.; Mu, W.; Xu, J.; Zhang, X.; Zhang, W.; Li, W.; Xu, L.; Chen, K. Phosphorus Doping in Si Nanocrystals/SiO2 Multilayers and Light Emission with Wavelength Compatible for Optical Telecommunication. *Scientific Reports* **2016**, *6* (1), 22888. DOI: 10.1038/srep22888. Li, D.; Jiang, Y.; Liu, J.; Zhang, P.; Xu, J.; Li, W.; Chen, K. Modulation of surface states by phosphorus to improve the optical properties of ultra-small Si nanocrystals. *Nanotechnology* **2017**, *28* (47), 475704. DOI: 10.1088/1361-6528/aa852e.
(145) Hiller, D.; López-Vidrier, J.; Gutsch, S.; Zacharias, M.; Wahl, M.; Bock, W.; Brodyanski, A.; Kopnarski, M.; Nomoto, K.; Valenta, J.; et al. Boron-Incorporating Silicon Nanocrystals Embedded in SiO2: Absence of Free Carriers vs. B-Induced Defects. *Scientific Reports* **2017**, *7*

(1). DOI: 10.1038/s41598-017-08814-0. Nakamura, T.; Adachi, S.; Fujii, M.; Sugimoto, H.; Miura, K.; Yamamoto, S. Size and dopant-concentration dependence of photoluminescence properties of ion-implanted phosphorus- and boron-codoped Si nanocrystals. *Physical Review B* **2015**, *91* (16), 165424. DOI: 10.1103/PhysRevB.91.165424.
(146) Veettil, B. P.; Wu, L.; Jia, X.; Lin, Z.; Zhang, T.; Yang, T.; Johnson, C.; McCamey, D.; Conibeer, G.; Perez-Würfl, I. Passivation effects in B doped self-assembled Si nanocrystals. *Applied Physics Letters* **2014**, *105* (22), 222108. DOI: 10.1063/1.4903776. Sugimoto, H.; Zhou, H.; Takada, M.; Fushimi, J.; Fujii, M. Visible-light driven photocatalytic hydrogen generation by water-soluble all-inorganic core–shell silicon quantum dots. *Journal of Materials Chemistry A* **2020**, *8* (31), 15789-15794, 10.1039/D0TA01071E. DOI: 10.1039/D0TA01071E. Stegner, A. R.; Pereira, R. N.; Lechner, R.; Klein, K.; Wiggers, H.; Stutzmann, M.; Brandt, M. S. Doping efficiency in freestanding silicon nanocrystals from the gas phase: Phosphorus incorporation and defect-induced compensation. *Physical Review B* **2009**, *80* (16), 165326. DOI: 10.1103/PhysRevB.80.165326. Fujii, M.; Mimura, A.; Hayashi, S.; Yamamoto, K. Photoluminescence from Si nanocrystals dispersed in phosphosilicate glass thin films: Improvement of photoluminescence efficiency. *Applied Physics Letters* **1999**, *75* (2), 184-186. DOI: 10.1063/1.124313.
(147) Iori, F.; Ossicini, S. Effects of simultaneous doping with boron and phosphorous on the structural, electronic and optical properties of silicon nanostructures. *Physica E: Low-dimensional Systems and Nanostructures* **2009**, *41* (6), 939-946. DOI: https://doi.org/10.1016/j.physe.2008.08.010.
(148) Fujii, M.; Sugimoto, H.; Imakita, K. All-inorganic colloidal silicon nanocrystals—surface modification by boron and phosphorus co-doping. *Nanotechnology* **2016**, *27* (26), 262001. DOI: 10.1088/0957-4484/27/26/262001.
(149) Li, H.; Guan, L.; Zhang, X.; Yu, H.; Huang, D.; Sun, M.; Wang, S. A cyanine-based near-infrared fluorescent probe for highly sensitive and selective detection of hypochlorous acid and bioimaging. *Talanta* **2016**, *161*, 592-598. DOI: https://doi.org/10.1016/j.talanta.2016.09.008.
(150) Peng, F.; Cao, Z.; Ji, X.; Chu, B.; Su, Y.; He, Y. Silicon nanostructures for cancer diagnosis and therapy. *Nanomedicine* **2015**, *10* (13), 2109-2123. DOI: 10.2217/nnm.15.53. Ghosh, B.; Shirahata, N. Colloidal silicon quantum dots: synthesis and luminescence tuning from the near-UV to the near-IR range. *Sci Technol Adv Mater* **2014**, *15* (1), 014207. DOI: 10.1088/1468-6996/15/1/014207. Peng, F.; Su, Y.; Zhong, Y.; Fan, C.; Lee, S.-T.; He, Y. Silicon Nanomaterials Platform for Bioimaging, Biosensing, and Cancer Therapy. *Accounts of Chemical Research* **2014**, *47* (2), 612-623. DOI: 10.1021/ar400221g.
(151) Fujii, M.; Fujii, R.; Takada, M.; Sugimoto, H. Silicon Quantum Dot Supraparticles for Fluorescence Bioimaging. *ACS Applied Materials and Interfaces* **2020**, *3* (6), 6099-6107. DOI: 10.1021/acsanm.0c01295.
(152) Limpens, R.; Pach, G. F.; Neale, N. R. Nonthermal Plasma-Synthesized Phosphorus–Boron co-Doped Si Nanocrystals: A New Approach to Nontoxic NIR-Emitters. *Chemistry of Materials* **2019**, *31* (12), 4426-4435. DOI: 10.1021/acs.chemmater.9b00810.
(153) McVey, B. F. P.; König, D.; Cheng, X.; O'Mara, P. B.; Seal, P.; Tan, X.; Tahini, H. A.; Smith, S. C.; Gooding, J. J.; Tilley, R. D. Synthesis, optical properties and theoretical modelling of discrete emitting states in doped silicon nanocrystals for bioimaging. *Nanoscale* **2018**, *10* (33), 15600-15607, 10.1039/C8NR05071F. DOI: 10.1039/C8NR05071F.
(154) Clark, R. J.; Dang, M. K. M.; Veinot, J. G. C. Exploration of Organic Acid Chain Length on Water-Soluble Silicon Quantum Dot Surfaces. *Langmuir* **2010**, *26* (19), 15657-15664. DOI:

10.1021/la102983c. Aghajamali, M.; Xie, H.; Javadi, M.; Kalisvaart, W. P.; Buriak, J. M.; Veinot, J. G. C. Size and Surface Effects of Silicon Nanocrystals in Graphene Aerogel Composite Anodes for Lithium Ion Batteries. *Chemistry of Materials* **2018**, *30* (21), 7782-7792. DOI: 10.1021/acs.chemmater.8b03198. Yang, Z.; Gonzalez, C. M.; Purkait, T. K.; Iqbal, M.; Meldrum, A.; Veinot, J. G. C. Radical Initiated Hydrosilylation on Silicon Nanocrystal Surfaces: An Evaluation of Functional Group Tolerance and Mechanistic Study. *Langmuir* **2015**, *31* (38), 10540-10548. DOI: 10.1021/acs.langmuir.5b02307. Yu, Y.; Hessel, C. M.; Bogart, T. D.; Panthani, M. G.; Rasch, M. R.; Korgel, B. A. Room Temperature Hydrosilylation of Silicon Nanocrystals with Bifunctional Terminal Alkenes. *Langmuir* **2013**, *29* (5), 1533-1540. DOI: 10.1021/la304874y.
(155) Dasog, M.; Bader, K.; Veinot, J. G. C. Influence of Halides on the Optical Properties of Silicon Quantum Dots. *Chemistry of Materials* **2015**, *27* (4), 1153-1156. DOI: 10.1021/acs.chemmater.5b00115.
(156) Islam, M. A.; Purkait, T. K.; Veinot, J. G. C. Chloride Surface Terminated Silicon Nanocrystal Mediated Synthesis of Poly(3-hexylthiophene). *Journal of the American Chemical Society* **2014**, *136* (43), 15130-15133. DOI: 10.1021/ja5075739.
(157) Wheeler, L. M.; Neale, N. R.; Chen, T.; Kortshagen, U. R. Hypervalent surface interactions for colloidal stability and doping of silicon nanocrystals. *Nature Communications* **2013**, *4* (1), 2197. DOI: 10.1038/ncomms3197.
(158) Kim, J.-S.; Yang, S.; Bae, B.-S. Thermally Stable Transparent Sol−Gel Based Siloxane Hybrid Material with High Refractive Index for Light Emitting Diode (LED) Encapsulation. *Chemistry of Materials* **2010**, *22* (11), 3549-3555. DOI: 10.1021/cm100903b.
(159) Bell, J. P.; Cloud, J. E.; Cheng, J.; Ngo, C.; Kodambaka, S.; Sellinger, A.; Ratanathanawongs Williams, S. K.; Yang, Y. N-Bromosuccinimide-based bromination and subsequent functionalization of hydrogen-terminated silicon quantum dots. *RSC Advances* **2014**, *4* (93), 51105-51110, 10.1039/C4RA08477B. DOI: 10.1039/C4RA08477B. Kehrle, J.; Höhlein, I. M. D.; Yang, Z.; Jochem, A.-R.; Helbich, T.; Kraus, T.; Veinot, J. G. C.; Rieger, B. Thermoresponsive and Photoluminescent Hybrid Silicon Nanoparticles by Surface-Initiated Group Transfer Polymerization of Diethyl Vinylphosphonate. *Angewandte Chemie International Edition* **2014**, *53* (46), 12494-12497. DOI: https://doi.org/10.1002/anie.201405946.
(160) Yu, Y.; Rowland, C. E.; Schaller, R. D.; Korgel, B. A. Synthesis and Ligand Exchange of Thiol-Capped Silicon Nanocrystals. *Langmuir* **2015**, *31* (24), 6886-6893. DOI: 10.1021/acs.langmuir.5b01246.
(161) Matsumoto, T.; Maeda, M.; Kobayashi, H. Photoluminescence Enhancement of Adsorbed Species on Si Nanoparticles. *Nanoscale Research Letters* **2016**, *11* (1), 7. DOI: 10.1186/s11671-015-1220-9.
(162) Sinelnikov, R.; Dasog, M.; Beamish, J.; Meldrum, A.; Veinot, J. G. C. Revisiting an Ongoing Debate: What Role Do Surface Groups Play in Silicon Nanocrystal Photoluminescence? *ACS Photonics* **2017**, *4* (8), 1920-1929. DOI: 10.1021/acsphotonics.7b00102.
(163) Wen, X.; Dao, L. V.; Hannaford, P. Temperature dependence of photoluminescence in silicon quantum dots. *Journal of Physics D: Applied Physics* **2007**, *40* (12), 3573-3578. DOI: 10.1088/0022-3727/40/12/005. Ledoux, G.; Gong, J.; Huisken, F.; Guillois, O.; Reynaud, C. Photoluminescence of size-separated silicon nanocrystals: Confirmation of quantum confinement. *Applied Physics Letters* **2002**, *80* (25), 4834-4836. DOI: 10.1063/1.1485302.

(164) Höhlein, I. M. D.; Angı, A.; Sinelnikov, R.; Veinot, J. G. C.; Rieger, B. Functionalization of Hydride-Terminated Photoluminescent Silicon Nanocrystals with Organolithium Reagents. *Chemistry – A European Journal* **2015**, *21* (7), 2755-2758. DOI: https://doi.org/10.1002/chem.201405555.
(165) Angı, A.; Sinelnikov, R.; Meldrum, A.; Veinot, J. G. C.; Balberg, I.; Azulay, D.; Millo, O.; Rieger, B. Photoluminescence through in-gap states in phenylacetylene functionalized silicon nanocrystals. *Nanoscale* **2016**, *8* (15), 7849-7853, 10.1039/C6NR01435F. DOI: 10.1039/C6NR01435F.
(166) Miyano, M.; Kitagawa, Y.; Wada, S.; Kawashima, A.; Nakajima, A.; Nakanishi, T.; Ishioka, J.; Shibayama, T.; Watanabe, S.; Hasegawa, Y. Photophysical properties of luminescent silicon nanoparticles surface-modified with organic molecules via hydrosilylation. *Photochemical & Photobiological Sciences* **2016**, *15* (1), 99-104. DOI: 10.1039/c5pp00364d.
(167) Yu, Y.; Korgel, B. A. Controlled Styrene Monolayer Capping of Silicon Nanocrystals by Room Temperature Hydrosilylation. *Langmuir* **2015**, *31* (23), 6532-6537. DOI: 10.1021/acs.langmuir.5b01291.
(168) Liu, X.; Zhao, S.; Gu, W.; Zhang, Y.; Qiao, X.; Ni, Z.; Pi, X.; Yang, D. Light-Emitting Diodes Based on Colloidal Silicon Quantum Dots with Octyl and Phenylpropyl Ligands. *ACS Applied Materials & Interfaces* **2018**, *10* (6), 5959-5966. DOI: 10.1021/acsami.7b16980.
Mastronardi, M. L.; Henderson, E. J.; Puzzo, D. P.; Chang, Y.; Wang, Z. B.; Helander, M. G.; Jeong, J.; Kherani, N. P.; Lu, Z.; Ozin, G. A. Organic Light-Emitting Diodes: Silicon Nanocrystal OLEDs: Effect of Organic Capping Group on Performance (Small 23/2012). *Small* **2012**, *8* (23), 3542-3542. DOI: https://doi.org/10.1002/smll.201290131.
(169) Angı, A.; Sinelnikov, R.; Heenen, H. H.; Meldrum, A.; Veinot, J. G. C.; Scheurer, C.; Reuter, K.; Ashkenazy, O.; Azulay, D.; Balberg, I.; et al. The influence of conjugated alkynyl(aryl) surface groups on the optical properties of silicon nanocrystals: photoluminescence through in-gap states. *Nanotechnology* **2018**, *29* (35), 355705. DOI: 10.1088/1361-6528/aac9ef.

Chapter 2:

Understanding and derivatizing the surface of boron-doped silicon nanoparticles

A version of the chapter has been published:

Milliken, S.; Cui, K.; Klein, B.; Cheong, I.; Yu, H.; Vladimir, M.; Veinot, J. Nanoscale. **2021**, 13, 1, 18281-18292.

2.1 Introduction

It is fair to say silicon and its semiconductor properties have helped to revolutionize modern society - it is a key component of all electronic devices and is the dominant active material in solar cells.[1] Silicon nanomaterials, particularly silicon nanoparticles (SiNPs), have emerged as intriguing systems that show a variety of promising and useful characteristics including, but not limited to photo- and electro-luminescence.[2] The optical and electronic properties of SiNPs of dimensions smaller than the Bohr-exciton radius of bulk Si (<5 nm) can be tuned spectrally (i.e., colour) and temporally (i.e., excited-state lifetimes) by judiciously defining particle size, shape, and surface chemistry.[3] SiNPs are attractive alternatives to the status quo heavy/toxic metal containing quantum dots because they are comprised of abundant elements (i.e., Si is the second most abundant element in the earth's crust),[4] have low toxicity,[5] and a broad spectral range over which their photoluminescence (PL) may be tuned (i.e., blue through NIR).[6] A significant challenge facing the development of all silicon nanomaterials is the naturally forming oxide layer, which can diminish crystallinity and influence luminescence intensity.[7] Fortunately, surface functionalization methods that involve covalent attachment of surface groups have proven effective in minimizing the deleterious effects of oxidation on SiNP optical properties and helped facilitate the development of high quality colloidal SiNPs with tunable band gaps.[8,9,10,11-13]

Strictly speaking silicon is a semiconductor, however, at room temperature its electronic properties approach those of an insulator because of the very low number of free carriers; this leads to poor conductivity.[14] Silicon's interesting electronic properties emerge once tailored low concentrations (10^{13} to 10^{18} cm^{-3}) of well-defined impurities are introduced to generate free-carriers.[15] Fujii et al. first demonstrated B doping in SiNPs embedded in SiO_2 and noticed the SiNPs PL could be tuned by defining the B concentration.[16] Pi et al. extended B-doping to

freestanding SiNPs, leading to extensive studies on the resulting change in optical and electronic characteristics.[17] Since then, several methods such as non-thermal plasma and laser ablation have been developed to produce freestanding B-doped SiNPs with concentrations of up 60 at. %.[18-21] These doped SiNPs present intriguing and important opportunities in microelectronics,[17] semiconductor plasmonics,[18-20,22,23,24] multimodal medical imaging agents,[13,16,25] among others.

Surface chemistry has proven to be an invaluable tool in controlling and tailoring the properties of intrinsic SiNPs; it imparts resistance to oxidation and compatibility with various media (e.g., polar and non-polar solvents), provides tailoring and enhancement of PL response,[10,11,26,27,28] tuning of electronic structure through the introduction of mid-gap states,[29] and offers interfacing with biological systems.[30] If doped SiNPs are to realize their full practical potential, it is essential that methods for tailoring their surface chemistry be established. Unfortunately, B-doped SiNPs are resistant to the standard post-synthesis surface derivatization protocols (e.g., hydrosilylation, dehydrocoupling, etc.).[9,11,12,27] Greenhagen et al. recently reported non-thermal plasma preparation and *in situ* functionalization of polyethylene glycol functionalized B-doped SiNPs; these SiNPs are soluble in biological buffer media,[31] however, the scope of studies investigating functionalization of B-doped SiNPs remains limited and solubility in non-polar organic-phase solvents has yet to be reported. As synthesized, heavily B-doped SiNPs (i.e., B concentrations of 7 – 60 %) are soluble in polar solvents, including water, and exhibit negative zeta-potential.[21,31-33] These characteristics are reasonably ascribed to a large number of ionized B-atoms being located at, or near, the particle surface, leading to an altered surface chemistry from that of intrinsic SiNPs.[21] An associated benefit of doping SiNPs with B is they are more resistant to oxidation than their non-doped counterparts, which can be explained by the Cabrera-Mott theory.[34] This may also be the origin of the limited reactivity of B-doped SiNPs. Previously, our

group has developed procedures that activated intrinsic SiNPs toward functionalization via *in situ* etching with reagents such as XeF_2 or PCl_5.[11,12] These procedures offer an intriguing possibility for B-doped systems. Herein, we report phosphorus pentachloride-mediated functionalization of B-doped SiNPs that were prepared using a scalable thermal processing method. Our approach provides a convenient method for introducing alkoxy surface functional groups of varied chain lengths, rendering the B-doped SiNPs organic-phase soluble.

2.2 Experimental Details

2.2.1 Reagents and Materials

Hydrofluoric acid (48-50%) and sulfuric (reagent grade, 95–98%) acids were purchased from Fisher Scientific and Caledon Laboratory Chemicals, respectively. Fuming sulfuric acid (reagent grade, 20% free SO_3 bases), trichlorosilane (99%), boric acid (reagent grade, 99.5%), 1-pentanol (reagent grade, 99.0%), 1-octanol (anhydrous, 99.0%), 1-nonanol (98.0%), 1-decanol (98.0%), 1-dodecanol (reagent grade, 98.0%), ethanol (anhydrous, ≤0.003% water) and toluene (HPLC grade) were purchased from Sigma-Aldrich. Acetonitrile was purified using a Pure-Solv purification system and collected immediately prior to use.

2.2.2 Synthesis of Hydrogen Silsesquioxane (HSQ)

HSQ was synthesized using a modified literature procedure.[35] Briefly, dry toluene (45.0 mL) is added dropwise to a solution of concentrated (15 mL) and fuming (7.2 mL) sulfuric acid. Subsequently, a mixture of trichlorosilane (16 mL) in dry toluene (110 mL) was added dropwise to the solution with stirring. The organic phase was isolated and washed with sulfuric acid solution. Removal of the solvent in vacuo to provide a white crystalline solid (25-30 g). The product was used without further characterization.

2.2.3 Preparation of Boron-Doped Silicon Nanoparticles (SiNPs)

B-doped SiNPs were synthesized using a modified literature procedure in which boric acid is used as a dopant source and incorporated into the HSQ prior to the formation of the SiNPs.[32] HSQ (0.21

mmol) was dissolved in methyl-isobutylketone (5 mL) and combined with ethanol solutions containing predefined quantities of boric acid (4, 8, 16, 32, and 48.5 mmol). The resulting mixture was stirred for no less than 3 hours after which the solution was dried overnight under nitrogen flow to provide a free-flowing white powder. This precursor was transferred to a standard tube furnace and thermally processed in a flowing atmosphere of 5% H_2:95% Ar for 1 hour at 1100 °C to induce formation of SiO_2-like matrix containing silicon nanodomains. Following cooling to room temperature, the resulting black solid was removed from the furnace, ground to a fine powder using an agate mortar and pestle, and etched with a mixture of hydrofluoric acid (HF), ethanol and water (v:v:v; 1:1:1) for one hour to remove the silica matrix. Caution, HF is extremely dangerous and must be handled with all recommended personal protective equipment in the chemical safety data sheet. The resulting solution was brown and transparent, it was then washed 3 times with a 2:1:2 ethanol, methanol, and n-pentane solution at 3000 rpm for 20 minutes.

2.2.4 Phosphorus Pentachloride (PCl_5) Initiated Functionalization of B-Doped SiNPs

Freshly etched B-doped SiNPs (20 mg) dispersed in dry acetonitrile (10 mL) were combined with PCl_5 (0.3 g) and stirred for one hour. The solvent was subsequently removed in vacuo and the product was redispersed in 10 mL (i.e., excess) of the ligand of choice (i.e., 1-decanol). This mixture was subjected to three freeze-pump-thaw cycles and subsequently refluxed for 12 hours with stirring. The resulting product mixture containing alkoxy-functionalized B-doped SiNPs was transferred to Nalgene® centrifuge tubes with 40 mL of ethanol and centrifuged at 11400 rpm for 50 minutes to yield a brown pellet. The clear colourless supernatant was decanted and discarded while the pellet was redispersed in a mixture of toluene (5 mL) and ethanol (45 mL) with sonication in a bath sonicator and then recovered upon centrifuging at 11400 rpm for 50 minutes. This

dispersion/centrifugation cycle was repeated twice after which the dark-brown pellet was redispersed in dry toluene to yield a transparent dark-yellow solution.

2.2.5 Fourier-Transform Infrared Spectroscopy

FT-IR spectra were collected by a Thermo Nicolet Continum FT-IR microscope of a freeze-dried B-doped SiNPs in a KBr pellet.

2.2.6 X-Ray Photoelectron Spectroscopy (XPS)

Samples were prepared by drop-casting toluene solutions of the B-doped SiNPs of interest onto copper foil. XP spectra were measured using Kratos Axis 165 Ultra X-ray Photoelectron Spectrometer with a monochromatic Al Kα source operating at 210W with an energy of 1486.6 eV. High resolution spectra were obtained using an analyzer pass energy of 20 eV and a step of 0.1 eV. For survey spectra, a pass energy of 160 eV and a step of 0.3 eV. Spectra were calibrated to C 1s 284.8 eV using adventitious carbon. Peak fitting was performed using CasaXPS software with a Shirley-type background. Spin-orbit coupling in Si 2p was fixed to an area ratio of 2:1 and 0.6 eV energy spacing, the 2 $p_{1/2}$ is not presented for clarity.

2.2.7 Electron Microscopy and Associated Methods

Transmission electron microscopy (TEM) and HR-TEM were performed on a JEOL JEM-ARM200CF S/TEM (Cold Field Emission Gun) electron microscope with an accelerating voltage of 200 kV using SiQDs drop-coated from a toluene solution onto a holey carbon-coated copper

grid. The SiQD size was determined by averaging the size of 300 particles using ImageJ software (version 1.51j8) and plotted as an average shifted histogram as outlined previously by Buriak and co-workers.[36] A representative set of histograms are formed by shifting the origin at even steps through the width of one bin. The ASH is generated by averaging all the histograms that were generated to form one plot. High-resolution TEM (HRTEM) measurements were conducted using TEM (TEM) (JEOL 2200FS, 200 kV). Electron energy loss spectroscopy (EELS) analysis was also conducted using a 200 kV JEOL 2200FS scanning TEM with a nominal beam size of 0.5 nm. Digital Micrograph (Gatan, Inc.) was employed for signal collection and data extraction from EELS spectra. Typical current densities for HRTEM imaging were 13.15 pA cm^{-2} at 400 K and 16.72 pA cm^{-2} at 500 K.

2.2.8 Solid-State Nuclear Magnetic Resonance (NMR)Spectroscopy

All NMR experiments were performed on a 14.1 T Varian Inova spectrometer equipped with a 3.2 mm triple resonance Varian magic-angle spinning (MAS) probe doubly tuned to ν_0 (^{1}H) = 599.94 MHz and ν_0 (^{11}B) = 192.48 MHz. Powdered samples of the nanoparticles were packed into ZrO_2 rotors (3.2 mm o.d., 22 μL, 30-40 mg) with Torlon drive and top caps. ^{11}B NMR spectra were referenced using 0.1 M $H_3BO_{3\ (aq)}$ as a secondary reference set at +19.6 ppm. All NMR data were processed using OpenVnmrJ v.2.1A.

The ^{11}B NMR data were acquired at ambient temperature (293 ± 2 K) with a MAS frequency of 16 kHz. ^{11}B MAS NMR experiments were obtained using a short 0.4 μs Bloch pulse (9° tip angle, $\gamma B1/2\pi$=62.5 kHz) with a 3 s recycle delay, 2 steady state scans and between 1024 and 24100 co-added transients. The ^{11}B[^{1}H] cross-polarization (CP) MAS NMR experiments were acquired on

the 9.6% B-doped SiNP using a series of mixing times ranging between 0.2 and 5 ms. All CPMAS NMR experiments were performed with a linear ramp on ^{1}H (ν_{rf} = 62.5 kHz) to obtain an optimized Hartman-Hahn match for each contact time with TPPM ^{1}H decoupling.[37]

2.2.9 Photoluminescence (PL) Spectroscopy

An argon ion laser with 351 nm emission wavelength was used to excite SiNPs suspended in toluene. The resulting photoluminescence was collected by an optic fiber, passed through a 400 nm long-pass filter to eliminate scattered light from the excitation source and fed into an Ocean Optics USB2000 spectrometer. Absorption was measured using the Ocean Optics spectrometer with a MINI-D2T Deuterium Tungsten light source for 9.6 %B SiNPs before and after functionalization with 1-decanol and compared with intrinsic SiNPs functionalized with 1-decanol. Absolute quantum yield (QY) measurements were performed using a homemade integrating sphere with a 365 nm light-emitting diode excitation source. The photoluminescence and excitation intensities were captured through a fiber attached to the sphere and analyzed with a calibrated Ocean Optics spectrometer. The equation $QY = (I_{PL,\,sample} - I_{PL,\,blank})/(I_{ex,\,blank} - I_{ex,\,sample})$ was used to calculate the absolute quantum efficiency, where I_{PL} is the integrated photoluminescence intensity and I_{ex} is the excitation intensity recorded inside the sphere.

2.3 Results and Discussion

2.3.1 Investigation of the structure of B-doped silicon nanoparticles

For the present study, B-doped SiNPs with an average diameter of 3.86 ± 0.92 nm (Figure 2.1 c) were prepared using a modified thermal annealing method in which boric acid provided the dopant source and hydrogen silsesquioxane was the Si precursor (Scheme 2.1).[32,35]

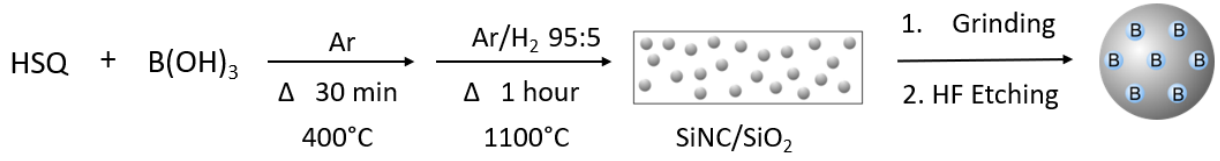

Scheme 2. 1 Preparation of B-doped of SiNPs via thermal-induced disproportionation of hydrogen silsesquioxane in the presence of boric acid.

The original white solid reactant mixture changes to a brown composite after the first thermal processing step and then to a black solid with further heating. Infrared spectra were acquired for the HSQ before and after mixing with boric acid and after each thermal processing stage (Figure 2.1 a). Additional features attributable to B-O, B-H, and O-H are observed after the initial mixing step at 1400, 2500, and 3300 cm^{-1} respectively, consistent with the addition of boric acid. The Si-H_x stretching region in the HSQ spectrum is significantly reduced after thermal processing and Si-O and B-O features become dominant; this is consistent with thermally-induced decomposition/crosslinking of HSQ. Thermogravimetric analysis (TGA) was also performed for mixtures containing the lowest and highest amounts of dopant precursor (0.25 g vs. 3 g); these analyses showed a greater weight-loss when more boric acid is added, suggesting that under the present conditions boric acid begins to decompose at approximately 200 °C (Figure 2.1 b). Upon etching the doped composite with hydrofluoric acid (HF) the starting cloudy dispersion becomes

a transparent brown solution and the liberated B-doped SiNPs are readily recovered via centrifugation. FTIR analysis of the liberated B-doped SiNPs reveals Si-H and Si-O stretching modes at 2250 and 1080 cm^{-1}, respectively (Figure 2.1 a).[11,28,38] We also note characteristic stretching modes for B-H and B-O at 2500 cm^{-1} and 1400 cm^{-1}.[24,33,29] These observations are strongly suggestive of the B dopants being located in/on the SiNPs and that they impact the particle surface chemistry.

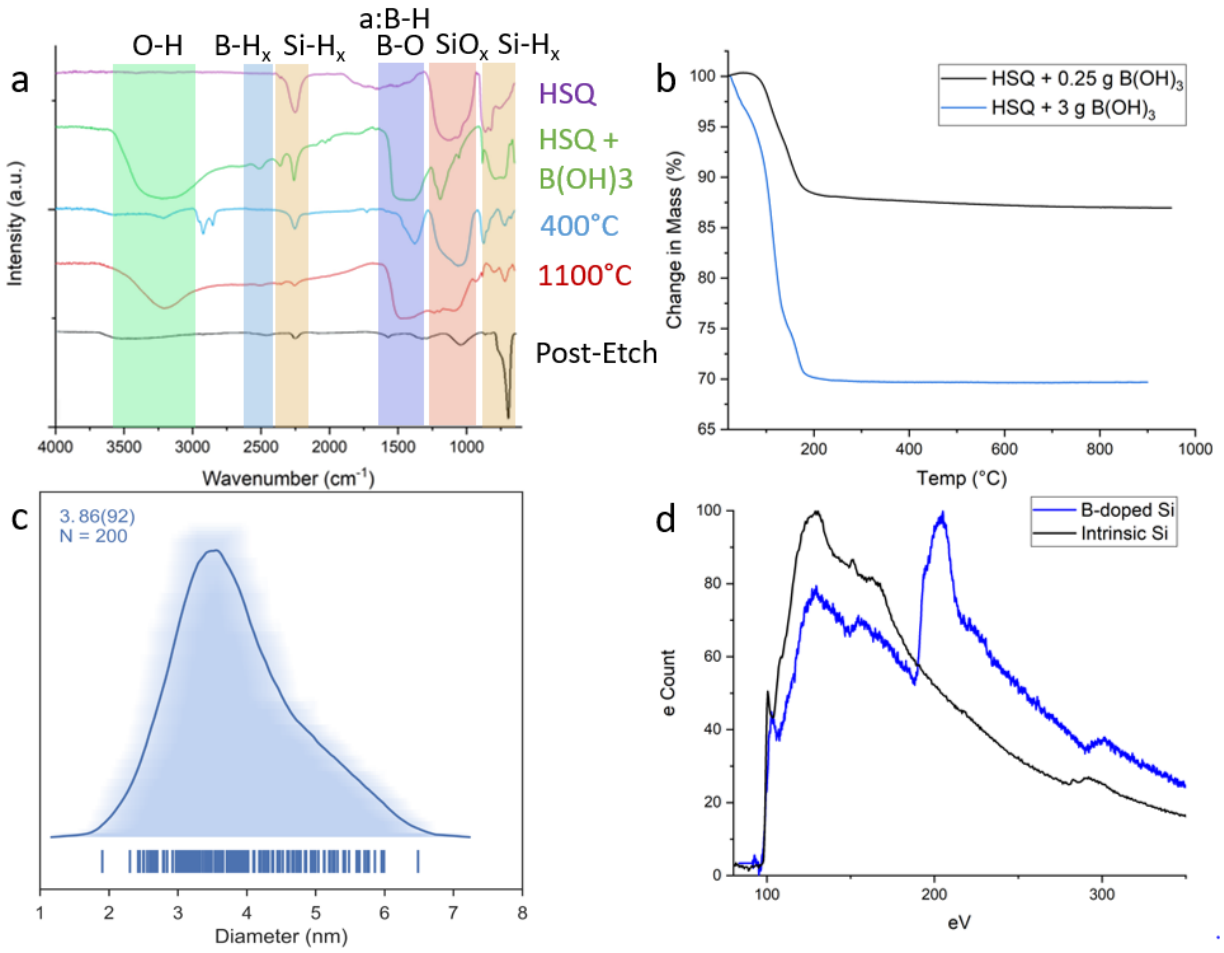

Figure 2. 1 a) Fourier-transform infrared spectra of undoped hydrogen silsesquioxane (HSQ), boric acid doped HSQ, the resulting composite after each thermal processing step and the resulting freestanding particles from Scheme 2.1. b) TGA of the lowest and highest concentration of B (0.25 g and 3 g of boric acid for 1.8 and 9.6 atomic % B). c) average shifted histogram for 9.6 atomic % B-doped SiNPs with resulting average diameter of 3.86 ± 0.92 nm. d) Electron energy loss spectroscopy (EELS) point spectrum of intrinsic Si and 9.6 atomic % B SiNPs showing L-edge of Si at 100 eV and the K-edge of B in the doped sample at 200 eV.

A key challenge when working with doped SiNPs is differentiating the doped system from a straightforward mixture of non-doped nanoparticles and other species; this requires confirmation of the localization of the doping atoms. Complicating matters, detecting light atoms like boron can be difficult. For the present systems, B content in the liberated SiNPs was confirmed using electron energy-loss spectroscopy (EELS); EELS point spectra show a sharp and intense feature at 200 eV consistent with the B K-edge (Figure 2.1 d).[40] EELS line scans also clearly show localization of the B within the SiNPs (Figure 2.2 b). Methodic variation of the amount of boric acid (0.25 – 3 g) added to the reaction mixture allowed definition of the B content within the SiNPs in the range of 1.8 - 9.6 atomic % as determined using ICP-MS (Figure 2.2 c). Even at these high doping concentrations, which exceed the solid solubility limit of B in Si (approx. 1 at.%),[32] the present SiNPs retain the diamond cubic Si crystalline structure as confirmed by powder X-ray diffraction (XRD; Figure 2.2 d) and high-resolution transmission-electron spectroscopy (HRTEM; Figure 2.2 a).[41]

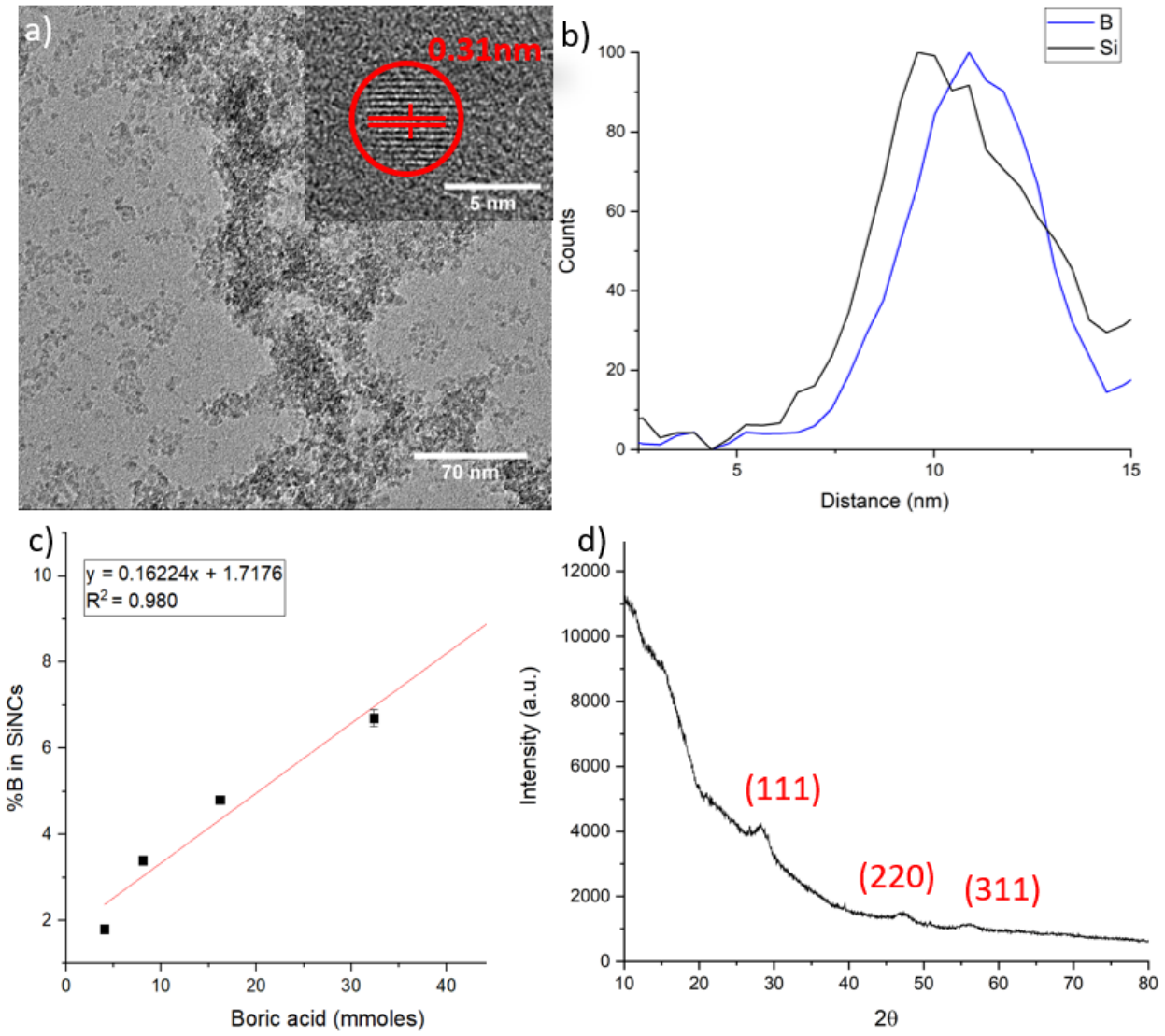

Figure 2. 2 a) TEM of bare 9.6 atomic % B-doped SiNPs after HF etching with a measured average diameter of 3.86 ± 0.92 nm determined from the average shifted histogram in Figure 2.1. HRTEM inset provides measured lattice fringe of 0.31 nm that is characteristic of crystalline Si. b) Integrated B and Si counts derived from EELS line scan of a single 9.6 atomic % B-doped SiNP using the L-edge of Si at 100 eV and K-edge of B at 188 eV. c) Atomic % B measured using ICP-MS shows a resulting B concentration of 1.8 – 9.6 atomic % B for B-doped SiNPs synthesized with varying amounts of boric acid precursor. d) X-ray diffraction pattern of as-

synthesized 9.6 atomic % B-doped SiNPs after HF etching, characteristic reflections for crystalline Si are observed.

X-ray photoelectron spectroscopy (XPS) provides insight into the nature (i.e., concentration, oxidation state) of the B and Si atoms in the doped SiNPs. High-resolution XP spectra of the Si 2p region were obtained for the highest (9.6 atomic %) and the lowest (1.8 atomic %) concentrations of B-doped SiNPs (Figure 2.3). The spectrum of the SiNPs containing 1.8 at. % B shows a decrease in intensity for the emissions arising from Si(I), Si(II), and Si(III) when compared to that of the SiNPs containing more B; this difference could, in part, be due to an increase in Si-B bonding, however, definitive assignment must be done with caution. The spectrum of the SiNPs containing a 1.8 atomic % B also sees the emergence of Si(IV), suggesting that these particles are more susceptible to oxidation.[42]

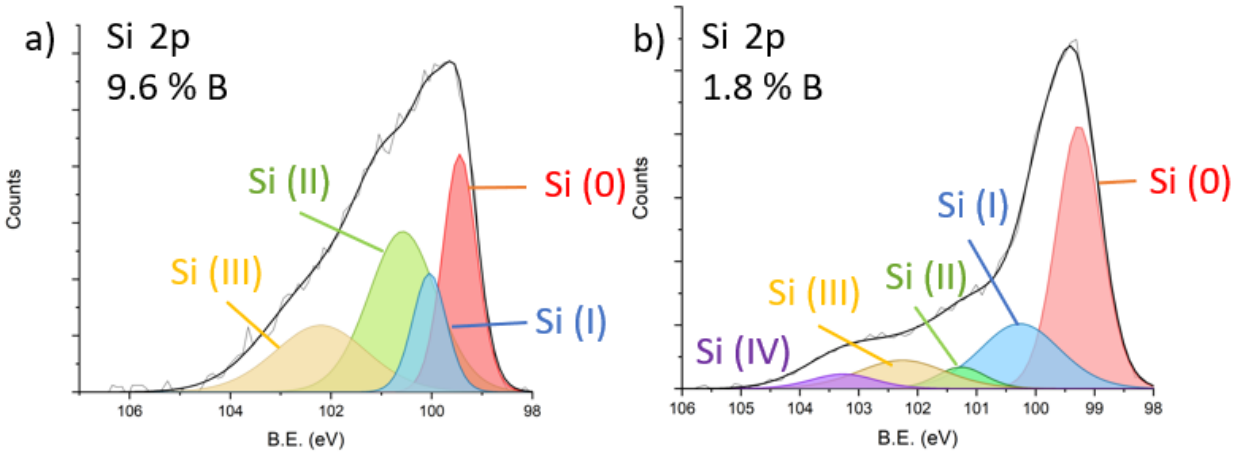

Figure 2. 3 High resolution XP spectra of Si 2P region for a) 9.6 and b) 1.8 atomic % B doped SiNPs.

High-resolution XP spectra of the B 1s spectral region reveals a single broad emission that is readily fit with two components corresponding to binding energies of 187 and 189 eV (Figures 2.4 a - d). The lower binding energy emission (i.e., 187 eV) has previously been attributed to substitutional B atoms bonded to four Si atoms.[43] The higher binding energy emission matches closely with that of hydrogenated B atoms bonded to two or three Si atoms and can reasonably attributed to B atoms residing at, or near the NP surface.[44] This assignment is further reinforced when considering the B concentration within the SiNPs far exceeds the solid solubility limit of B in bulk Si. As such, it is reasonable the NP core becomes saturated and excess B migrates to, or stays at, the particle surface.[18-21,24]

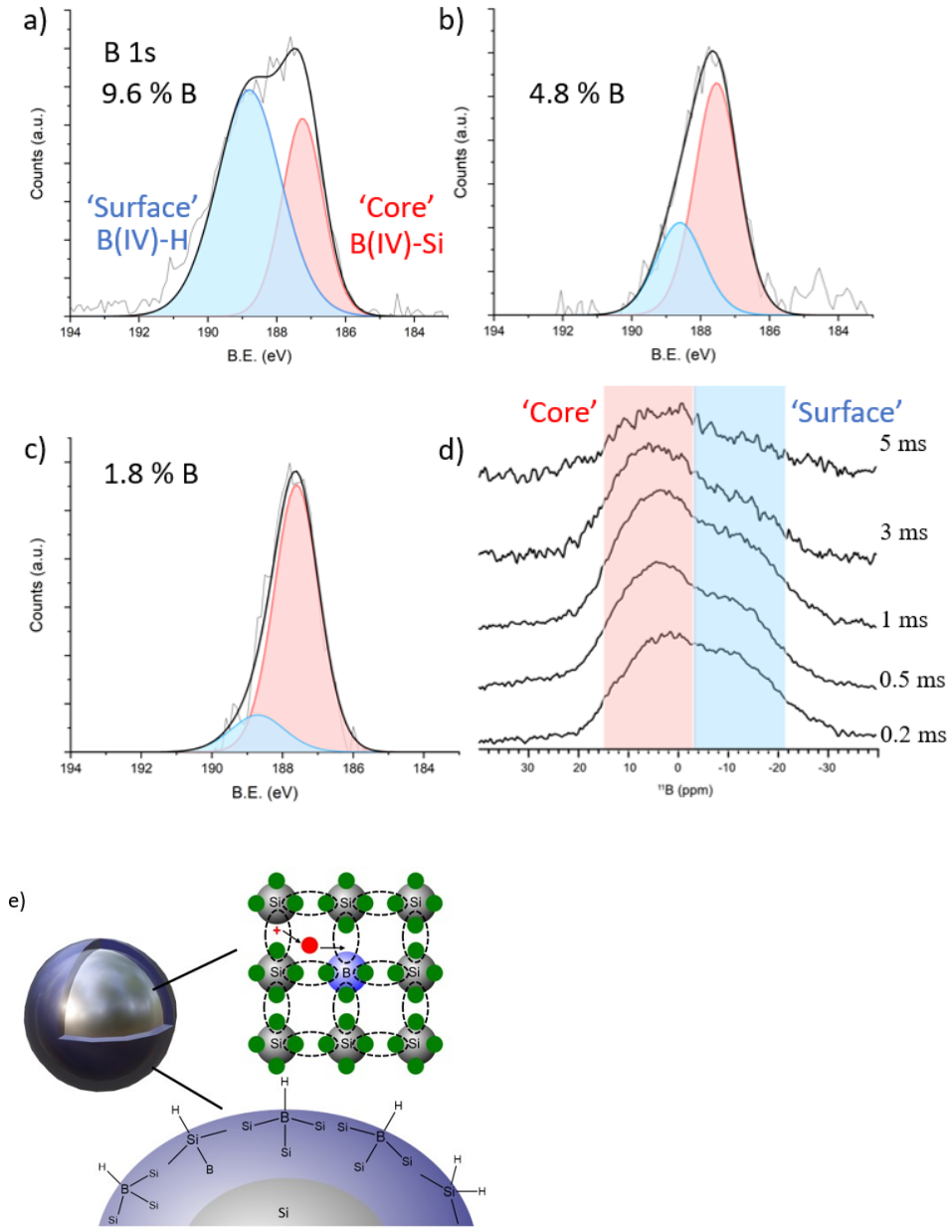

Figure 2. 4 High resolution B 1s XP spectra for a) 9.6, b) 6.7, and c) 1.8 atomic % B-doped SiNPs. d) CP ^{11}B MAS NMR spectra of 9.6 atomic % B-doped SiNPs acquired with the indicated contact times. e) Image representing the two dopant locations in the NP: the core (top) and the surface (bottom). The core B species corresponds to B substituted in the Si lattice, in this case an electron would be donated from a neighboring Si to B, creating a hole. The surface species B corresponds to a partially hydrogenated B bonded to two or three Si atoms.

Consistent with this proposal, we also note that the integrated area of the peak arising from the surface substituted B decreases when total B concentration decreases, while the integrated peak area of the feature we assign to internal substitutional B remains relatively constant (Table 2.1).

Table 2. 1 Integrated values of "surface" and "core" B species found by taking the area under the fitted peaks centred at 189 eV and 187 eV in the B 1s spectra for samples with 9.6, 6.7, and 1.8 atomic % B.

Sample	Area of "surface" species (189 eV)	Area of "core" species (187 eV)
9.6 %B	282.4	174.0
6.7 %B	74.3	178.2
1.8 %B	30.2	180.0

The ^{11}B magic-angle spinning nuclear magnetic resonance (MAS NMR) spectroscopy provides complementary atomic-level structural information to that provided by XPS; as such, it was used to investigate the NPs containing different B concentrations (Figure 2.5). In all cases, a broad ^{11}B resonance centred near 2.2 ppm is detected. The quadrupolar coupling constant of this resonance is ca. 1 MHz, indicating the B resides in a pseudo-tetrahedron 4-coordinate ($^{[4]}B$) chemical environment, consistent with our XPS analyses.[18,24] Together the low frequency center of mass and small quadrupolar coupling constant measured for this series of samples supports the presence of a dominant $^{[4]}B$ species. The breadth of this signal is reasonably attributed to the

influence of the surface ^{11}B species that reside in the more structurally disordered surface (Figure 2.5).[38,45] Cross polarization (CP) MAS NMR provides a convenient way to differentiate the NMR active species at the surface, sub-surface and core of nanoparticles.[38,46,47] For the present work, we employed $^{11}B[^{1}H]$ CP MAS NMR to differentiate between surface and core-like B species in SiNPs doped with 9.6 atomic % B. In $^{11}B[^{1}H]$ CP MAS NMR surface protons are polarized, and the nuclear spin polarization is transferred to ^{11}B via the ^{1}H -^{11}B nuclear spin bath in the sample.[48] ^{11}B atoms residing at, or near the NP surface interact more readily with the surface OH and H moieties than do the B atoms within the core-like region.[48] Therefore, at short contact times the surface B species are preferentially detected, while at longer contact times the growth of ^{11}B resonances arising from core species will emerge and become more prominent.[47] For the present system, two regions co-exist when contact times of less than 3 ms are used (Figure 2.4). The feature centred at ~0 ppm is attributed to the "core-like" region of the NP and is indicative of tetrahedral boron that substitutes into the diamond cubic lattice.[49,50] Based on the presented evidence from the B 1s XP spectra, we reasonably conclude this feature corresponds to substitutional B bonded to four Si atoms. The emerging peak detected at -11 ppm is related to the surface species and is assigned to hydrogenated B bonded to Si atoms.[49] As these particles are 4 nm (40 Å), the "core-like" region is still disordered resulting in a broad resonances similar to what has been previously observed in SiNPs.[38]

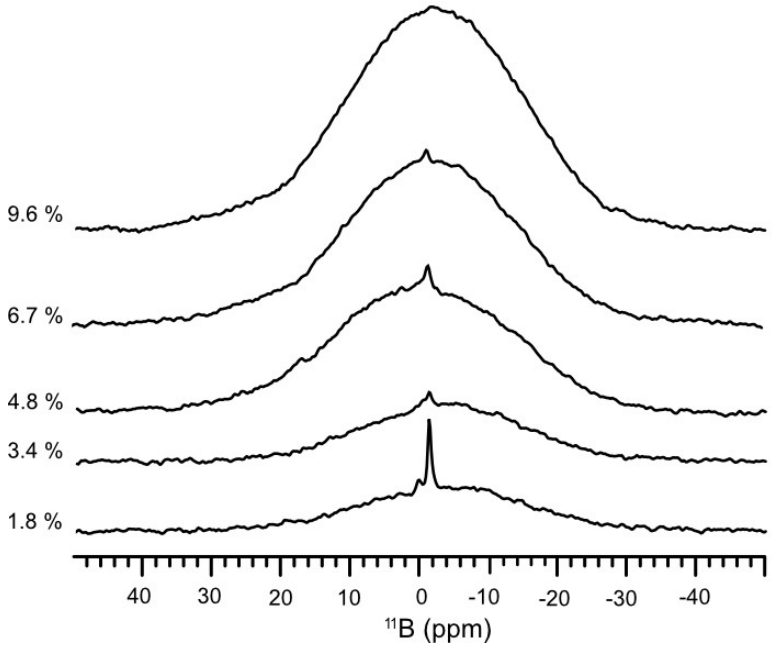

Figure 2. 5 Direct polarization ^{11}B MAS NMR of B-doped SiNPs with indicated atomic % B (ICP-MS).

From these complementary analyses we propose that for the present B-doped SiNPs, B atoms reside in the core and at the surface of the particles (Figure 2.4 e). Additionally, the core and surface B species are both 4-coordinate. This latter observation differs from reports describing B-doped SiNPs prepared using solvent-free plasma methods in which B atoms are present as 4-coordinate species within the particle core and 3-coordinate Lewis acidic species at the particle surfaces.[18,19,21,22,24,31] This difference is readily understood in the context of the liberation of freestanding SiNPs from oxide composites and involves treatment with hydrofluoric (HF) acid in solutions containing ethanol and water followed by centrifugation to isolate the solid. After decanting the supernatant, the solid is washed thoroughly with excess ethanol to remove residual HF; this can result in partial oxidation of the SiNP surface. Under these conditions, any Lewis acidic SiNP surface species is exposed to Lewis bases (e.g., water, ethanol, F^-, etc.) that would coordinate to and fill the empty B bonding site passivating the NP surface. Furthermore, the

passivating nature of this capping surface would be significant given coordinated Lewis bases would be linked to the NP through comparatively strong bonds (e.g., B-O; B.E. = 806 kJ/mol at 298 K).[51] In this context, any method used to derivatize these oxide-liberated SiNPs must effectively remove this passivating surface to induce appropriate reactivity.

2.3.2 Surface modification of boron-doped silicon nanoparticles

Previously we demonstrated that treatment of oxide liberated hydride-terminated SiNPs with dilute solutions of XeF_2 or PCl_5 (i.e., mild etchants) provides an effective approach to inducing surface reactivity while simultaneously removing ill-defined species (i.e., defects) that limit photoluminescent response.[11,12,28] These reagents effectively remove surface species providing a "clean" surface that is subsequently derivatized. For the present B-doped SiNPs, it is reasonable that surface species (e.g., oxides, coordinated Lewis bases, etc.) will be removed and a "clean" surface on which controlled reactions may proceed will be revealed. We have chosen to employ PCl_5 because associated reactions proceed more slowly and are more readily controlled. Alkoxy ligands are an ideal starting point for surface functionalization, as both B and Si have a high affinity to O atoms. In this context, we explore the reactivity of 9.6 atomic % B-doped SiNPs with alkoxy ligands of varying length after PCl_5 etching of the NP surface (Scheme 2.2).

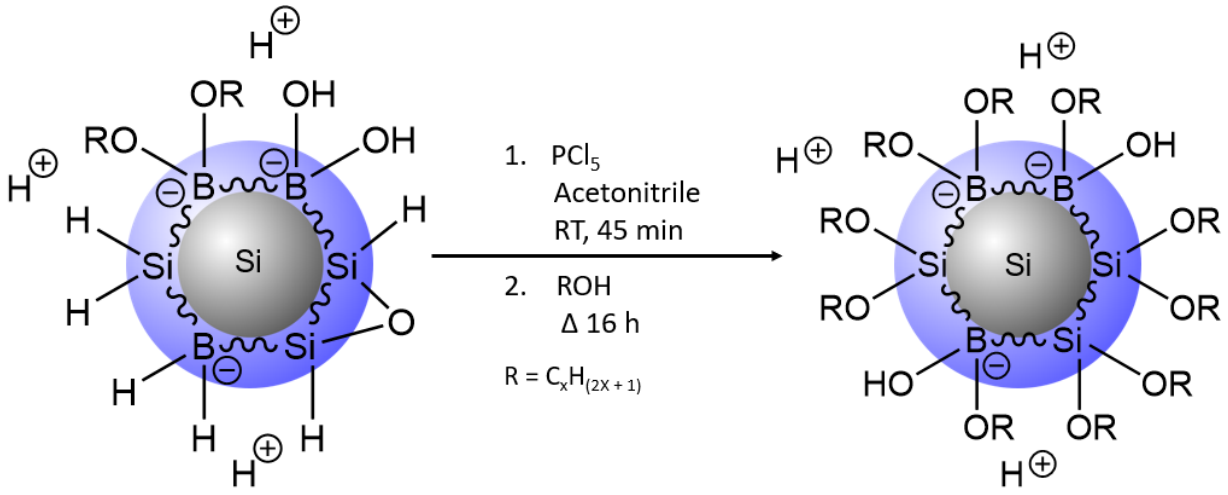

Scheme 2. 2 A pictorial representation of a 2-step etching/functionalization protocol for B-doped SiNPs derivatization.

Initial qualitative observations of the products of the PCl_5 activated reactions with a variety of alcohols show a dramatic change in the solvent compatibility of SiNPs – unlike the starting doped SiNPs, the alkoxide-terminated SiNPs are compatible with common organic solvents (e.g., toluene; Figure 2.6 a). The functionalization was subsequently investigated using thermogravimetry analysis (TGA). Surface coverage increased with the chain length of the alkoxy ligand, from 54.35% for 1-pentanol to 95.90% for 1-decanol, then decreased to 47.91% for 1-dodecanol (Figure 2.6 b; Table 2.2).

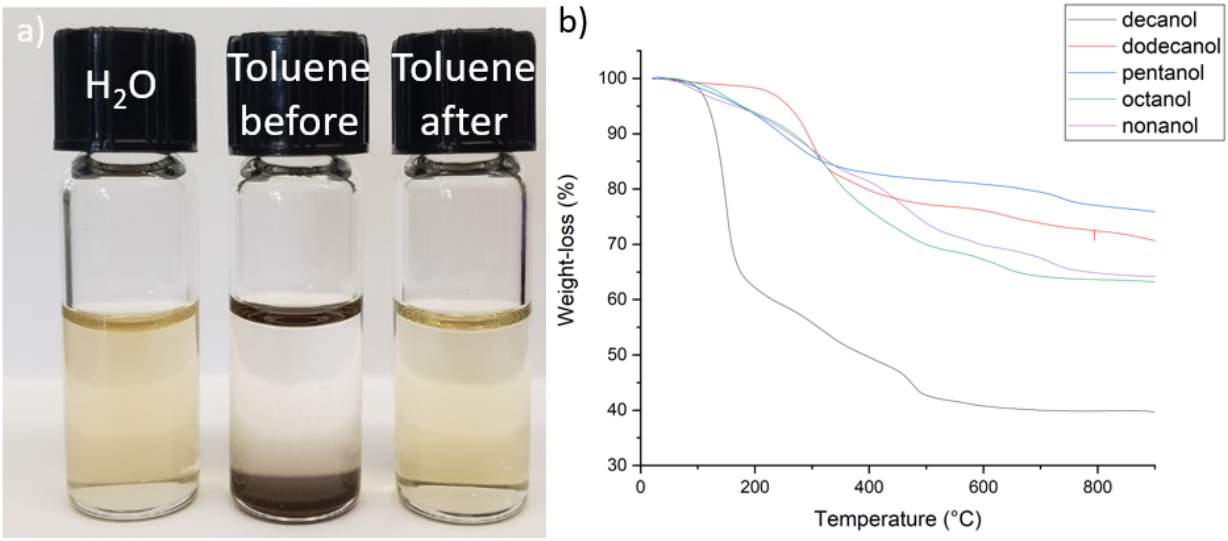

Figure 2. 6 a) B-doped SiNPs in indicated solvents, left: water, middle: toluene before PCl_5 etching/thermal treatment, right: toluene after PCl_5 etching/thermal functionalization with 1-decanol. b) TGA weight-loss plots for 9.6 atomic % B-doped SiNPs functionalized with the indicated alkoxy ligands using the PCl_5/thermal method described in Scheme 2.2.

The decrease in surface coverage from a carbon chain length of 10 to 12 is reasonably ascribed to the molecular packing interactions between surface bonded functionalities. In the case of shorter carbon chain alcohols, there is a possibility their lower boiling points contribute to limiting the effectiveness of the heating step of the surface functionalization – this is the subject of ongoing investigation in our labs.

Table 2. 2 Surface coverage of 9.6 atomic % B-doped SiNPs with different ligands calculated using TGA analysis. Detailed calculation in Appendix A.

Ligand	Theoretical Weight-loss (%)	Experimental Weight-loss (%)	Surface Coverage
1-pentanol	46.27	25.15	54.35
1-octanol	55.99	41.45	74.03
1-nonanol	58.50	48.07	82.78
1-decanol	60.70	58.20	95.90
1-dodecanol	64.54	30.90	47.91

A comparison of the FT-IR spectra of as-prepared B-doped SiNPs with that of SiNPs exposed to PCl_5 (Figure 2.7 a) gives more quantitative insight into the progression of surface functionalization. We find that features at 1080 and 1400 cm^{-1} are absent from the latter spectrum, consistent with the PCl_5 treatment removing Si-O and B-O containing surface species, respectively. After PCl_5 etching, the B-doped SiNPs were heated for 12 h in a neat alcohol of choice (i.e., 1-pentanol, 1-octanol, 1-nonanol, 1-decanol, 1-dodecanol), isolated via centrifugation, and purified via washing with a mixture of toluene/ethanol. In all cases, the IR spectra of the resulting products show diminished Si-H (2250 cm^{-1}) stretching features with concomitant increases in Si-O (1080 cm^{-1}) and B-O (1400 cm^{-1}) stretching features consistent with surface tethering of alkoxide moieties at the B and Si sites on the particle surface (Figure 2.7 b). Additionally, the prominent features associated with C-H_x stretching modes from 2850-2950 cm^{-1} attributed to surface tethered alkoxy moieties are visible after functionalization.[39] The symmetric

and assymetric stretching feature for -CH_2 visibily increases in intensity as the chain length of the alkoxy-ligand increases (2850 cm^{-1} and 2930 cm^{-1}, respectively). The broad feature appearing at 3100 - 3600 cm^{-1} is reasonably attributed to residual water and/or a result of solvent interactions similar to those previously reported for B-doped SiNPs.[21,31-33]

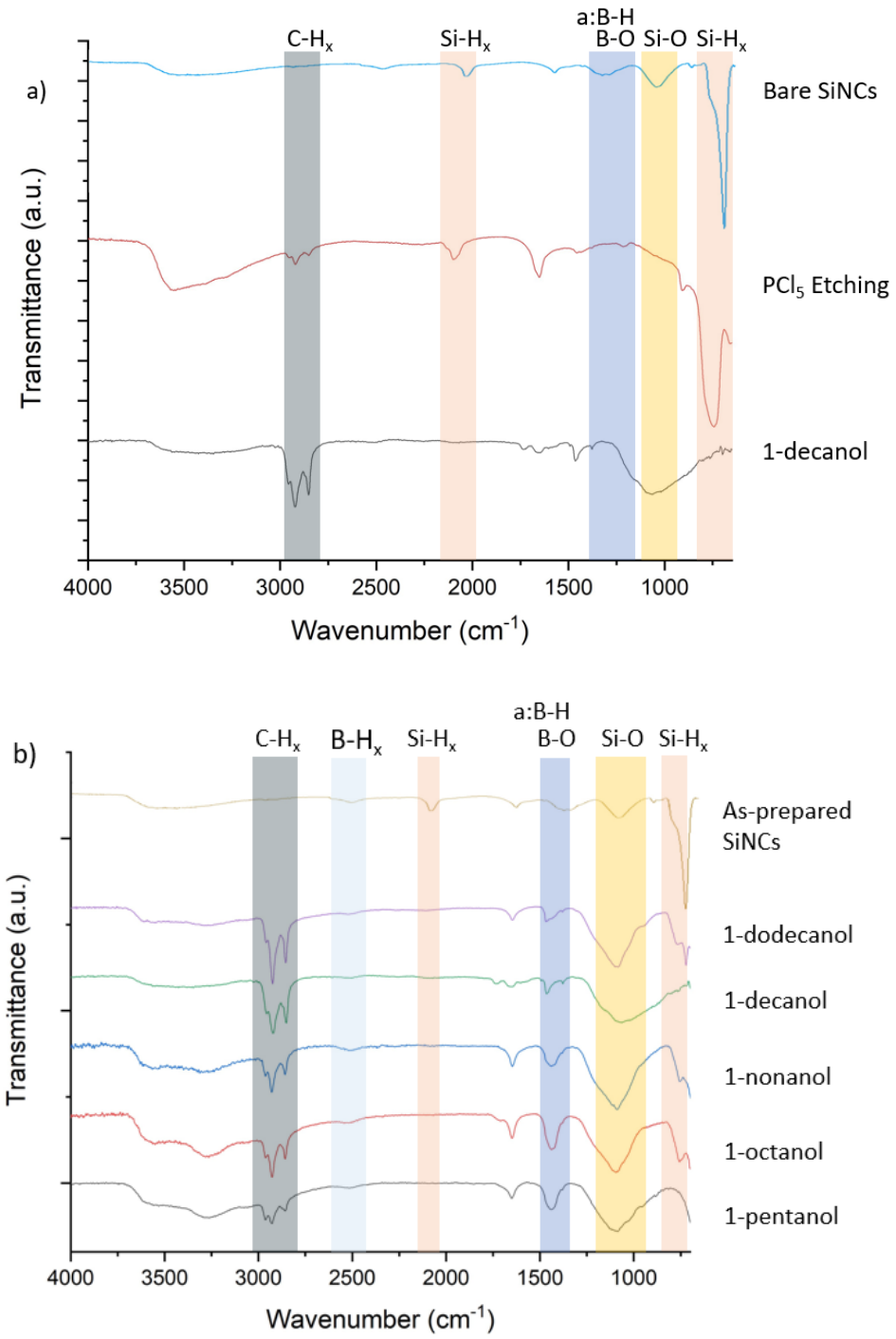

Figure 2. 7 a) FTIR of 9.6 atomic % B-doped SiNPs before functionalization (bare SiNPs), after the PCl_5 etching step, and after reaction with 1-decanol with 180°C heating. b) FTIR spectra of KBr pellets containing B-doped SiNPs before (as-prepared) and after functionalized with the indicated terminal alcohols.

Considering surface etching is essential to the present functionalization procedure, we endeavored to probe the B content within representative functionalized SiNPs using EELS to confirm doping was not compromised/lost. A line scan of toluene soluble particles functionalized with 1-decanol (Figure 2.8 a) shows the integrated B and Si signals of the respective characteristic K- and L-edge energy loss peaks that are co-localized within a single particle. This observation confirms surface etching with PCl_5 does not compromise the B content.[20] The average size, morphology and crystallinity of the B-doped SiNPs were evaluated by TEM and HRTEM (Figure 2.8 b - d). Statistically, the average diameter remained the same (3.80 ± 1.0 nm) as before PCl_5 mediated functionalization (3.86 ± 0.92 nm); this is consistent with PCl_5 being a comparatively mild etchant that removes only a surface layer of atoms from the NP when used at the presented concentrations. HRTEM also confirmed the characteristic lattice spacing for crystalline silicon remains intact after functionalization (Figure 2.8 d).

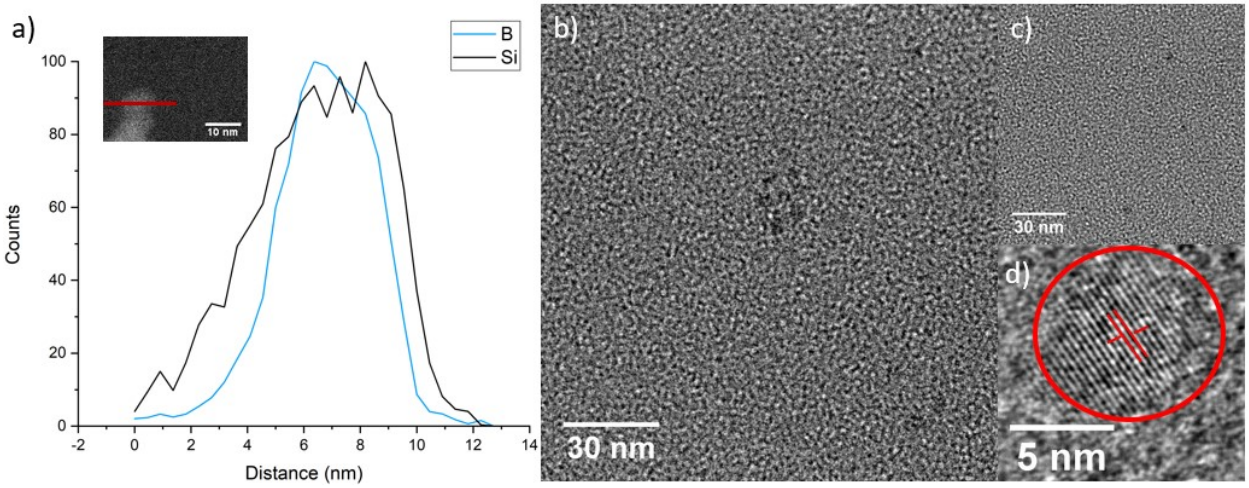

Figure 2. 8 a) Integrated B and Si counts derived from EELS line scan of a single 9.6 atomic % B-doped SiNP after functionalization with 1-decanol using the L-edge of Si at 100 eV and K-edge of B at 188 eV. The inset shows the bright-field TEM survey image and indicated beam-path across the particle. b) c) TEM of 9.6 atomic % B-doped SiNPs functionalized with 1-decanol with a measured average diameter of 3.80 ± 1.0 nm. d) HRTEM provides measured lattice fringe of 0.31 nm that is characteristic of the (111) lattice spacing of crystalline Si.

The doped particles also show a change in optical properties compared to those of intrinsic SiNPs of a similar size (3.7 nm). The UV-Visible absorption of the B-doped sample is increased in intensity relative to the intrinsic SiNPs; we tentatively attribute this to the introduction of defects resulting from doping (Figure 2.9 a). We also note a red-shift in photoluminescence (PL) peak energy is observed in B-doped SiNPs that spans from the visible to the near-IR range (550-850 nm), making it a potential candidate for use as a potential biological contrast agent (Figure 2.9 b). The broadening of the signal from the B-doped SiNPs can be attributed to the variation in doping levels between particles.

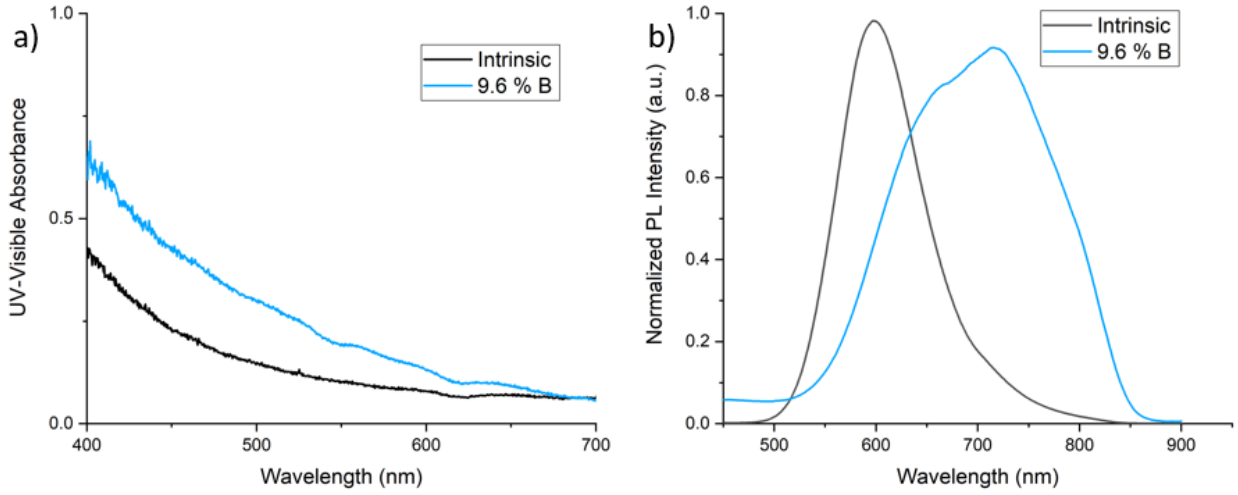

Figure 2. 9 a) UV-Visible absorbance and b) normalized PL intensity spectra of intrinsic and 9.6 atomic % B-doped SiNPs after functionalization with 1-decanol.

As the concentration of B is increased from 1.8 to 9.6 atomic % B the relative PL intensity is observed to decease dramatically (Figure 2.10). Upon functionalization with an alkoxy ligand, the PLQY can be improved significantly. The PLQY of 9.6 atomic % B-doped SiNPs were measured before and after functionalization with 1-decanol using the standardized integrating spheres method and increases from 2% to 15%; although this is still lower than the functionalized intrinsic SiNPs (PLQY = 31 %) which is attributed to doping-induced defects. Improving this efficiency is the subject of future work in the Veinot laboratory.

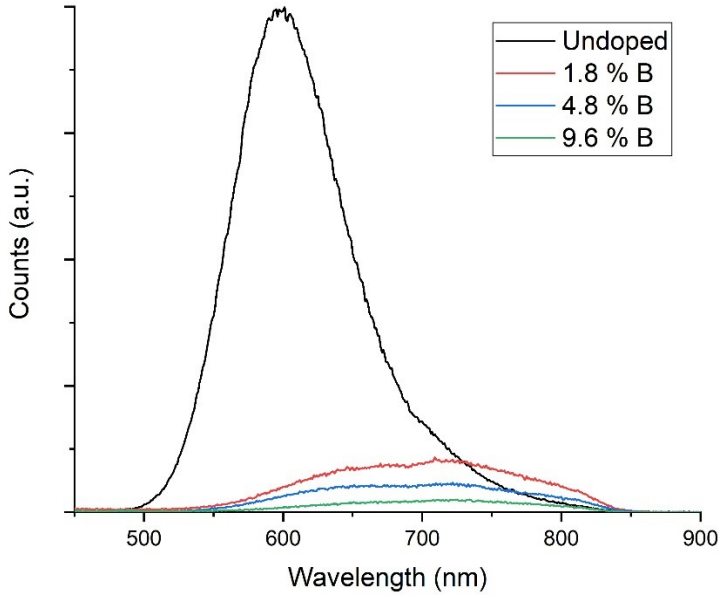

Figure 2. 10 Photoluminescence emission spectra obtained using an excitation wavelength of 350 nm of intrinsic and 1.8, 4.8, and 9.6 atomic % B-doped SiNPs after functionalizing with 1-decanol.

High resolution XP spectra of B 1s and Si 2p were also acquired before and after PCl_5/alkoxide functionalization (Figure 2.11). For convenience, representative B-doped SiNPs functionalized with 1-decanol will be the focus of the following discussion, for other alkoxy ligand XP spectra see Figure 2.11.

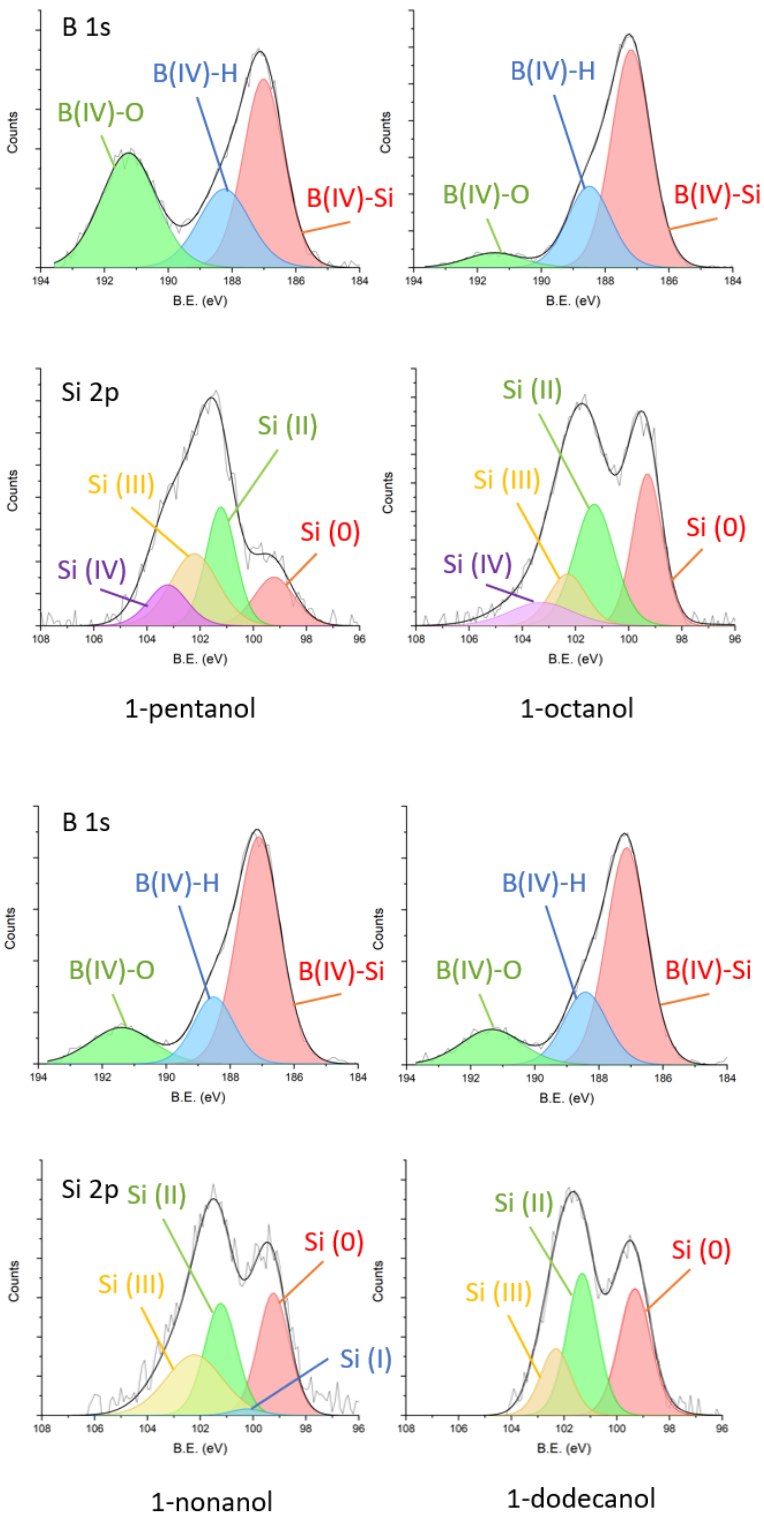

Figure 2. 11 High resolution XP spectra of B 1s and Si 2p of 9.6 atomic % B-doped SiNPs after functionalization with the alkoxy ligands indicated in the figure.

Before functionalization features associated with surface (189 eV) and core (187 eV) B species are evident (Figure 2.12 a). After functionalization with 1-decanol the relative intensity of the feature (189 eV) associated with a hydrogenated surface B is decreased and a new emission emerged at 191 eV (Figure 2.12 c). We confidently attribute this new feature to oxidized 4-coordinate B bonded to two or three Si atoms and one or two 'OR' functionalities; this feature is consistent with covalent attachment 1-decanol to the SiNP surface through a B-O linkage.[19,31,33] Turning our attention to the Si 2p region, before functionalization it is readily fit to four components that are routinely assigned to Si(0), Si(I), Si(II), and Si(III) (Figure 2.12 b).[42] After functionalization and consistent with attachment of OR surface moieties through Si-O linkages we note an increase in the intensity of Si(II) and Si(III) species in the XP spectrum of the 1-decanol functionalized SiNPs (Figure 2.12 d).

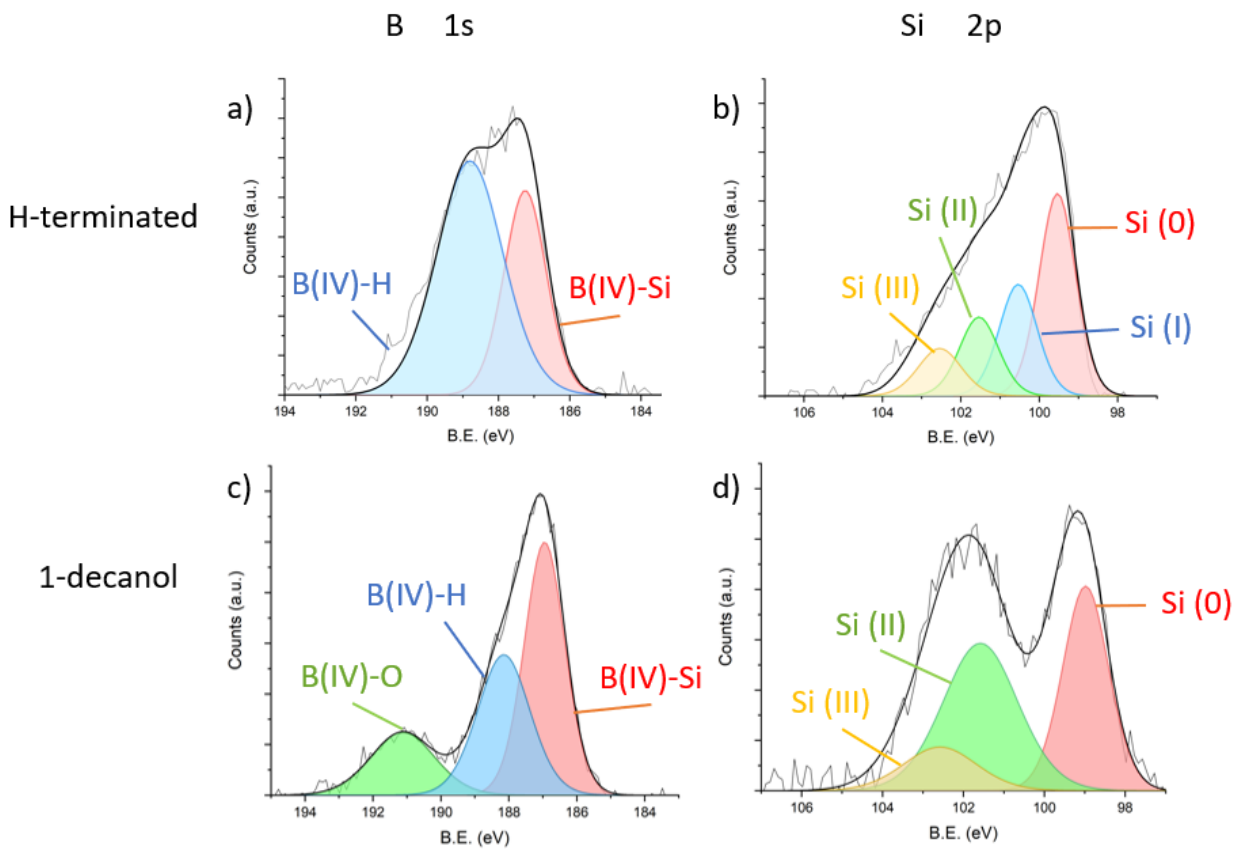

Figure 2. 12 High resolution XP spectra of B 1s (left column) and Si 2p (right column) of 9.6 atomic % B-doped SiNPs a), b) before and c), d) after functionalization with 1-decanol.

To further investigate the role/importance of heating in the presented functionalization protocol, we performed the alkoxy functionalization with PCl_5 etching using 1-pentanol (boiling point = 138 °C) under two different reaction conditions: 1) without heating and 2) in a pressure sealed-tube heated to 180 °C. The high-resolution B 1s and Si 2p XP spectra of the products obtained from each reaction are shown in Figure 2.13. The B 1s for the reaction without heating is readily fit to emissions related to core (187 eV) and the hydrogenated surface (189 eV) species (Figure 2.13 a). As expected, the relative peak intensity of the surface B species is decreased

compared to before PCl_5 etching (Figure 2.13 a). Interestingly, the B(IV)-O feature seen in the B 1s spectrum for the reaction with 180°C heating (Figure 2.13 c) is not present for the reaction without heating.

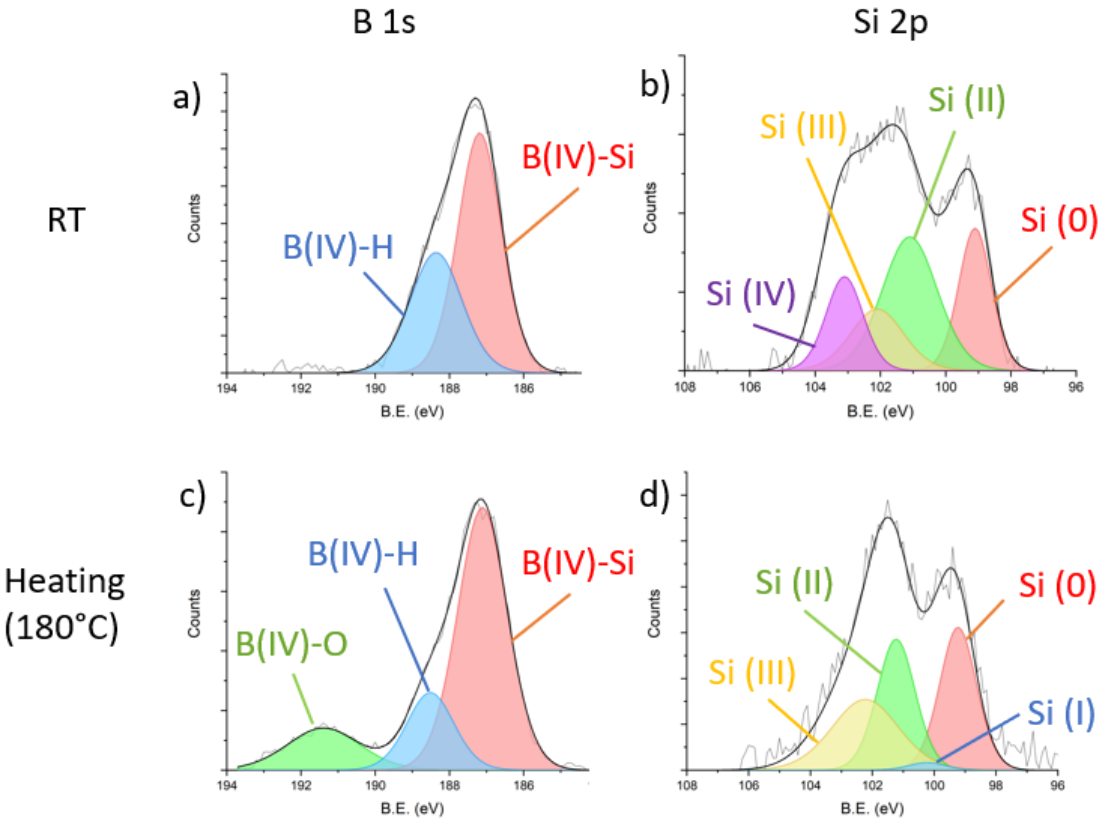

Figure 2. 13 High resolution XP spectra of B 1s (left column) and Si 2p (right column) of 9.6 atomic % B-doped SiNPs after functionalization with 1-pentanol a), b) without any heating (i.e., room temperature) and c), d) heated to 180°C in a pressure sealed flask.

These observations strongly suggest the surface B species does not (or very little) form a bond with the O atom of the alkoxy ligand without heating. Additionally, the Si 2p spectrum for the reaction without heating indicates a greater level of oxidation than the reaction performed at

180 ºC consistent with less effective/complete functionalization. TGA analysis confirms that the surface coverage decreases from 53.35 to 28.92 % when the functionalization reaction is performed without heating (Figure 2.14).

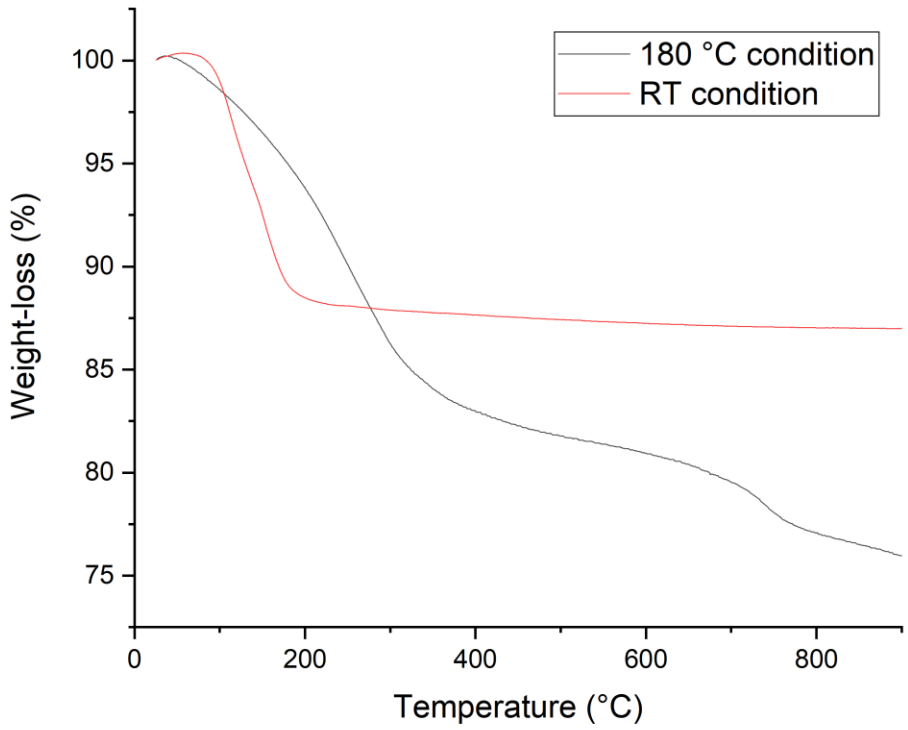

Figure 2. 14 TGA weight-loss plots for functionalization reaction of 9.6 atomic % B-doped SiNPs with 1-pentanol for two different reaction conditions: without heating (red curve) and heated to 180 °C in a pressure sealed flask (black curve).

Clearly, heating the reaction mixture is essential to introducing alkoxide moieties on the surface of B-doped SiNPs. Thermally-induced hydrosilylation is well established and proceeds at temperatures ≥ 140 °C.[52] B-H and Si-H bonds have similar bond strengths (i.e., 330 and 298

kJ/mol, respectively), and thermally-induced dehydrogenation of borane adducts has been reported.[53] Discerning the mechanism of the presented surface reaction is complicated by the diverse surface chemistry of the SiNPs and is the subject of ongoing investigations.

2.4 Conclusions

In conclusion, we have successfully demonstrated that PCl_5 is an effective mild etchant that removes partially oxidized Si and B species from the surfaces of B-doped SiNPs and facilitates alkoxide surface functionalization. The resulting alkoxy-functionalized B-doped SiNPs form stable colloids in common organic solvents. We find that heat and the formation of B-O bonds are critical for the successful functionalization with alkoxy ligands. Organic soluble B-doped SiNPs are expected to pave the way for exciting new applications including optoelectronic integration, the development of plasmonic devices and biomedical imaging.

2.5 References

(1) Oliva-Chatelain, B. L.; Ticich, T. M.; Barron, A. R. Doping silicon nanocrystals and quantum dots. *Nanoscale* **2016**, *8* (4), 1733-1745. DOI: 10.1039/c5nr04978d.
(2) Canham, L. Introductory lecture: origins and applications of efficient visible photoluminescence from silicon-based nanostructures. *Faraday Discussions* **2020**, *222*, 10-81. DOI: 10.1039/d0fd00018c.
(3) Brus, L. E. A simple model for the ionization potential, electron affinity, and aqueous redox potentials of small semiconductor crystallites. *The Journal of Chemical Physics* **1983**, *79* (11), 5566-5571. DOI: 10.1063/1.445676.
(4) Kuhlmann, A. M. The Second Most Abundant Element in the Earth's Crust. *JOM* **1963**, *15* (7), 502-505. DOI: 10.1007/bf03378936.
(5) Erogbogbo, F.; Yong, K.-T.; Roy, I.; Xu, G.; Prasad, P. N.; Swihart, M. T. Biocompatible Luminescent Silicon Quantum Dots for Imaging of Cancer Cells. *ACS Nano* **2008**, *2* (5), 873-878. DOI: 10.1021/nn700319z. Bhattacharjee, S.; Rietjens, I. M. C. M.; Singh, M. P.; Atkins, T. M.; Purkait, T. K.; Xu, Z.; Regli, S.; Shukaliak, A.; Clark, R. J.; Mitchell, B. S.; et al. Cytotoxicity of surface-functionalized silicon and germanium nanoparticles: the dominant role of surface charges. *Nanoscale* **2013**, *5* (11), 4870. DOI: 10.1039/c3nr34266b.
(6) Hessel, C. M.; Reid, D.; Panthani, M. G.; Rasch, M. R.; Goodfellow, B. W.; Wei, J.; Fujii, H.; Akhavan, V.; Korgel, B. A. Synthesis of ligand-stabilized silicon nanocrystals with size-dependent photoluminescence spanning visible to near-infrared wavelengths. *Chemistry of Materials* **2012**, *24* (2), 393-401. DOI: 10.1021/cm2032866. Mastronardi, M. L.; Maier-Flaig, F.; Faulkner, D.; Henderson, E. J.; Kübel, C.; Lemmer, U.; Ozin, G. A. Size-Dependent Absolute Quantum Yields for Size-Separated Colloidally-Stable Silicon Nanocrystals. *Nano Letters* **2011**, *12* (1), 337-342. DOI: 10.1021/nl2036194.
(7) Nakamine, Y.; Kodera, T.; Uchida, K.; Oda, S. Removal of Surface Oxide Layer from Silicon Nanocrystals by Hydrogen Fluoride Vapor Etching. *Japanese Journal of Applied Physics* **2011**, *50*, 115002. DOI: 10.1143/jjap.50.115002.
(8) Yang, Z.; De Los Reyes, G. B.; Titova, L. V.; Sychugov, I.; Dasog, M.; Linnros, J.; Hegmann, F. A.; Veinot, J. G. C. Evolution of the Ultrafast Photoluminescence of Colloidal Silicon Nanocrystals with Changing Surface Chemistry. *ACS Photonics* **2015**, *2* (5), 595-605. DOI: 10.1021/acsphotonics.5b00143. Boukherroub, R.; Morin, S.; Wayner, D. D. M.; Bensebaa, F.; Sproule, G. I.; Baribeau, J. M.; Lockwood, D. J. Ideal Passivation of Luminescent Porous Silicon by Thermal, Noncatalytic Reaction with Alkenes and Aldehydes†. *Chemistry of Materials* **2001**, *13* (6), 2002-2011. DOI: 10.1021/cm000790b. Jurbergs, D.; Rogojina, E.; Mangolini, L.; Kortshagen, U. Silicon nanocrystals with ensemble quantum yields exceeding 60%. *Appl. Phys. Lett.* **2006**, *88* (1), 233116. DOI: 10.1063/1.2210788. Rosso-Vasic, M.; Spruijt, E.; van Lagen, B.; De Cola, L.; Zuilhof, H. Alkyl-Functionalized Oxide-Free Silicon Nanoparticles: Synthesis and Optical Properties. *Small* **2008**, *4*, 1835-1841. DOI: 10.1002/smll.200800066. Sato, S.; Swihart, M. T. Propionic-Acid-Terminated Silicon Nanoparticles: Synthesis and Optical Characterization. *Chemistry of Materials* **2006**, *18* (17), 4083-4088. DOI: 10.1021/cm060750t.
(9) Kelly, J. A.; Veinot, J. G. C. An Investigation into Near-UV Hydrosilylation of Freestanding Silicon Nanocrystals. *ACS Nano* **2010**, *4* (8), 4645-4656. DOI: 10.1021/nn101022b.
(10) Dasog, M.; De Los Reyes, G. B.; Titova, L. V.; Hegmann, F. A.; Veinot, J. G. C. Size vs Surface: Tuning the Photoluminescence of Freestanding Silicon Nanocrystals Across the Visible

Spectrum via Surface Groups. *ACS Nano* **2014**, *8* (9), 9636-9648. DOI: 10.1021/nn504109a.
Dasog, M.; Bader, K.; Veinot, J. G. C. Influence of Halides on the Optical Properties of Silicon Quantum Dots. *Chemistry of Materials* **2015**, *27* (4), 1153-1156. DOI: 10.1021/acs.chemmater.5b00115.
(11) Islam, M. A.; Mobarok, M. H.; Sinelnikov, R.; Purkait, T. K.; Veinot, J. G. C. Phosphorus Pentachloride Initiated Functionalization of Silicon Nanocrystals. *Langmuir* **2017**, *33* (35), 8766-8773. DOI: 10.1021/acs.langmuir.7b00518.
(12) Mobarok, M. H.; Purkait, T. K.; Islam, M. A.; Miskolzie, M.; Veinot, J. G. C. Instantaneous Functionalization of Chemically Etched Silicon Nanocrystal Surfaces. *Angewandte Chemie International Edition* **2016**, *56* (22), 6073-6077. DOI: 10.1002/anie.201609651.
(13) Li, Z. F.; Ruckenstein, E. Water-Soluble Poly(acrylic acid) Grafted Luminescent Silicon Nanoparticles and Their Use as Fluorescent Biological Staining Labels. *Nano Letters* **2004**, *4* (8), 1463-1467. DOI: 10.1021/nl0492436.
(14) Hummel, R. E. *Electronic Properties of Materials*; Springer, New York, NY, 2011. DOI: https://doi.org/10.1007/978-1-4419-8164-6. Duran, C. Principles and Practice of Mechanical Ventilation. 2nd ed. New York: McGraw-Hill; 2006. (US$ 189.95). *Journal of Intensive Care Medicine* **2008**, *23* (5), 349-349. DOI: 10.1177/0885066608320839. D.B. Sirdeshmukh, L. S., K.G. Subhadra, and C.S. Sunandana. Electrical, Electronic and Magnetic Properties of Solids. *MRS Bulletin* **2015**, *40* (7), 613-613. DOI: 10.1557/mrs.2015.161.
(15) Freund, A. K.; Gillet, J.-A.; Zhang, L. Thermal conductivity of silicon, germanium, and silicon-germanium single crystals between 85 K and 300 K. *Crystal and Multilayer Optics* **1998**, *3448* (1), 362. DOI: 10.1117/12.332526. Lambrecht, W. Dopants and Defects in Semiconductors. *Materials Today* **2012**, *15* (7-8), 349. DOI: 10.1016/s1369-7021(12)70146-3.
(16) Fujii, M.; Hayashi, S.; Yamamoto, K. Photoluminescence from B-doped Si nanocrystals. *Journal of Applied Physics* **1998**, *83* (12), 7953-7957. DOI: 10.1063/1.367976.
(17) Pi, X. D.; Gresback, R.; Liptak, R. W.; Campbell, S. A.; Kortshagen, U. Doping efficiency, dopant location, and oxidation of Si nanocrystals. *Applied Physics Letters* **2008**, *92* (12), 123102. DOI: 10.1063/1.2897291.
(18) Zhou, S.; Pi, X.; Ni, Z.; Luan, Q.; Jiang, Y.; Jin, C.; Nozaki, T.; Yang, D. Boron- and Phosphorus-Hyperdoped Silicon Nanocrystals. *Particle & Particle Systems Characterization* **2014**, *32* (2), 213-221. DOI: 10.1002/ppsc.201400103.
(19) Zhou, S.; Pi, X.; Ni, Z.; Ding, Y.; Jiang, Y.; Jin, C.; Delerue, C.; Yang, D.; Nozaki, T. Comparative Study on the Localized Surface Plasmon Resonance of Boron- and Phosphorus-Doped Silicon Nanocrystals. *ACS Nano* **2015**, *9* (1), 378-386. DOI: 10.1021/nn505416r.
(20) Rohani, P.; Banerjee, S.; Sharifi-Asl, S.; Malekzadeh, M.; Shahbazian-Yassar, R.; Billinge, S. J. L.; Swihart, M. T. Synthesis and Properties of Plasmonic Boron-Hyperdoped Silicon Nanoparticles. *Advanced Functional Materials* **2019**, *29* (8), 1807788. DOI: 10.1002/adfm.201807788.
(21) Zhou, S.; Ni, Z.; Ding, Y.; Sugaya, M.; Pi, X.; Nozaki, T. Ligand-Free, Colloidal, and Plasmonic Silicon Nanocrystals Heavily Doped with Boron. *ACS Photonics* **2016**, *3* (3), 415-422. DOI: 10.1021/acsphotonics.5b00568.
(22) Ni, Z.; Pi, X.; Zhou, S.; Nozaki, T.; Grandidier, B.; Yang, D. Size-Dependent Structures and Optical Absorption of Boron-Hyperdoped Silicon Nanocrystals. *Advanced Optical Materials* **2016**, *4* (5), 700-707. DOI: 10.1002/adom.201500706.
(23) Ni, Z.; Ma, L.; Du, S.; Xu, Y.; Yuan, M.; Fang, H.; Wang, Z.; Xu, M.; Li, D.; Yang, J.; et al. Plasmonic Silicon Quantum Dots Enabled High-Sensitivity Ultrabroadband Photodetection of

Graphene-Based Hybrid Phototransistors. *ACS Nano* **2017**, *11* (10), 9854-9862. DOI: 10.1021/acsnano.7b03569. Rowe, D. J.; Jeong, J. S.; Mkhoyan, K. A.; Kortshagen, U. R. Phosphorus-Doped Silicon Nanocrystals Exhibiting Mid-Infrared Localized Surface Plasmon Resonance. *Nano Letters* **2013**, *13* (3), 1317-1322. DOI: 10.1021/nl4001184.
(24) Kramer, N. J.; Schramke, K. S.; Kortshagen, U. R. Plasmonic Properties of Silicon Nanocrystals Doped with Boron and Phosphorus. *Nano Letters* **2015**, *15* (8), 5597-5603. DOI: 10.1021/acs.nanolett.5b02287.
(25) Fujii, M.; Fujii, R.; Takada, M.; Sugimoto, H. Silicon Quantum Dot Supraparticles for Fluorescence Bioimaging. *ACS Applied Materials and Interfaces* **2020**, *3* (6), 6099-6107. DOI: 10.1021/acsanm.0c01295.
(26) Hessel, C. M.; Reid, D.; Panthani, M. G.; Rasch, M. R.; Goodfellow, B. W.; Wei, J.; Fujii, H.; Akhavan, V.; Korgel, B. A. Synthesis of Ligand-Stabilized Silicon Nanocrystals with Size-Dependent Photoluminescence Spanning Visible to Near-Infrared Wavelengths. *Chemistry of Materials* **2011**, *24* (2), 393-401. DOI: 10.1021/cm2032866. Li, Z.; Kortshagen, U. R. Aerosol-Phase Synthesis and Processing of Luminescent Silicon Nanocrystals. *Chemistry of Materials* **2019**, *31* (20), 8451-8458. DOI: 10.1021/acs.chemmater.9b02743. Li, Q.; Luo, T. Y.; Zhou, M.; Abroshan, H.; Huang, J.; Kim, H. J.; Rosi, N. L.; Shao, Z.; Jin, R. Silicon Nanoparticles with Surface Nitrogen: 90% Quantum Yield with Narrow Luminescence Bandwidth and the Ligand Structure Based Energy Law. *ACS Nano* **2016**, *10*, 8385-8393. DOI: 10.1021/acsnano.6b03113. Yu, Y.; Rowland, C. E.; Schaller, R. D.; Korgel, B. A. Synthesis and Ligand Exchange of Thiol-Capped Silicon Nanocrystals. *Langmuir* **2015**, *31* (24), 6886-6893. DOI: 10.1021/acs.langmuir.5b01246. Miyano, M.; Kitagawa, Y.; Wada, S.; Kawashima, A.; Nakajima, A.; Nakanishi, T.; Ishioka, J.; Shibayama, T.; Watanabe, S.; Hasegawa, Y. Photophysical properties of luminescent silicon nanoparticles surface-modified with organic molecules via hydrosilylation. *Photochemical & Photobiological Sciences* **2016**, *15* (1), 99-104. DOI: 10.1039/c5pp00364d. Mobarok, M. H.; Purkait, T. K.; Islam, M. A.; Miskolzie, M.; Veinot, J. G. C. Instantaneous Functionalization of Chemically Etched Silicon Nanocrystal Surfaces. *Angewandte Chemie* **2017**, *56* (22), 6073-6077. DOI: 10.1002/anie.201609651. Mazzaro, R.; Romano, F.; Ceroni, P. Long-lived luminescence of silicon nanocrystals: from principles to applications. *Phys. Chem. Chem. Phys.* **2017**, *19* (39), 26507-26526. DOI: 10.1039/c7cp05208a.
(27) Clark, R. J.; Aghajamali, M.; Gonzalez, C. M.; Hadidi, L.; Islam, M. A.; Javadi, M.; Mobarok, M. H.; Purkait, T. K.; Robidillo, C. J. T.; Sinelnikov, R.; et al. From hydrogen silsesquioxane to functionalized silicon nanocrystals. *Chemistry of Materials* **2017**, *29* (1), 80-89. DOI: 10.1021/acs.chemmater.6b02667.
(28) Sinelnikov, R.; Dasog, M.; Beamish, J.; Meldrum, A.; Veinot, J. G. C. Revisiting an Ongoing Debate: What Role Do Surface Groups Play in Silicon Nanocrystal Photoluminescence? *ACS Photonics* **2017**, *4* (8), 1920-1929. DOI: 10.1021/acsphotonics.7b00102.
(29) Angi, A.; Sinelnikov, R.; Meldrum, A.; Veinot, J. G. C.; Balberg, I.; Azulay, D.; Millo, O.; Rieger, B. Photoluminescence through in-gap states in phenylacetylene functionalized silicon nanocrystals. *Nanoscale* **2016**, *8* (15), 7849-7853. DOI: 10.1039/c6nr01435f.
(30) Robidillo, C. J. T.; Islam, M. A.; Aghajamali, M.; Faramus, A.; Sinelnikov, R.; Zhang, X.; Boekhoven, J.; Veinot, J. G. C. Functional Bioinorganic Hybrids from Enzymes and Luminescent Silicon-Based Nanoparticles. *Langmuir* **2018**, *34* (22), 6556-6569. DOI: 10.1021/acs.langmuir.8b01119. Robidillo, C. J. T.; Aghajamali, M.; Faramus, A.; Sinelnikov, R.;

Veinot, J. G. C. Interfacing enzymes with silicon nanocrystals through the thiol–ene reaction. *Nanoscale* **2018**, *10* (39), 18706-18719. DOI: 10.1039/c8nr05368e. Robidillo, C. J. T.; Wandelt, S.; Dalangin, R.; Zhang, L.; Yu, H.; Meldrum, A.; Campbell, R. E.; Veinot, J. G. C. Ratiometric Detection of Nerve Agents by Coupling Complementary Properties of Silicon-Based Quantum Dots and Green Fluorescent Protein. *ACS Applied Materials & Interfaces* **2019**, *11* (36), 33478-33488. DOI: 10.1021/acsami.9b10996. Robidillo, C. J. T.; Veinot, J. G. C. Functional Bio-inorganic Hybrids from Silicon Quantum Dots and Biological Molecules. *ACS Applied Materials & Interfaces* **2020**, *12* (47), 52251-52270. DOI: 10.1021/acsami.0c14199.
(31) Greenhagen, J. R.; Andaraarachchi, H. P.; Li, Z.; Kortshagen, U. R. Synthesis of PEG-grafted boron doped Si nanocrystals. *The Journal of chemical physics* **2019**, *151* (21), 211103-211103. DOI: 10.1063/1.5128608 PubMed.
(32) Sugimoto, H.; Fujii, M.; Imakita, K. Synthesis of boron and phosphorus codoped all-inorganic colloidal silicon nanocrystals from hydrogen silsesquioxane. *Nanoscale* **2014**, *6* (21), 12354-12359. DOI: 10.1039/c4nr03857f.
(33) Wheeler, L. M.; Kramer, N. J.; Kortshagen, U. R. Thermodynamic Driving Force in the Spontaneous Formation of Inorganic Nanoparticle Solutions. *Nano Letters* **2018**, *18* (3), 1888-1895. DOI: 10.1021/acs.nanolett.7b05187.
(34) Cabrera, N.; Mott, N. F. Theory of the oxidation of metals. *Reports on Progress in Physics* **1949**, *12* (1), 163-184. DOI: 10.1088/0034-4885/12/1/308.
(35) Hessel, C. M.; Henderson, E. J.; Veinot, J. G. C. Hydrogen Silsesquioxane: A Molecular Precursor for Nanocrystalline Si−SiO2 Composites and Freestanding Hydride-Surface-Terminated Silicon Nanoparticles. *Chemistry of Materials* **2006**, *18* (26), 6139-6146. DOI: 10.1021/cm0602803.
(36) Anderson, S. L.; Luber, E. J.; Olsen, B. C.; Buriak, J. M. Substance over Subjectivity: Moving beyond the Histogram. *Chemistry of Materials* **2016**, *28* (17), 5973-5975. DOI: 10.1021/acs.chemmater.6b03430.
(37) Bennett, A. E.; Rienstra, C. M.; Auger, M.; Lakshmi, K. V.; Griffin, R. G. Heteronuclear decoupling in rotating solids. *The Journal of Chemical Physics* **1995**, *103* (16), 6951-6958. DOI: 10.1063/1.470372.
(38) Thiessen, A. N.; Ha, M.; Hooper, R. W.; Yu, H.; Oliynyk, A. O.; Veinot, J. G. C.; Michaelis, V. K. Silicon Nanoparticles: Are They Crystalline from the Core to the Surface? *Chemistry of Materials* **2019**, *31* (3), 678-688. DOI: 10.1021/acs.chemmater.8b03074.
(39) Saß, M.; Annen, A.; Jacob, W. Hydrogen bonding in plasma-deposited amorphous hydrogenated boron films. *Journal of Applied Physics* **1997**, *82* (4), 1905-1908. DOI: 10.1063/1.365997.
(40) Taillon, J. A.; Klingshirn, C. J.; Jiao, C.; Zheng, Y.; Dhar, S.; Zheleva, T. S.; Lelis, A. J.; Salamanca-Riba, L. G. Analysis of the electronic and chemical structure in boron and phosphorus passivated 4H-SiC/SiO2 interfaces using HRTEM and STEM-EELS. *Applied Physics Letters* **2018**, *113* (19), 193503. DOI: 10.1063/1.5053595.
(41) Beljakowa, S.; Pichler, P.; Kalkofen, B.; Hübner, R. Diffusion of Phosphorus and Boron from Atomic Layer Deposition Oxides into Silicon. *physica status solidi (a)* **2019**, *216* (17), 1900306. DOI: 10.1002/pssa.201900306.
(42) Major, G. H.; Fairley, N.; Sherwood, P. M. A.; Linford, M. R.; Terry, J.; Fernandez, V.; Artyushkova, K. Practical guide for curve fitting in x-ray photoelectron spectroscopy. *Journal of Vacuum Science & Technology A* **2020**, *38* (6), 061203. DOI: 10.1116/6.0000377. Thøgersen, A.; Diplas, S.; Mayandi, J.; Finstad, T.; Olsen, A.; Watts, J. F.; Mitome, M.; Bando, Y. An

experimental study of charge distribution in crystalline and amorphous Si nanoclusters in thin silica films. *Journal of Applied Physics* **2008**, *103* (2), 024308. DOI: 10.1063/1.2832630.
(43) Yamauchi, J.; Yoshimoto, Y.; Suwa, Y. X-ray photoelectron spectroscopy analysis of boron defects in silicon crystal: A first-principles study. *Journal of Applied Physics* **2016**, *119* (17), 175704. DOI: 10.1063/1.4948572.
(44) Kazahaya, T.; Hirose, M. Coordination Number of Doped Boron Atoms in Photochemically-Deposited Amorphous Silicon Studied by X-Ray Photoelectron Spectroscopy. *Japanese Journal of Applied Physics* **1986**, *25* (Part 2, No. 1), L75-L77. DOI: 10.1143/jjap.25.l75. Li, L. H.; Xing, T.; Chen, Y.; Jones, R. Boron Nitride Nanosheets for Metal Protection. *Advanced Materials Interfaces* **2014**, *1* (8), 1300132. DOI: 10.1002/admi.201300132.
(45) Sundfors, R. K.; Holcomb, D. F. Nuclear Magnetic Resonance Studies of the Metallic Transition in Doped Silicon. *Physical Review* **1964**, *136* (3A), A810-A820. DOI: 10.1103/physrev.136.a810.
(46) Lee, D.; Kaushik, M.; Coustel, R.; Chenavier, Y.; Chanal, M.; Bardet, M.; Dubois, L.; Okuno, H.; Rochat, N.; Duclairoir, F.; et al. Solid-State NMR and DFT Combined for the Surface Study of Functionalized Silicon Nanoparticles. *Chemistry - A European Journal* **2015**, *21* (45), 16047-16058. DOI: 10.1002/chem.201502687. Ha, M.; Thiessen, A. N.; Sergeyev, I. V.; Veinot, J. G. C.; Michaelis, V. K. Endogenous dynamic nuclear polarization NMR of hydride-terminated silicon nanoparticles. *Solid State Nuclear Magnetic Resonance* **2019**, *100*, 77-84. DOI: 10.1016/j.ssnmr.2019.04.001. Hanrahan, M. P.; Fought, E. L.; Windus, T. L.; Wheeler, L. M.; Anderson, N. C.; Neale, N. R.; Rossini, A. J. Characterization of Silicon Nanocrystal Surfaces by Multidimensional Solid-State NMR Spectroscopy. *Chemistry of Materials* **2017**, *29* (24), 10339-10351. DOI: 10.1021/acs.chemmater.7b03306.
(47) Faulkner, R. A.; DiVerdi, J. A.; Yang, Y.; Kobayashi, T.; Maciel, G. E. The Surface of Nanoparticle Silicon as Studied by Solid-State NMR. *Materials (Basel)* **2012**, *6* (1), 18-46. DOI: 10.3390/ma6010018 PubMed.
(48) Baccile, N. Application of Advanced Solid-State NMR Techniques to the Characterization of Nanomaterials: A Focus on Interfaces and Structure. In *Ideas in Chemistry and Molecular Sciences*, 2010; pp 139-182.
(49) Murakami, M.; Shimizu, T.; Tansho, M.; Takano, Y. (11)B nuclear magnetic resonance in boron-doped diamond. *Sci Technol Adv Mater* **2009**, *9* (4), 044103-044103. DOI: 10.1088/1468-6996/9/4/044103 PubMed. Mukuda, H.; Tsuchida, T.; Harada, A.; Kitaoka, Y.; Takenouchi, T.; Takano, Y.; Nagao, M.; Sakaguchi, I.; Oguchi, T.; Kawarada, H. Microscopic evidence for evolution of superconductivity by effective carrier doping in boron-doped diamond:B11−NMRstudy. *Physical Review B* **2007**, *75* (3). DOI: 10.1103/physrevb.75.033301.
(50) Grafe, H.-J.; Löser, W.; Schmitz, S.; Sakaliyska, M.; Wurmehl, S.; Eisert, S.; Reichenbach, B.; Acker, J.; Rietig, A.; Ducke, J.; et al. NMR investigation of boron impurities in refined metallurgical grade silicon. *physica status solidi (a)* **2015**, *212* (9), 2031-2036. DOI: 10.1002/pssa.201431908.
(51) Darwent, B. d. *Bond dissociation energies in simple molecules*; 1970. DOI: http://dx.doi.org/10.6028/nbs.nsrds.31.
(52) Linford, M. R.; Fenter, P.; Eisenberger, P. M.; Chidsey, C. E. D. Alkyl Monolayers on Silicon Prepared from 1-Alkenes and Hydrogen-Terminated Silicon. *Journal of the American Chemical Society* **1995**, *117* (11), 3145-3155. DOI: 10.1021/ja00116a019. Yang, Z.; Iqbal, M.; Dobbie, A. R.; Veinot, J. G. C. Surface-Induced Alkene Oligomerization: Does Thermal

Hydrosilylation Really Lead to Monolayer Protected Silicon Nanocrystals? *Journal of the American Chemical Society* **2013**, *135* (46), 17595-17601. DOI: 10.1021/ja409657y.
(53) Petit, J.-F.; Demirci, U. B. Mechanistic Insights into Dehydrogenation of Partially Deuterated Ammonia Borane NH3BD3 Being Heating to 200 °C. *Inorganic Chemistry* **2018**, *58* (1), 489-494. DOI: 10.1021/acs.inorgchem.8b02721. Ciobanu, O.; Allouti, F.; Roquette, P.; Leingang, S.; Enders, M.; Wadepohl, H.; Himmel, H.-J. Thermal and Catalytic Dehydrogenation of the Guanidine-Borane Adducts H3B·hppH (hppH = 1,3,4,6,7,8-hexahydro-2H-pyrimido[1,2-a]pyrimidine) and H3B·N(H)C(NMe2)2: A Combined Experimental and Quantum Chemical Study. *European Journal of Inorganic Chemistry* **2008**, *2008* (35), 5482-5493. DOI: 10.1002/ejic.200800564. García-Vivó, D.; Huergo, E.; Ruiz, M. A.; Travieso-Puente, R. Thermally Induced Dehydrogenation of Amine-Borane Adducts and Ammonia-Borane by Group 6 Cyclopentadienyl Complexes Having Single and Triple -Metal-Metal Bonds. *European Journal of Inorganic Chemistry* **2013**, *2013* (28), 4998-5008. DOI: 10.1002/ejic.201300629.

Chapter 3:

Post-synthesis doping of silicon nanoparticles via hydrogen silsesquioxane-capped thermal diffusion

A version of the chapter is available as a preprint:

Milliken, S.; Cheong, I. T.; Cui, K.; Veinot, J. Post-Synthesis Boron Doping of Silicon Quantum Dots via Hydrosilsesquioxane-Capped Thermal Diffusion. *ChemRxiv* **2022**.

3.1 Introduction

Semiconductor particles of nanoscale dimensions (e.g., quantum dots; QDs) exhibit properties that have far reaching applications in next generation electronic devices, medical imaging,[1] and solar energy harvesting technologies.[2] It is well-established that the optoelectronic response of QDs can be tailored by exploiting the principles of quantum confinement and defining particle size. In this regard, diverse methods affording QDs of well-defined dimensions have been reported.[3,4,5,6] In some cases, tailoring surface chemistry has also offered control of QD optical properties.[7,8,9]

Controlled incorporation of dopants into QDs provides yet another important degree of freedom in tuning optoelectronic properties through the definition of the material electronic structure.[10] The characteristics of doped QDs strongly depend upon dopant type, concentration, and location within the nanoparticle.[10] Consequently, it is essential that the methods for doping QDs provide control over these parameters. Introducing dopants into QDs relies upon several key factors. If doping is occurring while the QDs are forming, one must consider the particle formation and growth, reaction rates as well as the formation energy of the host and dopant, which can strongly influence the final dopant concentration/location.[11] Often, chemical potentials vary with growth conditions and are subject to the thermodynamic formation of other phases.[12] This is well-illustrated by the work of Mikulec et al. that showed Mn-dopants in CdSe QDs segregated to the particle surface at temperatures > 300 °C,[13] however this thermodynamically driven process could be mitigated if surfactants were introduced to the particle surface.[14] It was proposed that the surfactants could bind with Mn and lower the chemical potential of the doped QDs.

The practical impact of many QDs is currently limited because of the legislation associated with the controlled use of toxic/heavy metals (e.g., Pb, Cd);[15] other QDs could be limited by the

natural abundance of their constituent elements (e.g., In).[16] Silicon is the workhorse semiconductor of the modern electronics and photovoltaics sectors; it is also naturally abundant,[17] biologically compatible, [18] and exhibits broad optical absorbance across the UV and visible spectral regions.[19,20] Silicon nanoparticles (SiNPs) are an attractive toxic-metal-free alternative and possess properties equivalent to, and in some cases surpassing, their compound semiconductor counterparts.[3,4,9,21,22] To date, incorporation of dopants such as B and/or P atoms into SiNPs has yielded optical and electronic properties that were previously inaccessible with intrinsic materials (e.g., conductivity, plasmonic response, catalytic surfaces, hydrophilic surfaces, etc.).[23-25,26-28] Doping SiNPs also brings with it outstanding challenges including control over dopant concentration and location due to physical size restraints, as well as limited experimental synthesis and analysis approaches. If the community is to gain an important fundamental understanding of doped SiNPs and their properties, it is essential that synthesis methods providing straightforward control over NP dimension, dopant concentration and distribution, as well as surface chemistry be established.

Methods for preparing doped SiNPs are routinely classified into the broad categories of in- and post-synthesis doping. In-synthesis doping incorporates dopant atoms into NPs during their formation and is typically achieved using chemical vapor deposition,[26,28,29] plasma synthesis,[24] laser ablation,[30,31] and co-sputtering.[32] Defining the location of the dopant within NPs while using these methods is non-trivial because it strongly depends upon reaction conditions, as well as the material properties of the Si host and chosen dopant.[33] A common challenge known as "self-purification" arises for small (*i.e.*, $d < 6$ nm) strongly confined NPs that expels dopants to the NP surface during in-synthesis doping. This phenomenon is a manifestation of the stress within the crystalline core of the NPs because of the incorporation of substitutional dopants.[34] Post-synthesis doping is anticipated to provide improved control over dopant distribution in NPs and minimize

the effects of self-purification that occurs during the formation of the nanoparticles.[35] Additionally, because the narrow particle size distributions of the intrinsic SiNPs are already accessible using well-established procedures, it is reasonable that these approaches will provide control over the dimensions of the resulting doped particles.[4,21]

Important progress has been realized in post-synthesis doping of a variety of Si nanostructures (e.g., porous Si,[36] oxide-embedded SiNPs,[37] Si nanowires[38]) that provides a valuable basis for doping in SiNPs. To date, post-synthesis doping of freestanding SiNPs has only been reported using ligand substitution.[9,39] This approach is limited in scope and only offers surface-type (s-type) doping that can produce very different material properties from those realized when dopants are incorporated into the material crystal lattice (c-type); furthermore, ligand substitution limits dopant concentration to the number of available surface sites.[40] In this context, realizing a post-synthesis doping method that exploits the narrow size distributions available for preformed SiNPs while providing high dopant concentrations, control over dopant distribution/incorporation into the crystalline lattice as well as offering tailorable surface chemistry is an important and timely goal.

Herein, we report a diffusion-based post-synthesis doping method that draws inspiration from conventional Si wafer doping and introduces B into preformed SiNPs. By optimizing the temperature of the annealing step and incorporating hydrogen into the flowing processing atmosphere we achieved dopant concentrations as high as 5 atomic percent while maintaining NP morphology. The resulting B-doped SiNPs show photoluminescence (PL) in the visible to near-infrared spectral regions, are soluble in aqueous solvents and are readily functionalized for compatibility with organic solvents.

3.2 Experimental Section

3.2.1 Reagents

Hydrofluoric acid (48-50%) and sulfuric (reagent grade, 95–98%) acid were purchased from Fisher Scientific and Caledon Laboratory Chemicals, respectively. Fuming sulfuric acid (reagent grade, 20% free SO_3 bases), trichlorosilane (99%), boric acid (reagent grade, 99.5%), phosphorus pentachloride (reagent grade, 95%), 1-decanol (98.0%), ethanol (anhydrous, ≤0.003% water), methyl isobutyl ketone (MIBK, reagent grade, 98.5%) and toluene (HPLC grade) were purchased from Sigma-Aldrich. Toluene was purified using a Pure-Solv purification system and collected immediately prior to use.

3.2.2 Synthesis of Hydrogen Silsesquioxane (HSQ)

HSQ was synthesized according to well-established literature procedures.[4] Dry toluene (45.0 mL) was added dropwise to a solution of concentrated (15 mL) and fuming (7.2 mL) sulfuric acid. Next, a mixture of trichlorosilane (16 mL) in dry toluene (110 mL) was added dropwise to the solution. The resulting product in the organic phase was washed with sulfuric acid solution and isolated from the aqueous layer. Most of the solvent was removed via rotary evaporation and any remaining solvent was removed *in vacuo* resulting in a white crystalline solid.

3.2.3 Synthesis of Silicon Nanoparticles (SiNPs)

The particles were synthesized using a previously established method involving the thermolysis of the Si precursor HSQ.[4] Briefly 3 g of HSQ was thermally processed in a standard

tube furnace in a flowing 5 % H_2/95 % Ar atmosphere at peak processing temperatures of 1100, 1200, and 1300 °C. This yielded a black solid composite containing SiNPs encapsulated in a silicon oxide matrix; the SiNPs possessed approximate average sizes of 3, 6 and 9 nm, respectively. The composite was then ground into a fine powder using an agate mortar and pestle, followed by shaking in a wrist action shaker with high-purity glass beads for 16 hours to yield a fine, free flowing brown powder.

To obtain freestanding SiNPs, 200 mg of the composite powder containing Si inclusions of the target size were etched using 9 mL of a 1:1:1 solution of ethanol:water:HF for one hour in ambient light. HF is extremely hazardous and must be handled with extreme care and in accordance with local regulations/guidelines For "crystalline" SiNPs, composites were etched for a total of 240 minutes to remove the amorphous Si capping layer. The SiNPs were extracted into toluene and purified using centrifugation for 5 min at 5000 rpm, followed by resuspension in dry toluene followed by centrifugation. This process was repeated 3 times after which the SiNPs were suspended in 5 mL of dry toluene.

3.2.4 Post Synthesis Doping of SiNPs with Boron

Freshly etched SiNPs (20 mg) suspended in 5 mL of dry toluene were added to a Ar purged Schlenk flask with 2 g of boric acid dissolved in 20 mL of ethanol under flowing Ar. The resulting mixture was stirred for 5 min then 5 ml of 15 % w/w HSQ in MIBK was added. The mixture was stirred at room temperature for an additional 1.5 hours under flowing Ar after which the solvents were removed using a rotary evaporator with a water bath temperature set to 45 °C. The resulting brown solid was redispersed in 2 mL of benzene and freeze-dried to obtain a free-flowing brown

powder that was thermally processed in a tube furnace with flowing 5 % H_2/95 % Ar (ramp rate = 10 °C/min, peak processing temperature = 500 °C, dwell time = 1 h). Optimization of the drive-in step was achieved by varying the peak processing temperature in the range of 400 to 600 °C and flowing processing atmosphere was either 100 % Ar or 5 % H_2/95 % Ar. The resulting brown powders were ground using an agate mortar and pestle, followed by shaking in a wrist action shaker with high-purity glass beads for 4 hours.

The resulting powder (200 mg) was then etched using 5 mL of a 1:1:1 solution of ethanol:water:HF for 50 min. The solution was centrifuged at 5000 rpm for 30 min then re-suspended in 5 mL anhydrous ethanol and centrifuged again, this was repeated twice more to remove residual HF. The resulting brown powder was suspended in anhydrous ethanol until further use. The calculated yield for the B-doped SiNPs liberated from the SiO_x composite was 10 %.

3.2.5 Phosphorus Pentachloride (PCl_5) Initiated Functionalization of B-Doped SiNPs Using 1-Decanol

Freshly etched B-doped SiNPs (20 mg) dispersed in dry acetonitrile (10 mL) were mixed with PCl_5 (0.3 g) for one hour. The solvent was then removed *in vacuo* and the product was redispersed in 10 mL of 1-decanol and subjected to three freeze-pump-thaw cycles. The solution was then heated overnight at 180°C with stirring. The alkoxy-functionalized B-doped SiNPs were transferred to Nalgene centrifuge tubes with 40 mL of ethanol and spun at 11400 rpm for 50 minutes. The isolated particles were then washed three times with a mixture of toluene (5 mL) and ethanol (45 mL) and spun at 11400 rpm for 50 minutes.

3.2.6 Fourier-Transform Infrared Spectroscopy (FTIR)

FT-IR spectra were collected by a Thermo Nicolet Continum FT-IR microscope of a freeze-dried B-doped SiNPs in a KBr pellet.

3.2.7 X-Ray Photoelectron Spectroscopy (XPS)

Samples were prepared by drop-casting B-doped SiNPs suspended in dry toluene onto copper foil. XP spectra were measured using Kratos Axis 165 Ultra X-ray Photoelectron Spectrometer with a monochromatic Al Kα source operating at 210W with an energy of 1486.6 eV. The high-resolution spectra were obtained using an analyzer pass energy of 20 eV and a step of 0.1 eV. For survey spectra, a pass energy of 160 eV and a step of 0.3 eV. Spectra were calibrated to C 1s 284.8 eV using adventitious carbon. Peak fitting was performed using CasaXPS software with a Shirley-type background. Spin-orbit coupling in Si 2p was fixed to an area ratio of 2:1 and 0.6 eV energy spacing.

3.2.8 Electron Microscopy

Transmission electron microscopy (TEM) and HR-TEM were performed on a JEOL JEM-ARM200CF S/TEM (Cold Field Emission Gun) electron microscope with an accelerating voltage of 200 kV using SiNPs drop-coated from a toluene solution onto a holey carbon-coated copper grid. The SiNP size was determined by averaging the size of 300 particles using ImageJ software (version 1.51j8) and plotted as an average shifted histogram (ASH) as outlined previously by

Buriak and co-workers. A representative set of histograms are formed by shifting the origin at even steps through the width of one bin. The ASH is generated by averaging all the histograms that were generated to form one plot. High-resolution TEM (HRTEM) measurements were conducted using scanning TEM (STEM) (JEOL 2200FS, 200 kV) with a nominal beam size of 0.5 nm. Electron energy loss spectroscopy (EELS) analysis was also conducted using a 200 kV JEOL 2200FS scanning TEM with a nominal beam size of 0.5 nm. Digital Micrograph (Gatan Inc.) was employed for signal collection and data extraction from EELS spectra. Typical current densities for HRTEM imaging were 13.15 pA cm^{-2} at 400 K and 16.72 pA cm^{-2} at 500 K.

3.2.9 Photoluminescence Measurements

Photoluminescence spectroscopy measurements were performed for the three size ranges of B-doped SiNPs before and after functionalization with 1-decanol in ethanol. B-doped SiNPs were excited using an argon ion laser with a 350 nm emission wavelength and collected by an optic fiber into an Ocean Optics USB2000+ spectrometer with a spectral range of 300 – 1000 nm and a sensitivity of 41 photons per count. Photoluminescence lifetime measurements were acquired of the B-doped SiNPs after functionalization with 1-decanol using an argon ion laser (351 nm, ~20 mW) modulated by an acousto-optic modulator (~50 ns response time) operated at a frequency of 200 Hz with a 50% duty cycle. The photoluminescence data were collected with a total of 10 000 sweeps for good signal-to-noise ratio using 1 μs time steps. The decay profiles were fit using a biexponential equation as shown in the supporting information.

3.2.10 Thermogravimetric analysis (TGA)

HSQ, boric acid, precursor mixtures, and annealed composites were prepared as a solid residue and transferred to a platinum pan. The weight loss of the samples was monitored in the temperature range of 25 to 800 °C at a temperature increment of 10 °C/min under Ar atmosphere using Mettler Toledo TGA/DSC 1 star system.

3.2.11 Powder X-ray Diffraction (PXRD)

PXRD measurements were carried out on a Bruker D8 Advance diffractometer (Cu-Kα1 (λ = 1.5406 Å) and Kα2 (λ = 1.5444 Å)) for freeze-dried samples of parent intrinsic SiNPs and B-doped SiNPs. Diffraction patterns were scanned between 2θ ranges of 20 – 80 ° with a scanning step of 0.02 °/s. The Scherrer equation was used to estimate crystallite sizes as shown in the Appendix.

3.3 Results and Discussion

3.3.1 Diffusion-Based Doping

Heating-induced diffusion is a common and readily accessible approach for introducing dopants into bulk crystalline silicon.[41,42] Typically this procedure involves two-steps: 'pre-deposition' and 'drive-in annealing'. Pre-deposition introduces the dopant to the silicon surface while the subsequent high temperature (e.g., 500 – 1200 °C) drive-in annealing promotes dopant diffusion into the silicon matrix.[41] In many cases, an SiO_2 capping layer is used to trap dopants within the Si and prevents their escape during annealing.[43] The general methodology offers an intriguing foundation for modification of SiNPs.

The multistep SiNP doping procedure used herein is summarized in Scheme 3.1 and described in detail in the Experimental Section.

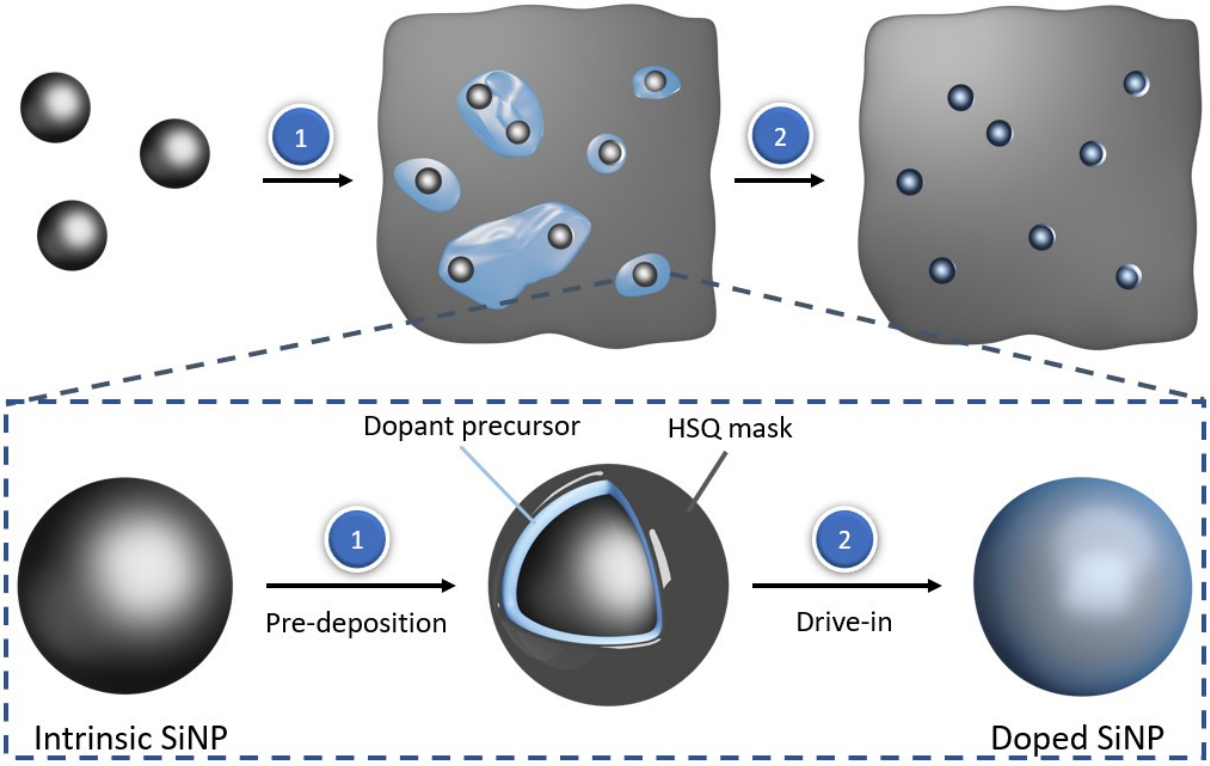

Scheme 3. 1 Post-synthesis B-doping of precursor SiNPs via thermal diffusion. The first step in the process is the "pre-deposition" step represented by "1" in which the dopant oxide is introduced to the surface of the SiNP. The second step in the diffusion-based doping method is the "drive-in" step which is performed at elevated temperatures to promote dopant diffusion into the SiNPs.

We began by preparing high-purity, hydrogen-terminated intrinsic SiNPs of well-defined dimensions and a size-dependent radially graded crystallinity.[4,44] Ethanolic hydrofluoric acid etching was used to liberate what we will refer to as predefined 'intrinsic SiNPs' from an appropriate hydrogen silsesquioxane (HSQ)-derived SiNP/SiO_2 composite. These hydrophobic

SiNPs were extracted into toluene and recovered by centrifugation. Despite challenges associated with solution processability and agglomeration we successfully determined particle dimensions (i.e., d = 2.99 ± 0.54, 6.30 ± 1.2, and 8.60 ± 1.4 nm; Figure 3.1) using bright-field transmission electron microscopy (TEM).

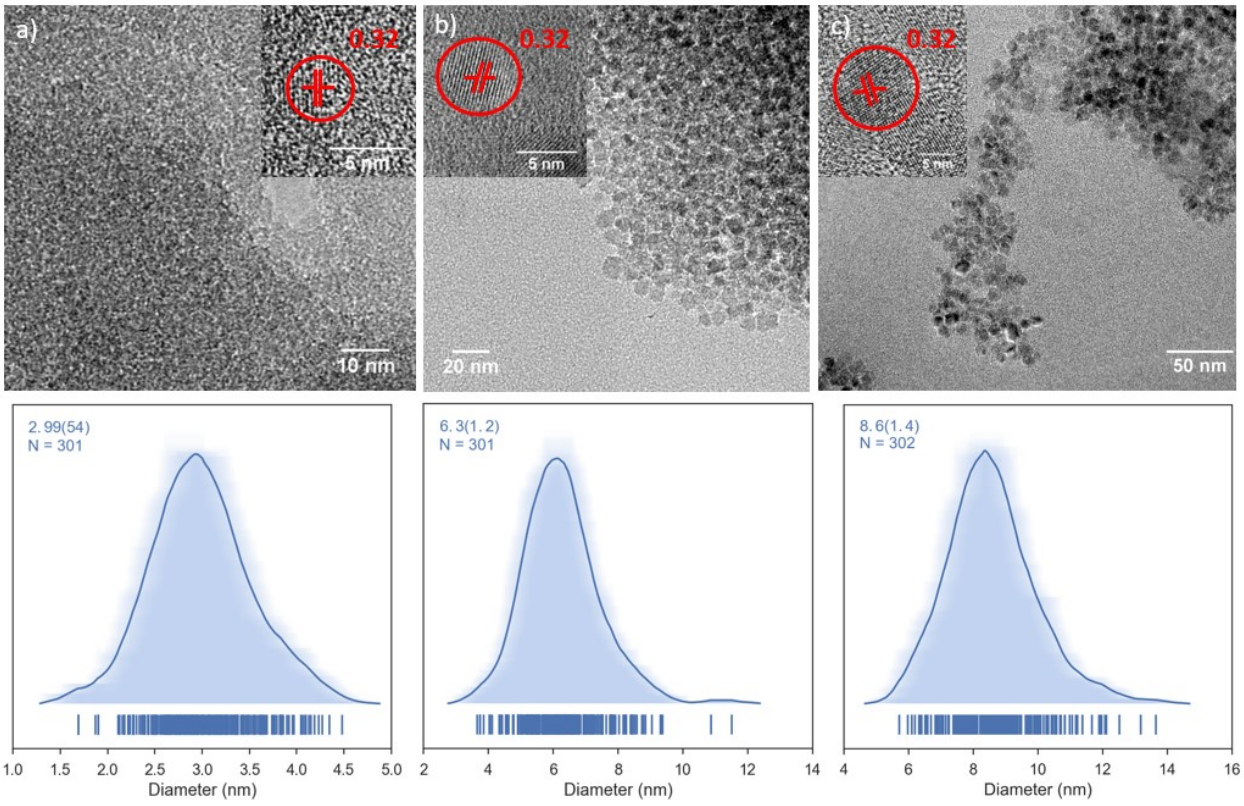

Figure 3. 1 Bright field transmission electron microscopy (TEM), corresponding average shifted histograms, and high-resolution (inset) imaging showing fringes separated by 0.32 nm characteristic of the (111) lattice spacing of crystalline Si. a) 2.99 ± 0.54 nm b) 6.30 ± 1.2 nm and c) 8.60 ± 1.4 nm.

Particle dimensions were further confirmed by applying Debye-Scherrer analysis to the broadened reflections in the powder X-ray diffraction (PXRD; Figure 3.2 a; Table 3.1). Further evidence of crystallinity was also observed using high-resolution TEM (HRTEM; Figure 3.1).

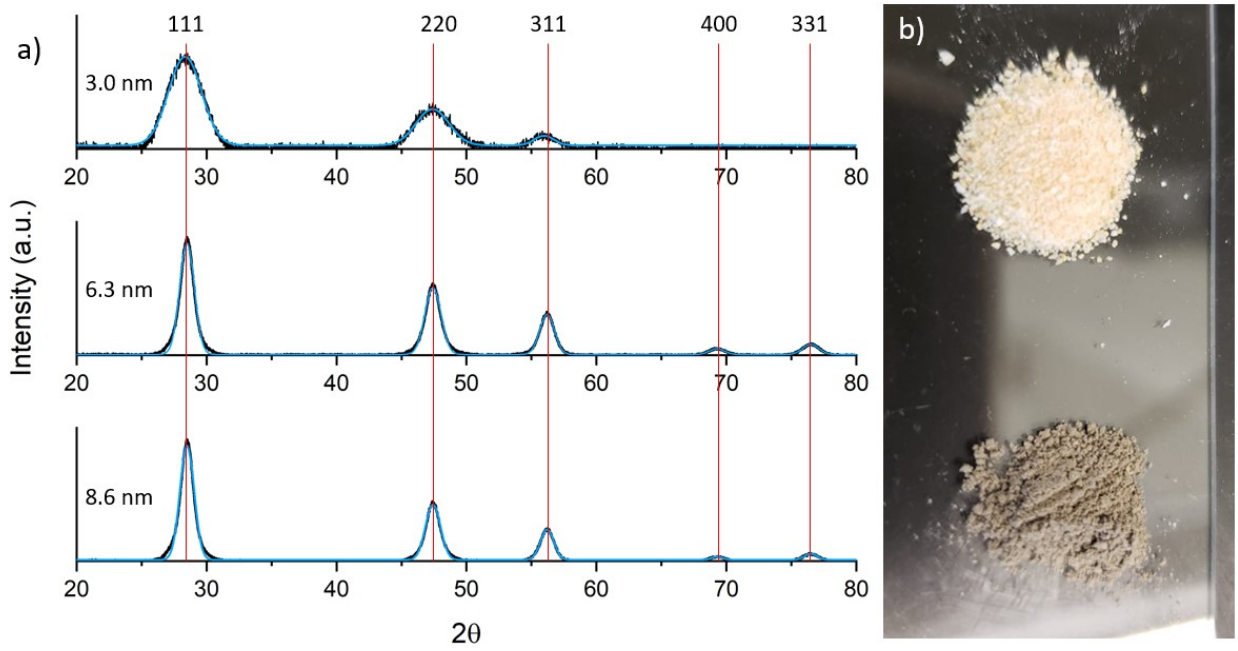

Figure 3. 2 a) Powder X-ray diffraction patterns obtained from the precursor intrinsic SiNPs bearing TEM determined particle sizes of 2.99 ± 0.54 nm, 6.30 ± 1.2 nm and 8.60 ± 1.4 nm. Each pattern shows broadened reflections characteristic Si 111, 220, 311, 400 and 331. Experimental data is shown as black traces. Blue traces show the Gaussian-Lorentzian multiple-peak fitting. b) A representative photograph showing a reaction mixture containing SiNPs, boric acid and HSQ before (top) and after (bottom) drive-in annealing.

Table 3. 1 Debye-Scherrer analysis of powder X-ray diffraction patterns collected from preformed intrinsic SiNPs of TEM determined sizes: 2.99 ± 0.54 nm, 6.30 ± 1.2 nm and 8.60 ± 1.4 nm.

d_{TEM} = 2.99 nm			**d_{TEM} = 6.30 nm**			**d_{TEM} = 8.60 nm**		
Peak position (2θ)	**FWHM**	**Crystallite Size (nm)**	**Peak position (2θ)**	**FWHM**	**Crystallite Size (nm)**	**Peak position (2θ)**	**FWHM**	**Crystallite Size (nm)**
28.40	4.40	1.88	28.50	2.33	3.52	28.50	1.28	6.40
47.43	3.61	2.40	47.42	2.45	3.54	47.42	1.35	6.41
56.13	3.39	2.65	56.20	2.33	3.86	56.20	1.21	7.43

As we broadly followed the diffusion-based doping methodology used for bulk silicon, it was necessary for us to introduce a dopant source and passivating oxide that prevents/minimizes annealing-induced B dopant loss. Boric acid was chosen as a convenient source of B. We chose to exploit HSQ solution properties as well as its compatibility with boric acid and used it as a 'silicon oxide' capping matrix. In our 'pre-deposition step' we combined freshly prepared intrinsic SiNPs with boric acid and HSQ in an ethanol/MIBK solvent mixture. After removing the solvent, the outlined procedure afforded light yellow/brown precursor powders that were used in the presented drive-in procedure (Figure 3.2 b). Details of the mixture compositions are provided in the section 3.2 of this chapter.

The "drive-in" step involves heating the dried powders in a standard tube furnace to promote B diffusion. As stated in the chapter introduction, the chemical potentials of the host and dopant material have a strong influence on doping and varies with the reaction conditions.[12] Ideally drive-in conditions should yield high concentrations of dopants in the SiNPs while maintaining particle shape and crystallinity. We first evaluated the influences of drive-in temperature and processing atmosphere composition using the predefined intrinsic SiNPs (d_{TEM} = 6.30 ± 1.2 nm). These particles were chosen for our initial investigations because they represent the intermediate size range of SiNPs used in the present study. We then methodically varied the peak processing temperature (i.e., 400, 500, and 600 °C) and employed flowing argon or 5% H_2:95% Ar processing atmospheres.

To explore the processes involved in drive-in heating, we first turned to thermogravimetric analysis (TGA) and evaluated temperature dependant weight loss for the powder precursors and doped-composites obtained from heating in a tube furnace (Figure 3.3; Table 3.2). In all cases an onset of weight loss occurs at ca. 100 °C. At this temperature, precursor powders consisting of SiNPs, boric acid, and HSQ experienced a weight loss of ca. 19.44 % (Black traces in Figures 3.3 a, b; Table 3.2). Turning our attention to doped composites obtained from heating to 500 and 600 °C both show similar weight loss characteristics (i.e., ca. 4 – 5 %) regardless of processing atmosphere. Somewhat surprisingly, composites obtained from heating to 400 °C show a heating profile similar to that of the precursor mixture (i.e., ca. 14 % weight loss) when processed in argon and substantially smaller weight loss (i.e., ca. 8 %) when processed in 5% H_2:95% Ar.

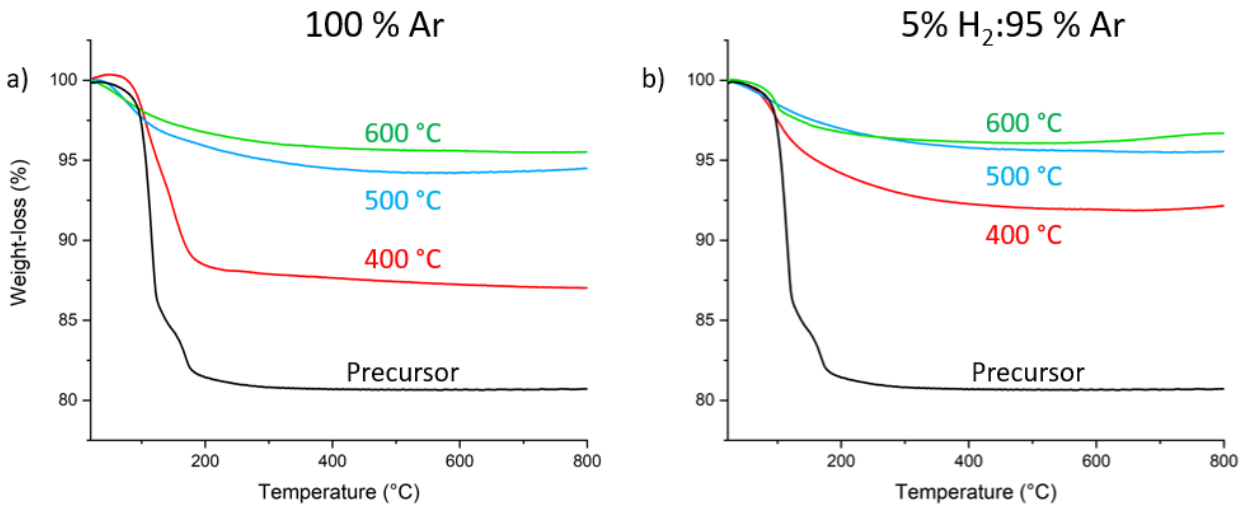

Figure 3. 3 Thermogravimetric analysis of precursor powders (i.e., d_{TEM} = 6.3 ± 1.2 nm SiNPs, boric acid, HSQ) and doped composites obtained from annealing precursors at indicated peak processing temperatures in flowing Ar (a) and 5% H_2:95% Ar (b) atmospheres.

Table 3. 2 Measured weight-loss of the HSQ/Boric acid/SiNP composites pre- and post-anneal for temperatures of 400 – 600 °C using Ar or 5:95 H_2:Ar atmosphere.

Temperature (°C)	**Annealing Atmosphere**	**Weight-loss**
Pre-anneal	N/A	19.71
400	Ar	14.44
500	Ar	5.80
600	Ar	4.47
400	5:95 H_2:Ar	7.96
500	5:95 H_2:Ar	4.45
600	5:95 H_2:Ar	3.80

While TGA data are largely qualitative and must be interpreted with caution, the observed weight losses can be reasonably attributed to boric acid dehydration (Figure 3.4).[45,46] We also note that, at the sensitivity of TGA, the processing atmosphere has little impact on the nature of the product mixture when the drive-in step is performed at temperatures of 500 °C or higher.

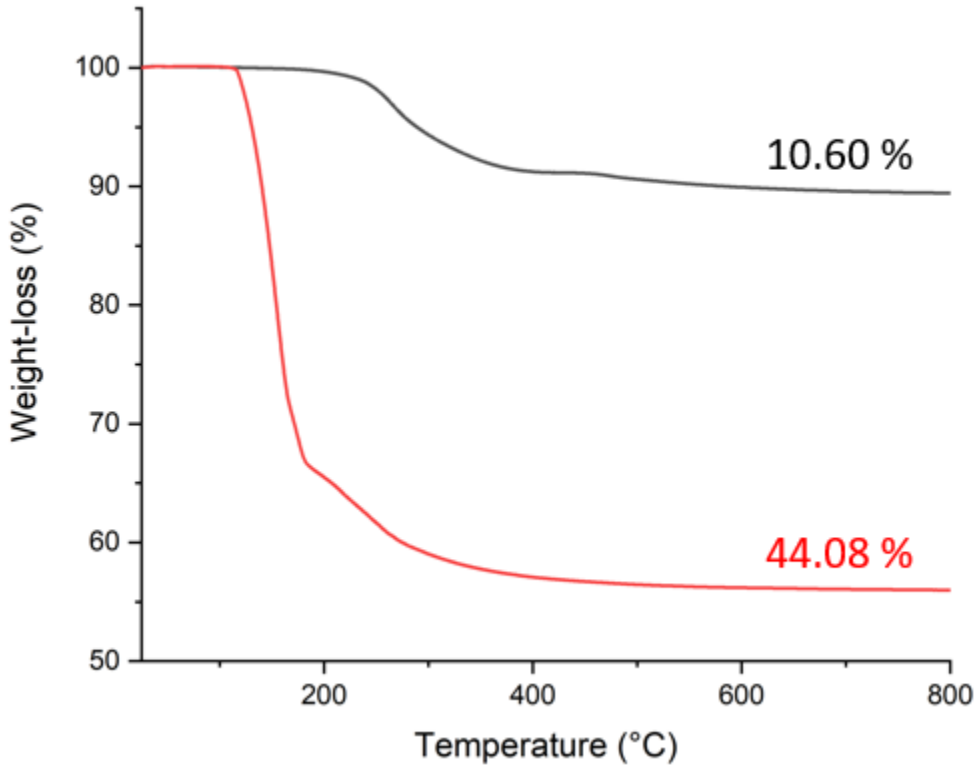

Figure 3. 4 Thermomgravimetric analysis of boric acid (dopant precursor; red curve) and hydrogen silsesquioxane (HSQ; capping agent; black curve)

Generally, for bulk systems, the elemental B required to dope silicon is produced in situ during drive-in annealing. B is formed via heat promoted Si reduction of boron oxide (supplied in the present system by dehydration of boric acid) that occurs at approximately 500 °C (Equation 3.1).[46] For the present nanocomposites there two possible sources of Si(0), i) the surfaces of pre-

formed intrinsic SiNPs, and ii) non-crystalline silicon domains that emerge upon thermal processing of HSQ in the same temperature regime.[47]

$$2B_2O_3 + 3Si \rightarrow 4B + 3SiO_2 \quad (3.1)$$

While the silicon-based reaction is almost certainly active, it does not explain the stark difference in weight loss that is evident when comparing the heating profiles of the reaction mixtures heated to low (i.e., 400 °C) versus high (i.e., 500 and 600) temperatures. It has been previously suggested that hydrogen can increase the diffusion of B in SiO_2 and amorphous silicon.[48] Additionally, the presence of hydrogen in annealing gas has been found to promote the reduction of dopants in silica glasses.[49] An alternative source of B is found in the reaction we propose could occur in the presence of hydrogen (Equation 3.2) that produces water which would readily evaporate under the presented reaction conditions. This reaction provides B while providing an explanation for the observed weight-loss.

$$H_2 + B_2O_3 + Si \rightarrow 2B + SiO_2 + H_2O \quad (3.2)$$

In this context, while the contribution to B production from the reaction summarized in Equation 3.1 cannot be completely discounted, we propose that the hydrogen promoted reduction of boron oxide (Equation 3.2) plays an important (and potentially primary) role.

Fourier transform infrared spectra (FTIR) of the doped composites provides further evidence supporting our hydrogen reduction hypothesis. A straightforward comparison of the spectra of composites obtained from drive-in annealing performed in 5% H_2:95% Ar as well as pure Ar (Figures 3.5 a and b, respectively) reveals more intense spectral features corresponding to silicon oxide (1080 cm^{-1}) and a decrease in the intensity of those associated with water (3250 – 3550 cm^{-1}) and boron oxide (1400 cm^{-1}) for composites prepared in a reducing environment.

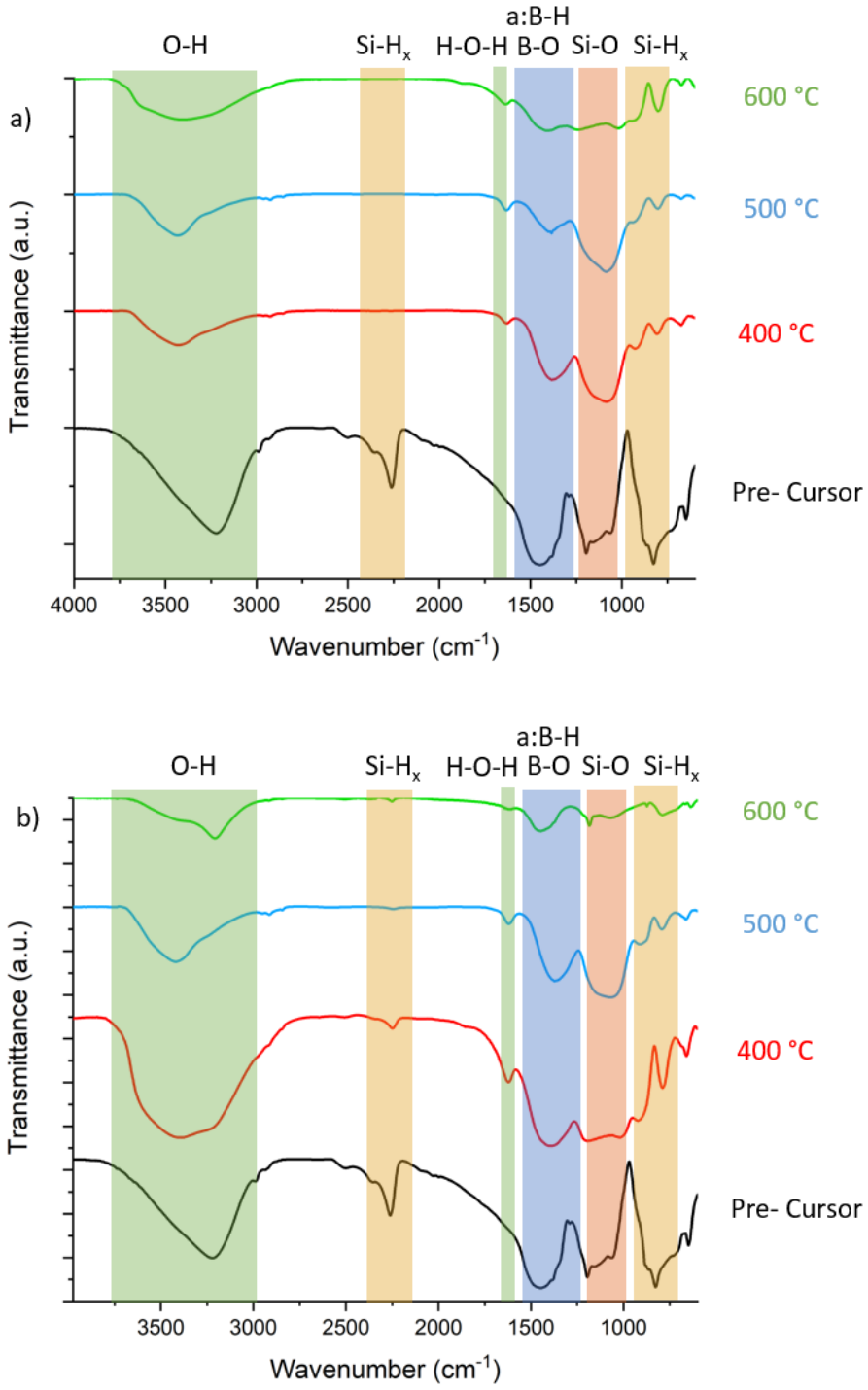

Figure 3. 5 FTIR spectra of the HSQ/Boric acid/SiNP precursor mixture and the corresponding composites produced after annealing at indicated temperatures using an atmosphere of a) 5 % H_2 :95 % Ar or b) Ar

To gain further insight into the processes by which B is introduced to the intrinsic SiNPs, we employed X-ray photoelectron spectroscopy (XPS) to evaluate the boron concentration in isolated SiNPs (Figure 3.6). Previously, we observed that when doping levels exceed the solid solubility limit of B in Si (i.e., $> 9.0 \times 10^{-4}$ atomic % B below 700 °C)[50] two B species appear in the XPS analysis that correspond to 'surface' and 'core' B dopants.[51] The same trend appears for the present systems. Figure 3.6 shows the high-resolution B 1s XP spectra for SiNPs (pre-formed intrinsic SiNPs $d_{TEM} = 6.3 \pm 1.2$ nm) prepared at indicated peak annealing temperatures in the range of 400 – 600 °C in a flowing Ar (Figures 3.6 a, c, e) and 5% H_2:95% Ar (Figures 3.6 b, d, f) atmospheres.

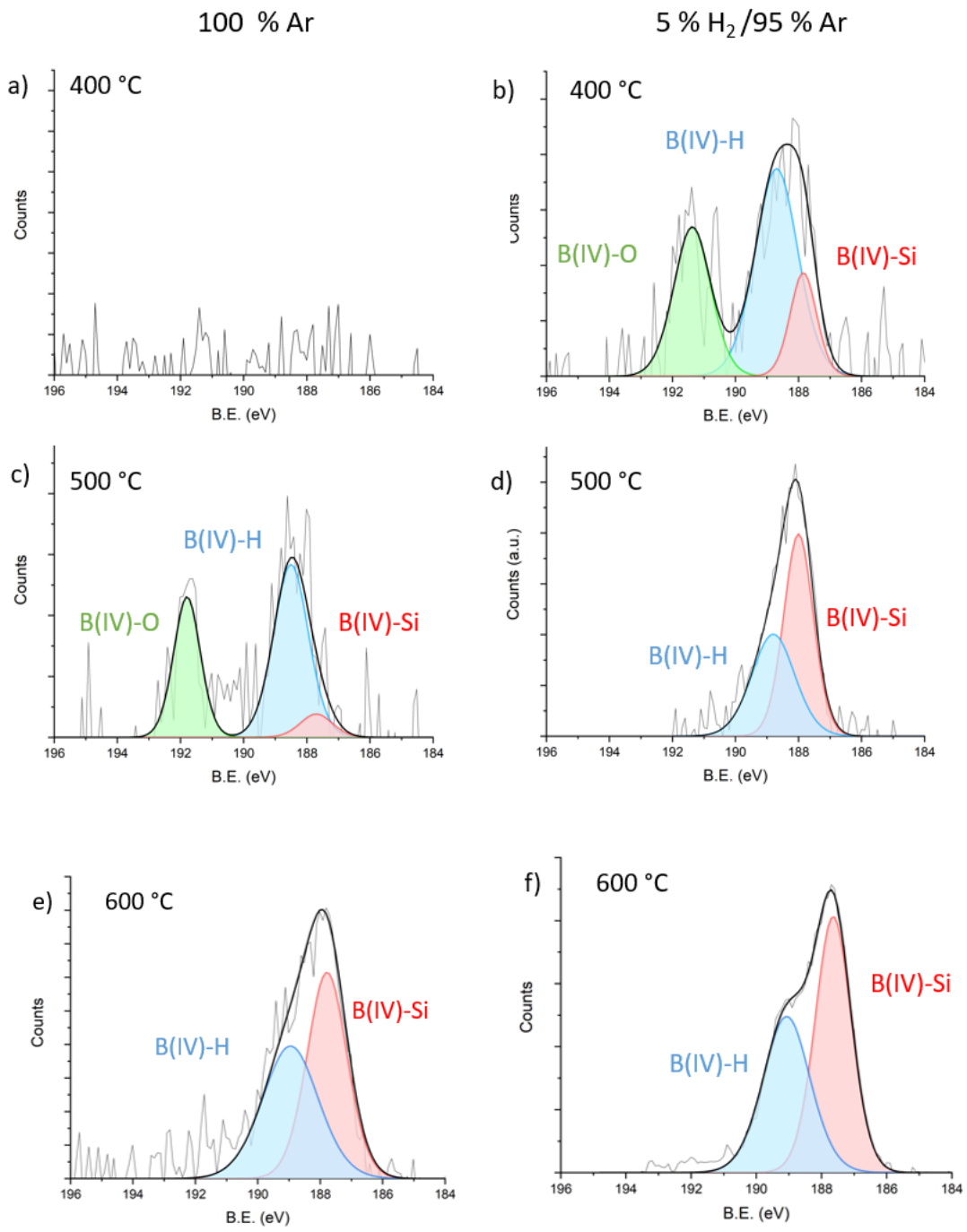

Figure 3. 6 High-resolution B 1s XP spectra of freshly liberated unfunctionalized B-doped SiNPs prepared from predefined intrinsic SiNPs d_{TEM} = 6.3 ± 1.2 nm in flowing argon (a - c) or 5% H_2:95% Ar (d - f) atmospheres at indicated peak drive-in annealing temperatures.

It is immediately evident there is a positive correlation between the drive-in annealing temperature and the intensity of the B emission (i.e., higher drive-in temperature = higher B concentration; Figure 3.7).

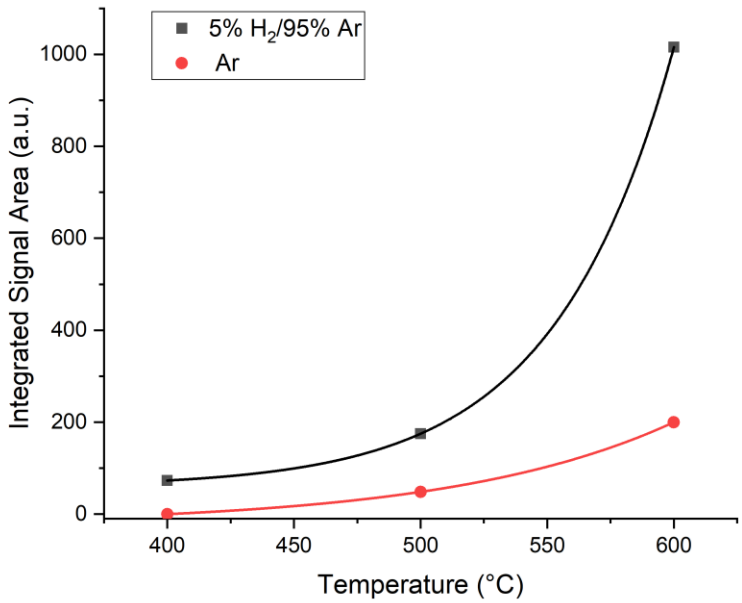

Figure 3. 7 Integrated area of signal in the B 1s XP spectra for composites produced after annealing at temperatures of 400 – 600 °C using an atmosphere of Ar (red curve) or 5 % H_2 : 95 % Ar (black curve).

Closer inspection reveals the emergence of a 'core' species in which the B atoms are bonded to four Si atoms (B.E. = 187.7 eV) with a decrease in the emission intensity arising from oxidized B species (B.E. = 191.5 eV) when samples are prepared at 500 and 400 °C in Ar and 5% H_2:95% Ar atmospheres, respectively. These observations are consistent with the reduction reaction summarized in Equation 3.2 and suggest that more boron oxide is being converted to elemental B

at increased temperature. Intriguingly, our data also suggest that using 5% H_2:95% Ar atmosphere lowers the annealing temperature required to induce doping by approximately 100 °C. High-resolution Si 2p XP spectra (Figure 3.8) were also obtained for each sample and show broad emissions that are readily fit to Si(0), (I), (II), (III), and (IV) components.

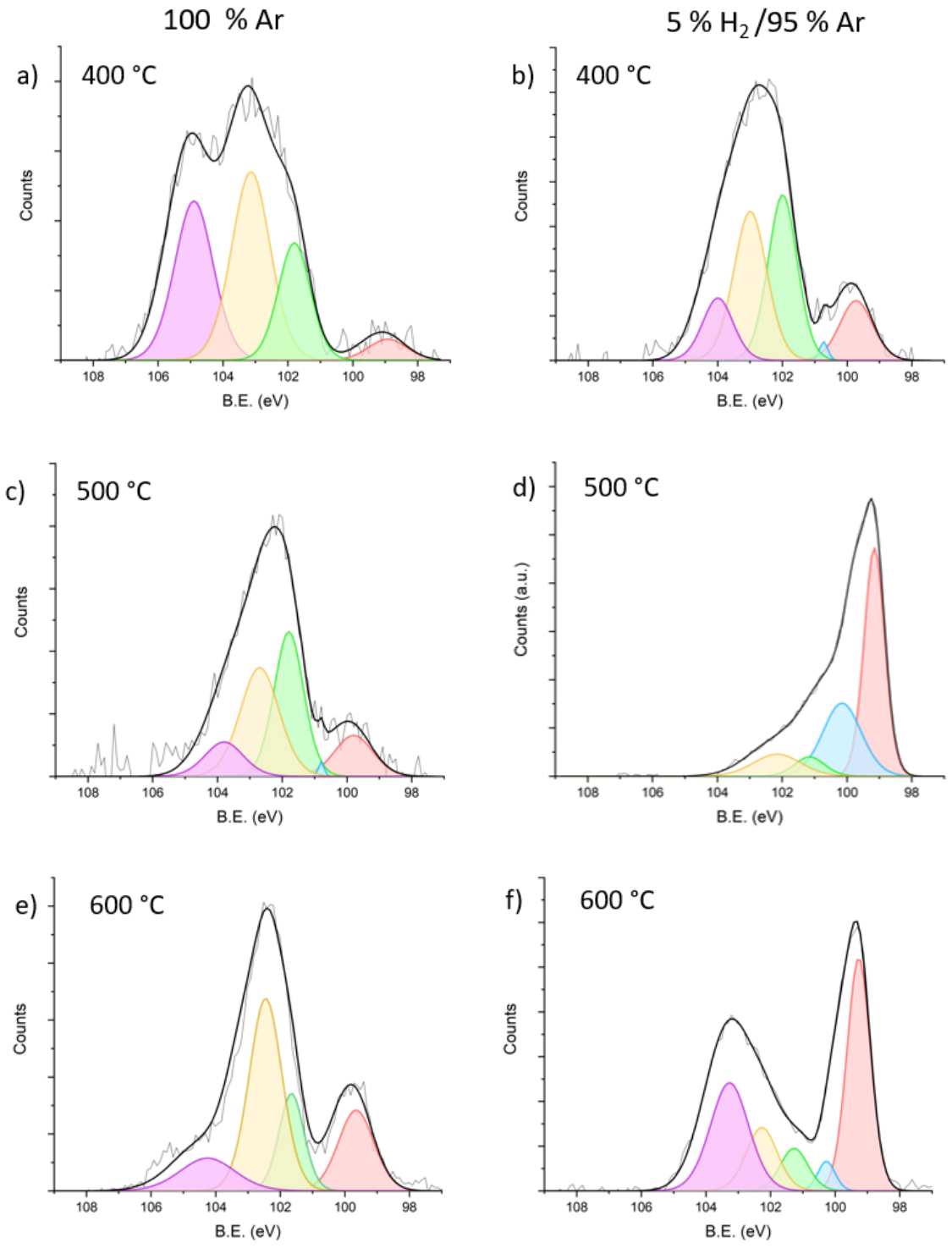

Figure 3. 8 High-resolution Si 2p XP spectra of B-doped SiNPs obtained from annealing precursor particles in flowing Ar and 5:95 H_2:Ar atmospheres at indicated temperatures.

The morphologies of the SiNPs liberated from the oxide composites produced from each set of drive-in conditions were investigated using bright-field TEM (Figure 3.9). SiNPs obtained from annealing at 400 and 500 °C appeared spherical with diameters of 4.90 ± 1.8 and 4.60 ± 2.1 nm for Ar atmosphere processed samples and 4.90 ± 1.7 and 4.38 ± 0.91 nm for those prepared in 5% H_2:95% Ar (Figures 3.9 and 3.10). These TEM determined dimensions are consistently smaller than those observed for the predefined intrinsic SiNPs (i.e., d_{TEM} = 6.3 ± 1.2 nm); we attribute these differences to the impacts of the second ethanolic HF etching step required for their liberation, as well as Si-based reduction of the boric acid dopant precursor. HRTEM of the present B-doped SiNPs revealed a characteristic Si (111) lattice spacing of 0.33 nm (Figure 3.9; insets). In contrast, equivalent analyses of materials obtained from drive-in annealing of reaction mixtures at 600 °C reveals the SiNP spherical morphology is compromised and networks of interconnected Si particles result (Figures 3.9 c, f). These networks are comparatively large and polydisperse (i.e., 15.0 ± 11.0 nm for Ar and 6.30 ± 8.2 nm for 5% H_2:95% Ar; Figure 3.10). We propose that the HSQ capping layer undergoes a well-understood thermal disproportionation reaction at temperatures over 450 °C to form amorphous Si that deposits onto and links SiNPs to form the observed networks.[4,47,52] From these observations, we chose to use a peak drive-in annealing temperature of 500 °C and 5% H_2:95% Ar processing atmosphere because these parameters offer what we have found to be the best conditions investigated here to achieve high concentrations of B-dopant while maintaining uniform spherical NP morphology.

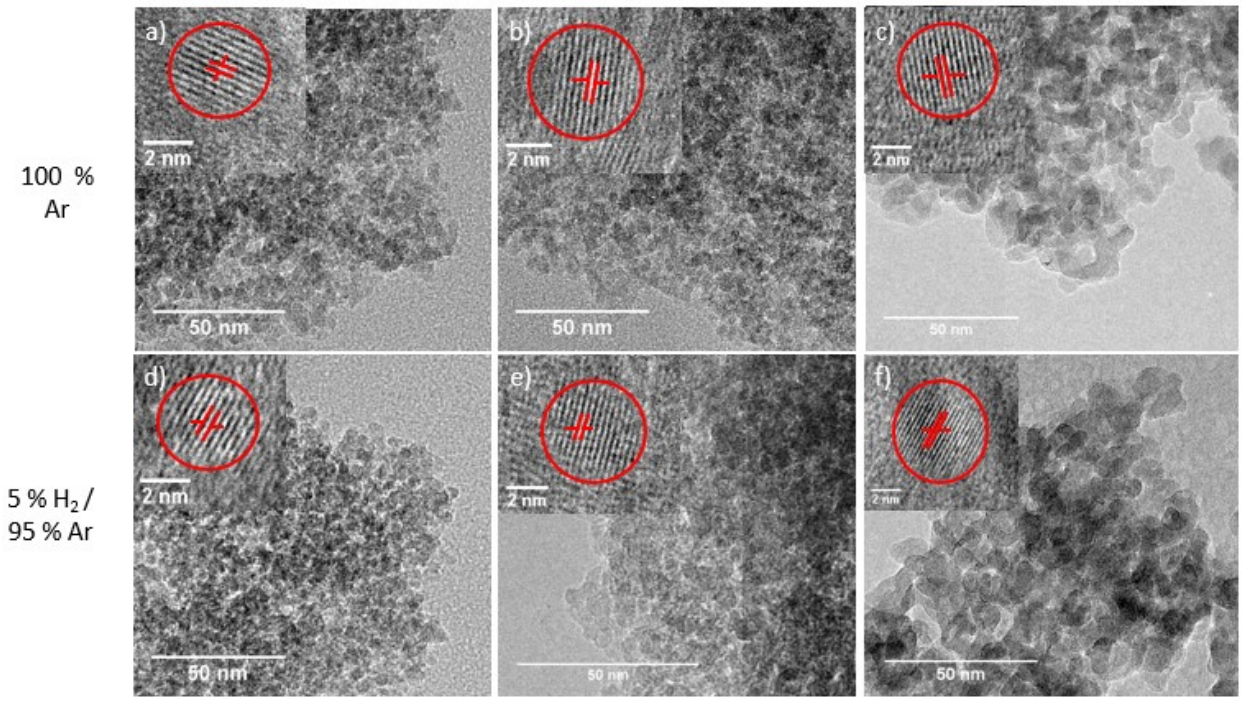

Figure 3. 9 Bright-field TEM of freshly liberated unfunctionalized B-doped SiNPs obtained from predefined intrinsic SiNPs (d_{TEM} = 6.3 nm) via drive-in annealing in Ar (a-c) and 5% H_2:95% Ar (d – f) at indicated peak processing temperatures for 1 h. Insets show HRTEM imaging that, in all cases, reveals characteristic Si (111) lattice spacing of 0.32 nm.

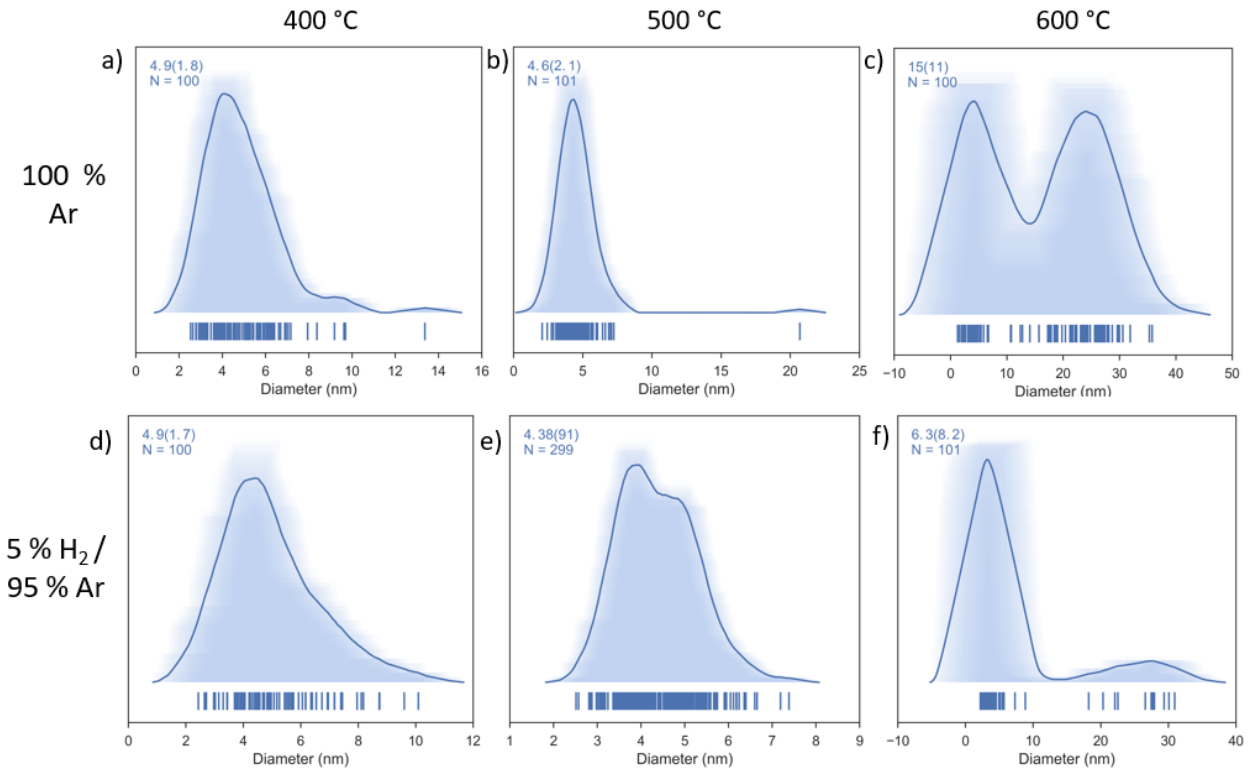

Figure 3. 10 Average shifted histograms of particle sizes obtained from bright field TEM images of B-doped SiNPs obtained from composites annealed in Ar at a) 400 °C, b) 500 °C, c) 600 °C and 5:95 H_2:Ar at d) 400 °C, e) 500 °C, f) 600 °C. N represents the number of particles measured.

3.3.2 Evaluating Dopant Concentration and Distribution

With our newfound insight into the active processes in diffusion-based doping of preformed SiNPs in hand, we turn our attention to preparing freestanding B-doped SiNPs of different sizes, interrogating their structure, and understanding the nature (e.g., location, bonding, etc.) of the dopant atoms. Qualitatively, the SiNPs liberated from the composites obtained from the drive-in procedure differ substantially from the preformed intrinsic SiNPs obtained from the

original HSQ-derived composites. The B-doped SiNPs form dark brown transparent solutions in ethanol (Figure 3.11 inset); this differs starkly from what is observed for the intrinsic SiNPs that form an orange/brown cloudy suspension that readily settle over 10 minutes (Figure 3.11 inset). These observations are consistent with other reports of doped SiNPs that did not require additional surface functionalization to render them compatible with polar solvents.[27,51,53] Looking to the infrared spectra of the doped SiNPs (Figure S8 a) features at 1400 cm^{-1} that are characteristic of B-O/B-H stretching are clearly present while equivalent analysis of the preformed intrinsic SiNPs show no evidence of B-related absorptions while Si-H related features (i.e., 900 and 2200 cm^{-1}) dominate the spectra.

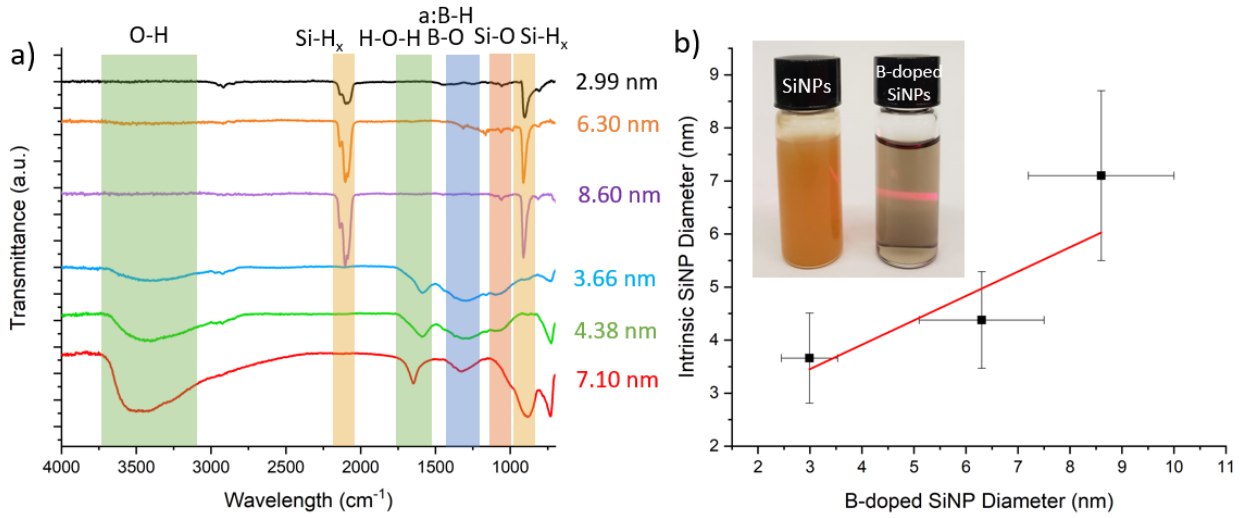

Figure 3. 11 a) Fourier transform infrared spectra (FTIR) for indicated precursor intrinsic SiNPs and corresponding as-synthesized B-doped SiNPs. Particle sizes indicated on the spectra correspond to the d_{TEM} of preformed intrinsic SiNPs (2.99, 6.30 and 8.60 nm) and B-doped SiNPs (3.66, 4.38 and 7.10 nm). b) Plot of measured d_{TEM} of intrinsic SiNPs vs. B-doped SiNPs. Inset: photograph of suspensions of intrinsic SiNPs (toluene; left) and B-doped SiNPs (ethanol; right). A standard handheld laser pointer is used to show the Tyndall effect exhibited by the doped particle suspension.

Bright-field TEM imaging of the presented B-doped SiNPs derived from preformed intrinsic SiNPs reveals a spherical morphology with average particle diameters of 3.66 ± 0.85, 4.38 ± 0.91, and 7.10 ± 1.6 nm (Figures 3.12 a-c and 3.13); as expected, and consistent with the mechanism outlined above d_{TEM} values are consistently smaller than those of the preformed intrinsic SiNP precursors, with the exception of the smallest particle diameter, which is statistically the same size as the intrinsic SiNP precursor (Figure 3.11 b).

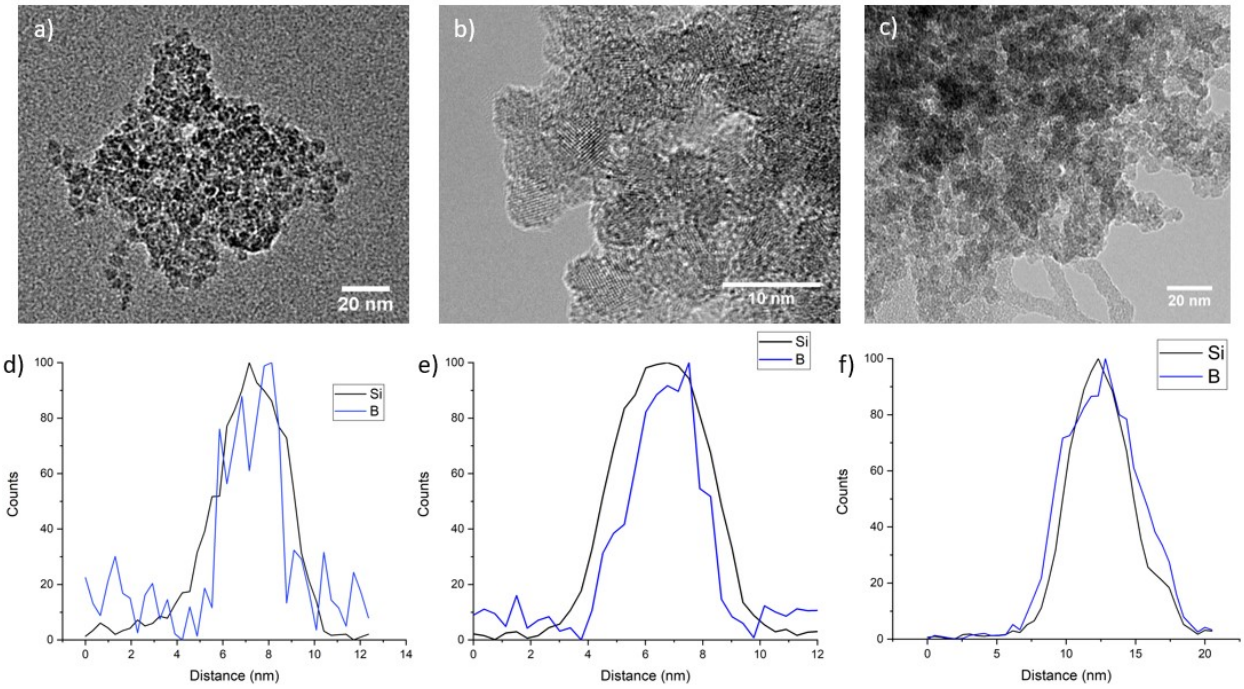

Figure 3. 12 Bright-field TEM images of as-synthesized B-doped SiNPs derived from parent intrinsic SiNPs with average diameters of a) 3.66 ± 0.85, b) 4.38 ± 0.91, and c) 7.10 ± 1.6 nm. d)-f) EELS line-scans of corresponding B-doped SiNPs shown in a – c.

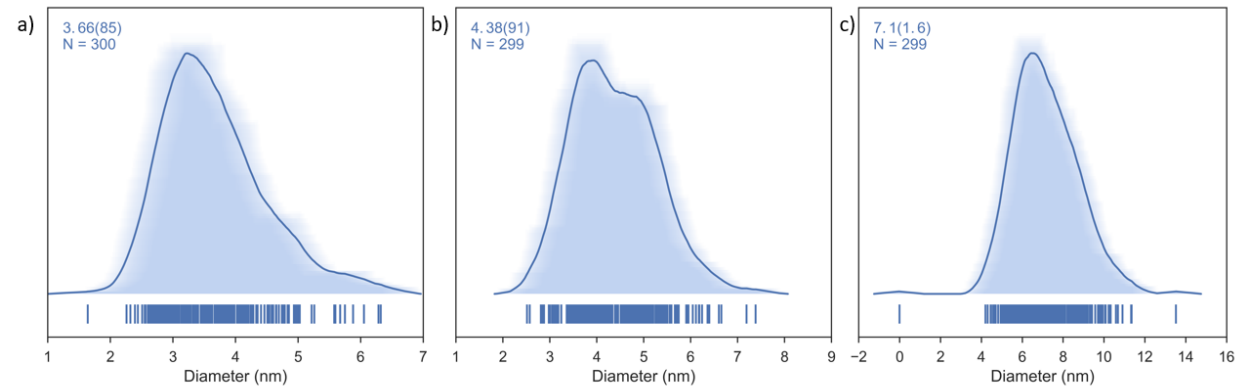

Figure 3. 13 Average shifted histograms obtained from bright field TEM images of B-doped SiNPs produced using precursor SiNPs with TEM determined dimensions of a) 3.66 ± 0.85 nm b) 4.38 ± 0.92 nm and c) 7.10 ± 1.6 nm.

We also note evidence of crystallinity in the HRTEM image (Figures 3.14 a-c) with the observation of characteristic Si (111) lattice spacing. Crystallinity was further confirmed via PXRD (Figures 3.14 d-f) analysis that showed characteristic broadened reflections associated with cubic silicon and provide crystallite dimensions through Debye-Scherrer analyses (Table 3.3).

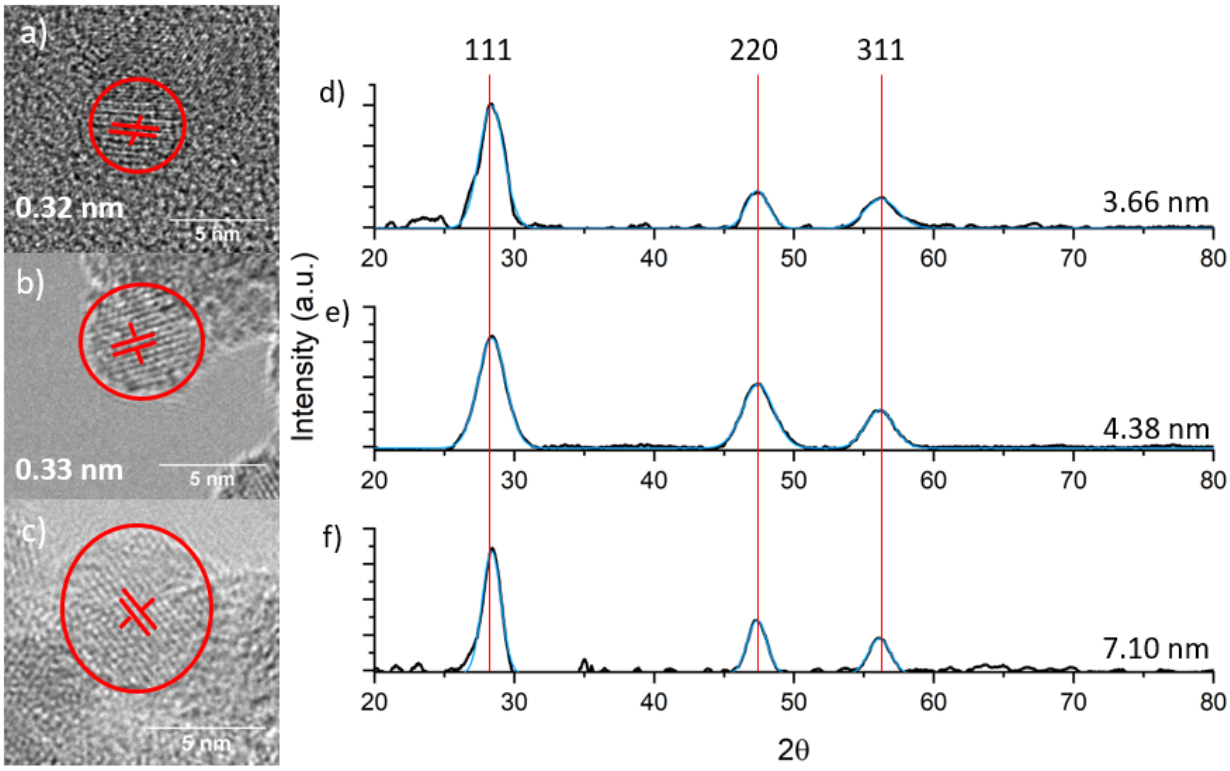

Figure 3. 14 High-resolution TEM of as-synthesized B-doped SiNPs with average TEM determined diameters of a) 3.66 ± 0.85 nm b) 4.38 ± 0.92 nm and c) 7.10 ± 1.6 nm. Powder X-ray diffraction patterns of as-synthesized B-doped SiNPs with diameters of d) 3.66 nm, e) 4.38 nm and f) 7.10 nm. Experimental data is shown as black traces. Blue lines show the Gaussian-Lorentzian multiple-peak fitting.

Table 3. 3 Debye-Scherrer analysis of powder X-ray diffraction patterns collected from B-doped SiNPs of three different sizes: 3.66 ± 0.85 nm, 4.38 ± 0.92 nm and 7.10 ± 1.6 nm.

d_{TEM} = 3.66 nm			**d_{TEM} = 4.38 nm**			**d_{TEM} = 7.10 nm**		
Peak position (2θ)	**FWHM**	**Crystallite Size (nm)**	**Peak position (2θ)**	**FWHM**	**Crystallite Size (nm)**	**Peak position (2θ)**	**FWHM**	**Crystallite Size (nm)**
28.34	4.00	2.05	28.38	2.11	3.89	28.38	1.581	5.18
47.39	3.98	2.18	47.38	1.88	4.62	47.36	1.63	5.32
55.96	3.78	2.38	56.23	2.74	3.28	56.11	1.87	4.81

The presence and location of B atoms within the present SiNPs was investigated using electron energy loss spectroscopy (EELS). EELS point spectra of all three sizes of B-doped SiNPs were compared with the preformed intrinsic crystalline Si (Figure 3.15). In all cases the L-edge of Si is clearly resolved at 100 eV; we do note that the fine structure of the Si L-edge is impacted by doping consistent with anticipated changes in electronic properties. All three sizes of B-doped SiNPs show an additional energy-loss peak at 200 eV corresponding to the B K-edge. An EELS line-scan for each size of the B-doped SiNP samples was performed to evaluate the relative positioning of B within the particles (Figures 3.12 d-f). In all cases, the integrated B K-edge and Si L-edge energy loss peaks were coincident and consistent with the B being integrated into the entire the SiNP.

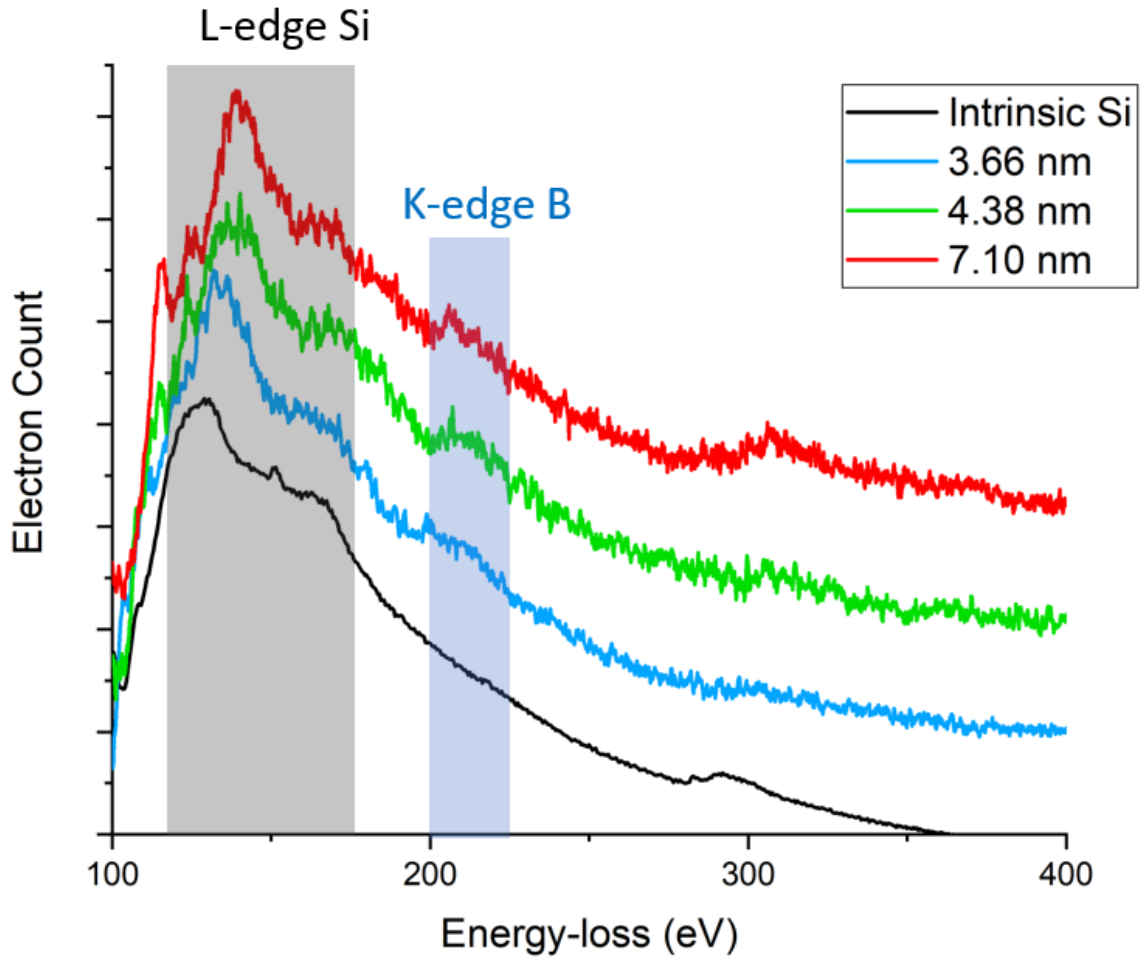

Figure 3. 15 Electron energy-loss spectrum of as-synthesized B-doped SiNPs with average diameter of 3.66 ± 0.85 (blue), 4.38 ± 0.91 (green) and 7.10 ± 1.6 nm (red) compared to intrinsic Si (black).

XPS provides additional insight into the nature and the relative location of the dopant atoms within the SiNPs, while ICP-MS offers complementary bulk quantitative analysis of dopant concentration. The B 1s high-resolution XP spectra (Figures 3.16 a - c) obtained for each size of B-doped SiNPs derived from predefined intrinsic SiNPs are readily deconvoluted into two components appearing at 187.7 and 188.7 eV. These features are confidently attributed to substitutional B atoms bonded to four Si atoms located in the 'core' of the particles,[23,54] and

partially hydrogenated B atoms bonded to two or three Si atoms residing at the particle surface.[55] We observe that the intensity of the B 1s emission is dependent upon the dimensions of the SiNPs. The integrated intensity of the 'surface' species related feature decreases relative to that of the 'core' species emission with larger SiNPs (Table 3.4). This trend can be understood in the context of total B concentration in each sample. ICP-MS analyses provide 5.03, 3.83 and 2.49 atomic percent B for average d_{TEM} dimensions of 3.66, 4.38, and 7.10 nm, respectively. Considering the XPS and ICP-MS data together it is clear that as the total B concentration decreases, so too does the relative intensity of the photoelectron emission arising from the 'surface' species. This is consistent with our previous proposal that, during doping, the NP core becomes saturated with B and excess dopant migrates to, and/or stays at, the particle surface.[23,26,27,31,56]

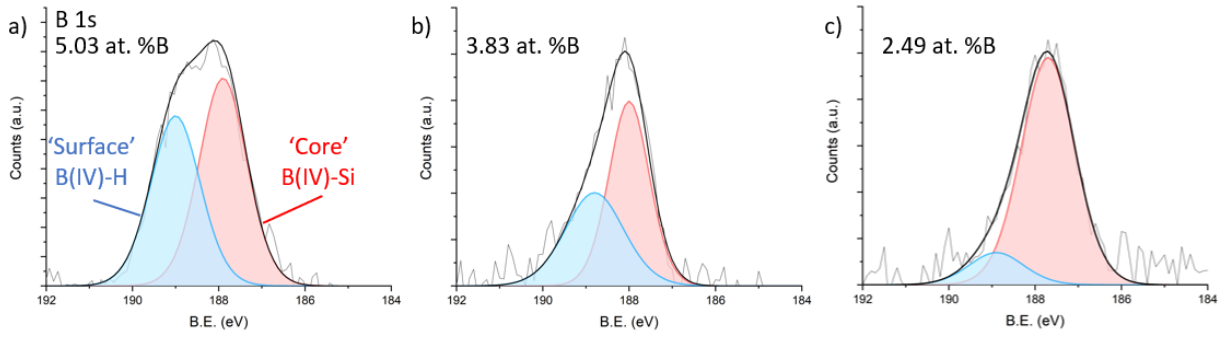

Figure 3. 16 High-resolution B 1s XP spectra and corresponding ICP-MS determined atomic percent B (insets) for as-synthesized B-doped SiNPs with d_{TEM} of a) 3.66 ± 0.85, b) 4.38 ± 0.91, and c) 7.10 ± 1.6 nm.

Table 3. 4 Integrated intensities of the "surface" and "core" B species determined by taking the area under the fitted peaks centred at 188.7 eV and 187.7 eV, respectively, in the B 1s XP spectra for samples with average d_{TEM} dimensions of 3.66, 4.38, and 7.10 nm.

d_{TEM}	Area of "surface" species (188.7 eV)	Area of "core" species (187.7 eV)
3.66	169.5	108.0
4.38	69.7	105.1
7.10	49.9	102.0

3.3.3 The influence of NP Size and Crystallinity on Dopant Concentration

Looking to the size dependence of the boron doping, we observe that total B concentration decreases with increasing particle size. Interestingly, this trend persists despite the presence of an excess of B source in all the investigated reaction mixtures. In bulk semiconductors, dopants behave differently depending upon the crystallinity of the semiconductor host. In fact, for the temperature range used herein (i.e., ca. 500 °C) B diffusivity is 5 orders of magnitude higher in amorphous Si than the crystalline phase.[57,58] This dramatic difference has been attributed to the influence of defects (e.g., dangling bonds) that create a metastable mobile B that can hop between adjacent sites.[41,58] In this context, one can expect the core structure (e.g., structural strain, degree of crystallinity) of SiNPs to impact boron uptake and diffusion.

Previously, we demonstrated that SiNPs obtained from thermally-induced disproportionation of HSQ possess size dependent structures.[4,47] The smallest SiNPs (i.e., d_{TEM}~ 3 nm) investigated in our earlier study (and here) primarily comprise a quasi-crystalline structure.[44] Increasing the particle size sees this quasi-crystalline structure grow (i.e., d_{TEM}~ 6 nm) and evolve providing a crystalline core capped by a quasi-crystalline shell and a disordered surface for the largest SiNP investigated here (i.e., d_{TEM}~ 9 nm).[44] In our earlier report we also noted an inverse dependence of crystal strain on particle size for SiNPs of dimensionality equivalent to those

investigated here. In this context, it follows that the noted quasi-crystallinity of, and strain in smaller SiNPs (i.e., d_{TEM} < 6 nm) will manifest as defects that include dangling bonds, distorted Si-Si bonds and co-ordination defects that will undoubtedly impact B diffusivity and increase the maximum possible B dopants in the SiNPs.[44,59] Furthermore, the size dependence of the quasi-crystallinity and strain of the preformed intrinsic SiNPs is expected to impart size-dependent B uptake. Looking to as-synthesized B-doped SiNPs prepared from preformed intrinsic SiNPs we find they exhibit PXRD patterns with broadened reflections of characteristic cubic Si (Figure 3.14). A comparison of the TEM- and Debeye-Scherrer analysis-determined dimensions reveals SiNPs with the largest d_{TEM} have the largest crystallite size (i.e., d_{XRD}) while those with the smallest d_{TEM} show the smallest d_{XRD} (See Table 3.5). This is consistent with the gradient structure of the predefined intrinsic SiNPs influencing B uptake while being preserved throughout the drive-in doping procedure.

Table 3. 5 Corresponding TEM dimensions and crystallite sizes of precursor SiNPs and B-doped SiNPs determined using the Debye-Scherrer Equation.

Precursor SiNP d_{TEM} (nm)	**Precursor SiNP d_{XRD} (nm)**	**B-doped SiNPs d_{TEM} (nm)**	**B-doped SiNPs d_{XRD} (nm)**
2.99	2.11	3.66	2.02
6.30	3.93	4.38	3.63
8.60	6.75	7.10	5.11
6.02	5.74	5.42	4.89

To further explore the impact of the quasi-crystalline structure of the SiNP on B uptake/doping we 'over-etched' the identical HSQ-derived SiNP/SiO_2 composite. This over-etching procedure reduces the overall NC physical dimension, as well as the thickness of the quasi-crystalline outer layer and yields preformed 'crystalline' SiNPs with $d_{TEM} = 6.02 \pm 0.94$ nm (Figure 3.17) and calculated $d_{XRD} = 5.74$ nm (Table 3.5) that was B doped using the presented drive-in procedures.

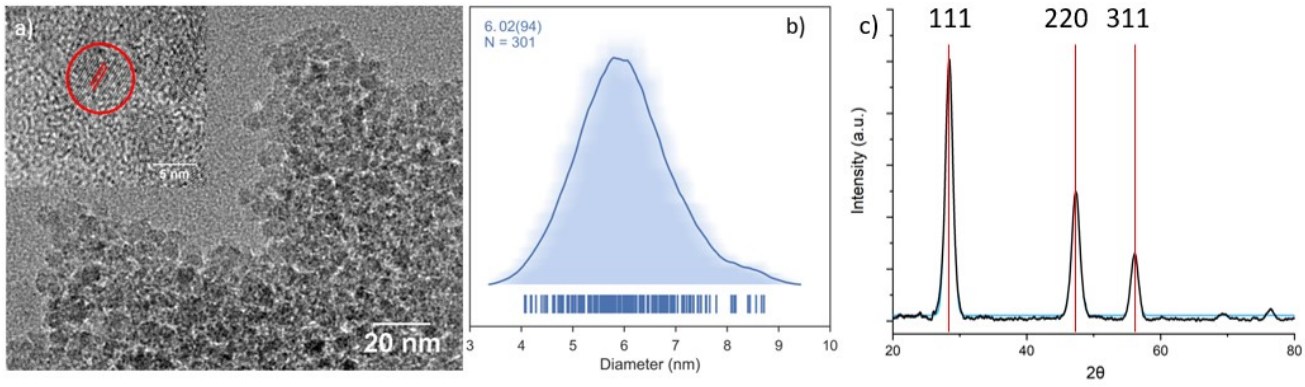

Figure 3. 17 a) Bright field and high-resolution (inset) TEM of 9 nm intrinsic SiNPs that were "over-etched" to 6 nm using ethanolic HF to remove their amorphous shell and b) the corresponding average shifted histogram. c) PXRD pattern obtained from a representative over-etched sample showing characteristic reflections from crystalline silicon. Experimental data is shown as black traces. Blue lines show the Gaussian-Lorentzian multiple-peak fitting.

A comparison of B-doped particles obtained from 'crystalline' SiNPs ($d_{TEM} = 6.02 \pm 0.92$ nm; $d_{XRD} = 5.74$ nm) and similarly sized (i.e., $d_{TEM} = 6.30 \pm 1.2$ nm; $d_{XRD} = 3.93$ nm) standard intrinsic SiNPs that bore a quasi-crystalline shell showed distinct differences in B uptake. The high-

resolution B 1s XP spectra of doped 'crystalline' and standard SiNPs indicate both types of SiNPs contain B, however, the intensity of the B emission from the 'crystalline' sample is significantly less intense than that observed from the standard SiNPs doped under identical conditions (Figure 3.18 a, b). Bulk ICP-MS measurements confirm the concentration of B in standard SiNPs (i.e., 3.83 atomic %) is approximately 7x higher than that observed for 'crystalline' SiNPs (i.e., 0.52 atomic %). In both cases, the B emission is readily deconvoluted into components arising from 'core' and 'surface' B species evidenced by emissions at 187.7 and 188.7 eV, respectively. From this data, we conclude that quasi-crystalline shells on SiNPs dramatically promote B uptake during thermal drive-in and that the observed size-dependent B concentration is reasonably attributed to smaller SiNPs possessing quasi-crystalline structures.

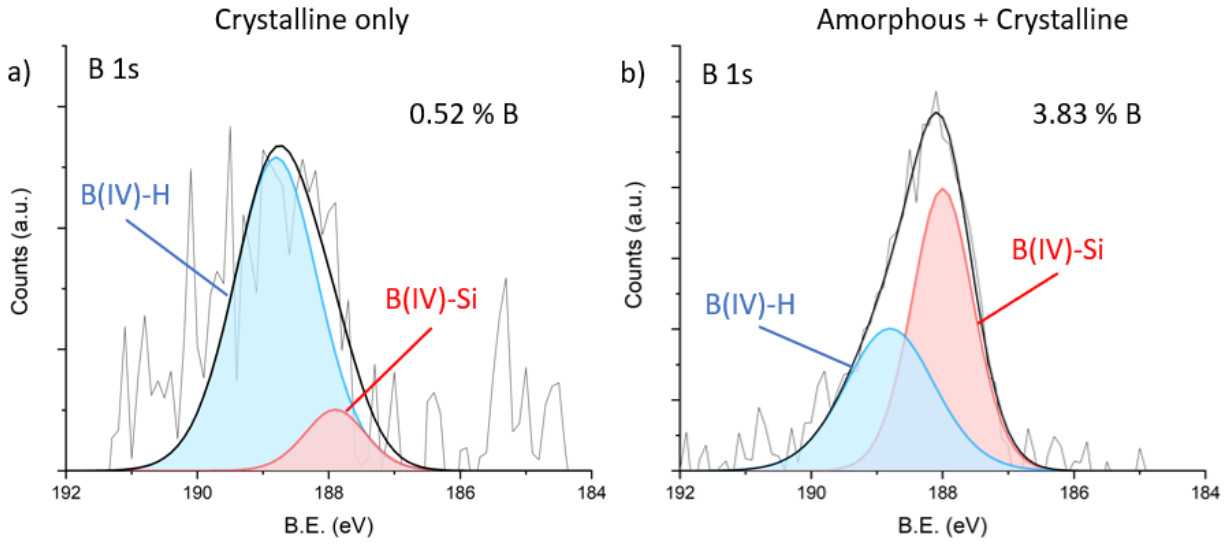

Figure 3. 18 High-resolution B 1s XP spectra of B-doped SiNPs that were synthesized from the predefined SiNPs bearing quasi-crystalline shells (a) and over-etched crystalline SiNPs (b).

3.3.4 Tailoring surface chemistry

Having shown that drive-in doping of SiNPs provides a convenient approach to size-controlled preparation of B-doped SiNPs, it is important to demonstrate tailoring of the surface chemistry of these new systems because surface chemistry provides solution processability, stability, and can even impart size-independent tailoring of optical response.[7,9,60] As-synthesized, the B-doped SiNPs are soluble in ethanol, however, rendering them compatible with organic (non-polar) solvents has proven challenging. In Chapter 2 we demonstrated the surface chemistry of B-doped SiNPs is readily tailored using a two-step approach involving phosphorus pentachloride (PCl_5) etching followed by heating in the presence of an appropriate alcohol that binds to the particle surface as an alkoxide ligand.[51] To investigate the potential size dependence of this functionalization procedure, we functionalized B-doped SiNPs of different sizes/B-doping concentrations (i.e., 3.66 ± 0.85/5.03 atomic %, 4.38 ± 0.91/3.83 atomic %, and 7.10 ± 1.6 nm/2.49 atomic %) with 1-decanol surface groups derived from 1-decanol and evaluated their size-dependent optical response. After functionalization, all the presented SiNPs readily disperse in common organic solvents (e.g., toluene) to yield a transparent yellow/brown 'solutions' that show a Tyndall effect when exposed to the emission of a standard laser pointer (Figure 3.19 a). FTIR spectra of the functionalized particles (Figure 3.19 b) show boron and silicon oxide associated features at 1080 cm^{-1} and 1400 cm^{-1} consistent with attachment of the OR ligand through Si-O and B-O linkages. In addition, the C-H_x stretching of the surface tethered decyl chain is noted at 2900 cm^{-1}.

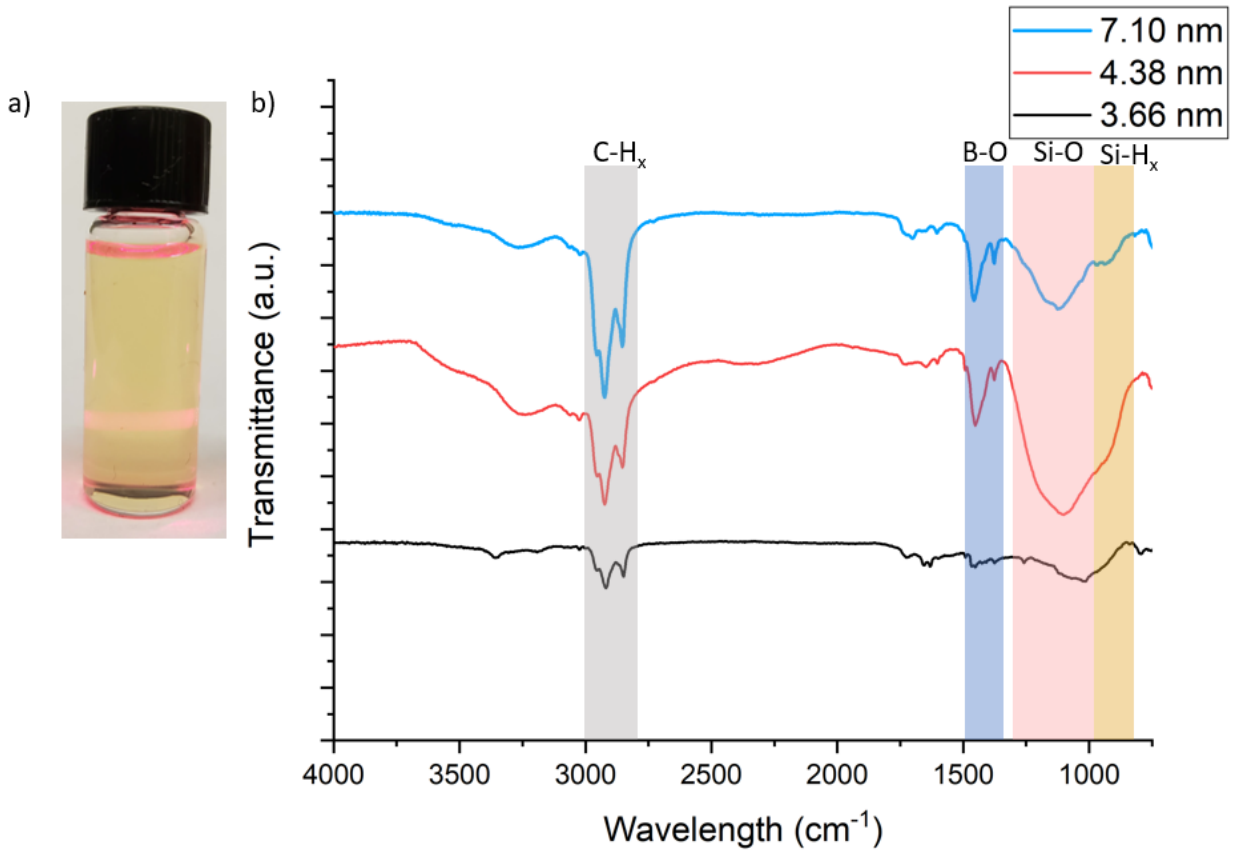

Figure 3. 19 a) A photograph of a toluene suspension of d_{TEM} = 4.38 nm B-doped SiNPs obtained from their reaction with PCl_5 and 1-decanol. The beam of a standard handheld laser pointer is used to show a Tyndall effect. b) FTIR of 1-decylate functionalized B-doped SiNPs for the indicated particle sizes.

Further confirming 1-decanol functionalization, the high-resolution B1s XP spectra of all functionalized SiNPs show evidence of an emission at 192 eV that we attribute to oxidized four-coordinate B bonded to two or three Si atoms and one or two "OR" functionalities at the SiNP surface which are not observed for non-functionalized B-doped SiNPs (Figure 3.20).[26,51,53,61] In addition, Si 2p high-resolution XP spectra show increased relative intensity of the Si(III) and Si

(IV) species at binding energies of 102 and 103 eV, respectively that is consistent with introduction of alkoxide surface ligands (Figure 3.21).

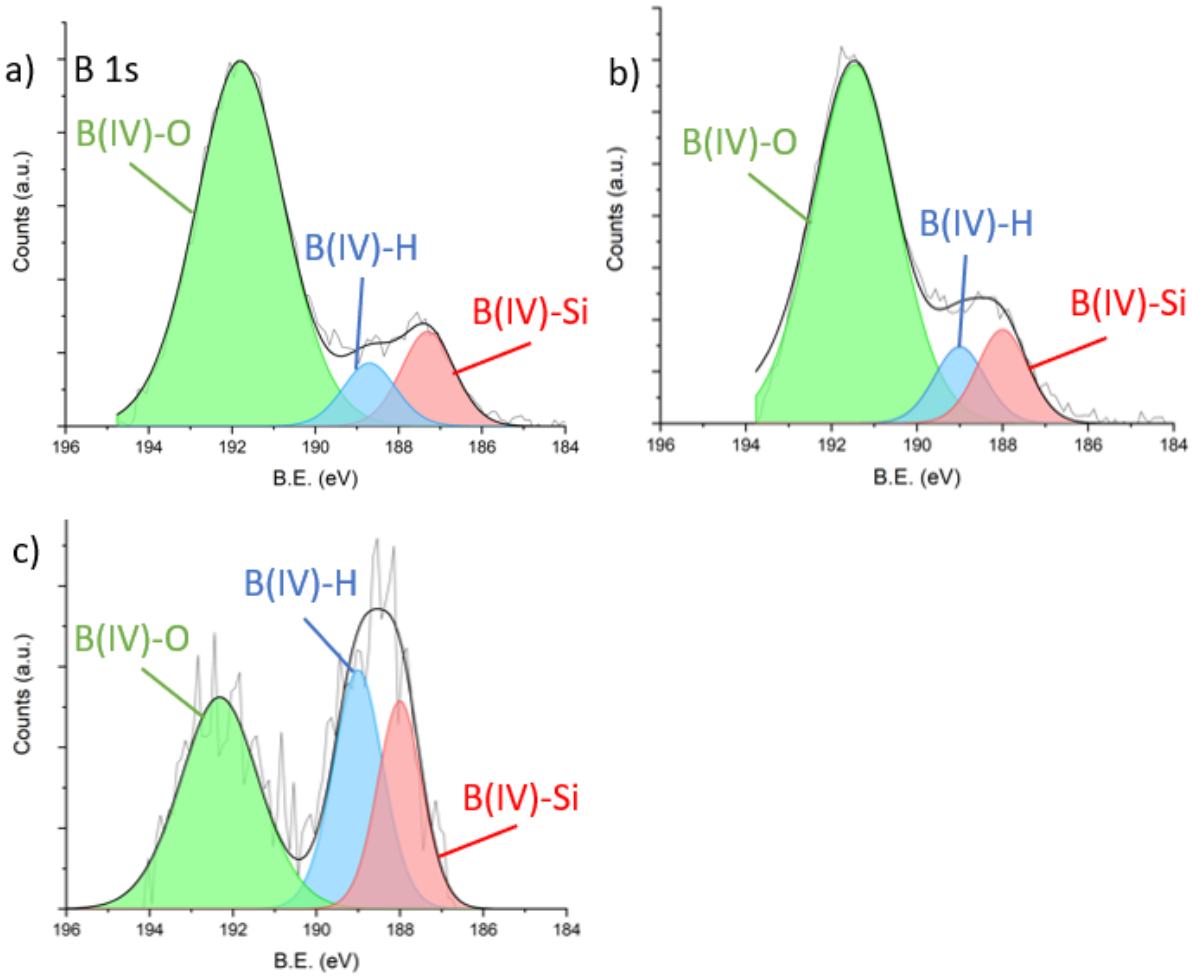

Figure 3. 20 High-resolution XP spectra of B 1s for 1-decylate functionalized B-doped SiNPs with average TEM determined sizes of a) 3.66 nm, b) 4.38 nm and c) 7.10 nm.

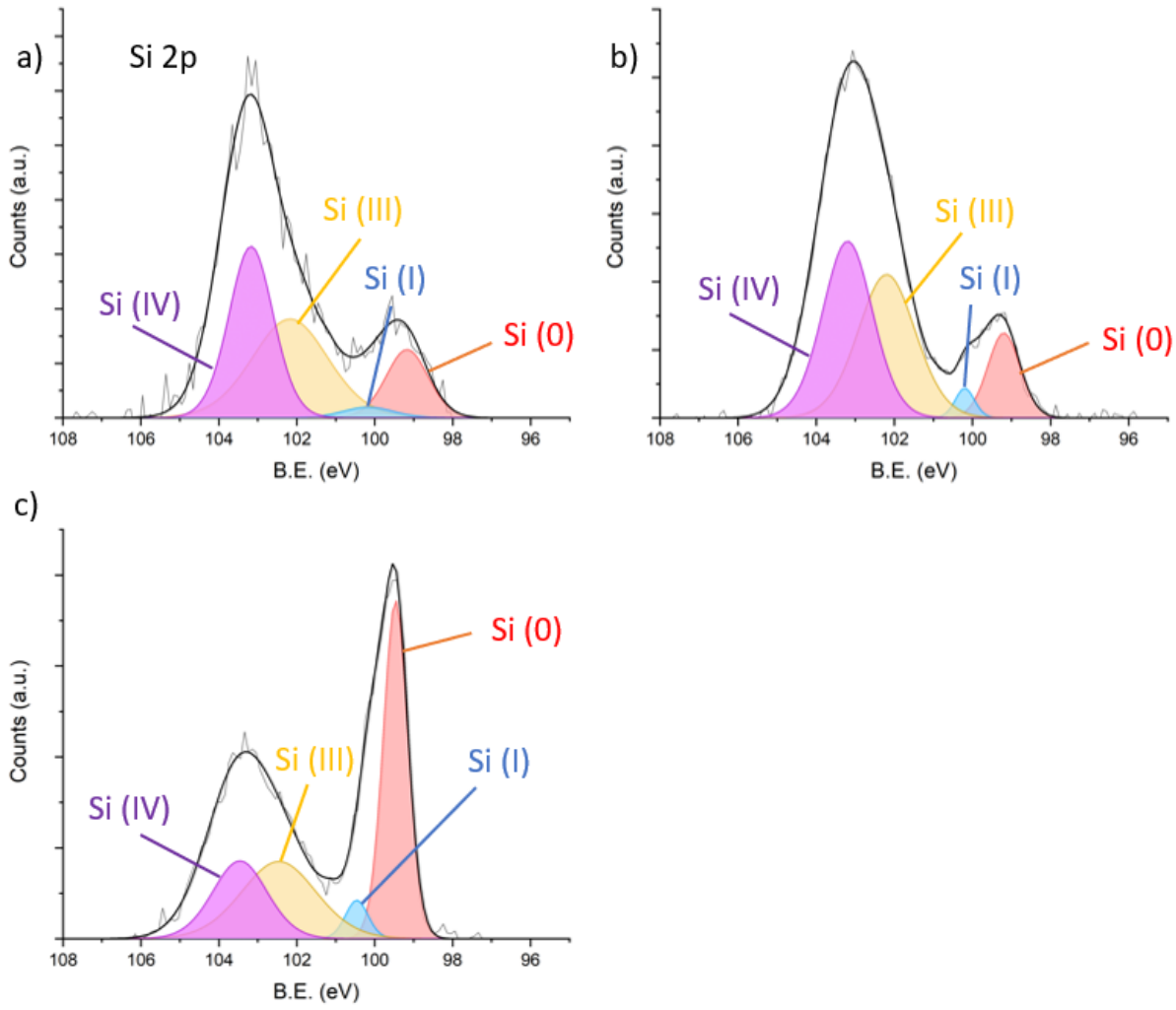

Figure 3. 21 High-resolution XP spectra of Si 2p region for 1-decylate functionalized B-doped SiNPs with TEM determined average sizes of a) 3.66 nm, b) 4.38 nm and c) 7.10 nm.

With the combination of tailored size and surface chemistry afforded by the present methods, we endeavored to investigate and compare the size dependent photoluminescence response of B-doped SiNPs. Figure 3.22 shows the absorbance and photoluminescence spectra of the three sizes/B-doping concentrations (i.e., 3.66 ± 0.85/5.03 atomic %, 4.38 ± 0.91/3.83 atomic %, and 7.10 ± 1.6 nm/2.49 atomic %) of B-doped SiNPs before and after PCl_5 mediated alkoxide

functionalization. Like intrinsic Si, the B-doped SiNPs absorb light over the entire UV spectral region tailing into the visible (Figure 3.22 a).

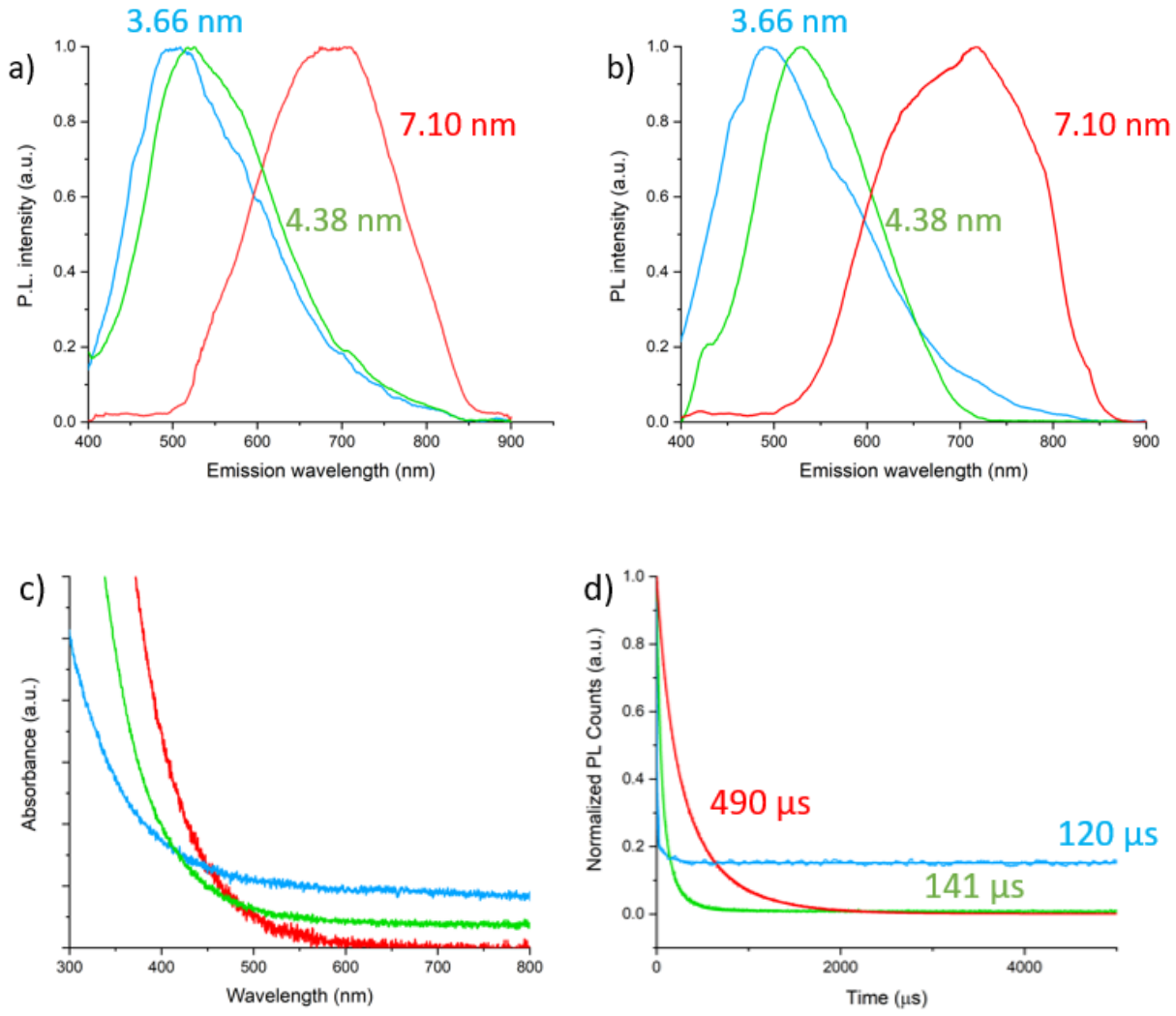

Figure 3. 22 Normalized PL emission spectra for B-doped SiNPs with diameters/B-dopant concentrations of 3.66 ± 0.85/5.03 atomic % (blue), 4.38 ± 0.91/3.83 atomic % (green), and 7.10 ± 1.6 nm/2.49 atomic % (red) a) as-synthesized in ethanol and b) after functionalization with 1-decanol in toluene. c) UV-Visible absorbance and d) Time-resolved fluorescence decay profiles of the emission of B-doped SiNPs after functionalization with 1-decanol. Data are fit with a biexponential decay model detailed in the supplemental information.

Ethanol solutions of as-synthesized B-doped SiNPs show peak PL energies spanning the visible region of the spectrum that red-shift through 500, 550 to 745 nm as d_{TEM} increases through 3.66 ± 0.85, 4.38± 0.91, to 7.10±1.6 nm, respectively (Figure 3.22 b). Functionalization with 1-decanol moieties saw the PL maxima of all the B-doped SiNPs remain unchanged (Figure 3.22 c), however we did note an increase in maximum PL intensity (Figure 3.23).

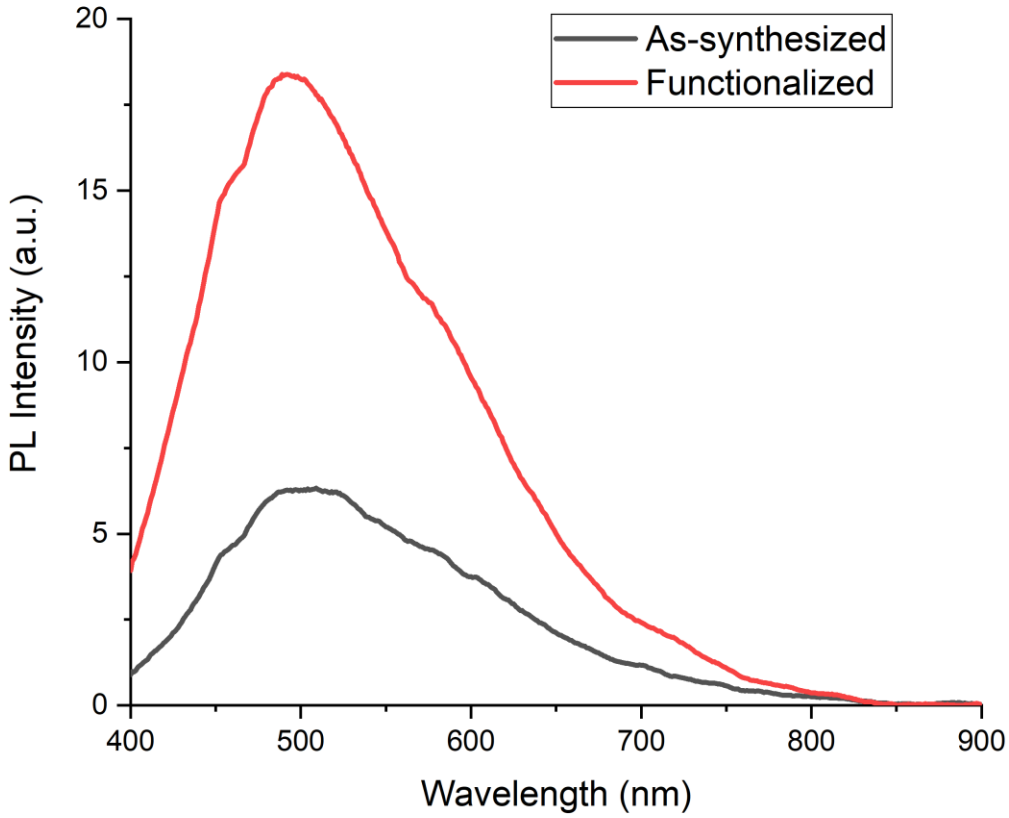

Figure 3. 23 Photoluminescence spectra of B-doped SiNPs with TEM determined average diameters of 3.66 nm before (black) and after functionalization with 1-decanol (red). This data illustrates the impact of functionalization on PL intensity.

We also note that PL quantum yields (PLQY) of B-doped SiNPs depended on particle size/dopant concentration showing an increase from 7 % to 19 % as d_{TEM} increased from 3.66 to 7.10 nm and B concentration decreased from 5.03 to 2.49 atomic %. This trend in PLQY is opposite to what is normally observed with increasing SiNP size,[6] hence we tentatively attribute it to the influences of non-radiative Auger recombination, which increases with dopant concentration. [106] PL lifetime measurements were calculated using the time-resolved emission decay profiles of each size of B-doped SiNPs after functionalization with 1-decanol (Figure 3.22 d and Table 3.6). As the size of the NC increased from 3.66 to 7.10 nm, the recorded microsecond lifetimes increased from 120.5 to 489.6 μs, consistent with other studies reporting longer lifetimes for larger SiNPs.[20,63] The ability to tailor the surface chemistry of the B-doped particles to render them soluble in either aqueous or organic solvent and retain PL emission wavelength is desirable for many far-reaching applications such as photovoltaics and multimodal biomedical imaging.

Table 3. 6 PL decay lifetimes of B-doped 1-decanol functionalized SiNPs

Particle d_{TEM}	**a_1**	**τ_1**	**a_2**	**τ_2**	**R^2**
3.66 nm	0.8795	4.633	0.05567	120.5	0.9975
4.38 nm	0.5797	38.98	0.4053	141.1	0.9984
7.10 nm	0.4634	153.4	0.5341	489.6	0.9997

3.4 Conclusions

In conclusion SiNPs were doped with B using a novel post-synthesis diffusion-based method which uses an HSQ “mask” to prevent volatilization of the B dopant during the “drive-in”

step. Raising the annealing temperature of the drive-in step promotes the reduction of the dopant oxide and incorporation into the SiNP, however, at temperatures > 500 °C fused particle networks begin to form and compromise the NC structure. Additionally, it was found that the presence of hydrogen in the flowing annealing atmosphere further promotes B incorporation, and likely increases chemical potential for an alternative reaction pathway. The concentration of B dopant incorporated into the NC increased as the size of the SiNP decreased, which was attributed to the increase in disorder in the smaller NCs. As-synthesized the B-doped SiNPs exhibited PL emissions which ranged from the visible to NIR wavelengths, which could be rendered organic-phase soluble upon functionalization with 1-decanol and increase the overall PL emission intensity of the particles. The tailorability of the size and surface chemistry of the B-doped SiNPs make them excellent candidates for use in targeted applications such as multimodal imaging and photovoltaic devices.

3.5 References

(1) Lee, J.-H.; Huh, Y.-M.; Jun, Y.-w.; Seo, J.-w.; Jang, J.-t.; Song, H.-T.; Kim, S.; Cho, E.-J.; Yoon, H.-G.; Suh, J.-S.; et al. Artificially engineered magnetic nanoparticles for ultra-sensitive molecular imaging. *Nature Medicine* **2006**, *13* (1), 95-99. DOI: 10.1038/nm1467.
(2) Oh, J.; Yuan, H.-C.; Branz, H. M. An 18.2%-efficient black-silicon solar cell achieved through control of carrier recombination in nanostructures. *Nature Nanotechnology* **2012**, *7* (11), 743-748. DOI: 10.1038/nnano.2012.166.
(3) Milliken, S.; Thiessen, A. N.; Cheong, I. T.; O'Connor, K. M.; Li, Z.; Hooper, R. W.; Robidillo, C. J. T.; Veinot, J. G. C. "Turning the dials": controlling synthesis, structure, composition, and surface chemistry to tailor silicon nanoparticle properties. *Nanoscale* **2021**. DOI: 10.1039/d1nr04701a. McVey, B. F. P.; Tilley, R. D. Solution Synthesis, Optical Properties, and Bioimaging Applications of Silicon Nanocrystals. *Accounts of Chemical Research* **2014**, *47* (10), 3045-3051. DOI: 10.1021/ar500215v.
(4) Hessel, C. M.; Henderson, E. J.; Veinot, J. G. C. Hydrogen Silsesquioxane: A Molecular Precursor for Nanocrystalline Si−SiO2 Composites and Freestanding Hydride-Surface-Terminated Silicon Nanoparticles. *Chemistry of Materials* **2006**, *18* (26), 6139-6146. DOI: 10.1021/cm0602803.
(5) Kortshagen, U. R.; Sankaran, R. M.; Pereira, R. N.; Girshick, S. L.; Wu, J. J.; Aydil, E. S. Nonthermal Plasma Synthesis of Nanocrystals: Fundamental Principles, Materials, and Applications. *Chemical Reviews* **2016**, *116* (18), 11061-11127. DOI: 10.1021/acs.chemrev.6b00039. Li, X.; He, Y.; Talukdar, S. S.; Swihart, M. T. Process for Preparing Macroscopic Quantities of Brightly Photoluminescent Silicon Nanoparticles with Emission Spanning the Visible Spectrum. *Langmuir* **2003**, *19* (20), 8490-8496. DOI: 10.1021/la034487b.
(6) Mastronardi, M. L.; Maier-Flaig, F.; Faulkner, D.; Henderson, E. J.; Kübel, C.; Lemmer, U.; Ozin, G. A. Size-Dependent Absolute Quantum Yields for Size-Separated Colloidally-Stable Silicon Nanocrystals. *Nano Letters* **2012**, *12* (1), 337-342. DOI: 10.1021/nl2036194.
(7) Mobarok, M. H.; Purkait, T. K.; Islam, M. A.; Miskolzie, M.; Veinot, J. G. C. Instantaneous Functionalization of Chemically Etched Silicon Nanocrystal Surfaces. *Angewandte Chemie International Edition* **2016**, *56* (22), 6073-6077. DOI: 10.1002/anie.201609651. Dasog, M.; Bader, K.; Veinot, J. G. C. Influence of Halides on the Optical Properties of Silicon Quantum Dots. *Chemistry of Materials* **2015**, *27* (4), 1153-1156. DOI: 10.1021/acs.chemmater.5b00115.
(8) Clark, R. J.; Dang, M. K. M.; Veinot, J. G. C. Exploration of Organic Acid Chain Length on Water-Soluble Silicon Quantum Dot Surfaces. *Langmuir* **2010**, *26* (19), 15657-15664. DOI: 10.1021/la102983c. Aghajamali, M.; Xie, H.; Javadi, M.; Kalisvaart, W. P.; Buriak, J. M.; Veinot, J. G. C. Size and Surface Effects of Silicon Nanocrystals in Graphene Aerogel Composite Anodes for Lithium Ion Batteries. *Chemistry of Materials* **2018**, *30* (21), 7782-7792. DOI: 10.1021/acs.chemmater.8b03198. Islam, M. A.; Purkait, T. K.; Veinot, J. G. C. Chloride Surface Terminated Silicon Nanocrystal Mediated Synthesis of Poly(3-hexylthiophene). *Journal of the American Chemical Society* **2014**, *136* (43), 15130-15133. DOI: 10.1021/ja5075739. Dasog, M.; Yang, Z.; Regli, S.; Atkins, T. M.; Faramus, A.; Singh, M. P.; Muthuswamy, E.; Kauzlarich, S. M.; Tilley, R. D.; Veinot, J. G. C. Chemical Insight into the Origin of Red and Blue Photoluminescence Arising from Freestanding Silicon Nanocrystals. *ACS Nano* **2013**, *7* (3), 2676-2685. DOI: 10.1021/nn4000644. Bell, J. P.; Cloud, J. E.; Cheng, J.; Ngo, C.; Kodambaka, S.; Sellinger, A.; Ratanathanawongs Williams, S. K.; Yang, Y. N-Bromosuccinimide-based bromination and subsequent functionalization of hydrogen-terminated silicon quantum dots. *RSC*

Adv. **2014**, *4* (93), 51105-51110. DOI: 10.1039/c4ra08477b. Kehrle, J.; Höhlein, I. M. D.; Yang, Z.; Jochem, A.-R.; Helbich, T.; Kraus, T.; Veinot, J. G. C.; Rieger, B. Thermoresponsive and Photoluminescent Hybrid Silicon Nanoparticles by Surface-Initiated Group Transfer Polymerization of Diethyl Vinylphosphonate. *Angewandte Chemie International Edition* **2014**, n/a-n/a. DOI: 10.1002/anie.201405946. Yu, Y.; Rowland, C. E.; Schaller, R. D.; Korgel, B. A. Synthesis and Ligand Exchange of Thiol-Capped Silicon Nanocrystals. *Langmuir* **2015**, *31* (24), 6886-6893. DOI: 10.1021/acs.langmuir.5b01246.
(9) Dasog, M.; De Los Reyes, G. B.; Titova, L. V.; Hegmann, F. A.; Veinot, J. G. C. Size vs Surface: Tuning the Photoluminescence of Freestanding Silicon Nanocrystals Across the Visible Spectrum via Surface Groups. *ACS Nano* **2014**, *8* (9), 9636-9648. DOI: 10.1021/nn504109a.
(10) Oliva-Chatelain, B. L.; Ticich, T. M.; Barron, A. R. Doping silicon nanocrystals and quantum dots. *Nanoscale* **2016**, *8* (4), 1733-1745. DOI: 10.1039/c5nr04978d. Makkar, M.; Viswanatha, R. Frontier challenges in doping quantum dots: synthesis and characterization. *RSC Advances* **2018**, *8* (39), 22103-22112. DOI: 10.1039/c8ra03530j.
(11) Peng, X.; Ai, F.; Yan, L.; Ha, E.; Hu, X.; He, S.; Hu, J. Synthesis strategies and biomedical applications for doped inorganic semiconductor nanocrystals. *Cell Reports Physical Science* **2021**, *2* (5), 100436. DOI: https://doi.org/10.1016/j.xcrp.2021.100436.
(12) Van De Walle, C. G.; Laks, D. B.; Neumark, G. F.; Pantelides, S. T. First-principles calculations of solubilities and doping limits: Li, Na, and N in ZnSe. *Physical Review B* **1993**, *47* (15), 9425-9434. DOI: 10.1103/physrevb.47.9425.
(13) Mikulec, F. V.; Kuno, M.; Bennati, M.; Hall, D. A.; Griffin, R. G.; Bawendi, M. G. Organometallic Synthesis and Spectroscopic Characterization of Manganese-Doped CdSe Nanocrystals. *Journal of the American Chemical Society* **2000**, *122* (11), 2532-2540. DOI: 10.1021/ja991249n.
(14) Erwin, S. C.; Zu, L.; Haftel, M. I.; Efros, A. L.; Kennedy, T. A.; Norris, D. J. Doping semiconductor nanocrystals. *Nature* **2005**, *436* (7047), 91-94. DOI: 10.1038/nature03832.
(15) Hardman, R. A toxicologic review of quantum dots: toxicity depends on physicochemical and environmental factors. *Environ Health Perspect* **2006**, *114* (2), 165-172. DOI: 10.1289/ehp.8284 PubMed.
(16) Reiss, P.; Carrière, M.; Lincheneau, C.; Vaure, L.; Tamang, S. Synthesis of Semiconductor Nanocrystals, Focusing on Nontoxic and Earth-Abundant Materials. *Chemical Reviews* **2016**, *116* (18), 10731-10819. DOI: 10.1021/acs.chemrev.6b00116.
(17) Kuhlmann, A. M. The Second Most Abundant Element in the Earth's Crust. *JOM* **1963**, *15* (7), 502-505. DOI: 10.1007/bf03378936.
(18) Erogbogbo, F.; Yong, K.-T.; Roy, I.; Xu, G.; Prasad, P. N.; Swihart, M. T. Biocompatible Luminescent Silicon Quantum Dots for Imaging of Cancer Cells. *ACS Nano* **2008**, *2* (5), 873-878. DOI: 10.1021/nn700319z. Bhattacharjee, S.; Rietjens, I. M. C. M.; Singh, M. P.; Atkins, T. M.; Purkait, T. K.; Xu, Z.; Regli, S.; Shukaliak, A.; Clark, R. J.; Mitchell, B. S.; et al. Cytotoxicity of surface-functionalized silicon and germanium nanoparticles: the dominant role of surface charges. *Nanoscale* **2013**, *5* (11), 4870. DOI: 10.1039/c3nr34266b.
(19) Hessel, C. M.; Reid, D.; Panthani, M. G.; Rasch, M. R.; Goodfellow, B. W.; Wei, J.; Fujii, H.; Akhavan, V.; Korgel, B. A. Synthesis of ligand-stabilized silicon nanocrystals with size-dependent photoluminescence spanning visible to near-infrared wavelengths. *Chemistry of Materials* **2012**, *24* (2), 393-401. DOI: 10.1021/cm2032866.

(20) Mastronardi, M. L.; Maier-Flaig, F.; Faulkner, D.; Henderson, E. J.; Kübel, C.; Lemmer, U.; Ozin, G. A. Size-Dependent Absolute Quantum Yields for Size-Separated Colloidally-Stable Silicon Nanocrystals. *Nano Letters* **2011**, *12* (1), 337-342. DOI: 10.1021/nl2036194.
(21) Clark, R. J.; Aghajamali, M.; Gonzalez, C. M.; Hadidi, L.; Islam, M. A.; Javadi, M.; Mobarok, M. H.; Purkait, T. K.; Robidillo, C. J. T.; Sinelnikov, R.; et al. From hydrogen silsesquioxane to functionalized silicon nanocrystals. *Chemistry of Materials* **2017**, *29* (1), 80-89. DOI: 10.1021/acs.chemmater.6b02667.
(22) Hessel, C. M.; Reid, D.; Panthani, M. G.; Rasch, M. R.; Goodfellow, B. W.; Wei, J.; Fujii, H.; Akhavan, V.; Korgel, B. A. Synthesis of Ligand-Stabilized Silicon Nanocrystals with Size-Dependent Photoluminescence Spanning Visible to Near-Infrared Wavelengths. *Chemistry of Materials* **2011**, *24* (2), 393-401. DOI: 10.1021/cm2032866. Canham, L. Introductory lecture: origins and applications of efficient visible photoluminescence from silicon-based nanostructures. *Faraday Discussions* **2020**, *222*, 10-81. DOI: 10.1039/d0fd00018c. Mangolini, L.; Thimsen, E.; Kortshagen, U. High-Yield Plasma Synthesis of Luminescent Silicon Nanocrystals. *Nano Letters* **2005**, *5* (4), 655-659. DOI: 10.1021/nl050066y.
(23) Kramer, N. J.; Schramke, K. S.; Kortshagen, U. R. Plasmonic Properties of Silicon Nanocrystals Doped with Boron and Phosphorus. *Nano Letters* **2015**, *15* (8), 5597-5603. DOI: 10.1021/acs.nanolett.5b02287.
(24) Ni, Z.; Pi, X.; Zhou, S.; Nozaki, T.; Grandidier, B.; Yang, D. Size-Dependent Structures and Optical Absorption of Boron-Hyperdoped Silicon Nanocrystals. *Advanced Optical Materials* **2016**, *4* (5), 700-707. DOI: 10.1002/adom.201500706.
(25) Chen, J.; Rohani, P.; Karakalos, S. G.; Lance, M. J.; Toops, T. J.; Swihart, M. T.; Kyriakidou, E. A. Boron-hyperdoped silicon for the selective oxidative dehydrogenation of propane to propylene. *Chemical Communications* **2020**, *56* (68), 9882-9885. DOI: 10.1039/d0cc02822c. Sugimoto, H.; Fujii, M.; Imakita, K. Synthesis of boron and phosphorus codoped all-inorganic colloidal silicon nanocrystals from hydrogen silsesquioxane. *Nanoscale* **2014**, *6* (21), 12354-12359. DOI: 10.1039/c4nr03857f.
(26) Zhou, S.; Pi, X.; Ni, Z.; Ding, Y.; Jiang, Y.; Jin, C.; Delerue, C.; Yang, D.; Nozaki, T. Comparative Study on the Localized Surface Plasmon Resonance of Boron- and Phosphorus-Doped Silicon Nanocrystals. *ACS Nano* **2015**, *9* (1), 378-386. DOI: 10.1021/nn505416r.
(27) Zhou, S.; Ni, Z.; Ding, Y.; Sugaya, M.; Pi, X.; Nozaki, T. Ligand-Free, Colloidal, and Plasmonic Silicon Nanocrystals Heavily Doped with Boron. *ACS Photonics* **2016**, *3* (3), 415-422. DOI: 10.1021/acsphotonics.5b00568.
(28) Gutsch, S.; Laube, J.; Hiller, D.; Bock, W.; Wahl, M.; Kopnarski, M.; Gnaser, H.; Puthen-Veettil, B.; Zacharias, M. Electronic properties of phosphorus doped silicon nanocrystals embedded in SiO2. *Applied Physics Letters* **2015**, *106* (11), 113103. DOI: 10.1063/1.4915307.
(29) Lechner, R.; Stegner, A. R.; Pereira, R. N.; Dietmueller, R.; Brandt, M. S.; Ebbers, A.; Trocha, M.; Wiggers, H.; Stutzmann, M. Electronic properties of doped silicon nanocrystal films. *Journal of Applied Physics* **2008**, *104* (5), 053701. DOI: 10.1063/1.2973399. Stegner, A. R.; Pereira, R. N.; Klein, K.; Lechner, R.; Dietmueller, R.; Brandt, M. S.; Stutzmann, M.; Wiggers, H. Electronic Transport in Phosphorus-Doped Silicon Nanocrystal Networks. *Physical Review Letters* **2008**, *100* (2). DOI: 10.1103/physrevlett.100.026803. Gnaser, H.; Gutsch, S.; Wahl, M.; Schiller, R.; Kopnarski, M.; Hiller, D.; Zacharias, M. Phosphorus doping of Si nanocrystals embedded in silicon oxynitride determined by atom probe tomography. *Journal of Applied Physics* **2014**, *115* (3), 034304. DOI: 10.1063/1.4862174. Samia, A. C. S.; Lou, Y.; Burda, C.; Senter, R. A.; Coffer, J. L. Effect of the erbium dopant architecture on the

femtosecond relaxation dynamics of silicon nanocrystals. *The Journal of Chemical Physics* **2004**, *120* (18), 8716-8723. DOI: 10.1063/1.1695318. Borowik, Ł.; Nguyen-Tran, T.; Roca i Cabarrocas, P.; Mélin, T. Doped semiconductor nanocrystal junctions. *Journal of Applied Physics* **2013**, *114* (20), 204305. DOI: 10.1063/1.4834516.
(30) Meseth, M.; Lamine, K.; Dehnen, M.; Kayser, S.; Brock, W.; Behrenberg, D.; Orthner, H.; Elsukova, A.; Hartmann, N.; Wiggers, H.; et al. Laser-doping of crystalline silicon substrates using doped silicon nanoparticles. *Thin Solid Films* **2013**, *548*, 437-442. DOI: 10.1016/j.tsf.2013.09.056. Lechner, R.; Wiggers, H.; Ebbers, A.; Steiger, J.; Brandt, M. S.; Stutzmann, M. Thermoelectric effect in laser annealed printed nanocrystalline silicon layers. *physica status solidi (RRL) – Rapid Research Letters* **2007**, *1* (6), 262-264. DOI: 10.1002/pssr.200701198.
(31) Rohani, P.; Banerjee, S.; Sharifi-Asl, S.; Malekzadeh, M.; Shahbazian-Yassar, R.; Billinge, S. J. L.; Swihart, M. T. Synthesis and Properties of Plasmonic Boron-Hyperdoped Silicon Nanoparticles. *Advanced Functional Materials* **2019**, *29* (8), 1807788. DOI: 10.1002/adfm.201807788.
(32) Hao, X. J.; Cho, E. C.; Scardera, G.; Shen, Y. S.; Bellet-Amalric, E.; Bellet, D.; Conibeer, G.; Green, M. A. Phosphorus-doped silicon quantum dots for all-silicon quantum dot tandem solar cells. *Solar Energy Materials and Solar Cells* **2009**, *93* (9), 1524-1530. DOI: 10.1016/j.solmat.2009.04.002. Huang, S.; So, Y. H.; Conibeer, G.; Green, M. Doping of Silicon Quantum Dots Embedded in Nitride Matrix for All-Silicon Tandem Cells. *Japanese Journal of Applied Physics* **2012**, *51*, 10NE10. DOI: 10.1143/jjap.51.10ne10. Cho, E.-C.; Green, M. A.; Conibeer, G.; Song, D.; Cho, Y.-H.; Scardera, G.; Huang, S.; Park, S.; Hao, X. J.; Huang, Y.; et al. Silicon Quantum Dots in a Dielectric Matrix for All-Silicon Tandem Solar Cells. *Advances in OptoElectronics* **2007**, *2007*, 1-11. DOI: 10.1155/2007/69578. Lim, K. H.; Sun, Y.; Lim, W. C.; Soh, S. Charging Organic Liquids by Static Charge. *Journal of the American Chemical Society* **2020**, *142* (50), 21004-21016. DOI: 10.1021/jacs.0c06000. Sugimoto, H.; Fujii, M.; Imakita, K.; Hayashi, S.; Akamatsu, K. All-Inorganic Near-Infrared Luminescent Colloidal Silicon Nanocrystals: High Dispersibility in Polar Liquid by Phosphorus and Boron Codoping. *The Journal of Physical Chemistry C* **2012**, *116* (33), 17969-17974. DOI: 10.1021/jp305832x. Sato, K.; Fukata, N.; Hirakuri, K. Doping and characterization of boron atoms in nanocrystalline silicon particles. *Applied Physics Letters* **2009**, *94* (16), 161902. DOI: 10.1063/1.3120768. Xie, M.; Li, D.; Chen, L.; Wang, F.; Zhu, X.; Yang, D. The location and doping effect of boron in Si nanocrystals embedded silicon oxide film. *Applied Physics Letters* **2013**, *102* (12), 123108. DOI: 10.1063/1.4798834.
(33) Norris, D. J.; Efros, A. L.; Erwin, S. C. Doped Nanocrystals. *Science* **2008**, *319* (5871), 1776-1779. DOI: 10.1126/science.1143802.
(34) Chan, T.-L.; Zhang, S. B.; Chelikowsky, J. R. An effective one-particle theory for formation energies in doping Si nanostructures. *Applied Physics Letters* **2011**, *98* (13), 133116. DOI: 10.1063/1.3571552. Hiller, D.; López-Vidrier, J.; Gutsch, S.; Zacharias, M.; Wahl, M.; Bock, W.; Brodyanski, A.; Kopnarski, M.; Nomoto, K.; Valenta, J.; et al. Boron-Incorporating Silicon Nanocrystals Embedded in SiO2: Absence of Free Carriers vs. B-Induced Defects. *Scientific Reports* **2017**, *7* (1). DOI: 10.1038/s41598-017-08814-0. Dalpian, G. M.; Chelikowsky, J. R. Self-Purification in Semiconductor Nanocrystals. *Physical Review Letters* **2006**, *96* (22), 226802. DOI: 10.1103/PhysRevLett.96.226802.

(35) Vlaskin, V. A.; Barrows, C. J.; Erickson, C. S.; Gamelin, D. R. Nanocrystal Diffusion Doping. *Journal of the American Chemical Society* **2013**, *135* (38), 14380-14389. DOI: 10.1021/ja4072207.
(36) Garrone, E.; Geobaldo, F.; Rivolo, P.; Amato, G.; Boarino, L.; Chiesa, M.; Giamello, E.; Gobetto, R.; Ugliengo, P.; Viale, A. A Nanostructured Porous Silicon Near Insulator Becomes Either a p- or an n-Type Semiconductor upon Gas Adsorption. *Advanced Materials* **2005**, *17* (5), 528-531. DOI: 10.1002/adma.200401200. Ashby, S. P.; Chao, Y. Use of Electrochemical Etching to Produce Doped Phenylacetylene Functionalized Particles and Their Thermal Stability. *Journal of Electronic Materials* **2013**, *43* (6), 2006-2010. DOI: 10.1007/s11664-013-2935-y.
(37) Jones, K. S.; Prussin, S.; Weber, E. R. A systematic analysis of defects in ion-implanted silicon. *Applied Physics A Solids and Surfaces* **1988**, *45* (1), 1-34. DOI: 10.1007/bf00618760. Stolk, P. A.; Gossmann, H. J.; Eaglesham, D. J.; Jacobson, D. C.; Rafferty, C. S.; Gilmer, G. H.; Jaraíz, M.; Poate, J. M.; Luftman, H. S.; Haynes, T. E. Physical mechanisms of transient enhanced dopant diffusion in ion-implanted silicon. *Journal of Applied Physics* **1997**, *81* (9), 6031-6050. DOI: 10.1063/1.364452. Tchebotareva, A. L.; de Dood, M. J. A.; Biteen, J. S.; Atwater, H. A.; Polman, A. Quenching of Si nanocrystal photoluminescence by doping with gold or phosphorous. *Journal of Luminescence* **2005**, *114* (2), 137-144. DOI: 10.1016/j.jlumin.2004.12.014. Ruffino, F.; Romano, L.; Carria, E.; Miritello, M.; Grimaldi, M. G.; Privitera, V.; Marabelli, F. A Combined Ion Implantation/Nanosecond Laser Irradiation Approach towards Si Nanostructures Doping. *Journal of Nanotechnology* **2012**, *2012*, 635705. DOI: 10.1155/2012/635705.
(38) Byon, K.; Tham, D.; Fischer, J. E.; Johnson, A. T. Synthesis and postgrowth doping of silicon nanowires. *Applied Physics Letters* **2005**, *87* (19), 193104. DOI: 10.1063/1.2128070.
(39) Carroll, G. M.; Limpens, R.; Neale, N. R. Tuning Confinement in Colloidal Silicon Nanocrystals with Saturated Surface Ligands. *Nano Letters* **2018**, *18* (5), 3118-3124. DOI: 10.1021/acs.nanolett.8b00680.
(40) Robin, A.; Livache, C.; Ithurria, S.; Lacaze, E.; Dubertret, B.; Lhuillier, E. Surface Control of Doping in Self-Doped Nanocrystals. *ACS Applied Materials & Interfaces* **2016**, *8* (40), 27122-27128. DOI: 10.1021/acsami.6b09530.
(41) Lambrecht, W. Dopants and Defects in Semiconductors. *Materials Today* **2012**, *15* (7-8), 349. DOI: 10.1016/s1369-7021(12)70146-3.
(42) Wang, F. F. Y. *Impurity Doping Processes in Silicon*; Elsevier Science, 2012.
(43) Chen, R.; Bent, S. F. Highly Stable Monolayer Resists for Atomic Layer Deposition on Germanium and Silicon. *Chemistry of Materials* **2006**, *18* (16), 3733-3741. DOI: 10.1021/cm0607785.
(44) Thiessen, A. N.; Ha, M.; Hooper, R. W.; Yu, H.; Oliynyk, A. O.; Veinot, J. G. C.; Michaelis, V. K. Silicon Nanoparticles: Are They Crystalline from the Core to the Surface? *Chemistry of Materials* **2019**, *31* (3), 678-688. DOI: 10.1021/acs.chemmater.8b03074.
(45) Balcı, S.; Sezgi, N. A.; Eren, E. Boron Oxide Production Kinetics Using Boric Acid as Raw Material. *Industrial & Engineering Chemistry Research* **2012**, *51* (34), 11091-11096. DOI: 10.1021/ie300685x.
(46) Frésart, E. d.; Rhee, S. S.; Wang, K. L. Boron oxide interaction with silicon in silicon molecular beam epitaxy. *Applied Physics Letters* **1986**, *49* (14), 847-849. DOI: 10.1063/1.97513.
(47) Hessel, C. M.; Henderson, E. J.; Veinot, J. G. C. An Investigation of the Formation and Growth of Oxide-Embedded Silicon Nanocrystals in Hydrogen Silsesquioxane-Derived

Nanocomposites. *The Journal of Physical Chemistry C* **2007**, *111* (19), 6956-6961. DOI: 10.1021/jp070908c.
(48) Carlson, D. E.; Smith, R. W.; Magee, C. W.; Zanzucchi, P. J. The role of hydrogen in heavily doped amorphous silicon. *Philosophical Magazine B* **1982**, *45* (1), 51-68. DOI: 10.1080/13642818208246388. Shacham-Diamand, Y. Y.; Oldham, W. G. The effect of hydrogen on boron diffusion in SiO2. *Journal of Electronic Materials* **1986**, *15*, 229-233.
(49) Nogami, M.; Quang, V. X.; Ohki, S.; Deguchi, K.; Shimizu, T. Reduction Mechanisms of Cu2+-Doped Na2O–Al2O3–SiO2 Glasses during Heating in H2 Gas. *The Journal of Physical Chemistry B* **2018**, *122* (3), 1315-1322. DOI: 10.1021/acs.jpcb.7b10913. Cao, J.; Li, X.; Wang, L.; Zhang, Z.; Xu, S.; Peng, M. New strategy to enhance the broadband near-infrared emission of bismuth-doped laser glasses. *Journal of the American Ceramic Society* **2018**, *101* (6), 2297-2304. DOI: https://doi.org/10.1111/jace.15412. Nogami, M. Reduction Mechanism for Eu Ions in Al2O3-Containing Glasses by Heat Treatment in H2 Gas. *The Journal of Physical Chemistry B* **2015**, *119* (4), 1778-1784. DOI: 10.1021/jp511513n. Nogami, M.; Watanabe, K.; Ito, Y.; Ito, H.; Nakano, H. Hydrogen Gas Reaction with Eu3+-Doped Al2O3–SiO2 Glasses. *Journal of the American Ceramic Society* **2010**, *93* (6), 1663-1667. DOI: https://doi.org/10.1111/j.1551-2916.2010.03653.x.
(50) Dirkx, R. R.; Spear, K. E. Optimization of thermodynamic data for silicon borides. *Calphad* **1987**, *11* (2), 167-175. DOI: 10.1016/0364-5916(87)90011-3. Mostafa, A.; Medraj, M. Binary Phase Diagrams and Thermodynamic Properties of Silicon and Essential Doping Elements (Al, As, B, Bi, Ga, In, N, P, Sb and Tl). *Materials* **2017**, *10* (6), 676. DOI: 10.3390/ma10060676.
(51) Milliken, S.; Cui, K.; Klein, B. A.; Cheong, I. T.; Yu, H.; Michaelis, V. K.; Veinot, J. G. C. Tailoring B-doped silicon nanocrystal surface chemistry via phosphorus pentachloride – mediated surface alkoxylation. *Nanoscale* **2021**, *13* (43), 18281-18292, 10.1039/D1NR05255A. DOI: 10.1039/D1NR05255A.
(52) Belot, V.; Corriu, R.; Leclercq, D.; Mutin, P. H.; Vioux, A. Thermal reactivity of hydrogenosilsesquioxane gels. *Chemistry of Materials* **1991**, *3* (1), 127-131. DOI: 10.1021/cm00013a029.
(53) Wheeler, L. M.; Kramer, N. J.; Kortshagen, U. R. Thermodynamic Driving Force in the Spontaneous Formation of Inorganic Nanoparticle Solutions. *Nano Letters* **2018**, *18* (3), 1888-1895. DOI: 10.1021/acs.nanolett.7b05187.
(54) Yamauchi, J.; Yoshimoto, Y.; Suwa, Y. X-ray photoelectron spectroscopy analysis of boron defects in silicon crystal: A first-principles study. *Journal of Applied Physics* **2016**, *119* (17), 175704. DOI: 10.1063/1.4948572.
(55) Kazahaya, T.; Hirose, M. Coordination Number of Doped Boron Atoms in Photochemically-Deposited Amorphous Silicon Studied by X-Ray Photoelectron Spectroscopy. *Japanese Journal of Applied Physics* **1986**, *25* (Part 2, No. 1), L75-L77. DOI: 10.1143/jjap.25.l75. Li, L. H.; Xing, T.; Chen, Y.; Jones, R. Boron Nitride Nanosheets for Metal Protection. *Advanced Materials Interfaces* **2014**, *1* (8), 1300132. DOI: 10.1002/admi.201300132.
(56) Zhou, S.; Pi, X.; Ni, Z.; Luan, Q.; Jiang, Y.; Jin, C.; Nozaki, T.; Yang, D. Boron- and Phosphorus-Hyperdoped Silicon Nanocrystals. *Particle & Particle Systems Characterization* **2014**, *32* (2), 213-221. DOI: 10.1002/ppsc.201400103.
(57) Mirabella, S.; De Salvador, D.; Bruno, E.; Napolitani, E.; Pecora, E. F.; Boninelli, S.; Priolo, F. Mechanism of Boron Diffusion in Amorphous Silicon. *Physical Review Letters* **2008**, *100* (15). DOI: 10.1103/physrevlett.100.155901.

(58) Mirabella, S.; De Salvador, D.; Napolitani, E.; Bruno, E.; Priolo, F. Mechanisms of boron diffusion in silicon and germanium. *Journal of Applied Physics* **2013**, *113* (3), 031101. DOI: 10.1063/1.4763353.
(59) Sadigh, B.; Lenosky, T. J.; Caturla, M.-J.; Quong, A. A.; Benedict, L. X.; Diaz De La Rubia, T.; Giles, M. M.; Foad, M.; Spataru, C. D.; Louie, S. G. Large enhancement of boron solubility in silicon due to biaxial stress. *Applied Physics Letters* **2002**, *80* (25), 4738-4740. DOI: 10.1063/1.1484557.
(60) Yang, Z.; De Los Reyes, G. B.; Titova, L. V.; Sychugov, I.; Dasog, M.; Linnros, J.; Hegmann, F. A.; Veinot, J. G. C. Evolution of the Ultrafast Photoluminescence of Colloidal Silicon Nanocrystals with Changing Surface Chemistry. *ACS Photonics* **2015**, *2* (5), 595-605. DOI: 10.1021/acsphotonics.5b00143. Kelly, J. A.; Veinot, J. G. C. An Investigation into Near-UV Hydrosilylation of Freestanding Silicon Nanocrystals. *ACS Nano* **2010**, *4* (8), 4645-4656. DOI: 10.1021/nn101022b. Boukherroub, R.; Morin, S.; Wayner, D. D. M.; Bensebaa, F.; Sproule, G. I.; Baribeau, J. M.; Lockwood, D. J. Ideal Passivation of Luminescent Porous Silicon by Thermal, Noncatalytic Reaction with Alkenes and Aldehydes†. *Chemistry of Materials* **2001**, *13* (6), 2002-2011. DOI: 10.1021/cm000790b. Jurbergs, D.; Rogojina, E.; Mangolini, L.; Kortshagen, U. Silicon nanocrystals with ensemble quantum yields exceeding 60%. *Appl. Phys. Lett.* **2006**, *88* (1), 233116. DOI: 10.1063/1.2210788. Islam, M. A.; Mobarok, M. H.; Sinelnikov, R.; Purkait, T. K.; Veinot, J. G. C. Phosphorus Pentachloride Initiated Functionalization of Silicon Nanocrystals. *Langmuir* **2017**, *33* (35), 8766-8773. DOI: 10.1021/acs.langmuir.7b00518. Rosso-Vasic, M.; Spruijt, E.; van Lagen, B.; De Cola, L.; Zuilhof, H. Alkyl-Functionalized Oxide-Free Silicon Nanoparticles: Synthesis and Optical Properties. *Small* **2008**, *4*, 1835-1841. DOI: 10.1002/smll.200800066. Li, Z. F.; Ruckenstein, E. Water-Soluble Poly(acrylic acid) Grafted Luminescent Silicon Nanoparticles and Their Use as Fluorescent Biological Staining Labels. *Nano Letters* **2004**, *4* (8), 1463-1467. DOI: 10.1021/nl0492436. Sato, S.; Swihart, M. T. Propionic-Acid-Terminated Silicon Nanoparticles: Synthesis and Optical Characterization. *Chemistry of Materials* **2006**, *18* (17), 4083-4088. DOI: 10.1021/cm060750t.
(61) Greenhagen, J. R.; Andaraarachchi, H. P.; Li, Z.; Kortshagen, U. R. Synthesis of PEG-grafted boron doped Si nanocrystals. *The Journal of chemical physics* **2019**, *151* (21), 211103-211103. DOI: 10.1063/1.5128608 PubMed.
(62) Fujii, M.; Sugimoto, H.; Imakita, K. All-inorganic colloidal silicon nanocrystals-surface modification by boron and phosphorus co-doping. *Nanotechnology* **2016**, *27* (26), 262001. DOI: 10.1088/0957-4484/27/26/262001 From NLM.
(63) Thiessen, A. N.; Zhang, L.; Oliynyk, A. O.; Yu, H.; O'Connor, K. M.; Meldrum, A.; Veinot, J. G. C. A Tale of Seemingly "Identical" Silicon Quantum Dot Families: Structural Insight into Silicon Quantum Dot Photoluminescence. *Chemistry of Materials* **2020**, *32* (16), 6838-6846. DOI: 10.1021/acs.chemmater.0c00650. Belyakov, V. A.; Burdov, V. A.; Lockwood, R.; Meldrum, A. Silicon Nanocrystals: Fundamental Theory and Implications for Stimulated Emission. *Advances in Optical Technologies* **2008**, *2008*, 279502. DOI: 10.1155/2008/279502.

Chapter 4:

Monolayer doping of silicon nanoparticles via a self-capping molecular phosphorus precursor

4.1 Introduction

Intentional doping of silicon nanoparticles (SiNPs) has gained substantial attention as a method to impart desirable properties such as electrical, optical, magnetic, and catalytic activity.[1,2] In fact, recent studies illustrate that SiNPs are excellent candidate materials for incorporation into photovoltaic devices[3] and phototransistors,[4] as well as for use in bioimaging,[5] and catalysis.[2,6] Further advancement of these applications is contingent upon the development of reliable methods that afford the predictable incorporation of dopants into these promising systems while providing precise control over dopant location.

To date, several doping approaches have been established for SiNPs. Non-thermal plasma and laser pyrolysis are popular methods for producing doped SiNPs that can provide extremely high (up to 60 atomic %) dopant concentrations. These concentrations are accessible because of the nonequilibrium conditions that characterize these approaches and kinetically trap dopants.[7] Dopant concentrations can be controlled by defining the amount of dopant precursor contained in the carrier gas, however, tuning the SiNP size and surface chemistry is difficult. The Fujii group developed a sputtering method to synthesize B and P co-doped SiNPs from Si-rich borophosphosilicate glass matrices.[8] They demonstrated SiNP size could be controlled by defining the annealing temperature and dopant concentration could be tuned by varying the glass matrix composition. Chapter 3 described a thermal diffusion-based post-synthesis doping method that allows for tuning of SiNP size through the use of a predefined silsesequioxane precursor and tailorable surface chemistry using the functionalization protocol outlined in Chapter 2. The concentration of the B-dopant depended upon the NP crystallinity and the annealing conditions.

Despite the associated advances and understanding realized during these studies, precise control over the location of the dopants within the NPs remains elusive.

Monolayer doping is used by the semiconductor industry to introduce impurities into ultra-shallow nanoscale dopant layers on silicon substrates.[9] This approach employs dopant-containing molecules that bind to the silicon surface to form a monolayer. A capping layer (typically SiO_2) is then deposited to prevent dopant-loss during the subsequent annealing step. The assembly is then annealed to decompose surface bonded molecule and drives the dopant into the silicon host. The SiO_2 capping layer is then removed and a thin dopant layer is achieved, thanks to the self-limiting nature of the molecular dopant monolayer which allows for a well-defined dopant dose.[10]

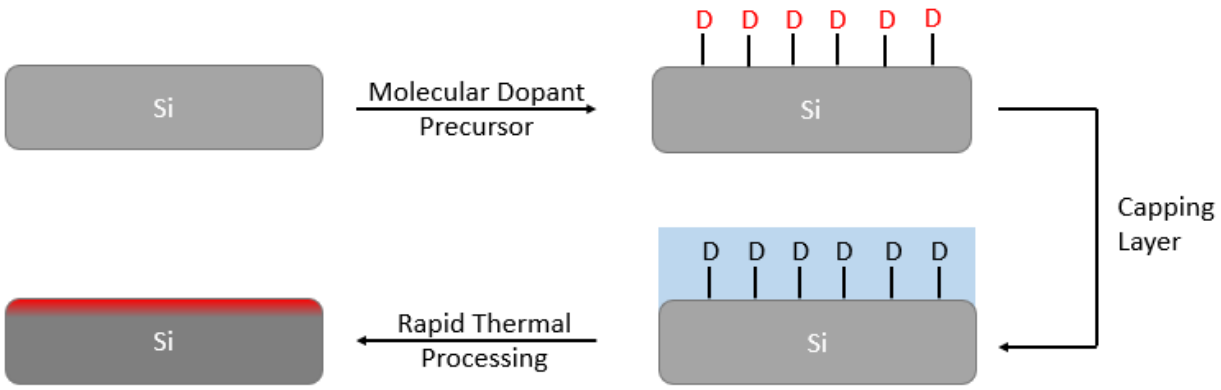

Figure 4. 1 Diagram depicting the application of monolayer doping in silicon wafers. A monolayer is first formed with the dopant containing molecule. The functionalized substrate is then rapidly heated to promote decomposition of the monolayer and thermal diffusion of the dopant into a shallow region of the wafer.

Self-capping dopant molecules have recently gained attention as an alternative to depositing thick SiO_2 capping layers in monolayer doping. Organoboron precursors have been

previously studied for monolayer doping of bulk silicon, however carbon contamination remained an outstanding issue.[11] A carbon-free self-capping molecule was achieved through the use of a phosphorus containing polyhedral oligomeric silsesquioxane (POSS) scaffold that formed a nanolayer of SiO_2 with thermal treatment.[12] The grafting of the POSS-P scaffold was demonstrated successfully on silica nanoparticles with a diameter of 20 nm, however, rapid thermal processing was only performed with Si wafers. As the POSS-P structure shows strong interactions with silicon surfaces it has the potential to be used as a molecular dopant for silicon nanoparticles. In this Chapter we explored grafting the POSS-P structure to the surface of preformed SiNPs and using thermal-processing to selectively dope the surface and/or subsurface of the particles.

4.2 Experimental Details

4.2.1 Reagents and Materials:

Hydrofluoric acid (48-50%) and sulfuric (reagent grade, 95–98%) acids were purchased from Fisher Scientific and Caledon Laboratory Chemicals, respectively. Fuming sulfuric acid (reagent grade, 20% free SO_3 bases), toluene (HPLC grade), trichlorosilane (99%), triethylamine (>99%), phosphorus trichloride (99%), and 1,3,5,7,9,11,14-Heptaisobutyltricyclo[7.3.3.15,11]heptasiloxane-endo-3,7,14-triol (isobutyltrisilanol-POSS; 97%) were purchased from Sigma-Aldrich. Toluene was purified using a Pure-Solv purification system and collected immediately prior to use. All reactions were performed under inert atmosphere conditions using standard Schlenk techniques in dry and oxygen free glassware.

4.2.2 Synthesis of Hydrogen Silsesquioxane (HSQ)

HSQ was synthesized according to well-established literature procedures.[13] Dry toluene (45.0 mL) was added dropwise to a solution of concentrated (15 mL) and fuming (7.2 mL) sulfuric acid. Next, a mixture of trichlorosilane (16 mL) in dry toluene (110 mL) was added dropwise to the solution. The resulting product in the organic phase was washed with sulfuric acid solution and isolated from the aqueous layer. Most of the solvent was removed via rotary evaporation and any remaining solvent was removed *in vacuo* resulting in a white crystalline solid.

4.2.3 Preparation of H-SiNPs

Precursor hydride terminated silicon nanocrystals (H-SiNPs) were synthesized using a previously established method involving the thermally induced disproportionation of HSQ.[13] Briefly, six grams of HSQ was thermally processed in a standard tube furnace at 1100, 1200, and 1300 °C for one hour with a ramp rate of 4 °C/min and 5% H_2:95% Ar flowing atmosphere. This procedure yielded oxide composites containing SiNPs of sizes ranging from 3 to 9 nm depending upon the processing temperature. The resulting solids were ground in pentane using an agate mortar and pestle and further processed using a wrist action shaker and high purity glass beads for 16 h to yield a fine powder.

The resulting powder was etched using a 1:1:1 solution of ethanol:deionized water:HF to liberate the H-SiNPs. A typical etching procedure employed 400 mg of composite and 9 mL of etching solution that was combined and stirred for 1 h after which the H-SiNPs were then extracted into toluene and washed three times using centrifugation and dry toluene. The isolated H-SiNPs were then resuspended in 5 mL of dry toluene until further use.

4.2.4 Synthesis of hepta-isobutyl-polyhedral oligomeric silsesquioxane phosphorus triester (POSS-P)

POSS-P was prepared using a modified literature procedure.[12] Isobutyltrisilanol-POSS (1.159 g, 1.46 mmol) was added to a purged Schlenk flask and dissolved in 20 mL dry toluene. Once dissolved, 0.730 mL of triethylamine was added to the solution and stirred for 10 minutes. In a purged additional funnel, 10 mL dry toluene was mixed with 0.145 mL of phosphorus trichloride (1.60 mmol) and added dropwise to the solution over 10 min. A white suspension immediately appeared upon addition. The reaction was left stirring for 2 h after which the solvent and volatiles were removed *in vacuo* to afford a white solid that was suspended in pentane and filtered over Celite. The resulting solution is then subjected to rotary evaporation to remove excess solvent and further dried under vacuum to yield a white crystalline solid. Yield: 31% (0.363 g). ^{1}H NMR ($C_6D_5CD_3$, 25 °C, ppm): δ_H= 2.05 (m, 1H, $CH_2CH(CH_3)_2$), 1.05 (m, 6H, $CH_2CH(CH_3)_2$), 0.89 (m, 2H, $CH_2CH(CH_3)_2$). ^{13}C NMR (ppm): δ_C= 26.0 (2C, $CH_2CH(CH_3)_2$), 24.2 (1C, $CH_2CH(CH_3)_2$), 23.0 (1C, $CH_2CH(CH_3)_2$). ^{31}P NMR (ppm): δ_P= -47.5 (1P, $PCl(OR)_2$), -19.0 (1P, $P(OR)_3O$)

4.2.5 Grafting of POSS-P to H-SiNPs

A toluene suspension (5 mL) of freshly etched SiNPs (40 mg) was added to an Ar purged Schlenk flask. Subsequently a toluene (5 mL) solution of POSS-P (0.3 g) was added with stirring. The reaction mixture was stirred for 2 hours under flowing Ar and excess solvent was removed *in vacuo*. The resulting brown gel was further dried under vacuum to yield a brown solid.

4.2.6 Thermal treatment of POSS-P grafted SiNPs

The SiNPs grafted POSS-P (0.340 g) was heated in a standard tube furnace to 500 °C at a ramp rate of 10 °C/min where it was held for 2 hours in a flowing Ar atmosphere. After cooling to room

temperature, the sample was heated in flowing Ar with a ramp rate of 20 °C/min to 1000 °C where it was maintained for 30 minutes to promote the thermal diffusion of P into the SiNPs.

4.2.7 Thermogravimetric analysis (TGA)

POSS-P SiNP composites before and after thermal treatment were prepared as solid residue and transferred to a platinum pan. The weight loss of the samples was monitored in the temperature range of 25 to 800 °C at a temperature increment of 10 °C/min under Ar atmosphere using Mettler Toledo TGA/DSC 1 star system.

4.2.8 Fourier-Transform Infrared Spectroscopy (FTIR)

FT-IR spectra were collected using a Thermo Nicolet Continum FT-IR microscope. Samples were prepared as a solid residue of POSS-P grafted SiNPs in a KBr pellet.

4.2.9 X-Ray Photoelectron Spectroscopy (XPS)

Samples were prepared by drop-casting toluene suspensions of SiNPs grafted with POSS-P before and after thermal treatment onto copper foil. XP spectra were measured using Kratos Axis 165 Ultra X-ray Photoelectron Spectrometer with a monochromatic Al Kα source operating at 210 W with an energy of 1486.6 eV. The high-resolution spectra were obtained using an analyzer pass energy of 20 eV and a step of 0.1 eV. For survey spectra, a pass energy of 160 eV and a step size of 0.3 eV was used. Spectra were calibrated to C 1s 284.8 eV using adventitious carbon. Peak fitting was performed using CasaXPS software and a Shirley-type background was subtracted to account for the intrinsic lass. Spin-orbit coupling in Si 2p was fixed to an area ratio of 2:1 and 0.6 eV energy spacing and in P 2p was fixed to an area ratio of 2:1 and 0.87 eV.

4.2.10 Electron Microscopy

Bright-field transmission electron microscopy (TEM) and High-resolution TEM (HR-TEM) were performed on a JEOL JEM-ARM200CF S/TEM (Cold Field Emission Gun) electron microscope with an accelerating voltage of 200 kV using SiQDs drop-coated from a toluene solution onto a holey carbon-coated copper grid. The SiNP size was determined by averaging the size of 300 particles using ImageJ software (Version 1.51j8) and plotted as an average shifted histogram. [51] HRTEM measurements were conducted using scanning TEM (STEM) (JEOL 2200FS, 200 kV) with a nominal beam size of 0.5 nm. Electron energy loss spectroscopy (EELS) analysis was also conducted using a 200 kV JEOL 2200FS scanning TEM with a nominal beam size of 0.5 nm. Digital Micrograph (Gatan, Inc.) was employed for signal collection and data extraction from EELS spectra. Typical current densities for HRTEM imaging were 13.15 pA cm^{-2} at 400 K and 16.72 pA cm^{-2} at 500 K.

4.3 Results and Discussion

4.3.1 Grafting of Dopant Scaffold onto SiNPs

P-containing polyhedral oligiomeric silsesquioxane (POSS-P) dopant scaffold was synthesized according to a modified literature procedure, in which phosphorus trichloride (PCl_3) was added dropwise to a solution of isobutyltrisilanol-POSS and triethylamine (Scheme 4.1).[12,14]

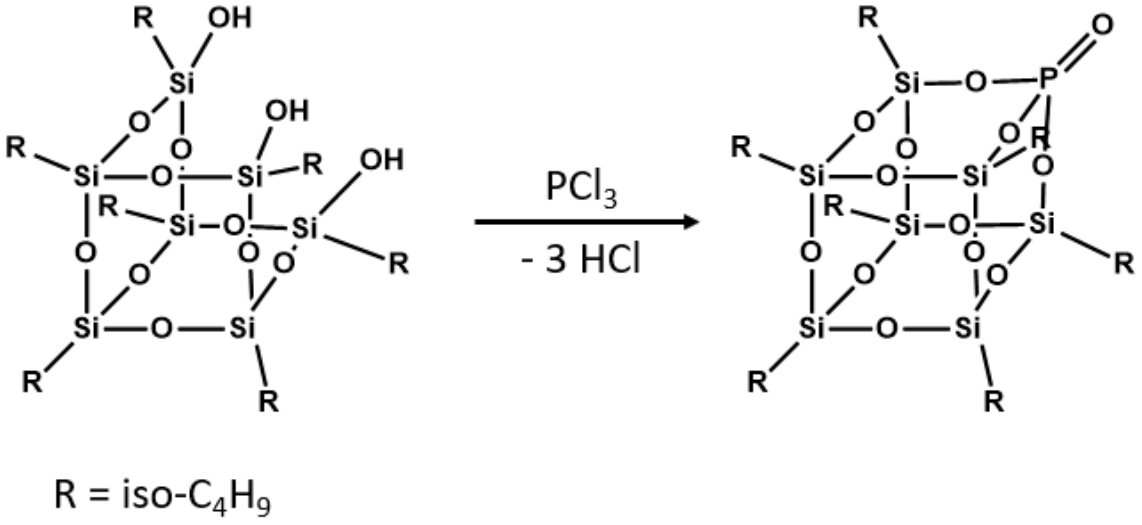

Scheme 4. 1 Synthesis of POSS-P from isobutyltrisilanol-POSS and PCl_3. Details of the reaction conditions are provided in Section 4.2.4 of the Experimental section.

Infrared (IR) spectroscopy was used to investigate the bonding within the resulting white solid (POSS-P) and compared with that of the starting material (Figure 4.2). The bands appearing in the 2870-2950 cm^{-1} and 1340-1460 cm^{-1} regions arise from the isobutyl groups pendant on the POSS structure.[15] Features confidently attributed to Si-O bonds within the POSS structure appear at ca. 1100 cm^{-1}.[16] Evidence of the consumption of the hydroxyl groups of the isobutyltrisilanol-POSS starting material is supported by a noted decrease in the intensity of the v(O-H) associated stretch

at 3400 cm^{-1}.[12] The appearance of bands at 2445 cm^{-1} and 995 cm^{-1} are consistent with the presence of v(P-H) and v(P-O), respectively and incorporation of P.[15] Additionally, intense feature at 1230 cm^{-1} matches closely with literature reports of v(P=O) arising from phosphonate containing species.[84] The presence of P-H and O-H have previously been attributed to POSS-P open cage structures that are side products of the presented the reaction (Scheme 4.1).[12,14]

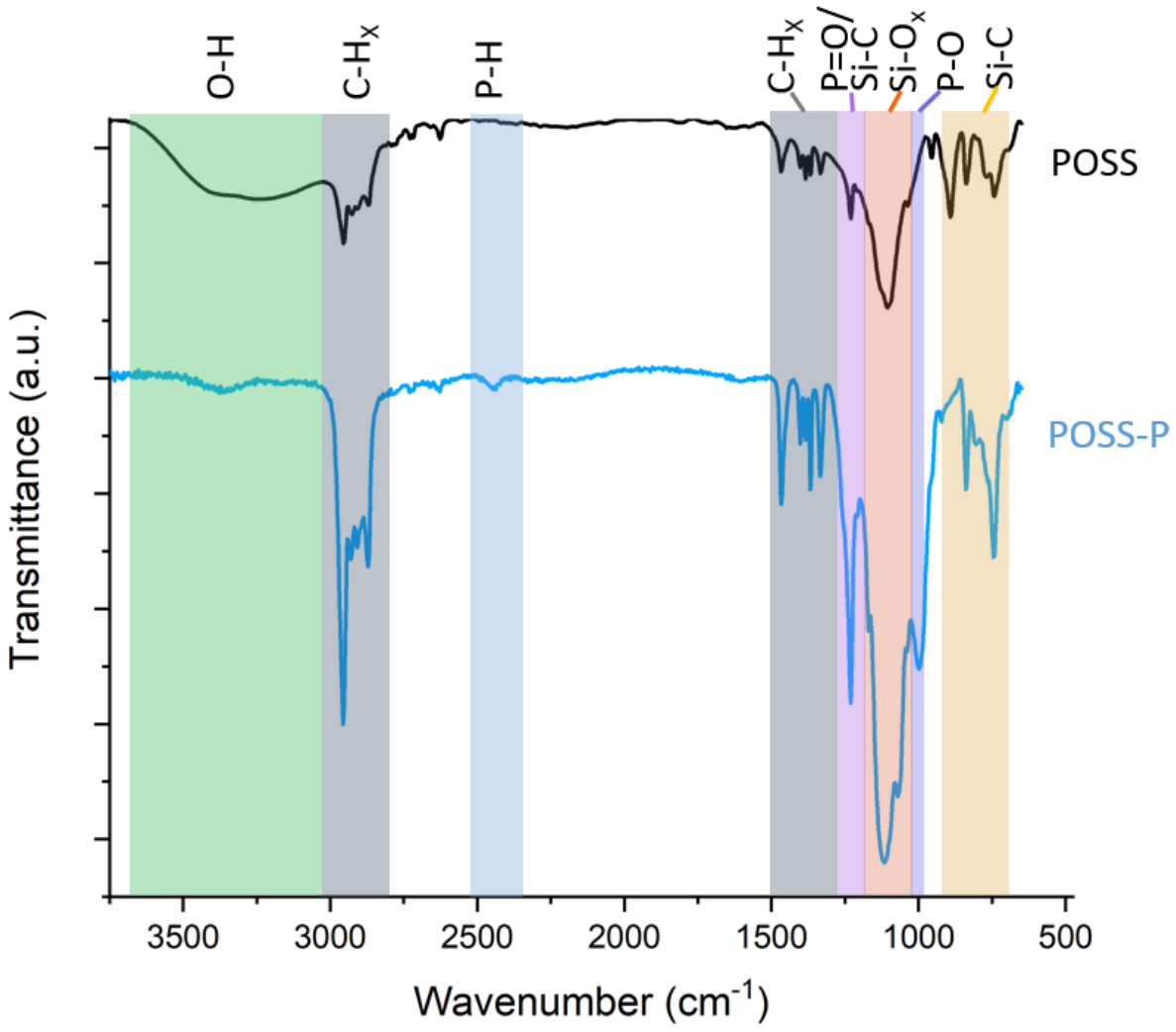

Figure 4. 2 IR spectra of as-synthesized P containing POSS (blue) and isobutyltrisilanol-POSS starting material (black).

The composition of the P containing POSS structures were further investigated using X-ray photoelectron spectroscopy (XPS). The high-resolution P 2p XP spectrum (Figure 4.3 a) reveals the presence of oxidized P species through an emission which can be deconvoluted into a spin-orbit couple (i.e., $2p_{1/2}$ and $2p_{3/2}$) corresponding to a species with P bonded to three or four O atoms (134 eV).[18] Evidence of this P species is also noted in the O 1s XP emission (532 eV).[18] The O 1s spectral region also shows features attributed to Si-O and Si-OH species at 532.5 and 533.7 eV, respectively (Figure 4.3 b).[19] The presence of Si(IV) species (103.2 eV) and Si(III) species (102.2 eV) in the Si 2p XP spectrum further supports the proposal that Si-O and Si-R bonded species are present (Figure 4.3 d).[20]

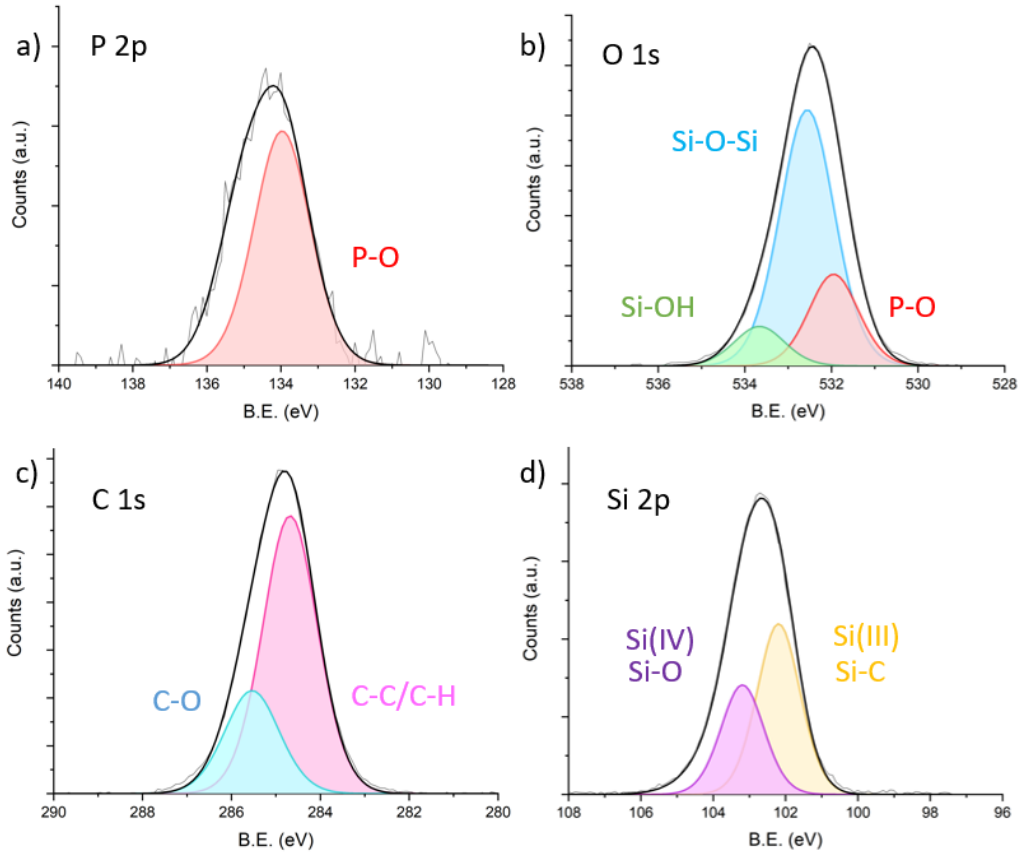

Figure 4. 3 High-resolution XPS of a) P 2p b) O 1s c) C 1s and d) Si 2p for as-synthesized POSS-P structures. The P 2p and Si 2p show only the $2p_{3/2}$ emission ($2p_{1/2}$ is omitted for clarity).

After establishing the presence of P in the POSS structures, the material could be utilized as a dopant scaffold for P-doping of SiNPs. The approach to NP doping described in this chapter loosely follows the well-established wafer-scale monolayer doping procedure.[12] We start with the predefined parent SiNPs described in Chapter 3 that are prepared using a protocol developed by our group that exploits thermally-induced disproportionation of HSQ.[13,21] Three different sizes of parent SiNPs were used in this study with diameters of 2.99 ± 0.54, 6.30 ± 1.2 and 8.60 ± 1.4 nm. For detailed characterization of the parent SiNPs please refer to Chapter 3. The freshly prepared POSS-P can then be grafted to the surface of the SiNPs according to Scheme 4.2.

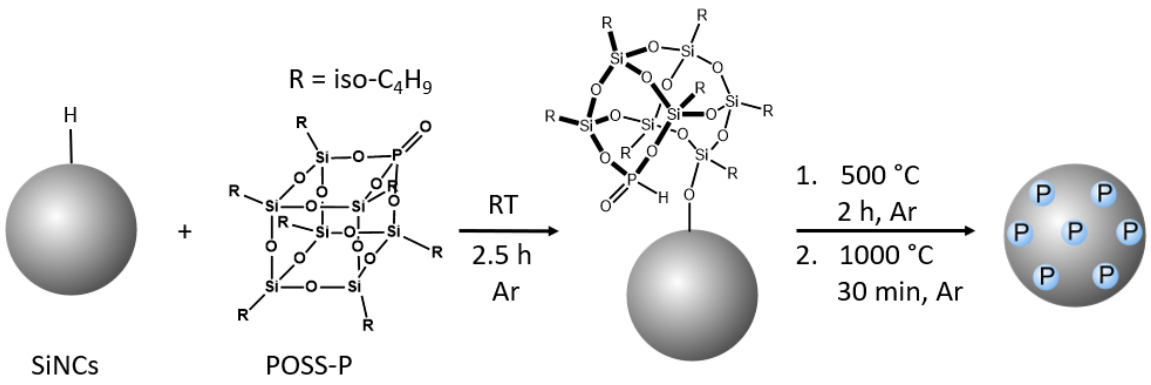

Scheme 4. 2 Monolayer-doping inspired method for preparing well-defined P-doped SiNPs. A P-containing POSS structure is grafted to the surface of parent SiNPs and subjected to two-step high temperature annealing to promote the thermal diffusion of P into the SiNPs.

We propose that the phosphate group of POSS-P reacts with the H-terminated SiNPs to yield a hydroxyl terminated surface, which has been previously observed by our group and is thermodynamically driven by the high bond energy of the Si-O bond (P=O: 575 kJ/mol and Si-O:

798 kJ/mol).[22] These surface silanol sites can then act as anchors for ligand attachment through a well-known nucleophilic reaction with the siloxy group with the proposed mechanism shown in Scheme 4.3. However, further studies would be required to confirm this mechanism.[12,23]

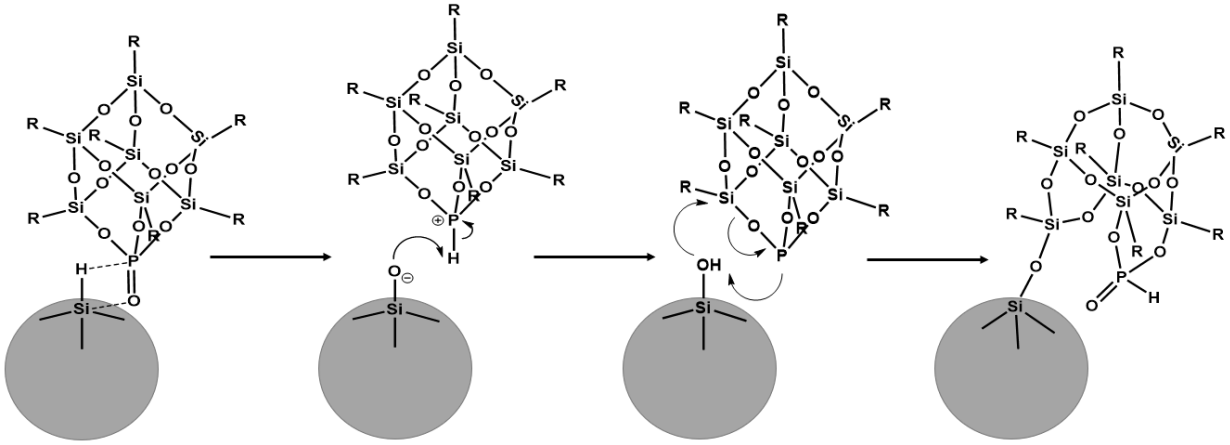

Scheme 4. 3 Proposed mechanism for the attachment of the POSS-P to the surface of H-terminated parent intrinsic SiNPs.

To verify the attachment of the POSS-P molecule to the surface of the SiNP we employed FTIR (Figure 4.4) and XPS (Figure 4.5) for the median size range of parent H-SiNPs (d = 6.30 ± 1.2 nm). Comparing the FTIR spectra of SiNPs before and after grafting with POSS-P we note that grafting results in a notable decrease in the intensity of Si-H_x associated features at 914 cm^{-1} and 2100 cm^{-1} (Figure 4.4). Additionally, the feature previously attributed to Si-O (1100 cm^{-1}), P-O (1230 cm^{-1}) and isobutyl (1340-1460 cm^{-1} and 2870-2950 cm^{-1}) species identified in the POSS-P IR spectrum emerge after grafting onto the SiNPs (Figure 4.4). The high-resolution P 2p (P-O: 134 eV), O 1s (P-O: 532 eV, Si-O: 532.5, Si-OH: 533.7 eV) and C 1s (C-C: 284.8 eV, C-O: 285.8) of the grafted SiNPs show the same spectral signatures noted for neat POSS-P consistent with the presence of POSS-P or a similar species (Figure 4.5 a-c). Looking to the Si 2p XP spectrum, the Si(III) and Si(IV) emissions noted in the POSS-P emission are also present in the spectrum of the

SiNP/ POSS-P system. In addition, we see the emergence of Si(II), Si(I), and Si(0) that are confidently attributed to the presence of SiNPs (Figure 4.5 d).[21] Everything combined, these observations are consistent with successful grafting of POSS-P to SiNPs.

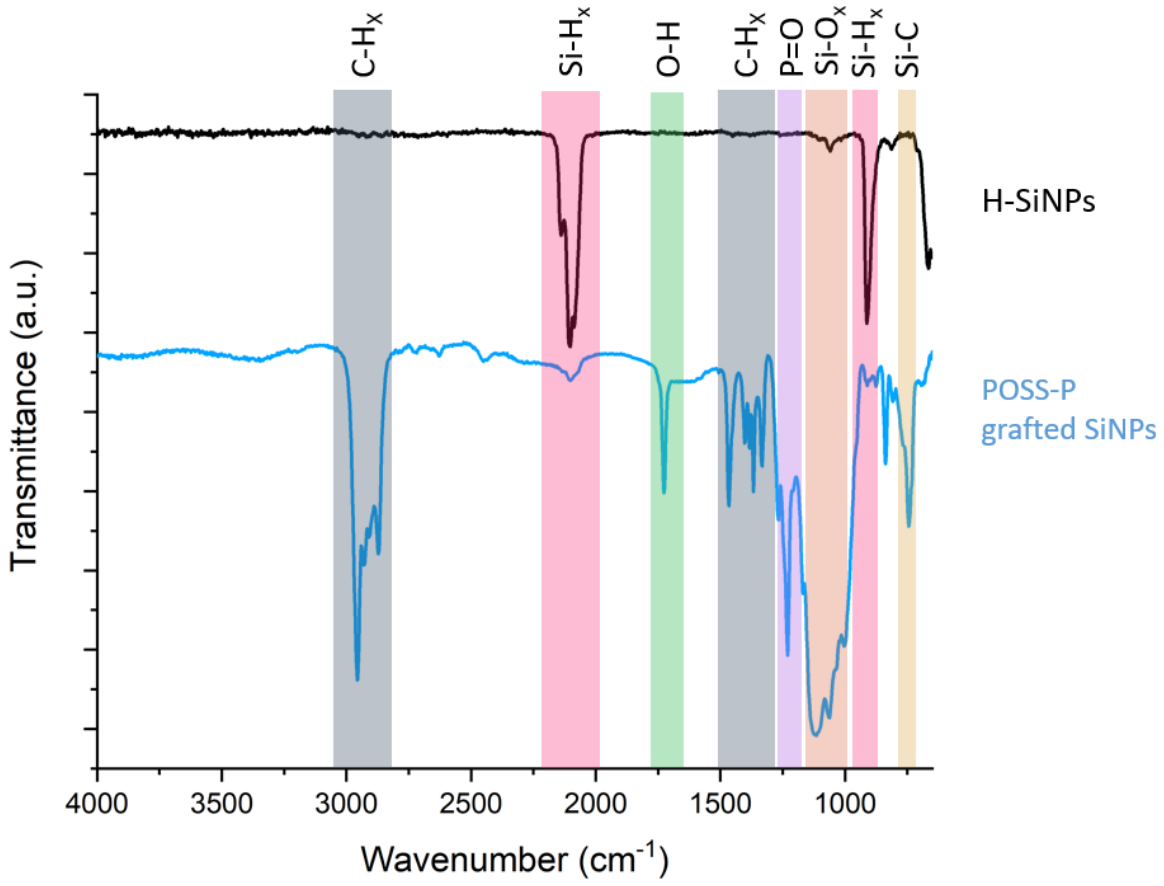

Figure 4. 4 FTIR of a) H-terminated parent SiNPs (d = 6.30 ± 1.2 nm; black) and POSS-P grafted SiNPs (blue).

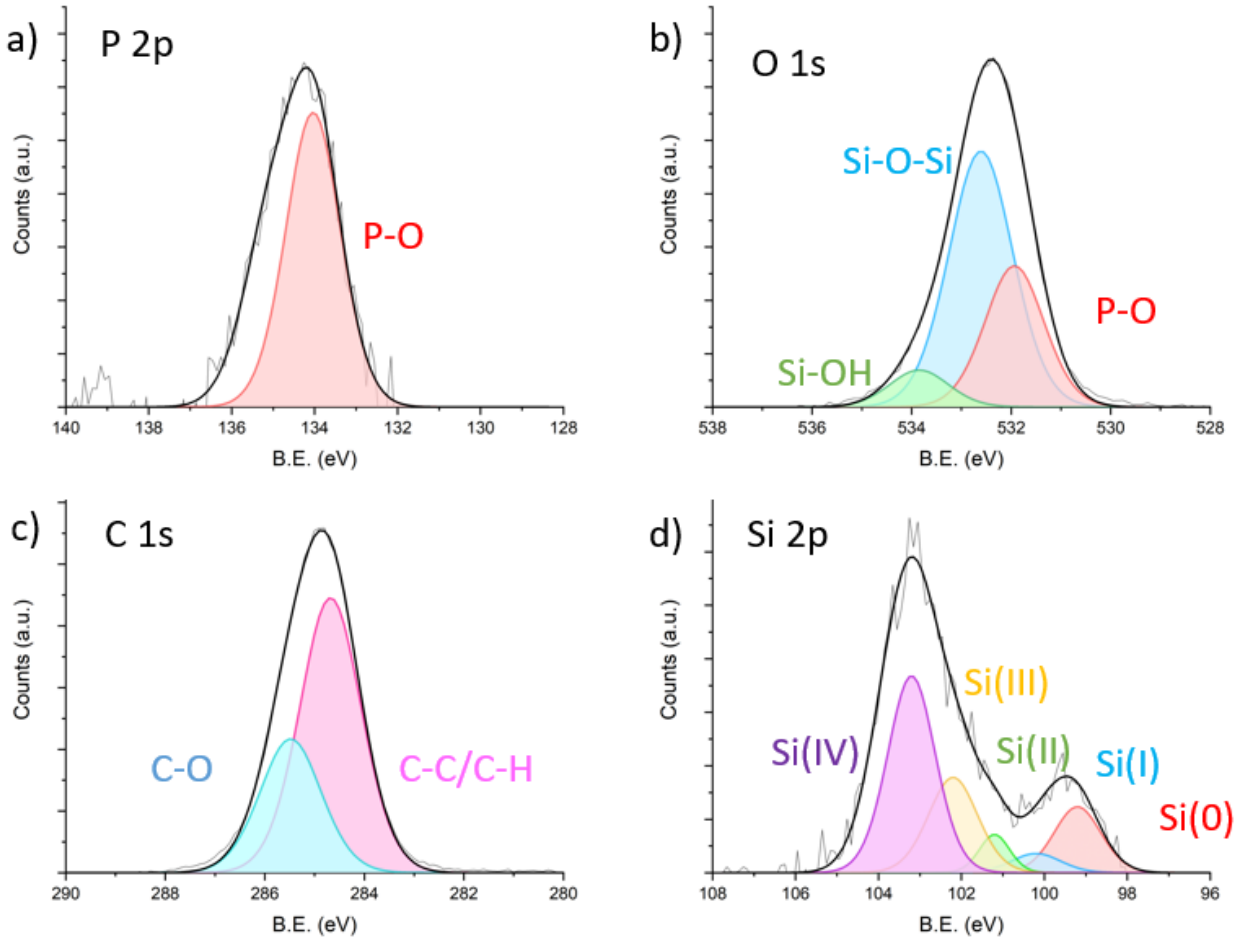

Figure 4. 5 High-resolution XPS a) P 2p b) O 1s c) C 1s and d) Si 2p spectra of POSS-P grafted SiNPs. The P 2p and Si 2p show only the $2p_{3/2}$ emission ($2p_{1/2}$ is omitted for clarity).

The surface coverage of the POSS-P on the SiNPs can be indirectly evaluated using the atomic percent P obtained from the XPS survey spectrum (Figure 4.6 a) and thermal gravimetric analysis (Figure 4.6 b). The elemental composition of the POSS-P grafted SiNPs can be evaluated using the XPS survey spectrum (Figure 4.6 a), in which emissions for O 1s, C 1s, Si 2p and P 2p are clearly visible. The atomic percent P was determined to be 1.82 % which would translate to the dopant molecules bonding to 31.7 % of the available NP surface Si sites (Table 4.1), details of

this calculation can be found in the Appendix. These findings can then be compared to another indirect method that uses thermogravimetric analysis (TGA) to determine the surface coverage of the POSS-P monolayers (Figure 4.6 b). The recorded experimental weight loss for the POSS-P grafted SiNPs was 5.124 %, we make the assumption that the weight-loss is attributed to the loss of the organic groups in the POSS-P molecule and calculate the theoretical weight-loss based for seven isobutyl groups per molecule. The surface coverage is calculated by dividing the experimental weight-loss by the calculated theoretical weight loss and yields a surface coverage of 16.67 % (Table 4.1), further details of the calculation can be found in the Appendix. The observed difference in surface coverage values can be attributed to the surface sensitivity of XPS, because of the limited escape depth of the photoelectrons the surface and subsurface species will have a more significant contribution to the resulting emission.[24] Since the monolayer doping method aims to concentrate the P atoms near the surface of the particle it would follow that the observed concentration of P would appear higher in a surface analysis technique compared to complimentary bulk analysis methods such as TGA.

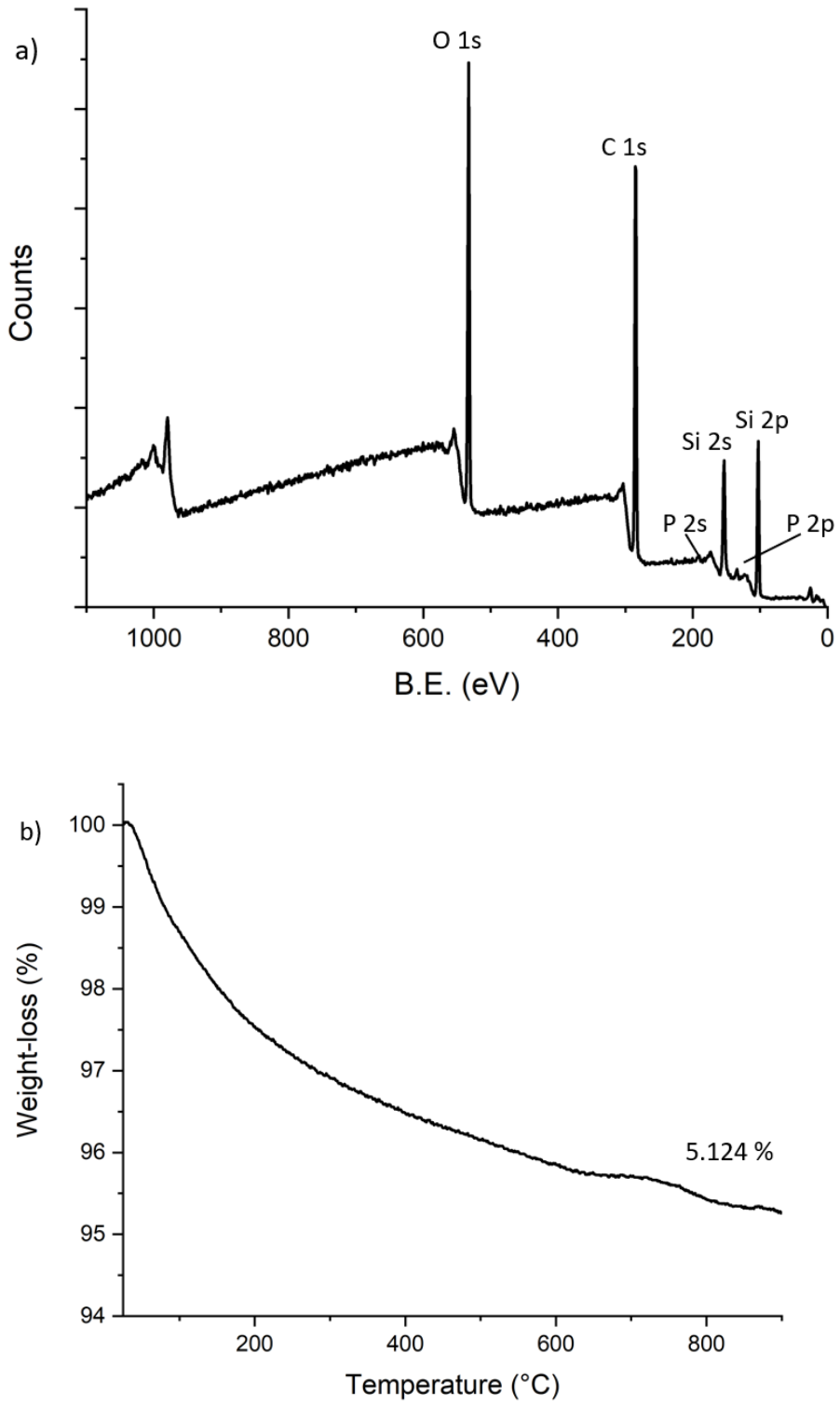

Figure 4. 6 a) XPS survey spectrum and b) TGA of SiNPs (d = 6.30 ± 1.2 nm) after grafting POSS-P to the particle surface.

Table 4. 1 Calculated surface coverage for POSS-P molecules on SiNPs (d = 6.30 ± 1.2 nm) using two different indirect methods: XPS and TGA.

Method	Theoretical Weight-loss (%)	Experimental Weight-loss (%)	Surface Coverage
XPS	-	-	31.7
TGA	27.57	5.12	16.67

4.3.2 Two-Step Thermal Treatment for P-doped SiNCs

Once the POSS-P is successfully grafted to the SiNPs, thermal treatment is needed to promote the diffusion of phosphorus into the NP. Because the dopant POSS-P possesses C-containing isobutyl functional groups, it is necessary to remove these groups to prevent C contamination and minimize the formation of trap states that could impact doping efficiency.[25] The formation of a silica capping-layer is also required to prevent evaporation of the dopant during the thermal treatment process.[26] Low temperature thermal annealing can serve a dual-purpose removing unwanted organic functionalities from the POSS cage structure and providing a thin protective capping oxide layer.[12]

The medium size range of SiNPs (d = 6.30 ± 1.2 nm) bearing grafted POSS-P were subjected to thermal annealing (500 °C, 2h) in Ar in a standard tube furnace. The resulting materials were then evaluated with FTIR and TGA to gain insight into the thermal decomposition (Figure 4.7). Evaluation of the IR spectrum after annealing clearly shows the C-H_x (1340-1460 cm^{-1} and 2870-2950 $cm^{-1)}$ and Si-C features (744 cm^{-1}) arising from the isobutyl groups are diminished compared to the freshly grafted POSS-P-SiNPs (Figure 4.7 a). We also note the P=O vibration evident in the grafted POSS-P-SiNPs at 1230 cm^{-1} is absent and the SiO_x band (1050 cm^{-}

^{1}) shows significant broadening suggesting there may be overlap with a P-O related species (1215 cm^{-1}).[17,27] From these analyses we propose the partial thermal decomposition of the dopant cage structure and the formation of P-containing SiO_x. TGA of the SiNPs after low-temperature thermal treatment shows no further mass loss, confirming that the majority of the organic groups have been removed (Figure 4.7 b).

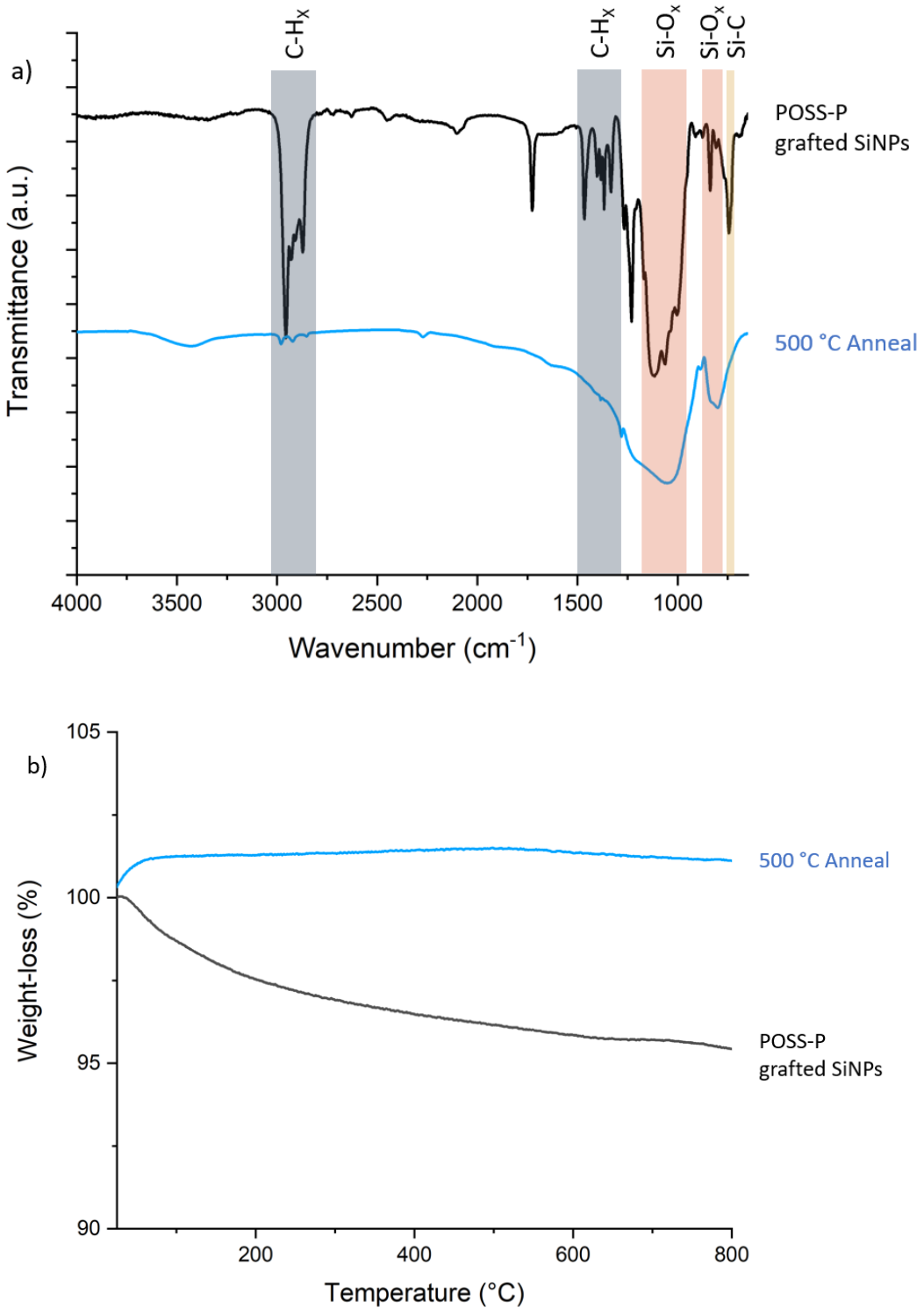

Figure 4. 7 a) FTIR and b) TGA of POSS-P grafted SiNPs (d = 6.30 ± 1.2 nm) before (black) and after (blue) annealing at 500 °C for 2 hours under flowing Ar.

With carbon contamination minimized and a protective capping layer established, the thermally promoted diffusion of P-atoms can proceed. To study the effect of temperature on the concentration of P dopants in the SiNPs two different temperatures were chosen for thermal treatment (i.e., 800 and 1000 °C for 30 min under Ar flow). For convenience the d = 6.30 ± 1.2 nm SiNPs grafted with POSS-P were used to evaluate doping. After being subjected to low-temperature heating to induce formation of the capping layer prior to annealing. The P dopant concentration for both annealing temperatures was evaluated via XPS for POSS-P grafted SiNPs after thermal treatment (Figure 4.8); ethanolic HF etching was used to remove the SiO_x capping layer after high-temperature annealing. No emission is detected in the P 2p XP spectrum for the materials obtained from 800 °C annealing (Figure 4.8 a), however, increasing the annealing temperature to 1000 °C results in an emission that is readily fit with two components corresponding to spin-orbit couple of a substitutional P dopant species (130.4 and 129.8 eV for $2p_{1/2}$ and $2p_{3/2,}$ respectively) bonded to four Si atoms (Figure 4.8 b).[28] These results differ from recent reports for monolayer-doped silicon wafers, where P dopants were observed for annealing temperatures of 800 °C.[79] This implies that more energy is needed to incorporate dopants in nanoscale silicon as compared to bulk, most likely due to a higher formation energy, which is consistent with previous observations in literature.[29]

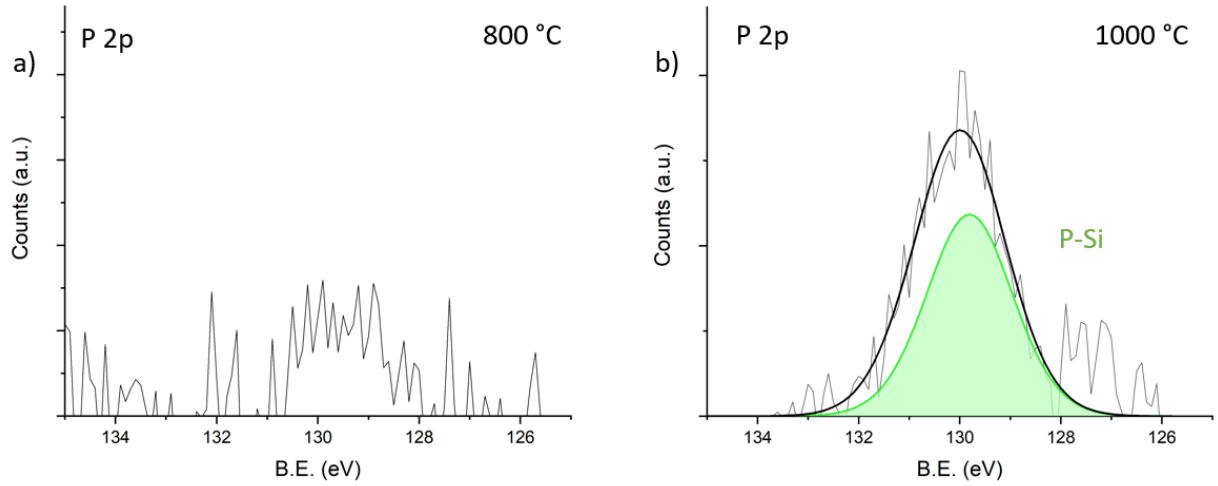

Figure 4. 8 High-resolution P 2p XP spectra of P dopant atoms in SiNPs for annealing temperatures of a) 800 °C and b) 1000 °C after low-temperature thermal pre-treatment. The P 2p XP spectra show only the $2p_{3/2}$ emission (2 $p_{1/2}$ is omitted for clarity).

We also studied the impact of NP size on P dopant concentration by grafting POSS-P to three sizes of parent SiNPs (2.99 ± 0.54, 6.30 ± 1.2 and 8.60 ± 1.4 nm) and subjecting them to a two-step thermal treatment (2 h at 500 °C under Ar and 30 min at 1000 °C under Ar) and removing the SiO_x capping layer with ethanolic HF etching. For all three sizes of SiNPs an emission that can be fit to substituted P-Si species (130.4 and 129.8 eV for $2p_{1/2}$ and $2p_{3/2}$ respectively) was observed in the P 2p XP spectra (Figure 4.9). The concentration of the P dopant was determined using the obtained XPS spectra and calculated as 0.78, 0.41 and 0.27 atomic % for parent SiNP diameters of 2.99 ± 0.54, 6.30 ± 1.2 and 8.60 ± 1.4 nm (Figure 4.9 a-c). Similar to Chapter 3, a trend of increasing dopant concentration is observed for decreasing parent NP size. This trend is most likely due to the increased structure disorder seen for smaller SiNPs, allowing for increased diffusion of

P dopant atoms during thermal treatment, however, this would have to be confirmed with future studies.

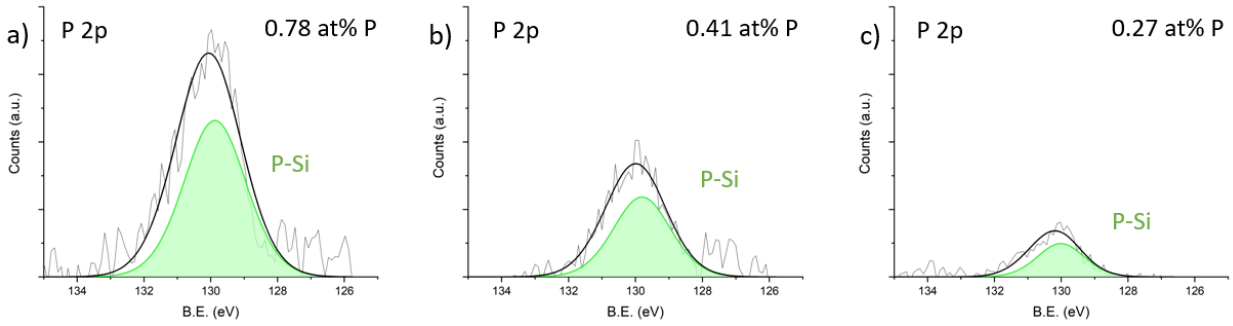

Figure 4. 9 High-resolution P 2p XP spectra of P-doped SiNPs using parent SiNPs with diameters of a) 2.99 ± 0.54, b) 6.30 ± 1.2 and c) 8.60 ± 1.4 nm. The P 2p XP spectra show only the $2p_{3/2}$ emission ($2\ p_{1/2}$ is omitted for clarity).

The particle size and morphology of the resulting P-doped SiNPs were evaluated using transmission electron microscopy (TEM). The SiNPs were found to have a spherical morphology (Figure 4.10 a-c) and the average NP diameters were determined from bright-field TEM images by measuring 300 particles and were found to be 2.74 ± 0.56, 5.4 ± 1.5, and 8.2 ± 1.2 nm (Figure 4.10 d-e). High-resolution TEM (HRTEM) identified characteristic (111) lattice spacing for crystalline Si confirming that the crystallinity of the parent SiNPs is retained after doping with P (Figure 4.10 a-c insets).

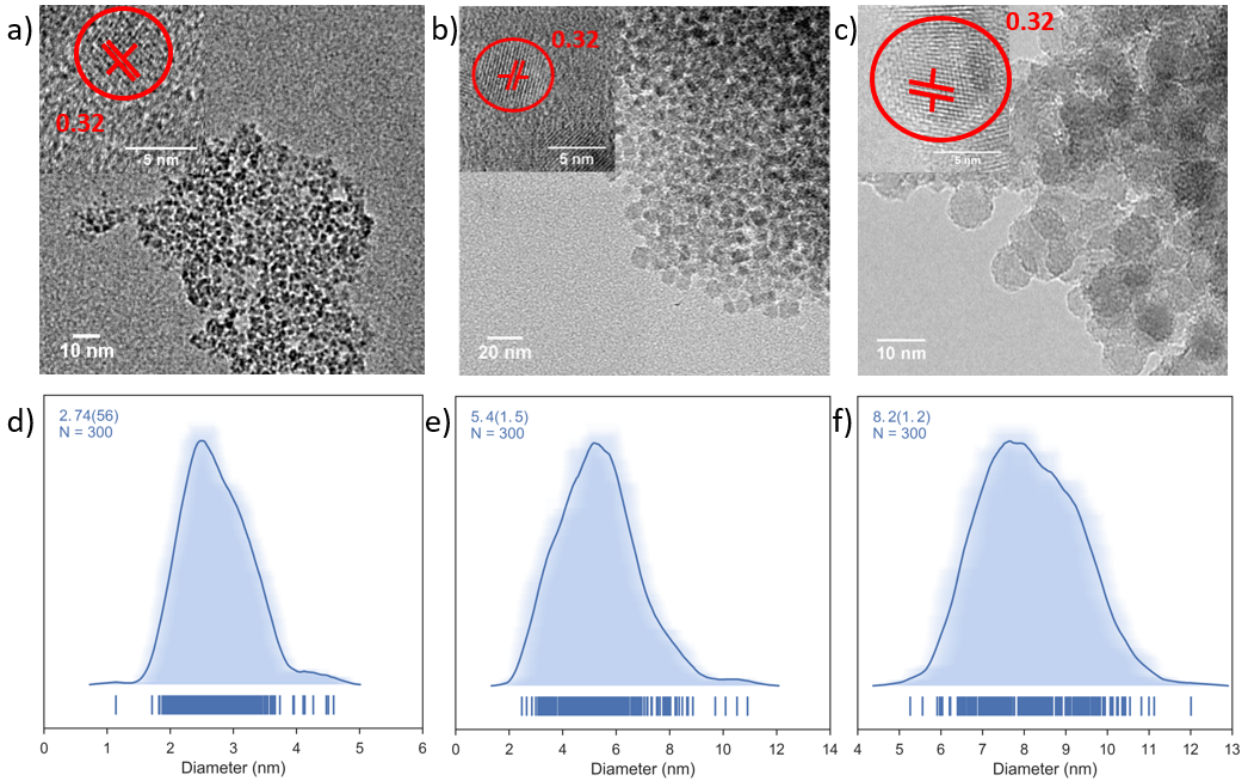

Figure 4. 10 Bright field transmission electron microscopy (TEM) and high-resolution (inset) imaging showing fringes separated by 0.32 nm which is characteristic of the (111) lattice spacing of crystalline Si for P-doped SiNPs with diameters of a) 2.74 ± 0.54 b) 5.40 ± 1.5 nm and c) 8.20 ± 1.2 nm determined from corresponding average shifted histograms d), e) and f).

4.4 Conclusions and Future Work

This chapter aimed at laying the groundwork for controlling dopant location in SiNPs through the development of a self-capping monolayer doping method. POSS-P was used as molecular dopant scaffold and successfully grafted to the surface of SiNPs. The unique silica cage structure possessed self-capping abilities that upon low-temperature annealing formed a protective capping layer around the SiNPs, preventing the evaporation of P atoms during thermally promoted diffusion. It was determined that an annealing temperature of 1000 °C was required to successfully dope SiNPs with P and the concentration of the dopant increased with decreasing particle size.

There are several experiments that could be performed for future studies on the self-capping monolayer doping method for SiNPs. Similar to the previous chapter, a primarily crystalline parent SiNP could be doped using the established post-synthesis doping method and the concentration of resulting P atoms would then be compared to the structurally disordered SiNPs. The bulk concentration of the P dopant in the SiNPs can be determined using ICP-MS and compared to the concentration found by XPS. The dopant distribution within the NP could be studied using a combination of time-of-flight secondary ion mass spectrometry and cross-polarization magic angle spinning nuclear magnetic resonance (CP MAS NMR). Dynamic nuclear polarization surface enhanced NMR (DNP SENS) could be used to determine the structure of the dopant molecule grafted to the NP particle surface. The previously established surface functionalization method for B-doped SiNPs from Chapter 2 could be adapted for the P-doped SiNPs to enable solution processibility, prevent oxidation and potentially enable photoluminescent properties.

4.5 References

(1) Oliva-Chatelain, B. L.; Ticich, T. M.; Barron, A. R. Doping silicon nanocrystals and quantum dots. *Nanoscale* **2016**, *8* (4), 1733-1745. DOI: 10.1039/c5nr04978d. Makkar, M.; Viswanatha, R. Frontier challenges in doping quantum dots: synthesis and characterization. *RSC Advances* **2018**, *8* (39), 22103-22112. DOI: 10.1039/c8ra03530j. Iori, F.; Ossicini, S. Effects of simultaneous doping with boron and phosphorous on the structural, electronic and optical properties of silicon nanostructures. *Physica E: Low-dimensional Systems and Nanostructures* **2009**, *41* (6), 939-946. DOI: https://doi.org/10.1016/j.physe.2008.08.010. Sugimoto, H.; Fujii, M.; Imakita, K.; Hayashi, S.; Akamatsu, K. All-Inorganic Near-Infrared Luminescent Colloidal Silicon Nanocrystals: High Dispersibility in Polar Liquid by Phosphorus and Boron Codoping. *The Journal of Physical Chemistry C* **2012**, *116* (33), 17969-17974. DOI: 10.1021/jp305832x. Sugimoto, H.; Okazaki, T.; Fujii, M. Mie Resonator Color Inks of Monodispersed and Perfectly Spherical Crystalline Silicon Nanoparticles. *Advanced Optical Materials* **2020**, *8* (12), 2000033. DOI: https://doi.org/10.1002/adom.202000033. Sugimoto, H.; Zhou, H.; Takada, M.; Fushimi, J.; Fujii, M. Visible-light driven photocatalytic hydrogen generation by water-soluble all-inorganic core–shell silicon quantum dots. *Journal of Materials Chemistry A* **2020**, *8* (31), 15789-15794, 10.1039/D0TA01071E. DOI: 10.1039/D0TA01071E.

(2) Wong, A. P. Y.; Sun, W.; Qian, C.; Jelle, A. A.; Jia, J.; Zheng, Z.; Dong, Y.; Ozin, G. A. Tailoring CO2 Reduction with Doped Silicon Nanocrystals. *Advanced Sustainable Systems* **2017**, *1* (11), 1700118. DOI: https://doi.org/10.1002/adsu.201700118.

(3) Rocks, C.; Svrcek, V.; Velusamy, T.; Macias-Montero, M.; Maguire, P.; Mariotti, D. Type-I alignment in MAPbI3 based solar devices with doped-silicon nanocrystals. *Nano Energy* **2018**, *50*, 245-255. DOI: https://doi.org/10.1016/j.nanoen.2018.05.036. Cho, E.-C.; Green, M. A.; Conibeer, G.; Song, D.; Cho, Y.-H.; Scardera, G.; Huang, S.; Park, S.; Hao, X. J.; Huang, Y.; et al. Silicon Quantum Dots in a Dielectric Matrix for All-Silicon Tandem Solar Cells. *Advances in OptoElectronics* **2007**, *2007*, 1-11. DOI: 10.1155/2007/69578.

(4) Ni, Z.; Ma, L.; Du, S.; Xu, Y.; Yuan, M.; Fang, H.; Wang, Z.; Xu, M.; Li, D.; Yang, J.; et al. Plasmonic Silicon Quantum Dots Enabled High-Sensitivity Ultrabroadband Photodetection of Graphene-Based Hybrid Phototransistors. *ACS Nano* **2017**, *11* (10), 9854-9862. DOI: 10.1021/acsnano.7b03569.

(5) Fujii, M.; Fujii, R.; Takada, M.; Sugimoto, H. Silicon Quantum Dot Supraparticles for Fluorescence Bioimaging. *ACS Applied Materials and Interfaces* **2020**, *3* (6), 6099-6107. DOI: 10.1021/acsanm.0c01295. McVey, B. F. P.; Tilley, R. D. Solution Synthesis, Optical Properties, and Bioimaging Applications of Silicon Nanocrystals. *Accounts of Chemical Research* **2014**, *47* (10), 3045-3051. DOI: 10.1021/ar500215v.

(6) Chen, J.; Rohani, P.; Karakalos, S. G.; Lance, M. J.; Toops, T. J.; Swihart, M. T.; Kyriakidou, E. A. Boron-hyperdoped silicon for the selective oxidative dehydrogenation of propane to propylene. *Chemical Communications* **2020**, *56* (68), 9882-9885, 10.1039/D0CC02822C. DOI: 10.1039/D0CC02822C.

(7) Ni, Z.; Pi, X.; Zhou, S.; Nozaki, T.; Grandidier, B.; Yang, D. Size-Dependent Structures and Optical Absorption of Boron-Hyperdoped Silicon Nanocrystals. *Advanced Optical Materials* **2016**, *4* (5), 700-707. DOI: 10.1002/adom.201500706. Zhou, S.; Pi, X.; Ni, Z.; Luan, Q.; Jiang, Y.; Jin, C.; Nozaki, T.; Yang, D. Boron- and Phosphorus-Hyperdoped Silicon Nanocrystals. *Particle & Particle Systems Characterization* **2014**, *32* (2), 213-221. DOI: 10.1002/ppsc.201400103. Zhou, S.; Pi, X.; Ni, Z.; Ding, Y.; Jiang, Y.; Jin, C.; Delerue, C.; Yang, D.; Nozaki, T. Comparative Study on the Localized Surface Plasmon Resonance of

Boron- and Phosphorus-Doped Silicon Nanocrystals. *ACS Nano* **2015**, *9* (1), 378-386. DOI: 10.1021/nn505416r. Zhou, S.; Ni, Z.; Ding, Y.; Sugaya, M.; Pi, X.; Nozaki, T. Ligand-Free, Colloidal, and Plasmonic Silicon Nanocrystals Heavily Doped with Boron. *ACS Photonics* **2016**, *3* (3), 415-422. DOI: 10.1021/acsphotonics.5b00568. Rohani, P.; Banerjee, S.; Sharifi-Asl, S.; Malekzadeh, M.; Shahbazian-Yassar, R.; Billinge, S. J. L.; Swihart, M. T. Synthesis and Properties of Plasmonic Boron-Hyperdoped Silicon Nanoparticles. *Advanced Functional Materials* **2019**, *29* (8), 1807788. DOI: 10.1002/adfm.201807788.
(8) Fujii, M.; Sugimoto, H.; Imakita, K. All-inorganic colloidal silicon nanocrystals—surface modification by boron and phosphorus co-doping. *Nanotechnology* **2016**, *27* (26), 262001. DOI: 10.1088/0957-4484/27/26/262001.
(9) Ho, J. C.; Yerushalmi, R.; Smith, G.; Majhi, P.; Bennett, J.; Halim, J.; Faifer, V. N.; Javey, A. Wafer-Scale, Sub-5 nm Junction Formation by Monolayer Doping and Conventional Spike Annealing. *Nano Letters* **2009**, *9* (2), 725-730. DOI: 10.1021/nl8032526. Ho, J. C.; Yerushalmi, R.; Jacobson, Z. A.; Fan, Z.; Alley, R. L.; Javey, A. Controlled nanoscale doping of semiconductors via molecular monolayers. *Nature Materials* **2008**, *7* (1), 62-67. DOI: 10.1038/nmat2058.
(10) Ye, L.; de Jong, M. P.; Kudernac, T.; van der Wiel, W. G.; Huskens, J. Doping of semiconductors by molecular monolayers: monolayer formation, dopant diffusion and applications. *Materials Science in Semiconductor Processing* **2017**, *62*, 128-134. DOI: https://doi.org/10.1016/j.mssp.2016.12.018.
(11) Mathey, L.; Alphazan, T.; Valla, M.; Veyre, L.; Fontaine, H.; Enyedi, V.; Yckache, K.; Danielou, M.; Kerdiles, S.; Guerrero, J.; et al. Functionalization of Silica Nanoparticles and Native Silicon Oxide with Tailored Boron-Molecular Precursors for Efficient and Predictive p-Doping of Silicon. *The Journal of Physical Chemistry C* **2015**, *119* (24), 13750-13757. DOI: 10.1021/acs.jpcc.5b03408. Agarwala, A.; Subramani, T.; Goldbourt, A.; Danovich, D.; Yerushalmi, R. Facile Monolayer Formation on SiO2 Surfaces via Organoboron Functionalities. *Angewandte Chemie International Edition* **2013**, *52* (29), 7415-7418. DOI: https://doi.org/10.1002/anie.201302655.
(12) Alphazan, T.; Mathey, L.; Schwarzwälder, M.; Lin, T.-H.; Rossini, A. J.; Wischert, R.; Enyedi, V.; Fontaine, H.; Veillerot, M.; Lesage, A.; et al. Monolayer Doping of Silicon through Grafting a Tailored Molecular Phosphorus Precursor onto Oxide-Passivated Silicon Surfaces. *Chemistry of Materials* **2016**, *28* (11), 3634-3640. DOI: 10.1021/acs.chemmater.5b04291.
(13) Hessel, C. M.; Henderson, E. J.; Veinot, J. G. C. Hydrogen Silsesquioxane: A Molecular Precursor for Nanocrystalline Si−SiO2 Composites and Freestanding Hydride-Surface-Terminated Silicon Nanoparticles. *Chemistry of Materials* **2006**, *18* (26), 6139-6146. DOI: 10.1021/cm0602803.
(14) Feher, F. J.; Budzichowski, T. A. Heterosilsesquioxanes: synthesis and characterization of Group 15 containing polyhedral oligosilsesquioxanes. *Organometallics* **1991**, *10* (3), 812-815. DOI: 10.1021/om00049a051.
(15) Zeng, B.; He, K.; Wu, H.; Ye, J.; Zheng, X.; Luo, W.; Xu, Y.; Yuan, C.; Dai, L. Zirconium-Embedded Polyhedral Oligomeric Silsesquioxane Containing Phosphaphenanthrene-Substituent Group Used as Flame Retardants for Epoxy Resin Composites. *Macromolecular Materials and Engineering* **2021**, *306* (6), 2100012. DOI: https://doi.org/10.1002/mame.202100012.
(16) Owens, T. M.; Nicholson, K. T.; Fosnacht, D. R.; Orr, B. G.; Banaszak Holl, M. M. Formation of Mixed Monolayers of Silsesquioxanes and Alkylsilanes on Gold. *Langmuir* **2006**, *22* (23), 9619-9622. DOI: 10.1021/la061477c.

(17) Daasch, L.; Smith, D. Infrared Spectra of Phosphorus Compounds. *Analytical Chemistry* **1951**, *23* (6), 853-868. DOI: 10.1021/ac60054a008.
(18) Sherwood, P. M. A. Introduction to Studies of Phosphorus-Oxygen Compounds by XPS. *Surface Science Spectra* **2002**, *9* (1), 62-66. DOI: 10.1116/11.20030101.
(19) Hashemi, A.; Bahari, A. Structural and dielectric characteristic of povidone–silica nanocomposite films on the Si (n) substrate. *Applied Physics A* **2017**, *123* (8), 535. DOI: 10.1007/s00339-017-1152-6.
(20) Ciolacu, F. C. L.; Choudhury, N. R.; Dutta, N.; Kosior, E. Molecular Level Stabilization of Poly(ethylene terephthalate) with Nanostructured Open Cage Trisilanolisobutyl-POSS. *Macromolecules* **2007**, *40* (2), 265-272. DOI: 10.1021/ma061060d.
(21) Clark, R. J.; Aghajamali, M.; Gonzalez, C. M.; Hadidi, L.; Islam, M. A.; Javadi, M.; Mobarok, M. H.; Purkait, T. K.; Robidillo, C. J. T.; Sinelnikov, R.; et al. From hydrogen silsesquioxane to functionalized silicon nanocrystals. *Chemistry of Materials* **2017**, *29* (1), 80-89. DOI: 10.1021/acs.chemmater.6b02667.
(22) Dasog, M.; Yang, Z.; Veinot, J. G. C. Size-controlled solid state synthesis of luminescent silicon nanocrystals using Stöber silica particles. *CrystEngComm* **2012**, *14* (22), 7576-7578, 10.1039/C2CE25950H. DOI: 10.1039/C2CE25950H. Chan, T.-H.; Melnyk, A. Kinetics and mechanism of the sulfoxide-silane reaction. *Journal of the American Chemical Society* **1970**, *92* (12), 3718-3722. DOI: 10.1021/ja00715a030.
(23) Hayichelaeh, C.; Reuvekamp, L. A. E. M.; Dierkes, W. K.; Blume, A.; Noordermeer, J. W. M.; Sahakaro, K. Enhancing the Silanization Reaction of the Silica-Silane System by Different Amines in Model and Practical Silica-Filled Natural Rubber Compounds. *Polymers* **2018**, *10* (6), 584.
(24) Sápi, A.; Kéri, A.; Kálomista, I.; Dobó, D. G.; Ákos, S.; Juhász, K. L.; Ákos, K.; Kónya, Z.; Galbács, G. Determination of the platinum concentration of a Pt/silica nanocomposite decorated with ultra small Pt nanoparticles using single particle inductively coupled plasma mass spectrometry. *Journal of Analytical Atomic Spectrometry* **2017**, *32* (5), 996-1003, 10.1039/C7JA00039A. DOI: 10.1039/C7JA00039A. Gorham, J. M.; Murphy, K.; Liu, J.; Tselenchuk, D.; Stan, G.; Nguyen, T. M.; Holbrook, R. D.; Winchester, M.; Cook, R. F.; MacCuspie, R. I.; et al. *Preparation of silver nanoparticle loaded cotton threads to facilitate measurement development for textile applications*; National Institute of Standards and Technology, 2015. DOI: 10.6028/NIST.SP.1200-8.
(25) Caccamo, S.; Puglisi, R. A. Carbon-Free Solution-Based Doping for Silicon. *Nanomaterials* **2021**, *11* (8), 2006. Su, Y.; Wang, C.; Hong, Z.; Sun, W. Thermal Disproportionation for the Synthesis of Silicon Nanocrystals and Their Photoluminescent Properties. *Frontiers in Chemistry* **2021**, *9*, Review. DOI: 10.3389/fchem.2021.721454.
(26) Shimizu, Y.; Takamizawa, H.; Inoue, K.; Yano, F.; Nagai, Y.; Lamagna, L.; Mazzeo, G.; Perego, M.; Prati, E. Behavior of phosphorous and contaminants from molecular doping combined with a conventional spike annealing method. *Nanoscale* **2014**, *6* (2), 706-710, 10.1039/C3NR03605G. DOI: 10.1039/C3NR03605G.
(27) Widjonarko, D.; Jumina, J.; Kartini, I.; Nuryono, N. Phosphonate modified silica for adsorption of Co(II), Ni(II), Cu(II), and Zn(II). *Indonesian Journal of Chemistry* **2014**, *14*, 143-151.
(28) Kovalev, A. I.; Wainstein, D. L.; Tetelbaum, D. I.; Hornig, W.; Kucherehko, Y. N. Investigation of the electronic structure of the phosphorus-doped Si and SiO2:Si quantum dots

by XPS and HREELS methods. *Surface and Interface Analysis* **2004**, *36* (8), 959-962. DOI: https://doi.org/10.1002/sia.1811.
(29) Hiller, D.; López-Vidrier, J.; Gutsch, S.; Zacharias, M.; Wahl, M.; Bock, W.; Brodyanski, A.; Kopnarski, M.; Nomoto, K.; Valenta, J.; et al. Boron-Incorporating Silicon Nanocrystals Embedded in SiO(2): Absence of Free Carriers vs. B-Induced Defects. *Scientific reports* **2017**, *7* (1), 8337-8337. DOI: 10.1038/s41598-017-08814-0 PubMed. He, W.; Li, Z.; Wen, C.; Liu, H.; Shen, W. Size dependence of phosphorus doping in silicon nanocrystals. *Nanotechnology* **2016**, *27* (42), 425710. DOI: 10.1088/0957-4484/27/42/425710. Limpens, R.; Neale, N. R. Free electron-driven photophysics in n-type doped silicon nanocrystals. *Nanoscale* **2018**, *10* (25), 12068-12077, 10.1039/C8NR02173B. DOI: 10.1039/C8NR02173B. Limpens, R.; Fujii, M.; Neale, N. R.; Gregorkiewicz, T. Negligible Electronic Interaction between Photoexcited Electron–Hole Pairs and Free Electrons in Phosphorus–Boron Co-Doped Silicon Nanocrystals. *The Journal of Physical Chemistry C* **2018**, *122* (11), 6397-6404. DOI: 10.1021/acs.jpcc.7b12313.

Chapter 5:

Conclusions and future work

5.1 Conclusions

Doping silicon nanoparticles provides another important degree of freedom for tailoring the material properties (e.g., electronic, optical, catalytic) for targeted applications such as solar cells, medical imaging, and light-emitting devices. Currently, synthetic methods for producing doped SiNPs provide very limited control over the dopant distribution and uniformity. Additionally, it can be difficult to tune the particle size and the resulting size distribution/morphology can be non-uniform. Tailoring the surface of doped SiNPs has also proven difficult and recent efforts to functionalize the surface of doped silicon quantum dots have proven unsuccessful using standard methods (e.g., hydrothermal, radical/Lewis-acid initiated, and photochemically-induced hydrosilylation). This thesis outlines efforts made to develop reliable methods for controllably incorporating dopants into SiNPs and tailoring the surface chemistry of the resulting doped particles. By developing doping and surface modification methods we can control key characteristics needed for targeted applications: 1) surface chemistry, 2) particle dimensions, and 3) dopant concentration and distribution.

Chapter 2 provides an etching-induced functionalization procedure for altering the surface of B-doped SiNPs. We found that PCl_5 is an effective mild etchant that can remove passivating surface species and subsequent heating can be used to promote the surface bonding an alkoxy-ligand (i.e., -OR). The resulting alkoxy-functionalized B-doped SiNPs form stable colloids in common organic solvents and exhibit size tunable PL in the visible to NIR range.

After establishing a convenient method for tailoring the surface chemistry of B-doped SiNPs we sought to control the size of the doped particles. This saw the development of a new diffusion-based post-synthesis doping method in Chapter 3 that drew inspiration from thermally-

induced diffusion doping of bulk silicon. This method exploits parent SiNPs with narrow size distributions and employs an HSQ capping agent. We found that the structural disorder within the SiNPs, as well as the "drive-in" conditions (e.g., annealing temperature and flowing gas) affected the resulting dopant concentration. As synthesized, the B-doped SiNPs were compatible with polar solvents (e.g., water) and showed size-controlled PL that could be tuned from the visible to NIR. Using the previously established surface functionalization method from Chapter 2 we successfully rendered the B-doped SiNPs organic phase soluble and improved the photoluminescent quantum yield of the size dependent PL.

In Chapter 4 we aimed to provide control of the dopant location in the SiNPs through the development of a monolayer doping method. We successfully demonstrated grafting of a self-capping dopant molecular precursor, POSS-P, to the surfaces of SiNPs of different sizes. Annealling this functionalized particle induces the diffusion of P dopants into the NP. It was found that parent NP size and annealing temperature influenced the resulting P dopant concentration. This work lays the foundation for future studies on tailoring dopant locations in SiNPs and provides avenues for well-defined doped SiNPs for targeted applications.

In this chapter, we focus on potential future studies focused on tailoring surface chemistry, dopant location, and resulting optoelectronic properties of doped SiNPs.

5.2 Future Directions

5.2.1. B-doped SiNPs as Lewis acidic surfaces

A recent report on B-doped SiNPs synthesized via a nonthermal plasma method observed three-fold coordinate acidic B sites on the particles that the authors proposed could behave as a reactive surface (Scheme 5.1).[1] In Chapter 2 we observed the presence of partially oxidized B surface species that were most likely formed from acidic B surface sites reacting with Lewis bases such as water or ethanol.[2] This presents the intriguing opportunity to use these surface B species as catalytic or reactive sites for dehydroborylation, hydroboration, carboboration, and haloboration.[3] This proposed study would focus on protecting these reactive surface sites from oxidation during etching, and subsequent activation for select reactions. Since NPs have a much higher surface area than bulk, these surface Lewis acidic sites present the opportunity for improved reaction yield.[4]

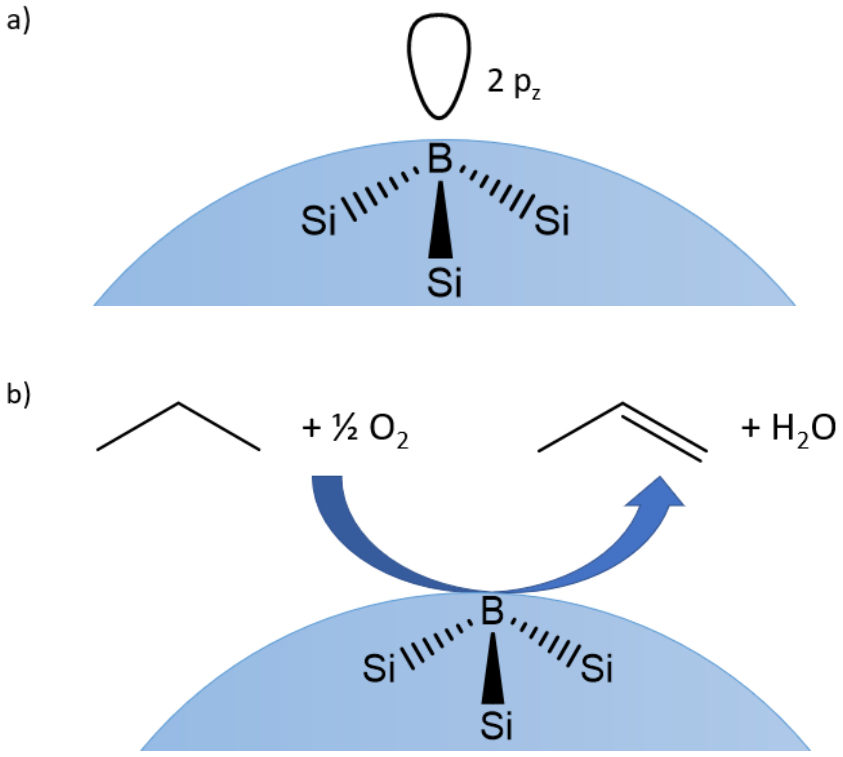

Scheme 5. 1 a) Graphic representing the surface Lewis acidic B-site, the empty 2 p_z orbital can accept a pair of electrons from a Lewis base. b) Example of a dehydrogenation reaction using an active surface B-site.

5.2.2 F-terminated B-doped SiNPs for multimodal imaging

Doped SiNPs, such as the ones produced in Chapter 3, are excellent candidates for use in multimodal medical imaging due to their visible to near-IR PL, solubility in polar mediums, and potential for ^{29}Si magnetic resonance imaging (MRI) in which the SiNPs are exploited as a targeted probe.[5] In addition, the presence of B dopants can allow for Boron neutron capture therapy (BCNT), an alternative cancer treatment strategy that enables cellular-level selective radiation therapy (Figure 5.1).[6] In addition, another low background imaging mode could be achieved by

bonding active surface B sites with positron-emitting radionuclei, such as ^{18}F, to enable positron emission tomography (PET) imaging.[7] Fluorinating agents, such as CsF could be used to attach ^{19}F atoms then exchanged with the isotope ^{18}F.[8] Alternatively, ^{19}F containing ligands (e.g., silicon fluoride acceptors) could be attached to the NP surface and exchanged with ^{19}F to provide better stability and prevent oxidation.[9]

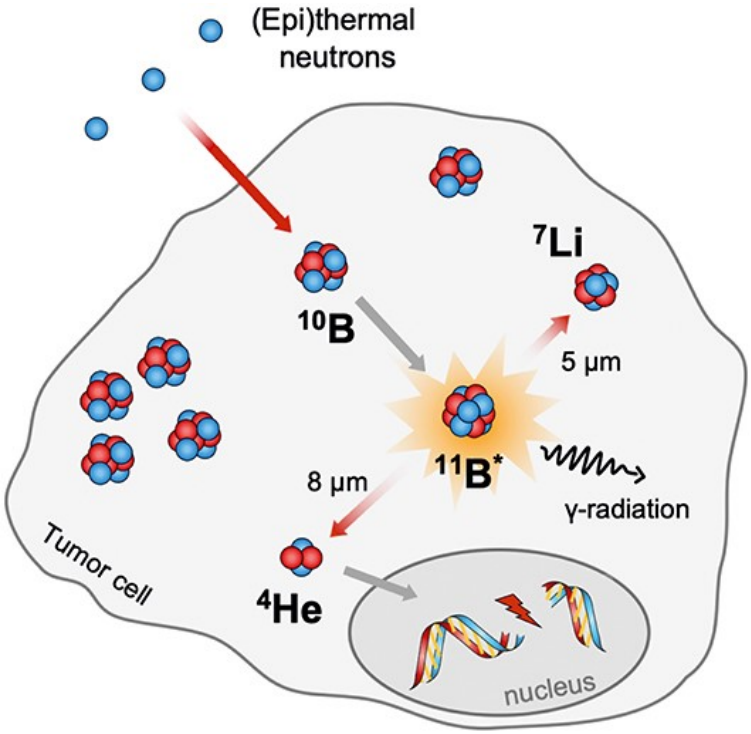

Figure 5. 1 Schematic representation of BNCT. Boronating agents are used to deliver ^{10}B to tumors which can then undergo irradiation with neutrons to create 7Li and an alpha particle which destroys the tumor tissue. Reprinted with permission from ref. 10.

5.2.3 Pair distribution function study of B-doped SiNPs

In the interest of securing a complete picture of the structure of B-doped SiNPs, additional methods of analysis should be explored that interrogate the local structure of the B dopants in post-

synthesis doped SiNPs described in Chapter 3. One such method is a newly emerging technique that generates an electron pair distribution function (PDF) using TEM-based diffraction patterns.[11] The diffraction pattern is transformed into information about the bond lengths in the NPs and can be used to create a 3D atomic-level reconstruction of the local structure using reverse Monte Carlo. A similar technique that uses high-energy XRD (HEXRD) to obtain the diffraction patterns has been previously employed to study the P distribution and efficacy of P-doped SiNPs.[12] One limitation of this method is HEXRD can only be used to analyze crystalline materials.[13] This creates a problem for studying SiNPs which contain both a crystalline core and an amorphous-like disordered shell, similar to the parent particles employed in Chapter 3 and 4. In addition, higher levels of doping (i.e., approaching the solid solubility limit) generate greater disorder in the SiNPs making it more difficult to obtain a PDF to investigate local atomic structure.[14] Electron diffraction patterns not only allow for the study of disordered or heterogenous materials but can also achieve atomic-level resolution due to the ability to focus electron beams to nano- or even angstrom-sized diameters.[11] By applying the TEM-based diffraction technique to post-synthesis doped SiNPs we can generate an ePDF of the dopants to study their location, local structure and efficacy to better understand their effect on the resulting SiNP optical and electronic properties.

5.2.4 P-,As-,Al-, and Sb-doped SiNPs via thermal diffusion based post-synthesis doping method

The post-synthesis doping method discussed in Chapter 3 provides an avenue for incorporating dopants into predefined SiNPs. Although only B dopants were studied, the method provides precedent for and could be expanded to include other dopants such as P, As, Al, and Sb. This would require picking suitable precursor materials that readily react with SiNPs and HSQ. Additionally, the drive-in step would have to be optimized for each dopant as diffusion coefficients

vary by element and temperature.[15] Once achieved, the post-synthesis doping method could become an essential toolkit for tuning the optical and electronic properties of SiNPs for targeted applications.

5.2.5 B- and P-doped SiNPs for all-Si tandem solar cells

With climate change rapidly emerging as one of, if not the most important and impactful global issues facing society, researchers are scrambling to develop new renewable energy technologies that can minimize and even eliminate society's reliance on fossil fuels.[16] Solar cell devices are one of the most practical ways to harness energy from sunlight and have seen an incredible improvement in performance over the past decade.[17] However, overall efficiency of single-junction solar cells remains limited to just 33% light-to-power conversions efficiency (PCE) according to the Schockley-Queisser limit.[18] Tandem solar cells make use of multiple stacked absorbers for different regions of the solar spectrum and can offer an improvement to the overall efficiency of the device.[19] Once quantum dots were discovered to have tunable band gaps, it was only natural to explore drawing on this property to improve tandem solar cell applications. Most studies employing QDs in solar applications have employed toxic metal containing compound semiconductors such as cadmium telluride. Si-based cells make up 90% of the current solar market with the opportunity for an enormous infrastructure dedicated to Si-based fabrication of solar devices already in place making SiNPs an attractive and cost-effective material for tandem solar cells.[20] A critical attribute required for the successful fabrication of an all-Si tandem cell is the ability to create both n- and p-type layers of SiNPs through appropriate doping.[21] If SiNPs are to be used in all-Si solar cells, doping them to form p–n junctions is a necessity for the cell structure. B-doped SiNPs synthesized in Chapter 3 and P-doped SiNPs produced in Chapter 4 have the

potential to be used in these tandem solar cell applications because of their well-defined structure and tunable size.

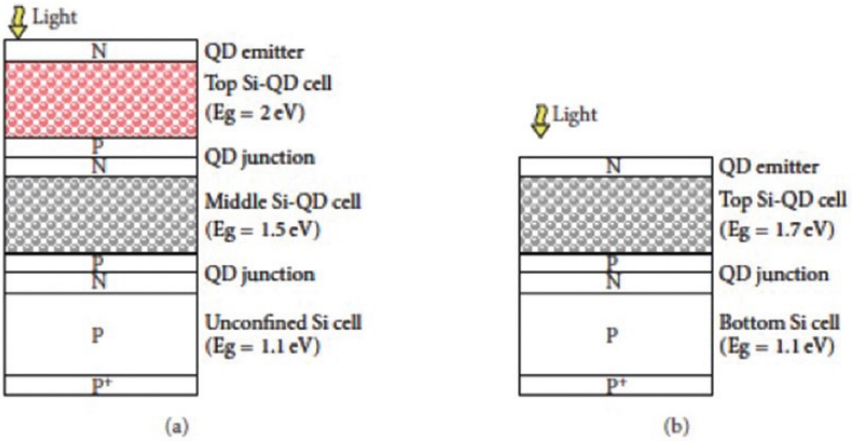

Figure 5. 2 Schematic of two different type of tandem cells using SiNPs. Reprinted with permission from [24].

5.3 References

(1) Wheeler, L. M.; Kramer, N. J.; Kortshagen, U. R. Thermodynamic Driving Force in the Spontaneous Formation of Inorganic Nanoparticle Solutions. *Nano Letters* **2018**, *18* (3), 1888-1895. DOI: 10.1021/acs.nanolett.7b05187.
(2) Milliken, S.; Cui, K.; Klein, B. A.; Cheong, I. T.; Yu, H.; Michaelis, V. K.; Veinot, J. G. C. Tailoring B-doped silicon nanocrystal surface chemistry via phosphorus pentachloride – mediated surface alkoxylation. *Nanoscale* **2021**, *13* (43), 18281-18292, 10.1039/D1NR05255A. DOI: 10.1039/D1NR05255A.
(3) Lawson, J. R.; Melen, R. L. Recent developments and applications of Lewis acidic boron reagents. In *Organometallic Chemistry: Volume 41*, Vol. 41; The Royal Society of Chemistry, 2017; pp 1-27.
(4) Astruc, D. Introduction: Nanoparticles in Catalysis. *Chemical Reviews* **2020**, *120* (2), 461-463. DOI: 10.1021/acs.chemrev.8b00696.
(5) Luu, Q. S.; Kim, J.; Jo, D.; Jeong, J.; Lee, Y. Applications and perspective of silicon particles in hyperpolarized 29Si magnetic resonance imaging. *Applied Spectroscopy Reviews* **2020**, *55* (6), 476-490. DOI: 10.1080/05704928.2019.1676255. Kosaka, N.; Ogawa, M.; Choyke, P. L.; Kobayashi, H. Clinical implications of near-infrared fluorescence imaging in cancer. *Future Oncol* **2009**, *5* (9), 1501-1511. DOI: 10.2217/fon.09.109 PubMed.
(6) Wu, C.-Y.; Hsieh, H.-H.; Chang, T.-Y.; Lin, J.-J.; Wu, C.-C.; Hsu, M.-H.; Lin, M.-C.; Peng, S.-L. Development of MRI-Detectable Boron-Containing Gold Nanoparticle-Encapsulated Biodegradable Polymeric Matrix for Boron Neutron Capture Therapy (BNCT). *International Journal of Molecular Sciences* **2021**, *22* (15), 8050.
(7) Alauddin, M. M. Positron emission tomography (PET) imaging with (18)F-based radiotracers. *Am J Nucl Med Mol Imaging* **2012**, *2* (1), 55-76. PubMed.
(8) Jeon, M. H.; Kwon, Y.-D.; Kim, M. P.; Torres, G. B.; Seo, J. K.; Son, J.; Ryu, Y. H.; Hong, S. Y.; Chun, J.-H. Late-Stage 18F/19F Isotopic Exchange for the Synthesis of 18F-Labeled Sulfamoyl Fluorides. *Organic Letters* **2021**, *23* (7), 2766-2771. DOI: 10.1021/acs.orglett.1c00671.
(9) Iovkova-Berends, L.; Wängler, C.; Zöller, T.; Höfner, G.; Wanner, K. T.; Rensch, C.; Bartenstein, P.; Kostikov, A.; Schirrmacher, R.; Jurkschat, K.; et al. t-Bu2SiF-derivatized D2-receptor ligands: the first SiFA-containing small molecule radiotracers for target-specific PET-imaging. *Molecules* **2011**, *16* (9), 7458-7479. DOI: 10.3390/molecules16097458 From NLM.
(10) Hoppenz, P.; Els-Heindl, S.; Beck-Sickinger, A. G. Peptide-Drug Conjugates and Their Targets in Advanced Cancer Therapies. *Frontiers in Chemistry* **2020**, *8*, Review. DOI: 10.3389/fchem.2020.00571.
(11) Ehrhardt, K. M.; Radomsky, R. C.; Warren, S. C. Quantifying the Local Structure of Nanocrystals, Glasses, and Interfaces Using TEM-Based Diffraction. *Chemistry of Materials* **2021**, *33* (23), 8990-9011. DOI: 10.1021/acs.chemmater.1c03017.
(12) Hunter, K. I.; Bedford, N.; Schramke, K.; Kortshagen, U. R. Probing Dopant Locations in Silicon Nanocrystals via High Energy X-ray Diffraction and Reverse Monte Carlo Simulation. *Nano Letters* **2020**, *20* (2), 852-859. DOI: 10.1021/acs.nanolett.9b03025.
(13) Fleck, N.; Amli, H.; Dhanak, V.; Ahmed, W. Chapter 11 - Characterization techniques in energy generation and storage. In *Emerging Nanotechnologies for Renewable Energy*, Ahmed, W., Booth, M., Nourafkan, E. Eds.; Elsevier, 2021; pp 259-285.
(14) Mocatta, D.; Cohen, G.; Schattner, J.; Millo, O.; Rabani, E.; Banin, U. Heavily doped semiconductor nanocrystal quantum dots. *Science* **2011**, *332* (6025), 77-81. DOI:

10.1126/science.1196321 From NLM. Pablo-Pedro, R.; Magaña-Fuentes, M. A.; Videa, M.; Kong, J.; Li, M.; Mendoza-Cortes, J. L.; Van Voorhis, T. Understanding Disorder in 2D Materials: The Case of Carbon Doping of Silicene. *Nano Letters* **2020**, *20* (9), 6336-6343. DOI: 10.1021/acs.nanolett.0c01775.
(15) McCluskey, M. D.; Haller, E. E. *Dopants and Defects in Semiconductors*; Taylor & Francis, 2012.
(16) Albert, M. J. The Climate Crisis, Renewable Energy, and the Changing Landscape of Global Energy Politics. *Alternatives* **2021**, *46* (3), 89-98. DOI: 10.1177/03043754211040698.
(17) Nayak, P. K.; Mahesh, S.; Snaith, H. J.; Cahen, D. Photovoltaic solar cell technologies: analysing the state of the art. *Nature Reviews Materials* **2019**, *4* (4), 269-285. DOI: 10.1038/s41578-019-0097-0.
(18) Rühle, S. Tabulated values of the Shockley–Queisser limit for single junction solar cells. *Solar Energy* **2016**, *130*, 139-147. DOI: https://doi.org/10.1016/j.solener.2016.02.015.
(19) Li, H.; Zhang, W. Perovskite Tandem Solar Cells: From Fundamentals to Commercial Deployment. *Chemical Reviews* **2020**, *120* (18), 9835-9950. DOI: 10.1021/acs.chemrev.9b00780.
(20) Oliva-Chatelain, B. L.; Ticich, T. M.; Barron, A. R. Doping silicon nanocrystals and quantum dots. *Nanoscale* **2016**, *8* (4), 1733-1745. DOI: 10.1039/c5nr04978d.
(21) Rocks, C.; Svrcek, V.; Velusamy, T.; Macias-Montero, M.; Maguire, P.; Mariotti, D. Type-I alignment in MAPbI3 based solar devices with doped-silicon nanocrystals. *Nano Energy* **2018**, *50*, 245-255. DOI: https://doi.org/10.1016/j.nanoen.2018.05.036.
(22) Cho, E.-C.; Green, M. A.; Conibeer, G.; Song, D.; Cho, Y.-H.; Scardera, G.; Huang, S.; Park, S.; Hao, X. J.; Huang, Y.; et al. Silicon Quantum Dots in a Dielectric Matrix for All-Silicon Tandem Solar Cells. *Advances in OptoElectronics* **2007**, *2007*, 069578. DOI: 10.1155/2007/69578.

Bibliography

Chapter 1:

(1) Vidanapathirana, A. K. Use of Nanotechnology in Pregnancy. In *Encyclopedia of Nanotechnology*, Bhushan, B. Ed.; Springer Netherlands, 2014; pp 1-8.
(2) González-Díaz, J. B.; García-Martín, A.; García-Martín, J. M.; Cebollada, A.; Armelles, G.; Sepúlveda, B.; Alaverdyan, Y.; Käll, M. Plasmonic Au/Co/Au Nanosandwiches with Enhanced Magneto-optical Activity. *Small* **2008**, *4* (2), 202-205. DOI: https://doi.org/10.1002/smll.200700594.
(3) Jeevanandam, J.; Barhoum, A.; Chan, Y. S.; Dufresne, A.; Danquah, M. K. Review on nanoparticles and nanostructured materials: history, sources, toxicity and regulations. *Beilstein J Nanotechnol* **2018**, *9*, 1050-1074. DOI: 10.3762/bjnano.9.98 PubMed.
(4) Veinot, J. G. C. Synthesis, surface functionalization, and properties of freestanding silicon nanocrystals. *Chemical Communications* **2006**, (40), 4160-4168, 10.1039/B607476F. DOI: 10.1039/B607476F.
(5) Requejo-Isidro, J.; Coso, R. d.; Solis, J.; Gonzalo, J.; Afonso, C. N. Role of surface-to-volume ratio of metal nanoparticles in optical properties of Cu:Al2O3 nanocomposite films. *Applied Physics Letters* **2005**, *86* (19), 193104. DOI: 10.1063/1.1923198.
(6) Brus, L. E. A simple model for the ionization potential, electron affinity, and aqueous redox potentials of small semiconductor crystallites. *The Journal of Chemical Physics* **1983**, *79* (11), 5566-5571. DOI: 10.1063/1.445676.
(7) Chukwuocha, E. O.; Onyeaju, M. C.; Harry, T. S. T. Theoretical Studies on the Effect of Confinement on Quantum Dots Using the Brus Equation. *World Journal of Condensed Matter Physics* **2012**, *Vol.02No.02*, 5. DOI: 10.4236/wjcmp.2012.22017.
(8) Arquer, F. P. G. d.; Talapin, D. V.; Klimov, V. I.; Arakawa, Y.; Bayer, M.; Sargent, E. H. Semiconductor quantum dots: Technological progress and future challenges. *Science* **2021**, *373* (6555), eaaz8541. DOI: doi:10.1126/science.aaz8541.
(9) Bailes, J. Photostability of Semiconductor Quantum Dots in Response to UV Exposure. *Methods Mol Biol* **2020**, *2118*, 343-349. DOI: 10.1007/978-1-0716-0319-2_25 From NLM.
(10) Lee, T.; Kim, B. J.; Lee, H.; Hahm, D.; Bae, W. K.; Lim, J.; Kwak, J. Bright and Stable Quantum Dot Light-Emitting Diodes. *Advanced Materials* **2022**, *34* (4), 2106276. DOI: https://doi.org/10.1002/adma.202106276. Liu, Z.; Lin, C.-H.; Hyun, B.-R.; Sher, C.-W.; Lv, Z.; Luo, B.; Jiang, F.; Wu, T.; Ho, C.-H.; Kuo, H.-C.; et al. Micro-light-emitting diodes with quantum dots in display technology. *Light: Science & Applications* **2020**, *9* (1), 83. DOI: 10.1038/s41377-020-0268-1. Bang, S. Y.; Suh, Y.-H.; Fan, X.-B.; Shin, D.-W.; Lee, S.; Choi, H. W.; Lee, T. H.; Yang, J.; Zhan, S.; Harden-Chaters, W.; et al. Technology progress on quantum dot light-emitting diodes for next-generation displays. *Nanoscale Horizons* **2021**, *6* (2), 68-77, 10.1039/D0NH00556H. DOI: 10.1039/D0NH00556H.
(11) Song, H.; Lin, Y.; Zhang, Z.; Rao, H.; Wang, W.; Fang, Y.; Pan, Z.; Zhong, X. Improving the Efficiency of Quantum Dot Sensitized Solar Cells beyond 15% via Secondary Deposition. *Journal of the American Chemical Society* **2021**, *143* (12), 4790-4800. DOI: 10.1021/jacs.1c01214. Nozik, A. J. Quantum dot solar cells. *Physica E: Low-dimensional Systems and Nanostructures* **2002**, *14* (1), 115-120. DOI: https://doi.org/10.1016/S1386-9477(02)00374-0. Emin, S.; Singh, S. P.; Han, L.; Satoh, N.; Islam, A. Colloidal quantum dot solar cells. *Solar Energy* **2011**, *85* (6), 1264-1282. DOI: https://doi.org/10.1016/j.solener.2011.02.005.
(12) Zhang, M.; Yue, J.; Cui, R.; Ma, Z.; Wan, H.; Wang, F.; Zhu, S.; Zhou, Y.; Kuang, Y.; Zhong, Y.; et al. Bright quantum dots emitting at ∼1,600 nm in the NIR-IIb window for

deep tissue fluorescence imaging. *Proceedings of the National Academy of Sciences* **2018**, *115* (26), 6590-6595. DOI: doi:10.1073/pnas.1806153115. Kang, Y.-F.; Li, Y.-H.; Fang, Y.-W.; Xu, Y.; Wei, X.-M.; Yin, X.-B. Carbon Quantum Dots for Zebrafish Fluorescence Imaging. *Scientific Reports* **2015**, *5* (1), 11835. DOI: 10.1038/srep11835. Yang, X.; Zhanghao, K.; Wang, H.; Liu, Y.; Wang, F.; Zhang, X.; Shi, K.; Gao, J.; Jin, D.; Xi, P. Versatile Application of Fluorescent Quantum Dot Labels in Super-resolution Fluorescence Microscopy. *ACS Photonics* **2016**, *3* (9), 1611-1618. DOI: 10.1021/acsphotonics.6b00178.
(13) Li, M.; Chen, T.; Gooding, J. J.; Liu, J. Review of Carbon and Graphene Quantum Dots for Sensing. *ACS Sensors* **2019**, *4* (7), 1732-1748. DOI: 10.1021/acssensors.9b00514. Ghosh, S.; Chen, Y.; George, A.; Dutta, M.; Stroscio, M. A. Fluorescence Resonant Energy Transfer-Based Quantum Dot Sensor for the Detection of Calcium Ions. *Frontiers in Chemistry* **2020**, *8*, Original Research. DOI: 10.3389/fchem.2020.00594.
(14) Reiss, P.; Carrière, M.; Lincheneau, C.; Vaure, L.; Tamang, S. Synthesis of Semiconductor Nanocrystals, Focusing on Nontoxic and Earth-Abundant Materials. *Chemical Reviews* **2016**, *116* (18), 10731-10819. DOI: 10.1021/acs.chemrev.6b00116.
(15) Erogbogbo, F.; Yong, K.-T.; Roy, I.; Xu, G.; Prasad, P. N.; Swihart, M. T. Biocompatible Luminescent Silicon Quantum Dots for Imaging of Cancer Cells. *ACS Nano* **2008**, *2* (5), 873-878. DOI: 10.1021/nn700319z. Bhattacharjee, S.; Rietjens, I. M. C. M.; Singh, M. P.; Atkins, T. M.; Purkait, T. K.; Xu, Z.; Regli, S.; Shukaliak, A.; Clark, R. J.; Mitchell, B. S.; et al. Cytotoxicity of surface-functionalized silicon and germanium nanoparticles: the dominant role of surface charges. *Nanoscale* **2013**, *5* (11), 4870-4883, 10.1039/C3NR34266B. DOI: 10.1039/C3NR34266B.
(16) Terada, S.; Xin, Y.; Saitow, K.-i. Cost-Effective Synthesis of Silicon Quantum Dots. *Chemistry of Materials* **2020**, *32* (19), 8382-8392. DOI: 10.1021/acs.chemmater.0c02320.
(17) Yu, Y.; Fan, G.; Fermi, A.; Mazzaro, R.; Morandi, V.; Ceroni, P.; Smilgies, D.-M.; Korgel, B. A. Size-Dependent Photoluminescence Efficiency of Silicon Nanocrystal Quantum Dots. *The Journal of Physical Chemistry C* **2017**, *121* (41), 23240-23248. DOI: 10.1021/acs.jpcc.7b08054.
(18) Yang, Z.; Dobbie, A. R.; Cui, K.; Veinot, J. G. C. A Convenient Method for Preparing Alkyl-Functionalized Silicon Nanocubes. *Journal of the American Chemical Society* **2012**, *134* (34), 13958-13961. DOI: 10.1021/ja3061497.
(19) Hessel, C. M.; Reid, D.; Panthani, M. G.; Rasch, M. R.; Goodfellow, B. W.; Wei, J.; Fujii, H.; Akhavan, V.; Korgel, B. A. Synthesis of ligand-stabilized silicon nanocrystals with size-dependent photoluminescence spanning visible to near-infrared wavelengths. *Chemistry of Materials* **2012**, *24* (2), 393-401. DOI: 10.1021/cm2032866.
(20) Hessel, C. M.; Henderson, E. J.; Veinot, J. G. C. Hydrogen Silsesquioxane: A Molecular Precursor for Nanocrystalline Si−SiO2 Composites and Freestanding Hydride-Surface-Terminated Silicon Nanoparticles. *Chemistry of Materials* **2006**, *18* (26), 6139-6146. DOI: 10.1021/cm0602803.
(21) Kramer, N. J.; Anthony, R. J.; Mamunuru, M.; Aydil, E. S.; Kortshagen, U. R. Plasma-induced crystallization of silicon nanoparticles. *Journal of Physics D: Applied Physics* **2014**, *47* (7), 075202. DOI: 10.1088/0022-3727/47/7/075202.
(22) Jurbergs, D.; Rogojina, E.; Mangolini, L.; Kortshagen, U. Silicon nanocrystals with ensemble quantum yields exceeding 60%. *Applied Physics Letters* **2006**, *88* (23), 233116. DOI: 10.1063/1.2210788.
(23) Yasar-Inceoglu, O.; Lopez, T.; Farshihagro, E.; Mangolini, L. Silicon nanocrystal production through non-thermal plasma synthesis: a comparative study between silicon

tetrachloride and silane precursors. *Nanotechnology* **2012**, *23* (25), 255604. DOI: 10.1088/0957-4484/23/25/255604.
(24) Ding, Y.; Yamada, R.; Gresback, R.; Zhou, S.; Pi, X.; Nozaki, T. A parametric study of non-thermal plasma synthesis of silicon nanoparticles from a chlorinated precursor. *Journal of Physics D: Applied Physics* **2014**, *47* (48), 485202. DOI: 10.1088/0022-3727/47/48/485202.
(25) Yuan, Z.; Nakamura, T.; Adachi, S.; Matsuishi, K. Improvement of Laser Processing for Colloidal Silicon Nanocrystal Formation in a Reactive Solvent. *The Journal of Physical Chemistry C* **2017**, *121* (15), 8623-8629. DOI: 10.1021/acs.jpcc.7b00288.
(26) Yu, J.; Hao, H.; Zhang, R.; Zheng, W.; Wu, W. Silicon Nanocrystals Prepared by Femtosecond Laser Ablation in solution under different ablation time. *IOP Conference Series: Materials Science and Engineering* **2018**, *322*, 022049. DOI: 10.1088/1757-899x/322/2/022049.
(27) Beekman, M.; Kauzlarich, S. M.; Doherty, L.; Nolas, G. S. Zintl Phases as Reactive Precursors for Synthesis of Novel Silicon and Germanium-Based Materials. *Materials* **2019**, *12* (7), 1139. Atkins, T. M.; Walton, J. H.; Singh, M. P.; Ganguly, S.; Janka, O.; Louie, A. Y.; Kauzlarich, S. M. EPR and Structural Characterization of Water-Soluble Mn2+-Doped Si Nanoparticles. *The Journal of Physical Chemistry C* **2017**, *121* (3), 1948-1956. DOI: 10.1021/acs.jpcc.6b11000. Zhang, X.; Brynda, M.; Britt, R. D.; Carroll, E. C.; Larsen, D. S.; Louie, A. Y.; Kauzlarich, S. M. Synthesis and Characterization of Manganese-Doped Silicon Nanoparticles: Bifunctional Paramagnetic-Optical Nanomaterial. *Journal of the American Chemical Society* **2007**, *129* (35), 10668-10669. DOI: 10.1021/ja074144q. Neiner, D.; Chiu, H. W.; Kauzlarich, S. M. Low-Temperature Solution Route to Macroscopic Amounts of Hydrogen Terminated Silicon Nanoparticles. *Journal of the American Chemical Society* **2006**, *128* (34), 11016-11017. DOI: 10.1021/ja064177q.
(28) McVey, B. F. P.; Butkus, J.; Halpert, J. E.; Hodgkiss, J. M.; Tilley, R. D. Solution Synthesis and Optical Properties of Transition-Metal-Doped Silicon Nanocrystals. *The Journal of Physical Chemistry Letters* **2015**, *6* (9), 1573-1576. DOI: 10.1021/acs.jpclett.5b00589.
(29) Shiohara, A.; Hanada, S.; Prabakar, S.; Fujioka, K.; Lim, T. H.; Yamamoto, K.; Northcote, P. T.; Tilley, R. D. Chemical Reactions on Surface Molecules Attached to Silicon Quantum Dots. *Journal of the American Chemical Society* **2010**, *132* (1), 248-253. DOI: 10.1021/ja906501v.
(30) Baldwin, R. K.; Pettigrew, K. A.; Ratai, E.; Augustine, M. P.; Kauzlarich, S. M. Solution reduction synthesis of surface stabilized silicon nanoparticles. *Chemical Communications* **2002**, (17), 1822-1823, 10.1039/B205301B. DOI: 10.1039/B205301B.
(31) Heath, J. R. A Liquid-Solution-Phase Synthesis of Crystalline Silicon. *Science* **1992**, *258* (5085), 1131-1133. DOI: doi:10.1126/science.258.5085.1131.
(32) Dasog, M.; Yang, Z.; Regli, S.; Atkins, T. M.; Faramus, A.; Singh, M. P.; Muthuswamy, E.; Kauzlarich, S. M.; Tilley, R. D.; Veinot, J. G. C. Chemical Insight into the Origin of Red and Blue Photoluminescence Arising from Freestanding Silicon Nanocrystals. *ACS Nano* **2013**, *7* (3), 2676-2685. DOI: 10.1021/nn4000644.
(33) Sun, W.; Qian, C.; Cui, X. S.; Wang, L.; Wei, M.; Casillas, G.; Helmy, A. S.; Ozin, G. A. Silicon monoxide – a convenient precursor for large scale synthesis of near infrared emitting monodisperse silicon nanocrystals. *Nanoscale* **2016**, *8* (6), 3678-3684, 10.1039/C5NR09128D. DOI: 10.1039/C5NR09128D.
(34) Nesbit, L. A. Annealing characteristics of Si-rich SiO2 films. *Applied Physics Letters* **1985**, *46* (1), 38-40. DOI: 10.1063/1.95842.

(35) Gupta, A.; Swihart, M. T.; Wiggers, H. Luminescent Colloidal Dispersion of Silicon Quantum Dots from Microwave Plasma Synthesis: Exploring the Photoluminescence Behavior Across the Visible Spectrum. *Advanced Functional Materials* **2009**, *19* (5), 696-703. DOI: https://doi.org/10.1002/adfm.200801548.
(36) Brus, L. E.; Szajowski, P. F.; Wilson, W. L.; Harris, T. D.; Schuppler, S.; Citrin, P. H. Electronic Spectroscopy and Photophysics of Si Nanocrystals: Relationship to Bulk c-Si and Porous Si. *Journal of the American Chemical Society* **1995**, *117* (10), 2915-2922. DOI: 10.1021/ja00115a025.
(37) Nayfeh, M. H.; Akcakir, O.; Belomoin, G.; Barry, N.; Therrien, J.; Gratton, E. Second harmonic generation in microcrystallite films of ultrasmall Si nanoparticles. *Applied Physics Letters* **2000**, *77* (25), 4086-4088. DOI: 10.1063/1.1334945. Nayfeh, M. H.; Barry, N.; Therrien, J.; Akcakir, O.; Gratton, E.; Belomoin, G. Stimulated blue emission in reconstituted films of ultrasmall silicon nanoparticles. *Applied Physics Letters* **2001**, *78* (8), 1131-1133. DOI: 10.1063/1.1347398.
(38) Li, X.; He, Y.; Talukdar, S. S.; Swihart, M. T. Process for Preparing Macroscopic Quantities of Brightly Photoluminescent Silicon Nanoparticles with Emission Spanning the Visible Spectrum. *Langmuir* **2003**, *19* (20), 8490-8496. DOI: 10.1021/la034487b.
(39) Li, X.; He, Y.; Swihart, M. T. Surface Functionalization of Silicon Nanoparticles Produced by Laser-Driven Pyrolysis of Silane followed by HF−HNO3 Etching. *Langmuir* **2004**, *20* (11), 4720-4727. DOI: 10.1021/la036219j. Hua, F.; Erogbogbo, F.; Swihart, M. T.; Ruckenstein, E. Organically Capped Silicon Nanoparticles with Blue Photoluminescence Prepared by Hydrosilylation Followed by Oxidation. *Langmuir* **2006**, *22* (9), 4363-4370. DOI: 10.1021/la0529106.
(40) Hua, F.; Swihart, M. T.; Ruckenstein, E. Efficient Surface Grafting of Luminescent Silicon Quantum Dots by Photoinitiated Hydrosilylation. *Langmuir* **2005**, *21* (13), 6054-6062. DOI: 10.1021/la0509394.
(41) Guruvenket, S.; Hoey, J. M.; Anderson, K. J.; Frohlich, M. T.; Krishnan, R.; Sivaguru, J.; Sibi, M. P.; Boudjouk, P. Synthesis of silicon quantum dots using cyclohexasilane (Si6H12). *Journal of Materials Chemistry C* **2016**, *4* (35), 8206-8213, 10.1039/C6TC01435F. DOI: 10.1039/C6TC01435F.
(42) Sato, S.; Yao, H.; Kimura, K. Self-Assembly of Si Nanoparticles: Emergence of Two-Dimensional Si Nanoparticle Lattices. *Japanese Journal of Applied Physics* **2004**, *43* (No. 7A), L927-L929. DOI: 10.1143/jjap.43.l927. Withrow, S. P.; White, C. W.; Meldrum, A.; Budai, J. D.; Jr., D. M. H.; Barbour, J. C. Effects of hydrogen in the annealing environment on photoluminescence from Si nanoparticles in SiO2. *Journal of Applied Physics* **1999**, *86* (1), 396-401. DOI: 10.1063/1.370699.
(43) Hessel, C. M.; Henderson, E. J.; Veinot, J. G. C. An Investigation of the Formation and Growth of Oxide-Embedded Silicon Nanocrystals in Hydrogen Silsesquioxane-Derived Nanocomposites. *The Journal of Physical Chemistry C* **2007**, *111* (19), 6956-6961. DOI: 10.1021/jp070908c.
(44) Shirahata, N.; Nakamura, J.; Inoue, J.-i.; Ghosh, B.; Nemoto, K.; Nemoto, Y.; Takeguchi, M.; Masuda, Y.; Tanaka, M.; Ozin, G. A. Emerging Atomic Energy Levels in Zero-Dimensional Silicon Quantum Dots. *Nano Letters* **2020**, *20* (3), 1491-1498. DOI: 10.1021/acs.nanolett.9b03157. Mastronardi, M. L.; Maier-Flaig, F.; Faulkner, D.; Henderson, E. J.; Kübel, C.; Lemmer, U.; Ozin, G. A. Size-Dependent Absolute Quantum Yields for Size-

Separated Colloidally-Stable Silicon Nanocrystals. *Nano Letters* **2012**, *12* (1), 337-342. DOI: 10.1021/nl2036194.
(45) Mastronardi, M. L.; Hennrich, F.; Henderson, E. J.; Maier-Flaig, F.; Blum, C.; Reichenbach, J.; Lemmer, U.; Kübel, C.; Wang, D.; Kappes, M. M.; et al. Preparation of Monodisperse Silicon Nanocrystals Using Density Gradient Ultracentrifugation. *Nano Letters* **2011**, *133*, 11928-11931. DOI: 10.1021/ja204865t.
(46) Islam, M. A.; Mobarok, M. H.; Sinelnikov, R.; Purkait, T. K.; Veinot, J. G. C. Phosphorus Pentachloride Initiated Functionalization of Silicon Nanocrystals. *Langmuir* **2017**, *33* (35), 8766-8773. DOI: 10.1021/acs.langmuir.7b00518.
(47) Sefannaser, M.; Thomas, S. A.; Anderson, K. J.; Petersen, R. J.; Brown, S. L.; Boudjouk, P. R.; Pringle, T. A.; Hobbie, E. K. Radiative Relaxation in Luminescent Silicon Nanocrystal Thiol-Ene Composites. *The Journal of Physical Chemistry C* **2021**, *125* (10), 5824-5831. DOI: 10.1021/acs.jpcc.0c11052.
(48) Dasog, M.; De Los Reyes, G. B.; Titova, L. V.; Hegmann, F. A.; Veinot, J. G. C. Size vs Surface: Tuning the Photoluminescence of Freestanding Silicon Nanocrystals Across the Visible Spectrum via Surface Groups. *ACS Nano* **2014**, *8* (9), 9636-9648. DOI: 10.1021/nn504109a.
(49) Sugimoto, H.; Okazaki, T.; Fujii, M. Mie Resonator Color Inks of Monodispersed and Perfectly Spherical Crystalline Silicon Nanoparticles. *Advanced Optical Materials* **2020**, *8* (12), 2000033. DOI: https://doi.org/10.1002/adom.202000033.
(50) Park, E.; Yoo, H.; Lee, J.; Park, M.-S.; Kim, Y.-J.; Kim, H. Dual-Size Silicon Nanocrystal-Embedded SiOx Nanocomposite as a High-Capacity Lithium Storage Material. *ACS Nano* **2015**, *9* (7), 7690-7696. DOI: 10.1021/acsnano.5b03166. Heitmann, J.; Müller, F.; Zacharias, M.; Gösele, U. Silicon Nanocrystals: Size Matters. *Advanced Materials* **2005**, *17* (7), 795-803. DOI: https://doi.org/10.1002/adma.200401126. Hartel, A. M.; Hiller, D.; Gutsch, S.; Löper, P.; Estradé, S.; Peiró, F.; Garrido, B.; Zacharias, M. Formation of size-controlled silicon nanocrystals in plasma enhanced chemical vapor deposition grown SiOxNy/SiO2 superlattices. *Thin Solid Films* **2011**, *520* (1), 121-125. DOI: https://doi.org/10.1016/j.tsf.2011.06.084. Zacharias, M.; Heitmann, J.; Scholz, R.; Kahler, U.; Schmidt, M.; Bläsing, J. Size-controlled highly luminescent silicon nanocrystals: A SiO/SiO2 superlattice approach. *Applied Physics Letters* **2002**, *80* (4), 661-663. DOI: 10.1063/1.1433906.
(51) Henderson, E. J.; Kelly, J. A.; Veinot, J. G. C. Influence of HSiO1.5 Sol−Gel Polymer Structure and Composition on the Size and Luminescent Properties of Silicon Nanocrystals. *Chemistry of Materials* **2009**, *21* (22), 5426-5434. DOI: 10.1021/cm902028q.
(52) Li, Z.; Kortshagen, U. R. Aerosol-Phase Synthesis and Processing of Luminescent Silicon Nanocrystals. *Chemistry of Materials* **2019**, *31* (20), 8451-8458. DOI: 10.1021/acs.chemmater.9b02743.
(53) Mangolini, L.; Thimsen, E.; Kortshagen, U. High-Yield Plasma Synthesis of Luminescent Silicon Nanocrystals. *Nano Letters* **2005**, *5* (4), 655-659. DOI: 10.1021/nl050066y.
(54) Anthony, R. J.; Cheng, K.-Y.; Holman, Z. C.; Holmes, R. J.; Kortshagen, U. R. An All-Gas-Phase Approach for the Fabrication of Silicon Nanocrystal Light-Emitting Devices. *Nano Letters* **2012**, *12* (6), 2822-2825. DOI: 10.1021/nl300164z.
(55) Jurbergs, D.; Rogojina, E.; Mangolini, L.; Kortshagen, U. Silicon nanocrystals with ensemble quantum yields exceeding 60%. *Appl. Phys. Lett.* **2006**, *88* (1), 233116. DOI: 10.1063/1.2210788.
(56) Pringle, T. A.; Hunter, K. I.; Brumberg, A.; Anderson, K. J.; Fagan, J. A.; Thomas, S. A.; Petersen, R. J.; Sefannaser, M.; Han, Y.; Brown, S. L.; et al. Bright Silicon Nanocrystals from a

Liquid Precursor: Quasi-Direct Recombination with High Quantum Yield. *ACS Nano* **2020**, *14* (4), 3858-3867. DOI: 10.1021/acsnano.9b09614.
(57) Kovalenko, M. V.; Manna, L.; Cabot, A.; Hens, Z.; Talapin, D. V.; Kagan, C. R.; Klimov, V. I.; Rogach, A. L.; Reiss, P.; Milliron, D. J.; et al. Prospects of Nanoscience with Nanocrystals. *ACS Nano* **2015**, *9* (2), 1012-1057. DOI: 10.1021/nn506223h.
(58) Švrček, V.; Sasaki, T.; Shimizu, Y.; Koshizaki, N. Blue luminescent silicon nanocrystals prepared by ns pulsed laser ablation in water. *Applied Physics Letters* **2006**, *89* (21), 213113. DOI: 10.1063/1.2397014.
(59) Nakamura, T.; Yuan, Z.; Watanabe, K.; Adachi, S. Bright and multicolor luminescent colloidal Si nanocrystals prepared by pulsed laser irradiation in liquid. *Applied Physics Letters* **2016**, *108* (2), 023105. DOI: 10.1063/1.4939902. Shirahata, N.; Hirakawa, D.; Sakka, Y. Interfacial-related color tuning of colloidal Si nanocrystals. *Green Chemistry* **2010**, *12* (12), 2139-2141, 10.1039/C0GC00502A. DOI: 10.1039/C0GC00502A.
(60) Hwang, J.; Jeong, Y.; Lee, K. H.; Seo, Y.; Kim, J.; Hong, J. W.; Kamaloo, E.; Camesano, T. A.; Choi, J. Simple Preparation of Fluorescent Silicon Nanoparticles from Used Si Wafers. *Industrial & Engineering Chemistry Research* **2015**, *54* (22), 5982-5989. DOI: 10.1021/acs.iecr.5b00446.
(61) Liao, B.; Wang, W.; Deng, X.; He, B.; Zeng, W.; Tang, Z.; Liu, Q. A facile one-step synthesis of fluorescent silicon quantum dots and their application for detecting Cu2+. *RSC Advances* **2016**, *6* (18), 14465-14467, 10.1039/C5RA25563E. DOI: 10.1039/C5RA25563E.
(62) Zou, J.; Sanelle, P.; Pettigrew, K. A.; Kauzlarich, S. M. Size and Spectroscopy of Silicon Nanoparticles Prepared via Reduction of SiCl4. *Journal of Cluster Science* **2006**, *17* (4), 565-578. DOI: 10.1007/s10876-006-0082-9.
(63) Wilcoxon, J. P.; Samara, G. A.; Provencio, P. N. Optical and electronic properties of Si nanoclusters synthesized in inverse micelles. *Physical Review B* **1999**, *60* (4), 2704-2714. DOI: 10.1103/PhysRevB.60.2704.
(64) Tilley, R. D.; Warner, J. H.; Yamamoto, K.; Matsui, I.; Fujimori, H. Micro-emulsion synthesis of monodisperse surface stabilized silicon nanocrystals. *Chemical Communications* **2005**, (14), 1833-1835, 10.1039/B416069J. DOI: 10.1039/B416069J.
(65) McVey, B. F. P.; Tilley, R. D. Solution Synthesis, Optical Properties, and Bioimaging Applications of Silicon Nanocrystals. *Accounts of Chemical Research* **2014**, *47* (10), 3045-3051. DOI: 10.1021/ar500215v.
(66) Shiohara, A.; Prabakar, S.; Faramus, A.; Hsu, C.-Y.; Lai, P.-S.; Northcote, P. T.; Tilley, R. D. Sized controlled synthesis, purification, and cell studies with silicon quantum dots. *Nanoscale* **2011**, *3* (8), 3364-3370, 10.1039/C1NR10458F. DOI: 10.1039/C1NR10458F.
(67) Rosso-Vasic, M.; Spruijt, E.; van Lagen, B.; De Cola, L.; Zuilhof, H. Alkyl-Functionalized Oxide-Free Silicon Nanoparticles: Synthesis and Optical Properties. *Small* **2008**, *4*, 1835-1841. DOI: 10.1002/smll.200800066.
(68) Zhong, Y.; Peng, F.; Bao, F.; Wang, S.; Ji, X.; Yang, L.; Su, Y.; Lee, S.-T.; He, Y. Large-Scale Aqueous Synthesis of Fluorescent and Biocompatible Silicon Nanoparticles and Their Use as Highly Photostable Biological Probes. *Journal of the American Chemical Society* **2013**, *135* (22), 8350-8356. DOI: 10.1021/ja4026227.
(69) Ddungu, John L. Z.; Silvestrini, S.; Tassoni, A.; De Cola, L. Shedding light on the aqueous synthesis of silicon nanoparticles by reduction of silanes with citrates. *Faraday Discussions* **2020**, *222* (0), 350-361, 10.1039/C9FD00127A. DOI: 10.1039/C9FD00127A.

(70) Yang, C.-S.; Bley, R. A.; Kauzlarich, S. M.; Lee, H. W. H.; Delgado, G. R. Synthesis of Alkyl-Terminated Silicon Nanoclusters by a Solution Route. *Journal of the American Chemical Society* **1999**, *121* (22), 5191-5195. DOI: 10.1021/ja9828509.
(71) Wilbrink, Jonathan L.; Huang, C.-C.; Dohnalova, K.; Paulusse, J. M. J. Critical assessment of wet-chemical oxidation synthesis of silicon quantum dots. *Faraday Discussions* **2020**, *222* (0), 149-165, 10.1039/C9FD00099B. DOI: 10.1039/C9FD00099B.
(72) Ma, X.; Xu, F.; Atkins, T. M.; Goforth, A. M.; Neiner, D.; Navrotsky, A.; Kauzlarich, S. M. A versatile low temperature synthetic route to Zintl phase precursors: Na4Si4, Na4Ge4 and K4Ge4 as examples. *Dalton Transactions* **2009**, (46), 10250-10255, 10.1039/B913320H. DOI: 10.1039/B913320H. Tu, C.; Ma, X.; Pantazis, P.; Kauzlarich, S. M.; Louie, A. Y. Paramagnetic, Silicon Quantum Dots for Magnetic Resonance and Two-Photon Imaging of Macrophages. *Journal of the American Chemical Society* **2010**, *132* (6), 2016-2023. DOI: 10.1021/ja909303g.
(73) Singh, M. P.; Atkins, T. M.; Muthuswamy, E.; Kamali, S.; Tu, C.; Louie, A. Y.; Kauzlarich, S. M. Development of Iron-Doped Silicon Nanoparticles As Bimodal Imaging Agents. *ACS Nano* **2012**, *6* (6), 5596-5604. DOI: 10.1021/nn301536n.
(74) Swihart, M. T.; Girshick, S. L. Thermochemistry and Kinetics of Silicon Hydride Cluster Formation during Thermal Decomposition of Silane. *The Journal of Physical Chemistry B* **1999**, *103* (1), 64-76. DOI: 10.1021/jp983358e. Swihart, M. T.; Girshick, S. L. Ab initio structures and energetics of selected hydrogenated silicon clusters containing six to ten silicon atoms. *Chemical Physics Letters* **1999**, *307* (5), 527-532. DOI: https://doi.org/10.1016/S0009-2614(99)00545-X. Onischuk, A. A.; Strunin, V. P.; Ushakova, M. A.; Panfilov, V. N. On the pathways of aerosol formation by thermal decomposition of silane. *Journal of Aerosol Science* **1997**, *28* (2), 207-222. DOI: https://doi.org/10.1016/S0021-8502(96)00061-4. Onischuk, A. A.; Strunin, V. P.; Ushakova, M. A.; Panfilov, V. N. Studying of silane thermal decomposition mechanism. *International Journal of Chemical Kinetics* **1998**, *30* (2), 99-110. DOI: https://doi.org/10.1002/(SICI)1097-4601(1998)30:2<99::AID-KIN1>3.0.CO;2-O.
(75) Liao, Y.; Xu, Y.; Chan, Y. Semiconductor nanocrystals in sol–gel derived matrices. *Physical Chemistry Chemical Physics* **2013**, *15* (33), 13694-13704, 10.1039/C3CP51351C. DOI: 10.1039/C3CP51351C.
(76) Mastronardi, M. L.; Hennrich, F.; Henderson, E. J.; Maier-Flaig, F.; Blum, C.; Reichenbach, J.; Lemmer, U.; Kübel, C.; Wang, D.; Kappes, M. M.; et al. Preparation of Monodisperse Silicon Nanocrystals Using Density Gradient Ultracentrifugation. *Journal of the American Chemical Society* **2011**, *133* (31), 11928-11931. DOI: 10.1021/ja204865t.
(77) Angı, A.; Loch, M.; Sinelnikov, R.; Veinot, J. G. C.; Becherer, M.; Lugli, P.; Rieger, B. The influence of surface functionalization methods on the performance of silicon nanocrystal LEDs. *Nanoscale* **2018**, *10* (22), 10337-10342, 10.1039/C7NR09525B. DOI: 10.1039/C7NR09525B. Maier-Flaig, F.; Rinck, J.; Stephan, M.; Bocksrocker, T.; Bruns, M.; Kübel, C.; Powell, A. K.; Ozin, G. A.; Lemmer, U. Multicolor Silicon Light-Emitting Diodes (SiLEDs). *Nano Letters* **2013**, *13* (2), 475-480. DOI: 10.1021/nl3038689.
(78) Cheong, I. T.; Morrish, W.; Sheard, W.; Yu, H.; Tavares Luppi, B.; Milburn, L.; Meldrum, A.; Veinot, J. G. C. Silicon Quantum Dot–Polymer Fabry–Pérot Resonators with Narrowed and Tunable Emissions. *ACS Applied Materials & Interfaces* **2021**, *13* (23), 27149-27158. DOI: 10.1021/acsami.1c01825.
(79) Zeng, P.; Wang, F.; Zhang, Y.; Zhou, W.; Guo, Z.; Wu, X.; Lu, M.; Zhang, S. Edge-Emitting Silicon Nanocrystal Distributed Feedback Laser with Extremely Low Exciton Threshold. *ACS Photonics* **2021**, *8* (5), 1353-1363. DOI: 10.1021/acsphotonics.0c01846.

(80) Bhandarkar, U. V.; Swihart, M. T.; Girshick, S. L.; Kortshagen, U. R. Modelling of silicon hydride clustering in a low-pressure silane plasma. *Journal of Physics D: Applied Physics* **2000**, *33* (21), 2731-2746. DOI: 10.1088/0022-3727/33/21/311.
(81) Schulte, P. A.; McKernan, L. T.; Heidel, D. S.; Okun, A. H.; Dotson, G. S.; Lentz, T. J.; Geraci, C. L.; Heckel, P. E.; Branche, C. M. Occupational safety and health, green chemistry, and sustainability: a review of areas of convergence. *Environmental Health* **2013**, *12* (1), 31. DOI: 10.1186/1476-069X-12-31. Ruby, D. S. Safety considerations for high-efficiency crystalline-silicon solar cell fabrication. In *Conference Record of the Twentieth IEEE Photovoltaic Specialists Conference*, 26-30 Sept. 1988, 1988; pp 523-528 vol.521. DOI: 10.1109/PVSC.1988.105757.
(82) He, Y.; Su, Y.; Yang, X.; Kang, Z.; Xu, T.; Zhang, R.; Fan, C.; Lee, S.-T. Photo and pH Stable, Highly-Luminescent Silicon Nanospheres and Their Bioconjugates for Immunofluorescent Cell Imaging. *Journal of the American Chemical Society* **2009**, *131* (12), 4434-4438. DOI: 10.1021/ja808827g. Cullis, A. G.; Canham, L. T. Visible light emission due to quantum size effects in highly porous crystalline silicon. *Nature* **1991**, *353* (6342), 335-338. DOI: 10.1038/353335a0. Cullis, A. G.; Canham, L. T.; Calcott, P. D. J. The structural and luminescence properties of porous silicon. *Journal of Applied Physics* **1997**, *82* (3), 909-965. DOI: 10.1063/1.366536. Heinrich, J. L.; Curtis, C. L.; Credo, G. M.; Sailor, M. J.; Kavanagh, K. L. Luminescent Colloidal Silicon Suspensions from Porous Silicon. *Science* **1992**, *255* (5040), 66-68. DOI: doi:10.1126/science.255.5040.66.
(83) Park, J.-H.; Gu, L.; von Maltzahn, G.; Ruoslahti, E.; Bhatia, S. N.; Sailor, M. J. Biodegradable luminescent porous silicon nanoparticles for in vivo applications. *Nature Materials* **2009**, *8* (4), 331-336. DOI: 10.1038/nmat2398. Lin, V. S.-Y.; Motesharei, K.; Dancil, K.-P. S.; Sailor, M. J.; Ghadiri, M. R. A Porous Silicon-Based Optical Interferometric Biosensor. *Science* **1997**, *278* (5339), 840-843. DOI: doi:10.1126/science.278.5339.840. Niccolai, L.; Bassetto, M.; Quarta, A. A.; Mengali, G. A review of Smart Dust architecture, dynamics, and mission applications. *Progress in Aerospace Sciences* **2019**, *106*, 1-14. DOI: https://doi.org/10.1016/j.paerosci.2019.01.003.
(84) Li, Q.; Luo, T.-Y.; Zhou, M.; Abroshan, H.; Huang, J.; Kim, H. J.; Rosi, N. L.; Shao, Z.; Jin, R. Silicon Nanoparticles with Surface Nitrogen: 90% Quantum Yield with Narrow Luminescence Bandwidth and the Ligand Structure Based Energy Law. *ACS Nano* **2016**, *10* (9), 8385-8393. DOI: 10.1021/acsnano.6b03113. Zhong, Y.; Sun, X.; Wang, S.; Peng, F.; Bao, F.; Su, Y.; Li, Y.; Lee, S.-T.; He, Y. Facile, Large-Quantity Synthesis of Stable, Tunable-Color Silicon Nanoparticles and Their Application for Long-Term Cellular Imaging. *ACS Nano* **2015**, *9* (6), 5958-5967. DOI: 10.1021/acsnano.5b00683. Gong, T.; Li, Y.; Lei, B.; Zhang, X.; Liu, Y.; Zhang, H. Solid-state silicon nanoparticles with color-tunable photoluminescence and multifunctional applications. *Journal of Materials Chemistry C* **2019**, *7* (20), 5962-5969, 10.1039/C9TC00938H. DOI: 10.1039/C9TC00938H.
(85) Pujari, S. P.; Driss, H.; Bannani, F.; van Lagen, B.; Zuilhof, H. One-Pot Gram-Scale Synthesis of Hydrogen-Terminated Silicon Nanoparticles. *Chemistry of Materials* **2018**, *30* (18), 6503-6512. DOI: 10.1021/acs.chemmater.8b03113.
(86) Hu, G.; Sun, Y.; Xie, Y.; Wu, S.; Zhang, X.; Zhuang, J.; Hu, C.; Lei, B.; Liu, Y. Synthesis of Silicon Quantum Dots with Highly Efficient Full-Band UV Absorption and Their Applications in Antiyellowing and Resistance of Photodegradation. *ACS Applied Materials & Interfaces* **2019**, *11* (6), 6634-6643. DOI: 10.1021/acsami.8b20138.

(87) Wells, A. S. On the Perils of Unexpected Silane Generation. *Organic Process Research & Development* **2010**, *14* (3), 484-484. DOI: 10.1021/op100080v.
(88) Rosso-Vasic, M.; Spruijt, E.; van Lagen, B.; De Cola, L.; Zuilhof, H. Alkyl-Functionalized Oxide-Free Silicon Nanoparticles: Synthesis and Optical Properties. *Small* **2008**, *4* (10), 1835-1841. DOI: https://doi.org/10.1002/smll.200800066.
(89) Wang, X.; Zhuang, J.; Peng, Q.; Li, Y. A general strategy for nanocrystal synthesis. *Nature* **2005**, *437* (7055), 121-124. DOI: 10.1038/nature03968.
(90) Albanese, A.; Tang, P. S.; Chan, W. C. W. The Effect of Nanoparticle Size, Shape, and Surface Chemistry on Biological Systems. *Annual Review of Biomedical Engineering* **2012**, *14* (1), 1-16. DOI: 10.1146/annurev-bioeng-071811-150124.
(91) Reiss, P.; Protière, M.; Li, L. Core/Shell Semiconductor Nanocrystals. *Small* **2009**, *5* (2), 154-168. DOI: https://doi.org/10.1002/smll.200800841.
(92) Thiessen, A. N.; Zhang, L.; Oliynyk, A. O.; Yu, H.; O'Connor, K. M.; Meldrum, A.; Veinot, J. G. C. A Tale of Seemingly "Identical" Silicon Quantum Dot Families: Structural Insight into Silicon Quantum Dot Photoluminescence. *Chemistry of Materials* **2020**, *32* (16), 6838-6846. DOI: 10.1021/acs.chemmater.0c00650.
(93) Thiessen, A. N.; Ha, M.; Hooper, R. W.; Yu, H.; Oliynyk, A. O.; Veinot, J. G. C.; Michaelis, V. K. Silicon Nanoparticles: Are They Crystalline from the Core to the Surface? *Chemistry of Materials* **2019**, *31* (3), 678-688. DOI: 10.1021/acs.chemmater.8b03074.
(94) Shu, Y.; Kortshagen, U. R.; Levine, B. G.; Anthony, R. J. Surface Structure and Silicon Nanocrystal Photoluminescence: The Role of Hypervalent Silyl Groups. *The Journal of Physical Chemistry C* **2015**, *119* (47), 26683-26691. DOI: 10.1021/acs.jpcc.5b08578. Rowland, C. E.; Hannah, D. C.; Demortière, A.; Yang, J.; Cook, R. E.; Prakapenka, V. B.; Kortshagen, U.; Schaller, R. D. Silicon Nanocrystals at Elevated Temperatures: Retention of Photoluminescence and Diamond Silicon to β-Silicon Carbide Phase Transition. *ACS Nano* **2014**, *8* (9), 9219-9223. DOI: 10.1021/nn5029967.
(95) Clark, R. J.; Aghajamali, M.; Gonzalez, C. M.; Hadidi, L.; Islam, M. A.; Javadi, M.; Mobarok, M. H.; Purkait, T. K.; Robidillo, C. J. T.; Sinelnikov, R.; et al. From hydrogen silsesquioxane to functionalized silicon nanocrystals. *Chemistry of Materials* **2017**, *29* (1), 80-89. DOI: 10.1021/acs.chemmater.6b02667.
(96) Pi, X. D.; Mangolini, L.; Campbell, S. A.; Kortshagen, U. Room-temperature atmospheric oxidation of Si nanocrystals after HF etching. *Physical Review B* **2007**, *75* (8), 085423. DOI: 10.1103/PhysRevB.75.085423.
(97) Yu, Y.; Lu, X.; Guillaussier, A.; Voggu, V. R.; Pineros, W.; de la Mata, M.; Arbiol, J.; Smilgies, D.-M.; Truskett, T. M.; Korgel, B. A. Orientationally Ordered Silicon Nanocrystal Cuboctahedra in Superlattices. *Nano Letters* **2016**, *16* (12), 7814-7821. DOI: 10.1021/acs.nanolett.6b04006.
(98) Hannah, D. C.; Yang, J.; Kramer, N. J.; Schatz, G. C.; Kortshagen, U. R.; Schaller, R. D. Ultrafast Photoluminescence in Quantum-Confined Silicon Nanocrystals Arises from an Amorphous Surface Layer. *ACS Photonics* **2014**, *1* (10), 960-967. DOI: 10.1021/ph500145p.
(99) Anthony, R.; Kortshagen, U. Photoluminescence quantum yields of amorphous and crystalline silicon nanoparticles. *Physical Review B* **2009**, *80* (11), 115407. DOI: 10.1103/PhysRevB.80.115407.
(100) Petkov, V.; Hessel, C. M.; Ovtchinnikoff, J.; Guillaussier, A.; Korgel, B. A.; Liu, X.; Giordano, C. Structure–Properties Correlation in Si Nanoparticles by Total Scattering and

Computer Simulations. *Chemistry of Materials* **2013**, *25* (11), 2365-2371. DOI: 10.1021/cm401099q.
(101) Mazzaro, R.; Romano, F.; Ceroni, P. Long-lived luminescence of silicon nanocrystals: from principles to applications. *Physical Chemistry Chemical Physics* **2017**, *19* (39), 26507-26526, 10.1039/C7CP05208A. DOI: 10.1039/C7CP05208A.
(102) Wheeler, L. M.; Anderson, N. C.; Palomaki, P. K. B.; Blackburn, J. L.; Johnson, J. C.; Neale, N. R. Silyl Radical Abstraction in the Functionalization of Plasma-Synthesized Silicon Nanocrystals. *Chemistry of Materials* **2015**, *27* (19), 6869-6878. DOI: 10.1021/acs.chemmater.5b03309.
(103) Jarolimek, K.; Hazrati, E.; de Groot, R. A.; de Wijs, G. A. Band Offsets at the Interface between Crystalline and Amorphous Silicon from First Principles. *Physical Review Applied* **2017**, *8* (1), 014026. DOI: 10.1103/PhysRevApplied.8.014026. Vatan Meidanshahi, R.; Bowden, S.; Goodnick, S. M. Electronic structure and localized states in amorphous Si and hydrogenated amorphous Si. *Physical Chemistry Chemical Physics* **2019**, *21* (24), 13248-13257, 10.1039/C9CP01121H. DOI: 10.1039/C9CP01121H.
(104) Guha, S.; Yang, J.; Yan, B. Amorphous and Nanocrystalline Silicon Solar Cells and Modules. In *Reference Module in Materials Science and Materials Engineering*, Elsevier, 2016.
(105) Park, N.-M.; Kim, T.-S.; Park, S.-J. Band gap engineering of amorphous silicon quantum dots for light-emitting diodes. *Applied Physics Letters* **2001**, *78* (17), 2575-2577. DOI: 10.1063/1.1367277.
(106) Park, N.-M.; Choi, C.-J.; Seong, T.-Y.; Park, S.-J. Quantum Confinement in Amorphous Silicon Quantum Dots Embedded in Silicon Nitride. *Physical Review Letters* **2001**, *86* (7), 1355-1357. DOI: 10.1103/PhysRevLett.86.1355.
(107) Askari, S.; Svrcek, V.; Maguire, P.; Mariotti, D. The Interplay of Quantum Confinement and Hydrogenation in Amorphous Silicon Quantum Dots. *Advanced Materials* **2015**, *27* (48), 8011-8016. DOI: https://doi.org/10.1002/adma.201503013.
(108) Lisovskyy, I.; Voitovych, M.; Litovchenko, V.; Voitovych, V.; Nasieka, I.; Bratus, V. Radiation Induced Enhancement of Hydrogen Influence on Luminescent Properties of nc-Si/SiO2 Structures. *Nanoscale Research Letters* **2016**, *11* (1), 545. DOI: 10.1186/s11671-016-1744-7. Cheylan, S.; Elliman, R. G. Effect of hydrogen on the photoluminescence of Si nanocrystals embedded in a SiO2 matrix. *Applied Physics Letters* **2001**, *78* (9), 1225-1227. DOI: 10.1063/1.1338492.
(109) Wang, Q.; Xu, B.; Sun, J.; Liu, H.; Zhao, Z.; Yu, D.; Fan, C.; He, J. Direct Band Gap Silicon Allotropes. *Journal of the American Chemical Society* **2014**, *136* (28), 9826-9829. DOI: 10.1021/ja5035792. Guo, Y.; Wang, Q.; Kawazoe, Y.; Jena, P. A New Silicon Phase with Direct Band Gap and Novel Optoelectronic Properties. *Scientific Reports* **2015**, *5* (1), 14342. DOI: 10.1038/srep14342.
(110) Hannah, D. C.; Yang, J.; Podsiadlo, P.; Chan, M. K. Y.; Demortière, A.; Gosztola, D. J.; Prakapenka, V. B.; Schatz, G. C.; Kortshagen, U.; Schaller, R. D. On the Origin of Photoluminescence in Silicon Nanocrystals: Pressure-Dependent Structural and Optical Studies. *Nano Letters* **2012**, *12* (8), 4200-4205. DOI: 10.1021/nl301787g.
(111) Kůsová, K.; Hapala, P.; Valenta, J.; Jelínek, P.; Cibulka, O.; Ondič, L.; Pelant, I. Direct Bandgap Silicon: Tensile-Strained Silicon Nanocrystals. *Advanced Materials Interfaces* **2014**, *1* (2), 1300042. DOI: https://doi.org/10.1002/admi.201300042.
(112) Hannah, D. C.; Yang, J.; Kramer, N. J.; Schatz, G. C.; Kortshagen, U. R.; Schaller, R. D. Reply to "Comment on 'Ultrafast Photoluminescence in Quantum-Confined Silicon

Nanocrystals Arises from an Amorphous Surface Layer'". *ACS Photonics* **2015**, *2* (3), 456-458. DOI: 10.1021/ph500490a. Kůsová, K.; Ondič, L.; Pelant, I. Comment on "Ultrafast Photoluminescence in Quantum-Confined Silicon Nanocrystals Arises from an Amorphous Surface Layer". *ACS Photonics* **2015**, *2* (3), 454-455. DOI: 10.1021/ph500403j.
(113) Mobarok, M. H.; Purkait, T. K.; Islam, M. A.; Miskolzie, M.; Veinot, J. G. C. Instantaneous Functionalization of Chemically Etched Silicon Nanocrystal Surfaces. *Angewandte Chemie International Edition* **2016**, *56* (22), 6073-6077. DOI: 10.1002/anie.201609651.
(114) Kovacs, G. T. A.; Maluf, N. I.; Petersen, K. E. Bulk micromachining of silicon. *Proceedings of the IEEE* **1998**, *86* (8), 1536-1551. DOI: 10.1109/5.704259. Bansal, A.; Li, X.; Lauermann, I.; Lewis, N. S.; Yi, S. I.; Weinberg, W. H. Alkylation of Si Surfaces Using a Two-Step Halogenation/Grignard Route. *Journal of the American Chemical Society* **1996**, *118* (30), 7225-7226. DOI: 10.1021/ja960348n. Rivillon, S.; Chabal, Y. J.; Webb, L. J.; Michalak, D. J.; Lewis, N. S.; Halls, M. D.; Raghavachari, K. Chlorination of hydrogen-terminated silicon (111) surfaces. *Journal of Vacuum Science & Technology A* **2005**, *23* (4), 1100-1106. DOI: 10.1116/1.1861941.
(115) Satpathy, R.; Pamuru, V. Chapter 4 - Making of crystalline silicon solar cells. In *Solar PV Power*, Satpathy, R., Pamuru, V. Eds.; Academic Press, 2021; pp 71-134.
(116) Johnson, N. M. Mechanism for hydrogen compensation of shallow-acceptor impurities in single-crystal silicon. *Physical Review B* **1985**, *31* (8), 5525-5528. DOI: 10.1103/PhysRevB.31.5525. Caldas, M. J.; Fazzio, A.; Zunger, A. A universal trend in the binding energies of deep impurities in semiconductors. *Applied Physics Letters* **1984**, *45* (6), 671-673. DOI: 10.1063/1.95351.
(117) Bullis, W. M. Properties of gold in silicon. *Solid-State Electronics* **1966**, *9* (2), 143-168. DOI: https://doi.org/10.1016/0038-1101(66)90085-2.
(118) Oliva-Chatelain, B. L.; Ticich, T. M.; Barron, A. R. Doping silicon nanocrystals and quantum dots. *Nanoscale* **2016**, *8* (4), 1733-1745. DOI: 10.1039/c5nr04978d.
(119) Chan, T.-L.; Zhang, S. B.; Chelikowsky, J. R. An effective one-particle theory for formation energies in doping Si nanostructures. *Applied Physics Letters* **2011**, *98* (13), 133116. DOI: 10.1063/1.3571552.
(120) Hiller, D.; López-Vidrier, J.; Gutsch, S.; Zacharias, M.; Wahl, M.; Bock, W.; Brodyanski, A.; Kopnarski, M.; Nomoto, K.; Valenta, J.; et al. Boron-Incorporating Silicon Nanocrystals Embedded in SiO2: Absence of Free Carriers vs. B-Induced Defects. *Scientific Reports* **2017**, *7* (1), 8337. DOI: 10.1038/s41598-017-08814-0.
(121) Dalpian, G. M.; Chelikowsky, J. R. Self-Purification in Semiconductor Nanocrystals. *Physical Review Letters* **2006**, *96* (22), 226802. DOI: 10.1103/PhysRevLett.96.226802.
(122) Gutsch, S.; Laube, J.; Hiller, D.; Bock, W.; Wahl, M.; Kopnarski, M.; Gnaser, H.; Puthen-Veettil, B.; Zacharias, M. Electronic properties of phosphorus doped silicon nanocrystals embedded in SiO2. *Applied Physics Letters* **2015**, *106* (11), 113103. DOI: 10.1063/1.4915307. Huang, S.; So, Y. H.; Conibeer, G.; Green, M. Doping of Silicon Quantum Dots Embedded in Nitride Matrix for All-Silicon Tandem Cells. *Japanese Journal of Applied Physics* **2012**, *51*, 10NE10. DOI: 10.1143/jjap.51.10ne10.
(123) Zhou, S.; Pi, X.; Ni, Z.; Ding, Y.; Jiang, Y.; Jin, C.; Delerue, C.; Yang, D.; Nozaki, T. Comparative Study on the Localized Surface Plasmon Resonance of Boron- and Phosphorus-Doped Silicon Nanocrystals. *ACS Nano* **2015**, *9* (1), 378-386. DOI: 10.1021/nn505416r.

(124) Kramer, N. J.; Schramke, K. S.; Kortshagen, U. R. Plasmonic Properties of Silicon Nanocrystals Doped with Boron and Phosphorus. *Nano Letters* **2015**, *15* (8), 5597-5603. DOI: 10.1021/acs.nanolett.5b02287.
(125) Rowe, D. J.; Jeong, J. S.; Mkhoyan, K. A.; Kortshagen, U. R. Phosphorus-Doped Silicon Nanocrystals Exhibiting Mid-Infrared Localized Surface Plasmon Resonance. *Nano Letters* **2013**, *13* (3), 1317-1322. DOI: 10.1021/nl4001184.
(126) Ni, Z.; Pi, X.; Zhou, S.; Nozaki, T.; Grandidier, B.; Yang, D. Size-Dependent Structures and Optical Absorption of Boron-Hyperdoped Silicon Nanocrystals. *Advanced Optical Materials* **2016**, *4* (5), 700-707. DOI: https://doi.org/10.1002/adom.201500706.
(127) Borowik, Ł.; Nguyen-Tran, T.; Cabarrocas, P. R. i.; Mélin, T. Doped semiconductor nanocrystal junctions. *Journal of Applied Physics* **2013**, *114* (20), 204305. DOI: 10.1063/1.4834516.
(128) Rohani, P.; Banerjee, S.; Sharifi-Asl, S.; Malekzadeh, M.; Shahbazian-Yassar, R.; Billinge, S. J. L.; Swihart, M. T. Synthesis and Properties of Plasmonic Boron-Hyperdoped Silicon Nanoparticles. *Advanced Functional Materials* **2019**, *29* (8), 1807788. DOI: https://doi.org/10.1002/adfm.201807788.
(129) Chandra, S.; Masuda, Y.; Shirahata, N.; Winnik, F. M. Transition-Metal-Doped NIR-Emitting Silicon Nanocrystals. *Angewandte Chemie International Edition* **2017**, *56* (22), 6157-6160. DOI: https://doi.org/10.1002/anie.201700436.
(130) Rocks, C.; Svrcek, V.; Velusamy, T.; Macias-Montero, M.; Maguire, P.; Mariotti, D. Type-I alignment in MAPbI3 based solar devices with doped-silicon nanocrystals. *Nano Energy* **2018**, *50*, 245-255. DOI: https://doi.org/10.1016/j.nanoen.2018.05.036.
(131) Fujii, M.; Fujii, R.; Takada, M.; Sugimoto, H. Silicon Quantum Dot Supraparticles for Fluorescence Bioimaging. *ACS Applied Nano Materials* **2020**, *3* (6), 6099-6107. DOI: 10.1021/acsanm.0c01295. Sugimoto, H.; Fujii, M.; Imakita, K.; Hayashi, S.; Akamatsu, K. All-Inorganic Near-Infrared Luminescent Colloidal Silicon Nanocrystals: High Dispersibility in Polar Liquid by Phosphorus and Boron Codoping. *The Journal of Physical Chemistry C* **2012**, *116* (33), 17969-17974. DOI: 10.1021/jp305832x.
(132) Almeida, A. J.; Sugimoto, H.; Fujii, M.; Brandt, M. S.; Stutzmann, M.; Pereira, R. N. Doping efficiency and confinement of donors in embedded and free standing Si nanocrystals. *Physical Review B* **2016**, *93* (11), 115425. DOI: 10.1103/PhysRevB.93.115425.
(133) Borowik, Ł.; Nguyen-Tran, T.; Roca i Cabarrocas, P.; Mélin, T. Doped semiconductor nanocrystal junctions. *Journal of Applied Physics* **2013**, *114* (20), 204305. DOI: 10.1063/1.4834516.
(134) Nayak, P. K.; Mahesh, S.; Snaith, H. J.; Cahen, D. Photovoltaic solar cell technologies: analysing the state of the art. *Nature Reviews Materials* **2019**, *4* (4), 269-285. DOI: 10.1038/s41578-019-0097-0. Mazzaro, R.; Gradone, A.; Angeloni, S.; Morselli, G.; Cozzi, P. G.; Romano, F.; Vomiero, A.; Ceroni, P. Hybrid Silicon Nanocrystals for Color-Neutral and Transparent Luminescent Solar Concentrators. *ACS Photonics* **2019**, *6* (9), 2303-2311. DOI: 10.1021/acsphotonics.9b00802. Meinardi, F.; Ehrenberg, S.; Dhamo, L.; Carulli, F.; Mauri, M.; Bruni, F.; Simonutti, R.; Kortshagen, U.; Brovelli, S. Highly efficient luminescent solar concentrators based on earth-abundant indirect-bandgap silicon quantum dots. *Nature Photonics* **2017**, *11* (3), 177-185. DOI: 10.1038/nphoton.2017.5.
(135) Velusamy, T.; Mitra, S.; Macias-Montero, M.; Svrcek, V.; Mariotti, D. Varying Surface Chemistries for p-Doped and n-Doped Silicon Nanocrystals and Impact on Photovoltaic Devices. *ACS Applied Materials & Interfaces* **2015**, *7* (51), 28207-28214. DOI: 10.1021/acsami.5b06577.

(136) Brongersma, M. L.; Shalaev, V. M. The Case for Plasmonics. *Science* **2010**, *328* (5977), 440-441. DOI: doi:10.1126/science.1186905.
(137) Zhong, Y.; Malagari, S. D.; Hamilton, T.; Wasserman, D. Review of mid-infrared plasmonic materials. *Journal of Nanophotonics* **2015**, *9* (1), 093791. Baldassarre, L.; Sakat, E.; Frigerio, J.; Samarelli, A.; Gallacher, K.; Calandrini, E.; Isella, G.; Paul, D. J.; Ortolani, M.; Biagioni, P. Midinfrared Plasmon-Enhanced Spectroscopy with Germanium Antennas on Silicon Substrates. *Nano Letters* **2015**, *15* (11), 7225-7231. DOI: 10.1021/acs.nanolett.5b03247.
(138) Ni, Z.; Ma, L.; Du, S.; Xu, Y.; Yuan, M.; Fang, H.; Wang, Z.; Xu, M.; Li, D.; Yang, J.; et al. Plasmonic Silicon Quantum Dots Enabled High-Sensitivity Ultrabroadband Photodetection of Graphene-Based Hybrid Phototransistors. *ACS Nano* **2017**, *11* (10), 9854-9862. DOI: 10.1021/acsnano.7b03569.
(139) Podhorodecki, A.; Zatryb, G.; Golacki, L. W.; Misiewicz, J.; Wojcik, J.; Mascher, P. On the origin of emission and thermal quenching of SRSO:Er3+ films grown by ECR-PECVD. *Nanoscale Research Letters* **2013**, *8* (1), 98. DOI: 10.1186/1556-276X-8-98. Hiller, D.; López-Vidrier, J.; Gutsch, S.; Zacharias, M.; Nomoto, K.; König, D. Defect-Induced Luminescence Quenching vs. Charge Carrier Generation of Phosphorus Incorporated in Silicon Nanocrystals as Function of Size. *Scientific Reports* **2017**, *7* (1), 863. DOI: 10.1038/s41598-017-01001-1. Tchebotareva, A. L.; de Dood, M. J. A.; Biteen, J. S.; Atwater, H. A.; Polman, A. Quenching of Si nanocrystal photoluminescence by doping with gold or phosphorous. *Journal of Luminescence* **2005**, *114* (2), 137-144. DOI: https://doi.org/10.1016/j.jlumin.2004.12.014.
(140) Limpens, R.; Fujii, M.; Neale, N. R.; Gregorkiewicz, T. Negligible Electronic Interaction between Photoexcited Electron–Hole Pairs and Free Electrons in Phosphorus–Boron Co-Doped Silicon Nanocrystals. *The Journal of Physical Chemistry C* **2018**, *122* (11), 6397-6404. DOI: 10.1021/acs.jpcc.7b12313.
(141) Limpens, R.; Sugimoto, H.; Neale, N. R.; Fujii, M. Critical Size for Carrier Delocalization in Doped Silicon Nanocrystals: A Study by Ultrafast Spectroscopy. *ACS Photonics* **2018**, *5* (10), 4037-4045. DOI: 10.1021/acsphotonics.8b00671.
(142) Limpens, R.; Neale, N. R. Free electron-driven photophysics in n-type doped silicon nanocrystals. *Nanoscale* **2018**, *10* (25), 12068-12077, 10.1039/C8NR02173B. DOI: 10.1039/C8NR02173B.
(143) Newman, R. C. Defects in silicon. *Reports on Progress in Physics* **1982**, *45* (10), 1163-1210. DOI: 10.1088/0034-4885/45/10/003.
(144) Lu, P.; Mu, W.; Xu, J.; Zhang, X.; Zhang, W.; Li, W.; Xu, L.; Chen, K. Phosphorus Doping in Si Nanocrystals/SiO2 Multilayers and Light Emission with Wavelength Compatible for Optical Telecommunication. *Scientific Reports* **2016**, *6* (1), 22888. DOI: 10.1038/srep22888. Li, D.; Jiang, Y.; Liu, J.; Zhang, P.; Xu, J.; Li, W.; Chen, K. Modulation of surface states by phosphorus to improve the optical properties of ultra-small Si nanocrystals. *Nanotechnology* **2017**, *28* (47), 475704. DOI: 10.1088/1361-6528/aa852e.
(145) Hiller, D.; López-Vidrier, J.; Gutsch, S.; Zacharias, M.; Wahl, M.; Bock, W.; Brodyanski, A.; Kopnarski, M.; Nomoto, K.; Valenta, J.; et al. Boron-Incorporating Silicon Nanocrystals Embedded in SiO2: Absence of Free Carriers vs. B-Induced Defects. *Scientific Reports* **2017**, *7* (1). DOI: 10.1038/s41598-017-08814-0. Nakamura, T.; Adachi, S.; Fujii, M.; Sugimoto, H.; Miura, K.; Yamamoto, S. Size and dopant-concentration dependence of photoluminescence properties of ion-implanted phosphorus- and boron-codoped Si nanocrystals. *Physical Review B* **2015**, *91* (16), 165424. DOI: 10.1103/PhysRevB.91.165424.

(146) Veettil, B. P.; Wu, L.; Jia, X.; Lin, Z.; Zhang, T.; Yang, T.; Johnson, C.; McCamey, D.; Conibeer, G.; Perez-Würfl, I. Passivation effects in B doped self-assembled Si nanocrystals. *Applied Physics Letters* **2014**, *105* (22), 222108. DOI: 10.1063/1.4903776. Sugimoto, H.; Zhou, H.; Takada, M.; Fushimi, J.; Fujii, M. Visible-light driven photocatalytic hydrogen generation by water-soluble all-inorganic core–shell silicon quantum dots. *Journal of Materials Chemistry A* **2020**, *8* (31), 15789-15794, 10.1039/D0TA01071E. DOI: 10.1039/D0TA01071E. Stegner, A. R.; Pereira, R. N.; Lechner, R.; Klein, K.; Wiggers, H.; Stutzmann, M.; Brandt, M. S. Doping efficiency in freestanding silicon nanocrystals from the gas phase: Phosphorus incorporation and defect-induced compensation. *Physical Review B* **2009**, *80* (16), 165326. DOI: 10.1103/PhysRevB.80.165326. Fujii, M.; Mimura, A.; Hayashi, S.; Yamamoto, K. Photoluminescence from Si nanocrystals dispersed in phosphosilicate glass thin films: Improvement of photoluminescence efficiency. *Applied Physics Letters* **1999**, *75* (2), 184-186. DOI: 10.1063/1.124313.
(147) Iori, F.; Ossicini, S. Effects of simultaneous doping with boron and phosphorous on the structural, electronic and optical properties of silicon nanostructures. *Physica E: Low-dimensional Systems and Nanostructures* **2009**, *41* (6), 939-946. DOI: https://doi.org/10.1016/j.physe.2008.08.010.
(148) Fujii, M.; Sugimoto, H.; Imakita, K. All-inorganic colloidal silicon nanocrystals—surface modification by boron and phosphorus co-doping. *Nanotechnology* **2016**, *27* (26), 262001. DOI: 10.1088/0957-4484/27/26/262001.
(149) Li, H.; Guan, L.; Zhang, X.; Yu, H.; Huang, D.; Sun, M.; Wang, S. A cyanine-based near-infrared fluorescent probe for highly sensitive and selective detection of hypochlorous acid and bioimaging. *Talanta* **2016**, *161*, 592-598. DOI: https://doi.org/10.1016/j.talanta.2016.09.008.
(150) Peng, F.; Cao, Z.; Ji, X.; Chu, B.; Su, Y.; He, Y. Silicon nanostructures for cancer diagnosis and therapy. *Nanomedicine* **2015**, *10* (13), 2109-2123. DOI: 10.2217/nnm.15.53. Ghosh, B.; Shirahata, N. Colloidal silicon quantum dots: synthesis and luminescence tuning from the near-UV to the near-IR range. *Sci Technol Adv Mater* **2014**, *15* (1), 014207. DOI: 10.1088/1468-6996/15/1/014207. Peng, F.; Su, Y.; Zhong, Y.; Fan, C.; Lee, S.-T.; He, Y. Silicon Nanomaterials Platform for Bioimaging, Biosensing, and Cancer Therapy. *Accounts of Chemical Research* **2014**, *47* (2), 612-623. DOI: 10.1021/ar400221g.
(151) Fujii, M.; Fujii, R.; Takada, M.; Sugimoto, H. Silicon Quantum Dot Supraparticles for Fluorescence Bioimaging. *ACS Applied Materials and Interfaces* **2020**, *3* (6), 6099-6107. DOI: 10.1021/acsanm.0c01295.
(152) Limpens, R.; Pach, G. F.; Neale, N. R. Nonthermal Plasma-Synthesized Phosphorus–Boron co-Doped Si Nanocrystals: A New Approach to Nontoxic NIR-Emitters. *Chemistry of Materials* **2019**, *31* (12), 4426-4435. DOI: 10.1021/acs.chemmater.9b00810.
(153) McVey, B. F. P.; König, D.; Cheng, X.; O'Mara, P. B.; Seal, P.; Tan, X.; Tahini, H. A.; Smith, S. C.; Gooding, J. J.; Tilley, R. D. Synthesis, optical properties and theoretical modelling of discrete emitting states in doped silicon nanocrystals for bioimaging. *Nanoscale* **2018**, *10* (33), 15600-15607, 10.1039/C8NR05071F. DOI: 10.1039/C8NR05071F.
(154) Clark, R. J.; Dang, M. K. M.; Veinot, J. G. C. Exploration of Organic Acid Chain Length on Water-Soluble Silicon Quantum Dot Surfaces. *Langmuir* **2010**, *26* (19), 15657-15664. DOI: 10.1021/la102983c. Aghajamali, M.; Xie, H.; Javadi, M.; Kalisvaart, W. P.; Buriak, J. M.; Veinot, J. G. C. Size and Surface Effects of Silicon Nanocrystals in Graphene Aerogel Composite Anodes for Lithium Ion Batteries. *Chemistry of Materials* **2018**, *30* (21), 7782-7792. DOI: 10.1021/acs.chemmater.8b03198. Yang, Z.; Gonzalez, C. M.; Purkait, T. K.; Iqbal, M.;

Meldrum, A.; Veinot, J. G. C. Radical Initiated Hydrosilylation on Silicon Nanocrystal Surfaces: An Evaluation of Functional Group Tolerance and Mechanistic Study. *Langmuir* **2015**, *31* (38), 10540-10548. DOI: 10.1021/acs.langmuir.5b02307. Yu, Y.; Hessel, C. M.; Bogart, T. D.; Panthani, M. G.; Rasch, M. R.; Korgel, B. A. Room Temperature Hydrosilylation of Silicon Nanocrystals with Bifunctional Terminal Alkenes. *Langmuir* **2013**, *29* (5), 1533-1540. DOI: 10.1021/la304874y.
(155) Dasog, M.; Bader, K.; Veinot, J. G. C. Influence of Halides on the Optical Properties of Silicon Quantum Dots. *Chemistry of Materials* **2015**, *27* (4), 1153-1156. DOI: 10.1021/acs.chemmater.5b00115.
(156) Islam, M. A.; Purkait, T. K.; Veinot, J. G. C. Chloride Surface Terminated Silicon Nanocrystal Mediated Synthesis of Poly(3-hexylthiophene). *Journal of the American Chemical Society* **2014**, *136* (43), 15130-15133. DOI: 10.1021/ja5075739.
(157) Wheeler, L. M.; Neale, N. R.; Chen, T.; Kortshagen, U. R. Hypervalent surface interactions for colloidal stability and doping of silicon nanocrystals. *Nature Communications* **2013**, *4* (1), 2197. DOI: 10.1038/ncomms3197.
(158) Kim, J.-S.; Yang, S.; Bae, B.-S. Thermally Stable Transparent Sol−Gel Based Siloxane Hybrid Material with High Refractive Index for Light Emitting Diode (LED) Encapsulation. *Chemistry of Materials* **2010**, *22* (11), 3549-3555. DOI: 10.1021/cm100903b.
(159) Bell, J. P.; Cloud, J. E.; Cheng, J.; Ngo, C.; Kodambaka, S.; Sellinger, A.; Ratanathanawongs Williams, S. K.; Yang, Y. N-Bromosuccinimide-based bromination and subsequent functionalization of hydrogen-terminated silicon quantum dots. *RSC Advances* **2014**, *4* (93), 51105-51110, 10.1039/C4RA08477B. DOI: 10.1039/C4RA08477B. Kehrle, J.; Höhlein, I. M. D.; Yang, Z.; Jochem, A.-R.; Helbich, T.; Kraus, T.; Veinot, J. G. C.; Rieger, B. Thermoresponsive and Photoluminescent Hybrid Silicon Nanoparticles by Surface-Initiated Group Transfer Polymerization of Diethyl Vinylphosphonate. *Angewandte Chemie International Edition* **2014**, *53* (46), 12494-12497. DOI: https://doi.org/10.1002/anie.201405946.
(160) Yu, Y.; Rowland, C. E.; Schaller, R. D.; Korgel, B. A. Synthesis and Ligand Exchange of Thiol-Capped Silicon Nanocrystals. *Langmuir* **2015**, *31* (24), 6886-6893. DOI: 10.1021/acs.langmuir.5b01246.
(161) Matsumoto, T.; Maeda, M.; Kobayashi, H. Photoluminescence Enhancement of Adsorbed Species on Si Nanoparticles. *Nanoscale Research Letters* **2016**, *11* (1), 7. DOI: 10.1186/s11671-015-1220-9.
(162) Sinelnikov, R.; Dasog, M.; Beamish, J.; Meldrum, A.; Veinot, J. G. C. Revisiting an Ongoing Debate: What Role Do Surface Groups Play in Silicon Nanocrystal Photoluminescence? *ACS Photonics* **2017**, *4* (8), 1920-1929. DOI: 10.1021/acsphotonics.7b00102.
(163) Wen, X.; Dao, L. V.; Hannaford, P. Temperature dependence of photoluminescence in silicon quantum dots. *Journal of Physics D: Applied Physics* **2007**, *40* (12), 3573-3578. DOI: 10.1088/0022-3727/40/12/005. Ledoux, G.; Gong, J.; Huisken, F.; Guillois, O.; Reynaud, C. Photoluminescence of size-separated silicon nanocrystals: Confirmation of quantum confinement. *Applied Physics Letters* **2002**, *80* (25), 4834-4836. DOI: 10.1063/1.1485302.
(164) Höhlein, I. M. D.; Angı, A.; Sinelnikov, R.; Veinot, J. G. C.; Rieger, B. Functionalization of Hydride-Terminated Photoluminescent Silicon Nanocrystals with Organolithium Reagents. *Chemistry – A European Journal* **2015**, *21* (7), 2755-2758. DOI: https://doi.org/10.1002/chem.201405555.

(165) Angı, A.; Sinelnikov, R.; Meldrum, A.; Veinot, J. G. C.; Balberg, I.; Azulay, D.; Millo, O.; Rieger, B. Photoluminescence through in-gap states in phenylacetylene functionalized silicon nanocrystals. *Nanoscale* **2016**, *8* (15), 7849-7853, 10.1039/C6NR01435F. DOI: 10.1039/C6NR01435F.
(166) Miyano, M.; Kitagawa, Y.; Wada, S.; Kawashima, A.; Nakajima, A.; Nakanishi, T.; Ishioka, J.; Shibayama, T.; Watanabe, S.; Hasegawa, Y. Photophysical properties of luminescent silicon nanoparticles surface-modified with organic molecules via hydrosilylation. *Photochemical & Photobiological Sciences* **2016**, *15* (1), 99-104. DOI: 10.1039/c5pp00364d.
(167) Yu, Y.; Korgel, B. A. Controlled Styrene Monolayer Capping of Silicon Nanocrystals by Room Temperature Hydrosilylation. *Langmuir* **2015**, *31* (23), 6532-6537. DOI: 10.1021/acs.langmuir.5b01291.
(168) Liu, X.; Zhao, S.; Gu, W.; Zhang, Y.; Qiao, X.; Ni, Z.; Pi, X.; Yang, D. Light-Emitting Diodes Based on Colloidal Silicon Quantum Dots with Octyl and Phenylpropyl Ligands. *ACS Applied Materials & Interfaces* **2018**, *10* (6), 5959-5966. DOI: 10.1021/acsami.7b16980. Mastronardi, M. L.; Henderson, E. J.; Puzzo, D. P.; Chang, Y.; Wang, Z. B.; Helander, M. G.; Jeong, J.; Kherani, N. P.; Lu, Z.; Ozin, G. A. Organic Light-Emitting Diodes: Silicon Nanocrystal OLEDs: Effect of Organic Capping Group on Performance (Small 23/2012). *Small* **2012**, *8* (23), 3542-3542. DOI: https://doi.org/10.1002/smll.201290131.
(169) Angı, A.; Sinelnikov, R.; Heenen, H. H.; Meldrum, A.; Veinot, J. G. C.; Scheurer, C.; Reuter, K.; Ashkenazy, O.; Azulay, D.; Balberg, I.; et al. The influence of conjugated alkynyl(aryl) surface groups on the optical properties of silicon nanocrystals: photoluminescence through in-gap states. *Nanotechnology* **2018**, *29* (35), 355705. DOI: 10.1088/1361-6528/aac9ef.

Chapter 2:

(1) Oliva-Chatelain, B. L.; Ticich, T. M.; Barron, A. R. Doping silicon nanocrystals and quantum dots. *Nanoscale* **2016**, *8* (4), 1733-1745. DOI: 10.1039/c5nr04978d.
(2) Canham, L. Introductory lecture: origins and applications of efficient visible photoluminescence from silicon-based nanostructures. *Faraday Discussions* **2020**, *222*, 10-81. DOI: 10.1039/d0fd00018c.
(3) Brus, L. E. A simple model for the ionization potential, electron affinity, and aqueous redox potentials of small semiconductor crystallites. *The Journal of Chemical Physics* **1983**, *79* (11), 5566-5571. DOI: 10.1063/1.445676.
(4) Kuhlmann, A. M. The Second Most Abundant Element in the Earth's Crust. *JOM* **1963**, *15* (7), 502-505. DOI: 10.1007/bf03378936.
(5) Erogbogbo, F.; Yong, K.-T.; Roy, I.; Xu, G.; Prasad, P. N.; Swihart, M. T. Biocompatible Luminescent Silicon Quantum Dots for Imaging of Cancer Cells. *ACS Nano* **2008**, *2* (5), 873-878. DOI: 10.1021/nn700319z. Bhattacharjee, S.; Rietjens, I. M. C. M.; Singh, M. P.; Atkins, T. M.; Purkait, T. K.; Xu, Z.; Regli, S.; Shukaliak, A.; Clark, R. J.; Mitchell, B. S.; et al. Cytotoxicity of surface-functionalized silicon and germanium nanoparticles: the dominant role of surface charges. *Nanoscale* **2013**, *5* (11), 4870. DOI: 10.1039/c3nr34266b.
(6) Hessel, C. M.; Reid, D.; Panthani, M. G.; Rasch, M. R.; Goodfellow, B. W.; Wei, J.; Fujii, H.; Akhavan, V.; Korgel, B. A. Synthesis of ligand-stabilized silicon nanocrystals with size-dependent photoluminescence spanning visible to near-infrared wavelengths. *Chemistry of Materials* **2012**, *24* (2), 393-401. DOI: 10.1021/cm2032866. Mastronardi, M. L.; Maier-Flaig, F.; Faulkner, D.; Henderson, E. J.; Kübel, C.; Lemmer, U.; Ozin, G. A. Size-Dependent Absolute

Quantum Yields for Size-Separated Colloidally-Stable Silicon Nanocrystals. *Nano Letters* **2011**, *12* (1), 337-342. DOI: 10.1021/nl2036194.
(7) Nakamine, Y.; Kodera, T.; Uchida, K.; Oda, S. Removal of Surface Oxide Layer from Silicon Nanocrystals by Hydrogen Fluoride Vapor Etching. *Japanese Journal of Applied Physics* **2011**, *50*, 115002. DOI: 10.1143/jjap.50.115002.
(8) Yang, Z.; De Los Reyes, G. B.; Titova, L. V.; Sychugov, I.; Dasog, M.; Linnros, J.; Hegmann, F. A.; Veinot, J. G. C. Evolution of the Ultrafast Photoluminescence of Colloidal Silicon Nanocrystals with Changing Surface Chemistry. *ACS Photonics* **2015**, *2* (5), 595-605. DOI: 10.1021/acsphotonics.5b00143. Boukherroub, R.; Morin, S.; Wayner, D. D. M.; Bensebaa, F.; Sproule, G. I.; Baribeau, J. M.; Lockwood, D. J. Ideal Passivation of Luminescent Porous Silicon by Thermal, Noncatalytic Reaction with Alkenes and Aldehydes†. *Chemistry of Materials* **2001**, *13* (6), 2002-2011. DOI: 10.1021/cm000790b. Jurbergs, D.; Rogojina, E.; Mangolini, L.; Kortshagen, U. Silicon nanocrystals with ensemble quantum yields exceeding 60%. *Appl. Phys. Lett.* **2006**, *88* (1), 233116. DOI: 10.1063/1.2210788. Rosso-Vasic, M.; Spruijt, E.; van Lagen, B.; De Cola, L.; Zuilhof, H. Alkyl-Functionalized Oxide-Free Silicon Nanoparticles: Synthesis and Optical Properties. *Small* **2008**, *4*, 1835-1841. DOI: 10.1002/smll.200800066. Sato, S.; Swihart, M. T. Propionic-Acid-Terminated Silicon Nanoparticles: Synthesis and Optical Characterization. *Chemistry of Materials* **2006**, *18* (17), 4083-4088. DOI: 10.1021/cm060750t.
(9) Kelly, J. A.; Veinot, J. G. C. An Investigation into Near-UV Hydrosilylation of Freestanding Silicon Nanocrystals. *ACS Nano* **2010**, *4* (8), 4645-4656. DOI: 10.1021/nn101022b.
(10) Dasog, M.; De Los Reyes, G. B.; Titova, L. V.; Hegmann, F. A.; Veinot, J. G. C. Size vs Surface: Tuning the Photoluminescence of Freestanding Silicon Nanocrystals Across the Visible Spectrum via Surface Groups. *ACS Nano* **2014**, *8* (9), 9636-9648. DOI: 10.1021/nn504109a. Dasog, M.; Bader, K.; Veinot, J. G. C. Influence of Halides on the Optical Properties of Silicon Quantum Dots. *Chemistry of Materials* **2015**, *27* (4), 1153-1156. DOI: 10.1021/acs.chemmater.5b00115.
(11) Islam, M. A.; Mobarok, M. H.; Sinelnikov, R.; Purkait, T. K.; Veinot, J. G. C. Phosphorus Pentachloride Initiated Functionalization of Silicon Nanocrystals. *Langmuir* **2017**, *33* (35), 8766-8773. DOI: 10.1021/acs.langmuir.7b00518.
(12) Mobarok, M. H.; Purkait, T. K.; Islam, M. A.; Miskolzie, M.; Veinot, J. G. C. Instantaneous Functionalization of Chemically Etched Silicon Nanocrystal Surfaces. *Angewandte Chemie International Edition* **2016**, *56* (22), 6073-6077. DOI: 10.1002/anie.201609651.
(13) Li, Z. F.; Ruckenstein, E. Water-Soluble Poly(acrylic acid) Grafted Luminescent Silicon Nanoparticles and Their Use as Fluorescent Biological Staining Labels. *Nano Letters* **2004**, *4* (8), 1463-1467. DOI: 10.1021/nl0492436.
(14) Hummel, R. E. *Electronic Properties of Materials*; Springer, New York, NY, 2011. DOI: https://doi.org/10.1007/978-1-4419-8164-6. Duran, C. Principles and Practice of Mechanical Ventilation. 2nd ed. New York: McGraw-Hill; 2006. (US$ 189.95). *Journal of Intensive Care Medicine* **2008**, *23* (5), 349-349. DOI: 10.1177/0885066608320839. D.B. Sirdeshmukh, L. S., K.G. Subhadra, and C.S. Sunandana. Electrical, Electronic and Magnetic Properties of Solids. *MRS Bulletin* **2015**, *40* (7), 613-613. DOI: 10.1557/mrs.2015.161.
(15) Freund, A. K.; Gillet, J.-A.; Zhang, L. Thermal conductivity of silicon, germanium, and silicon-germanium single crystals between 85 K and 300 K. *Crystal and Multilayer Optics* **1998**, *3448* (1), 362. DOI: 10.1117/12.332526. Lambrecht, W. Dopants and Defects in Semiconductors. *Materials Today* **2012**, *15* (7-8), 349. DOI: 10.1016/s1369-7021(12)70146-3.

(16) Fujii, M.; Hayashi, S.; Yamamoto, K. Photoluminescence from B-doped Si nanocrystals. *Journal of Applied Physics* **1998**, *83* (12), 7953-7957. DOI: 10.1063/1.367976.
(17) Pi, X. D.; Gresback, R.; Liptak, R. W.; Campbell, S. A.; Kortshagen, U. Doping efficiency, dopant location, and oxidation of Si nanocrystals. *Applied Physics Letters* **2008**, *92* (12), 123102. DOI: 10.1063/1.2897291.
(18) Zhou, S.; Pi, X.; Ni, Z.; Luan, Q.; Jiang, Y.; Jin, C.; Nozaki, T.; Yang, D. Boron- and Phosphorus-Hyperdoped Silicon Nanocrystals. *Particle & Particle Systems Characterization* **2014**, *32* (2), 213-221. DOI: 10.1002/ppsc.201400103.
(19) Zhou, S.; Pi, X.; Ni, Z.; Ding, Y.; Jiang, Y.; Jin, C.; Delerue, C.; Yang, D.; Nozaki, T. Comparative Study on the Localized Surface Plasmon Resonance of Boron- and Phosphorus-Doped Silicon Nanocrystals. *ACS Nano* **2015**, *9* (1), 378-386. DOI: 10.1021/nn505416r.
(20) Rohani, P.; Banerjee, S.; Sharifi-Asl, S.; Malekzadeh, M.; Shahbazian-Yassar, R.; Billinge, S. J. L.; Swihart, M. T. Synthesis and Properties of Plasmonic Boron-Hyperdoped Silicon Nanoparticles. *Advanced Functional Materials* **2019**, *29* (8), 1807788. DOI: 10.1002/adfm.201807788.
(21) Zhou, S.; Ni, Z.; Ding, Y.; Sugaya, M.; Pi, X.; Nozaki, T. Ligand-Free, Colloidal, and Plasmonic Silicon Nanocrystals Heavily Doped with Boron. *ACS Photonics* **2016**, *3* (3), 415-422. DOI: 10.1021/acsphotonics.5b00568.
(22) Ni, Z.; Pi, X.; Zhou, S.; Nozaki, T.; Grandidier, B.; Yang, D. Size-Dependent Structures and Optical Absorption of Boron-Hyperdoped Silicon Nanocrystals. *Advanced Optical Materials* **2016**, *4* (5), 700-707. DOI: 10.1002/adom.201500706.
(23) Ni, Z.; Ma, L.; Du, S.; Xu, Y.; Yuan, M.; Fang, H.; Wang, Z.; Xu, M.; Li, D.; Yang, J.; et al. Plasmonic Silicon Quantum Dots Enabled High-Sensitivity Ultrabroadband Photodetection of Graphene-Based Hybrid Phototransistors. *ACS Nano* **2017**, *11* (10), 9854-9862. DOI: 10.1021/acsnano.7b03569. Rowe, D. J.; Jeong, J. S.; Mkhoyan, K. A.; Kortshagen, U. R. Phosphorus-Doped Silicon Nanocrystals Exhibiting Mid-Infrared Localized Surface Plasmon Resonance. *Nano Letters* **2013**, *13* (3), 1317-1322. DOI: 10.1021/nl4001184.
(24) Kramer, N. J.; Schramke, K. S.; Kortshagen, U. R. Plasmonic Properties of Silicon Nanocrystals Doped with Boron and Phosphorus. *Nano Letters* **2015**, *15* (8), 5597-5603. DOI: 10.1021/acs.nanolett.5b02287.
(25) Fujii, M.; Fujii, R.; Takada, M.; Sugimoto, H. Silicon Quantum Dot Supraparticles for Fluorescence Bioimaging. *ACS Applied Materials and Interfaces* **2020**, *3* (6), 6099-6107. DOI: 10.1021/acsanm.0c01295.
(26) Hessel, C. M.; Reid, D.; Panthani, M. G.; Rasch, M. R.; Goodfellow, B. W.; Wei, J.; Fujii, H.; Akhavan, V.; Korgel, B. A. Synthesis of Ligand-Stabilized Silicon Nanocrystals with Size-Dependent Photoluminescence Spanning Visible to Near-Infrared Wavelengths. *Chemistry of Materials* **2011**, *24* (2), 393-401. DOI: 10.1021/cm2032866. Li, Z.; Kortshagen, U. R. Aerosol-Phase Synthesis and Processing of Luminescent Silicon Nanocrystals. *Chemistry of Materials* **2019**, *31* (20), 8451-8458. DOI: 10.1021/acs.chemmater.9b02743. Li, Q.; Luo, T. Y.; Zhou, M.; Abroshan, H.; Huang, J.; Kim, H. J.; Rosi, N. L.; Shao, Z.; Jin, R. Silicon Nanoparticles with Surface Nitrogen: 90% Quantum Yield with Narrow Luminescence Bandwidth and the Ligand Structure Based Energy Law. *ACS Nano* **2016**, *10*, 8385-8393. DOI: 10.1021/acsnano.6b03113. Yu, Y.; Rowland, C. E.; Schaller, R. D.; Korgel, B. A. Synthesis and Ligand Exchange of Thiol-Capped Silicon Nanocrystals. *Langmuir* **2015**, *31* (24), 6886-6893. DOI: 10.1021/acs.langmuir.5b01246. Miyano, M.; Kitagawa, Y.; Wada, S.; Kawashima, A.; Nakajima, A.; Nakanishi, T.; Ishioka, J.; Shibayama, T.; Watanabe, S.; Hasegawa, Y.

Photophysical properties of luminescent silicon nanoparticles surface-modified with organic molecules via hydrosilylation. *Photochemical & Photobiological Sciences* **2016**, *15* (1), 99-104. DOI: 10.1039/c5pp00364d. Mobarok, M. H.; Purkait, T. K.; Islam, M. A.; Miskolzie, M.; Veinot, J. G. C. Instantaneous Functionalization of Chemically Etched Silicon Nanocrystal Surfaces. *Angewandte Chemie* **2017**, *56* (22), 6073-6077. DOI: 10.1002/anie.201609651. Mazzaro, R.; Romano, F.; Ceroni, P. Long-lived luminescence of silicon nanocrystals: from principles to applications. *Phys. Chem. Chem. Phys.* **2017**, *19* (39), 26507-26526. DOI: 10.1039/c7cp05208a.
(27) Clark, R. J.; Aghajamali, M.; Gonzalez, C. M.; Hadidi, L.; Islam, M. A.; Javadi, M.; Mobarok, M. H.; Purkait, T. K.; Robidillo, C. J. T.; Sinelnikov, R.; et al. From hydrogen silsesquioxane to functionalized silicon nanocrystals. *Chemistry of Materials* **2017**, *29* (1), 80-89. DOI: 10.1021/acs.chemmater.6b02667.
(28) Sinelnikov, R.; Dasog, M.; Beamish, J.; Meldrum, A.; Veinot, J. G. C. Revisiting an Ongoing Debate: What Role Do Surface Groups Play in Silicon Nanocrystal Photoluminescence? *ACS Photonics* **2017**, *4* (8), 1920-1929. DOI: 10.1021/acsphotonics.7b00102.
(29) Angi, A.; Sinelnikov, R.; Meldrum, A.; Veinot, J. G. C.; Balberg, I.; Azulay, D.; Millo, O.; Rieger, B. Photoluminescence through in-gap states in phenylacetylene functionalized silicon nanocrystals. *Nanoscale* **2016**, *8* (15), 7849-7853. DOI: 10.1039/c6nr01435f.
(30) Robidillo, C. J. T.; Islam, M. A.; Aghajamali, M.; Faramus, A.; Sinelnikov, R.; Zhang, X.; Boekhoven, J.; Veinot, J. G. C. Functional Bioinorganic Hybrids from Enzymes and Luminescent Silicon-Based Nanoparticles. *Langmuir* **2018**, *34* (22), 6556-6569. DOI: 10.1021/acs.langmuir.8b01119. Robidillo, C. J. T.; Aghajamali, M.; Faramus, A.; Sinelnikov, R.; Veinot, J. G. C. Interfacing enzymes with silicon nanocrystals through the thiol–ene reaction. *Nanoscale* **2018**, *10* (39), 18706-18719. DOI: 10.1039/c8nr05368e. Robidillo, C. J. T.; Wandelt, S.; Dalangin, R.; Zhang, L.; Yu, H.; Meldrum, A.; Campbell, R. E.; Veinot, J. G. C. Ratiometric Detection of Nerve Agents by Coupling Complementary Properties of Silicon-Based Quantum Dots and Green Fluorescent Protein. *ACS Applied Materials & Interfaces* **2019**, *11* (36), 33478-33488. DOI: 10.1021/acsami.9b10996. Robidillo, C. J. T.; Veinot, J. G. C. Functional Bio-inorganic Hybrids from Silicon Quantum Dots and Biological Molecules. *ACS Applied Materials & Interfaces* **2020**, *12* (47), 52251-52270. DOI: 10.1021/acsami.0c14199.
(31) Greenhagen, J. R.; Andaraarachchi, H. P.; Li, Z.; Kortshagen, U. R. Synthesis of PEG-grafted boron doped Si nanocrystals. *The Journal of chemical physics* **2019**, *151* (21), 211103-211103. DOI: 10.1063/1.5128608 PubMed.
(32) Sugimoto, H.; Fujii, M.; Imakita, K. Synthesis of boron and phosphorus codoped all-inorganic colloidal silicon nanocrystals from hydrogen silsesquioxane. *Nanoscale* **2014**, *6* (21), 12354-12359. DOI: 10.1039/c4nr03857f.
(33) Wheeler, L. M.; Kramer, N. J.; Kortshagen, U. R. Thermodynamic Driving Force in the Spontaneous Formation of Inorganic Nanoparticle Solutions. *Nano Letters* **2018**, *18* (3), 1888-1895. DOI: 10.1021/acs.nanolett.7b05187.
(34) Cabrera, N.; Mott, N. F. Theory of the oxidation of metals. *Reports on Progress in Physics* **1949**, *12* (1), 163-184. DOI: 10.1088/0034-4885/12/1/308.
(35) Hessel, C. M.; Henderson, E. J.; Veinot, J. G. C. Hydrogen Silsesquioxane: A Molecular Precursor for Nanocrystalline Si−SiO2 Composites and Freestanding Hydride-Surface-Terminated Silicon Nanoparticles. *Chemistry of Materials* **2006**, *18* (26), 6139-6146. DOI: 10.1021/cm0602803.

(36) Anderson, S. L.; Luber, E. J.; Olsen, B. C.; Buriak, J. M. Substance over Subjectivity: Moving beyond the Histogram. *Chemistry of Materials* **2016**, *28* (17), 5973-5975. DOI: 10.1021/acs.chemmater.6b03430.
(37) Bennett, A. E.; Rienstra, C. M.; Auger, M.; Lakshmi, K. V.; Griffin, R. G. Heteronuclear decoupling in rotating solids. *The Journal of Chemical Physics* **1995**, *103* (16), 6951-6958. DOI: 10.1063/1.470372.
(38) Thiessen, A. N.; Ha, M.; Hooper, R. W.; Yu, H.; Oliynyk, A. O.; Veinot, J. G. C.; Michaelis, V. K. Silicon Nanoparticles: Are They Crystalline from the Core to the Surface? *Chemistry of Materials* **2019**, *31* (3), 678-688. DOI: 10.1021/acs.chemmater.8b03074.
(39) Saß, M.; Annen, A.; Jacob, W. Hydrogen bonding in plasma-deposited amorphous hydrogenated boron films. *Journal of Applied Physics* **1997**, *82* (4), 1905-1908. DOI: 10.1063/1.365997.
(40) Taillon, J. A.; Klingshirn, C. J.; Jiao, C.; Zheng, Y.; Dhar, S.; Zheleva, T. S.; Lelis, A. J.; Salamanca-Riba, L. G. Analysis of the electronic and chemical structure in boron and phosphorus passivated 4H-SiC/SiO2 interfaces using HRTEM and STEM-EELS. *Applied Physics Letters* **2018**, *113* (19), 193503. DOI: 10.1063/1.5053595.
(41) Beljakowa, S.; Pichler, P.; Kalkofen, B.; Hübner, R. Diffusion of Phosphorus and Boron from Atomic Layer Deposition Oxides into Silicon. *physica status solidi (a)* **2019**, *216* (17), 1900306. DOI: 10.1002/pssa.201900306.
(42) Major, G. H.; Fairley, N.; Sherwood, P. M. A.; Linford, M. R.; Terry, J.; Fernandez, V.; Artyushkova, K. Practical guide for curve fitting in x-ray photoelectron spectroscopy. *Journal of Vacuum Science & Technology A* **2020**, *38* (6), 061203. DOI: 10.1116/6.0000377. Thøgersen, A.; Diplas, S.; Mayandi, J.; Finstad, T.; Olsen, A.; Watts, J. F.; Mitome, M.; Bando, Y. An experimental study of charge distribution in crystalline and amorphous Si nanoclusters in thin silica films. *Journal of Applied Physics* **2008**, *103* (2), 024308. DOI: 10.1063/1.2832630.
(43) Yamauchi, J.; Yoshimoto, Y.; Suwa, Y. X-ray photoelectron spectroscopy analysis of boron defects in silicon crystal: A first-principles study. *Journal of Applied Physics* **2016**, *119* (17), 175704. DOI: 10.1063/1.4948572.
(44) Kazahaya, T.; Hirose, M. Coordination Number of Doped Boron Atoms in Photochemically-Deposited Amorphous Silicon Studied by X-Ray Photoelectron Spectroscopy. *Japanese Journal of Applied Physics* **1986**, *25* (Part 2, No. 1), L75-L77. DOI: 10.1143/jjap.25.l75. Li, L. H.; Xing, T.; Chen, Y.; Jones, R. Boron Nitride Nanosheets for Metal Protection. *Advanced Materials Interfaces* **2014**, *1* (8), 1300132. DOI: 10.1002/admi.201300132.
(45) Sundfors, R. K.; Holcomb, D. F. Nuclear Magnetic Resonance Studies of the Metallic Transition in Doped Silicon. *Physical Review* **1964**, *136* (3A), A810-A820. DOI: 10.1103/physrev.136.a810.
(46) Lee, D.; Kaushik, M.; Coustel, R.; Chenavier, Y.; Chanal, M.; Bardet, M.; Dubois, L.; Okuno, H.; Rochat, N.; Duclairoir, F.; et al. Solid-State NMR and DFT Combined for the Surface Study of Functionalized Silicon Nanoparticles. *Chemistry - A European Journal* **2015**, *21* (45), 16047-16058. DOI: 10.1002/chem.201502687. Ha, M.; Thiessen, A. N.; Sergeyev, I. V.; Veinot, J. G. C.; Michaelis, V. K. Endogenous dynamic nuclear polarization NMR of hydride-terminated silicon nanoparticles. *Solid State Nuclear Magnetic Resonance* **2019**, *100*, 77-84. DOI: 10.1016/j.ssnmr.2019.04.001. Hanrahan, M. P.; Fought, E. L.; Windus, T. L.; Wheeler, L. M.; Anderson, N. C.; Neale, N. R.; Rossini, A. J. Characterization of Silicon Nanocrystal Surfaces by Multidimensional Solid-State NMR Spectroscopy. *Chemistry of Materials* **2017**, *29* (24), 10339-10351. DOI: 10.1021/acs.chemmater.7b03306.

(47) Faulkner, R. A.; DiVerdi, J. A.; Yang, Y.; Kobayashi, T.; Maciel, G. E. The Surface of Nanoparticle Silicon as Studied by Solid-State NMR. *Materials (Basel)* **2012**, *6* (1), 18-46. DOI: 10.3390/ma6010018 PubMed.
(48) Baccile, N. Application of Advanced Solid-State NMR Techniques to the Characterization of Nanomaterials: A Focus on Interfaces and Structure. In *Ideas in Chemistry and Molecular Sciences*, 2010; pp 139-182.
(49) Murakami, M.; Shimizu, T.; Tansho, M.; Takano, Y. (11)B nuclear magnetic resonance in boron-doped diamond. *Sci Technol Adv Mater* **2009**, *9* (4), 044103-044103. DOI: 10.1088/1468-6996/9/4/044103 PubMed. Mukuda, H.; Tsuchida, T.; Harada, A.; Kitaoka, Y.; Takenouchi, T.; Takano, Y.; Nagao, M.; Sakaguchi, I.; Oguchi, T.; Kawarada, H. Microscopic evidence for evolution of superconductivity by effective carrier doping in boron-doped diamond:B11−NMRstudy. *Physical Review B* **2007**, *75* (3). DOI: 10.1103/physrevb.75.033301.
(50) Grafe, H.-J.; Löser, W.; Schmitz, S.; Sakaliyska, M.; Wurmehl, S.; Eisert, S.; Reichenbach, B.; Acker, J.; Rietig, A.; Ducke, J.; et al. NMR investigation of boron impurities in refined metallurgical grade silicon. *physica status solidi (a)* **2015**, *212* (9), 2031-2036. DOI: 10.1002/pssa.201431908.
(51) Darwent, B. d. *Bond dissociation energies in simple molecules*; 1970. DOI: http://dx.doi.org/10.6028/nbs.nsrds.31.
(52) Linford, M. R.; Fenter, P.; Eisenberger, P. M.; Chidsey, C. E. D. Alkyl Monolayers on Silicon Prepared from 1-Alkenes and Hydrogen-Terminated Silicon. *Journal of the American Chemical Society* **1995**, *117* (11), 3145-3155. DOI: 10.1021/ja00116a019. Yang, Z.; Iqbal, M.; Dobbie, A. R.; Veinot, J. G. C. Surface-Induced Alkene Oligomerization: Does Thermal Hydrosilylation Really Lead to Monolayer Protected Silicon Nanocrystals? *Journal of the American Chemical Society* **2013**, *135* (46), 17595-17601. DOI: 10.1021/ja409657y.
(53) Petit, J.-F.; Demirci, U. B. Mechanistic Insights into Dehydrogenation of Partially Deuterated Ammonia Borane NH3BD3 Being Heating to 200 °C. *Inorganic Chemistry* **2018**, *58* (1), 489-494. DOI: 10.1021/acs.inorgchem.8b02721. Ciobanu, O.; Allouti, F.; Roquette, P.; Leingang, S.; Enders, M.; Wadepohl, H.; Himmel, H.-J. Thermal and Catalytic Dehydrogenation of the Guanidine-Borane Adducts H3B·hppH (hppH = 1,3,4,6,7,8-hexahydro-2H-pyrimido[1,2-a]pyrimidine) and H3B·N(H)C(NMe2)2: A Combined Experimental and Quantum Chemical Study. *European Journal of Inorganic Chemistry* **2008**, *2008* (35), 5482-5493. DOI: 10.1002/ejic.200800564. García-Vivó, D.; Huergo, E.; Ruiz, M. A.; Travieso-Puente, R. Thermally Induced Dehydrogenation of Amine-Borane Adducts and Ammonia-Borane by Group 6 Cyclopentadienyl Complexes Having Single and Triple -Metal-Metal Bonds. *European Journal of Inorganic Chemistry* **2013**, *2013* (28), 4998-5008. DOI: 10.1002/ejic.201300629.

Chapter 3:

(1) Lee, J.-H.; Huh, Y.-M.; Jun, Y.-w.; Seo, J.-w.; Jang, J.-t.; Song, H.-T.; Kim, S.; Cho, E.-J.; Yoon, H.-G.; Suh, J.-S.; et al. Artificially engineered magnetic nanoparticles for ultra-sensitive molecular imaging. *Nature Medicine* **2006**, *13* (1), 95-99. DOI: 10.1038/nm1467.
(2) Oh, J.; Yuan, H.-C.; Branz, H. M. An 18.2%-efficient black-silicon solar cell achieved through control of carrier recombination in nanostructures. *Nature Nanotechnology* **2012**, *7* (11), 743-748. DOI: 10.1038/nnano.2012.166.
(3) Milliken, S.; Thiessen, A. N.; Cheong, I. T.; O'Connor, K. M.; Li, Z.; Hooper, R. W.; Robidillo, C. J. T.; Veinot, J. G. C. “Turning the dials”: controlling synthesis, structure,

composition, and surface chemistry to tailor silicon nanoparticle properties. *Nanoscale* **2021**. DOI: 10.1039/d1nr04701a. McVey, B. F. P.; Tilley, R. D. Solution Synthesis, Optical Properties, and Bioimaging Applications of Silicon Nanocrystals. *Accounts of Chemical Research* **2014**, *47* (10), 3045-3051. DOI: 10.1021/ar500215v.
(4) Hessel, C. M.; Henderson, E. J.; Veinot, J. G. C. Hydrogen Silsesquioxane: A Molecular Precursor for Nanocrystalline Si−SiO2 Composites and Freestanding Hydride-Surface-Terminated Silicon Nanoparticles. *Chemistry of Materials* **2006**, *18* (26), 6139-6146. DOI: 10.1021/cm0602803.
(5) Kortshagen, U. R.; Sankaran, R. M.; Pereira, R. N.; Girshick, S. L.; Wu, J. J.; Aydil, E. S. Nonthermal Plasma Synthesis of Nanocrystals: Fundamental Principles, Materials, and Applications. *Chemical Reviews* **2016**, *116* (18), 11061-11127. DOI: 10.1021/acs.chemrev.6b00039. Li, X.; He, Y.; Talukdar, S. S.; Swihart, M. T. Process for Preparing Macroscopic Quantities of Brightly Photoluminescent Silicon Nanoparticles with Emission Spanning the Visible Spectrum. *Langmuir* **2003**, *19* (20), 8490-8496. DOI: 10.1021/la034487b.
(6) Mastronardi, M. L.; Maier-Flaig, F.; Faulkner, D.; Henderson, E. J.; Kübel, C.; Lemmer, U.; Ozin, G. A. Size-Dependent Absolute Quantum Yields for Size-Separated Colloidally-Stable Silicon Nanocrystals. *Nano Letters* **2012**, *12* (1), 337-342. DOI: 10.1021/nl2036194.
(7) Mobarok, M. H.; Purkait, T. K.; Islam, M. A.; Miskolzie, M.; Veinot, J. G. C. Instantaneous Functionalization of Chemically Etched Silicon Nanocrystal Surfaces. *Angewandte Chemie International Edition* **2016**, *56* (22), 6073-6077. DOI: 10.1002/anie.201609651. Dasog, M.; Bader, K.; Veinot, J. G. C. Influence of Halides on the Optical Properties of Silicon Quantum Dots. *Chemistry of Materials* **2015**, *27* (4), 1153-1156. DOI: 10.1021/acs.chemmater.5b00115.
(8) Clark, R. J.; Dang, M. K. M.; Veinot, J. G. C. Exploration of Organic Acid Chain Length on Water-Soluble Silicon Quantum Dot Surfaces. *Langmuir* **2010**, *26* (19), 15657-15664. DOI: 10.1021/la102983c. Aghajamali, M.; Xie, H.; Javadi, M.; Kalisvaart, W. P.; Buriak, J. M.; Veinot, J. G. C. Size and Surface Effects of Silicon Nanocrystals in Graphene Aerogel Composite Anodes for Lithium Ion Batteries. *Chemistry of Materials* **2018**, *30* (21), 7782-7792. DOI: 10.1021/acs.chemmater.8b03198. Islam, M. A.; Purkait, T. K.; Veinot, J. G. C. Chloride Surface Terminated Silicon Nanocrystal Mediated Synthesis of Poly(3-hexylthiophene). *Journal of the American Chemical Society* **2014**, *136* (43), 15130-15133. DOI: 10.1021/ja5075739. Dasog, M.; Yang, Z.; Regli, S.; Atkins, T. M.; Faramus, A.; Singh, M. P.; Muthuswamy, E.; Kauzlarich, S. M.; Tilley, R. D.; Veinot, J. G. C. Chemical Insight into the Origin of Red and Blue Photoluminescence Arising from Freestanding Silicon Nanocrystals. *ACS Nano* **2013**, *7* (3), 2676-2685. DOI: 10.1021/nn4000644. Bell, J. P.; Cloud, J. E.; Cheng, J.; Ngo, C.; Kodambaka, S.; Sellinger, A.; Ratanathanawongs Williams, S. K.; Yang, Y. N-Bromosuccinimide-based bromination and subsequent functionalization of hydrogen-terminated silicon quantum dots. *RSC Adv.* **2014**, *4* (93), 51105-51110. DOI: 10.1039/c4ra08477b. Kehrle, J.; Höhlein, I. M. D.; Yang, Z.; Jochem, A.-R.; Helbich, T.; Kraus, T.; Veinot, J. G. C.; Rieger, B. Thermoresponsive and Photoluminescent Hybrid Silicon Nanoparticles by Surface-Initiated Group Transfer Polymerization of Diethyl Vinylphosphonate. *Angewandte Chemie International Edition* **2014**, n/a-n/a. DOI: 10.1002/anie.201405946. Yu, Y.; Rowland, C. E.; Schaller, R. D.; Korgel, B. A. Synthesis and Ligand Exchange of Thiol-Capped Silicon Nanocrystals. *Langmuir* **2015**, *31* (24), 6886-6893. DOI: 10.1021/acs.langmuir.5b01246.

(9) Dasog, M.; De Los Reyes, G. B.; Titova, L. V.; Hegmann, F. A.; Veinot, J. G. C. Size vs Surface: Tuning the Photoluminescence of Freestanding Silicon Nanocrystals Across the Visible Spectrum via Surface Groups. *ACS Nano* **2014**, *8* (9), 9636-9648. DOI: 10.1021/nn504109a.
(10) Oliva-Chatelain, B. L.; Ticich, T. M.; Barron, A. R. Doping silicon nanocrystals and quantum dots. *Nanoscale* **2016**, *8* (4), 1733-1745. DOI: 10.1039/c5nr04978d. Makkar, M.; Viswanatha, R. Frontier challenges in doping quantum dots: synthesis and characterization. *RSC Advances* **2018**, *8* (39), 22103-22112. DOI: 10.1039/c8ra03530j.
(11) Peng, X.; Ai, F.; Yan, L.; Ha, E.; Hu, X.; He, S.; Hu, J. Synthesis strategies and biomedical applications for doped inorganic semiconductor nanocrystals. *Cell Reports Physical Science* **2021**, *2* (5), 100436. DOI: https://doi.org/10.1016/j.xcrp.2021.100436.
(12) Van De Walle, C. G.; Laks, D. B.; Neumark, G. F.; Pantelides, S. T. First-principles calculations of solubilities and doping limits: Li, Na, and N in ZnSe. *Physical Review B* **1993**, *47* (15), 9425-9434. DOI: 10.1103/physrevb.47.9425.
(13) Mikulec, F. V.; Kuno, M.; Bennati, M.; Hall, D. A.; Griffin, R. G.; Bawendi, M. G. Organometallic Synthesis and Spectroscopic Characterization of Manganese-Doped CdSe Nanocrystals. *Journal of the American Chemical Society* **2000**, *122* (11), 2532-2540. DOI: 10.1021/ja991249n.
(14) Erwin, S. C.; Zu, L.; Haftel, M. I.; Efros, A. L.; Kennedy, T. A.; Norris, D. J. Doping semiconductor nanocrystals. *Nature* **2005**, *436* (7047), 91-94. DOI: 10.1038/nature03832.
(15) Hardman, R. A toxicologic review of quantum dots: toxicity depends on physicochemical and environmental factors. *Environ Health Perspect* **2006**, *114* (2), 165-172. DOI: 10.1289/ehp.8284 PubMed.
(16) Reiss, P.; Carrière, M.; Lincheneau, C.; Vaure, L.; Tamang, S. Synthesis of Semiconductor Nanocrystals, Focusing on Nontoxic and Earth-Abundant Materials. *Chemical Reviews* **2016**, *116* (18), 10731-10819. DOI: 10.1021/acs.chemrev.6b00116.
(17) Kuhlmann, A. M. The Second Most Abundant Element in the Earth's Crust. *JOM* **1963**, *15* (7), 502-505. DOI: 10.1007/bf03378936.
(18) Erogbogbo, F.; Yong, K.-T.; Roy, I.; Xu, G.; Prasad, P. N.; Swihart, M. T. Biocompatible Luminescent Silicon Quantum Dots for Imaging of Cancer Cells. *ACS Nano* **2008**, *2* (5), 873-878. DOI: 10.1021/nn700319z. Bhattacharjee, S.; Rietjens, I. M. C. M.; Singh, M. P.; Atkins, T. M.; Purkait, T. K.; Xu, Z.; Regli, S.; Shukaliak, A.; Clark, R. J.; Mitchell, B. S.; et al. Cytotoxicity of surface-functionalized silicon and germanium nanoparticles: the dominant role of surface charges. *Nanoscale* **2013**, *5* (11), 4870. DOI: 10.1039/c3nr34266b.
(19) Hessel, C. M.; Reid, D.; Panthani, M. G.; Rasch, M. R.; Goodfellow, B. W.; Wei, J.; Fujii, H.; Akhavan, V.; Korgel, B. A. Synthesis of ligand-stabilized silicon nanocrystals with size-dependent photoluminescence spanning visible to near-infrared wavelengths. *Chemistry of Materials* **2012**, *24* (2), 393-401. DOI: 10.1021/cm2032866.
(20) Mastronardi, M. L.; Maier-Flaig, F.; Faulkner, D.; Henderson, E. J.; Kübel, C.; Lemmer, U.; Ozin, G. A. Size-Dependent Absolute Quantum Yields for Size-Separated Colloidally-Stable Silicon Nanocrystals. *Nano Letters* **2011**, *12* (1), 337-342. DOI: 10.1021/nl2036194.
(21) Clark, R. J.; Aghajamali, M.; Gonzalez, C. M.; Hadidi, L.; Islam, M. A.; Javadi, M.; Mobarok, M. H.; Purkait, T. K.; Robidillo, C. J. T.; Sinelnikov, R.; et al. From hydrogen silsesquioxane to functionalized silicon nanocrystals. *Chemistry of Materials* **2017**, *29* (1), 80-89. DOI: 10.1021/acs.chemmater.6b02667.
(22) Hessel, C. M.; Reid, D.; Panthani, M. G.; Rasch, M. R.; Goodfellow, B. W.; Wei, J.; Fujii, H.; Akhavan, V.; Korgel, B. A. Synthesis of Ligand-Stabilized Silicon Nanocrystals with Size-

Dependent Photoluminescence Spanning Visible to Near-Infrared Wavelengths. *Chemistry of Materials* **2011**, *24* (2), 393-401. DOI: 10.1021/cm2032866. Canham, L. Introductory lecture: origins and applications of efficient visible photoluminescence from silicon-based nanostructures. *Faraday Discussions* **2020**, *222*, 10-81. DOI: 10.1039/d0fd00018c. Mangolini, L.; Thimsen, E.; Kortshagen, U. High-Yield Plasma Synthesis of Luminescent Silicon Nanocrystals. *Nano Letters* **2005**, *5* (4), 655-659. DOI: 10.1021/nl050066y.
(23) Kramer, N. J.; Schramke, K. S.; Kortshagen, U. R. Plasmonic Properties of Silicon Nanocrystals Doped with Boron and Phosphorus. *Nano Letters* **2015**, *15* (8), 5597-5603. DOI: 10.1021/acs.nanolett.5b02287.
(24) Ni, Z.; Pi, X.; Zhou, S.; Nozaki, T.; Grandidier, B.; Yang, D. Size-Dependent Structures and Optical Absorption of Boron-Hyperdoped Silicon Nanocrystals. *Advanced Optical Materials* **2016**, *4* (5), 700-707. DOI: 10.1002/adom.201500706.
(25) Chen, J.; Rohani, P.; Karakalos, S. G.; Lance, M. J.; Toops, T. J.; Swihart, M. T.; Kyriakidou, E. A. Boron-hyperdoped silicon for the selective oxidative dehydrogenation of propane to propylene. *Chemical Communications* **2020**, *56* (68), 9882-9885. DOI: 10.1039/d0cc02822c. Sugimoto, H.; Fujii, M.; Imakita, K. Synthesis of boron and phosphorus codoped all-inorganic colloidal silicon nanocrystals from hydrogen silsesquioxane. *Nanoscale* **2014**, *6* (21), 12354-12359. DOI: 10.1039/c4nr03857f.
(26) Zhou, S.; Pi, X.; Ni, Z.; Ding, Y.; Jiang, Y.; Jin, C.; Delerue, C.; Yang, D.; Nozaki, T. Comparative Study on the Localized Surface Plasmon Resonance of Boron- and Phosphorus-Doped Silicon Nanocrystals. *ACS Nano* **2015**, *9* (1), 378-386. DOI: 10.1021/nn505416r.
(27) Zhou, S.; Ni, Z.; Ding, Y.; Sugaya, M.; Pi, X.; Nozaki, T. Ligand-Free, Colloidal, and Plasmonic Silicon Nanocrystals Heavily Doped with Boron. *ACS Photonics* **2016**, *3* (3), 415-422. DOI: 10.1021/acsphotonics.5b00568.
(28) Gutsch, S.; Laube, J.; Hiller, D.; Bock, W.; Wahl, M.; Kopnarski, M.; Gnaser, H.; Puthen-Veettil, B.; Zacharias, M. Electronic properties of phosphorus doped silicon nanocrystals embedded in SiO2. *Applied Physics Letters* **2015**, *106* (11), 113103. DOI: 10.1063/1.4915307.
(29) Lechner, R.; Stegner, A. R.; Pereira, R. N.; Dietmueller, R.; Brandt, M. S.; Ebbers, A.; Trocha, M.; Wiggers, H.; Stutzmann, M. Electronic properties of doped silicon nanocrystal films. *Journal of Applied Physics* **2008**, *104* (5), 053701. DOI: 10.1063/1.2973399. Stegner, A. R.; Pereira, R. N.; Klein, K.; Lechner, R.; Dietmueller, R.; Brandt, M. S.; Stutzmann, M.; Wiggers, H. Electronic Transport in Phosphorus-Doped Silicon Nanocrystal Networks. *Physical Review Letters* **2008**, *100* (2). DOI: 10.1103/physrevlett.100.026803. Gnaser, H.; Gutsch, S.; Wahl, M.; Schiller, R.; Kopnarski, M.; Hiller, D.; Zacharias, M. Phosphorus doping of Si nanocrystals embedded in silicon oxynitride determined by atom probe tomography. *Journal of Applied Physics* **2014**, *115* (3), 034304. DOI: 10.1063/1.4862174. Samia, A. C. S.; Lou, Y.; Burda, C.; Senter, R. A.; Coffer, J. L. Effect of the erbium dopant architecture on the femtosecond relaxation dynamics of silicon nanocrystals. *The Journal of Chemical Physics* **2004**, *120* (18), 8716-8723. DOI: 10.1063/1.1695318. Borowik, Ł.; Nguyen-Tran, T.; Roca i Cabarrocas, P.; Mélin, T. Doped semiconductor nanocrystal junctions. *Journal of Applied Physics* **2013**, *114* (20), 204305. DOI: 10.1063/1.4834516.
(30) Meseth, M.; Lamine, K.; Dehnen, M.; Kayser, S.; Brock, W.; Behrenberg, D.; Orthner, H.; Elsukova, A.; Hartmann, N.; Wiggers, H.; et al. Laser-doping of crystalline silicon substrates using doped silicon nanoparticles. *Thin Solid Films* **2013**, *548*, 437-442. DOI: 10.1016/j.tsf.2013.09.056. Lechner, R.; Wiggers, H.; Ebbers, A.; Steiger, J.; Brandt, M. S.; Stutzmann, M. Thermoelectric effect in laser annealed printed nanocrystalline silicon layers.

physica status solidi (RRL) – Rapid Research Letters **2007**, *1* (6), 262-264. DOI: 10.1002/pssr.200701198.
(31) Rohani, P.; Banerjee, S.; Sharifi-Asl, S.; Malekzadeh, M.; Shahbazian-Yassar, R.; Billinge, S. J. L.; Swihart, M. T. Synthesis and Properties of Plasmonic Boron-Hyperdoped Silicon Nanoparticles. *Advanced Functional Materials* **2019**, *29* (8), 1807788. DOI: 10.1002/adfm.201807788.
(32) Hao, X. J.; Cho, E. C.; Scardera, G.; Shen, Y. S.; Bellet-Amalric, E.; Bellet, D.; Conibeer, G.; Green, M. A. Phosphorus-doped silicon quantum dots for all-silicon quantum dot tandem solar cells. *Solar Energy Materials and Solar Cells* **2009**, *93* (9), 1524-1530. DOI: 10.1016/j.solmat.2009.04.002. Huang, S.; So, Y. H.; Conibeer, G.; Green, M. Doping of Silicon Quantum Dots Embedded in Nitride Matrix for All-Silicon Tandem Cells. *Japanese Journal of Applied Physics* **2012**, *51*, 10NE10. DOI: 10.1143/jjap.51.10ne10. Cho, E.-C.; Green, M. A.; Conibeer, G.; Song, D.; Cho, Y.-H.; Scardera, G.; Huang, S.; Park, S.; Hao, X. J.; Huang, Y.; et al. Silicon Quantum Dots in a Dielectric Matrix for All-Silicon Tandem Solar Cells. *Advances in OptoElectronics* **2007**, *2007*, 1-11. DOI: 10.1155/2007/69578. Lim, K. H.; Sun, Y.; Lim, W. C.; Soh, S. Charging Organic Liquids by Static Charge. *Journal of the American Chemical Society* **2020**, *142* (50), 21004-21016. DOI: 10.1021/jacs.0c06000. Sugimoto, H.; Fujii, M.; Imakita, K.; Hayashi, S.; Akamatsu, K. All-Inorganic Near-Infrared Luminescent Colloidal Silicon Nanocrystals: High Dispersibility in Polar Liquid by Phosphorus and Boron Codoping. *The Journal of Physical Chemistry C* **2012**, *116* (33), 17969-17974. DOI: 10.1021/jp305832x. Sato, K.; Fukata, N.; Hirakuri, K. Doping and characterization of boron atoms in nanocrystalline silicon particles. *Applied Physics Letters* **2009**, *94* (16), 161902. DOI: 10.1063/1.3120768. Xie, M.; Li, D.; Chen, L.; Wang, F.; Zhu, X.; Yang, D. The location and doping effect of boron in Si nanocrystals embedded silicon oxide film. *Applied Physics Letters* **2013**, *102* (12), 123108. DOI: 10.1063/1.4798834.
(33) Norris, D. J.; Efros, A. L.; Erwin, S. C. Doped Nanocrystals. *Science* **2008**, *319* (5871), 1776-1779. DOI: 10.1126/science.1143802.
(34) Chan, T.-L.; Zhang, S. B.; Chelikowsky, J. R. An effective one-particle theory for formation energies in doping Si nanostructures. *Applied Physics Letters* **2011**, *98* (13), 133116. DOI: 10.1063/1.3571552. Hiller, D.; López-Vidrier, J.; Gutsch, S.; Zacharias, M.; Wahl, M.; Bock, W.; Brodyanski, A.; Kopnarski, M.; Nomoto, K.; Valenta, J.; et al. Boron-Incorporating Silicon Nanocrystals Embedded in SiO2: Absence of Free Carriers vs. B-Induced Defects. *Scientific Reports* **2017**, *7* (1). DOI: 10.1038/s41598-017-08814-0. Dalpian, G. M.; Chelikowsky, J. R. Self-Purification in Semiconductor Nanocrystals. *Physical Review Letters* **2006**, *96* (22), 226802. DOI: 10.1103/PhysRevLett.96.226802.
(35) Vlaskin, V. A.; Barrows, C. J.; Erickson, C. S.; Gamelin, D. R. Nanocrystal Diffusion Doping. *Journal of the American Chemical Society* **2013**, *135* (38), 14380-14389. DOI: 10.1021/ja4072207.
(36) Garrone, E.; Geobaldo, F.; Rivolo, P.; Amato, G.; Boarino, L.; Chiesa, M.; Giamello, E.; Gobetto, R.; Ugliengo, P.; Viale, A. A Nanostructured Porous Silicon Near Insulator Becomes Either a p- or an n-Type Semiconductor upon Gas Adsorption. *Advanced Materials* **2005**, *17* (5), 528-531. DOI: 10.1002/adma.200401200. Ashby, S. P.; Chao, Y. Use of Electrochemical Etching to Produce Doped Phenylacetylene Functionalized Particles and Their Thermal Stability. *Journal of Electronic Materials* **2013**, *43* (6), 2006-2010. DOI: 10.1007/s11664-013-2935-y.
(37) Jones, K. S.; Prussin, S.; Weber, E. R. A systematic analysis of defects in ion-implanted silicon. *Applied Physics A Solids and Surfaces* **1988**, *45* (1), 1-34. DOI: 10.1007/bf00618760.

Stolk, P. A.; Gossmann, H. J.; Eaglesham, D. J.; Jacobson, D. C.; Rafferty, C. S.; Gilmer, G. H.; Jaraíz, M.; Poate, J. M.; Luftman, H. S.; Haynes, T. E. Physical mechanisms of transient enhanced dopant diffusion in ion-implanted silicon. *Journal of Applied Physics* **1997**, *81* (9), 6031-6050. DOI: 10.1063/1.364452. Tchebotareva, A. L.; de Dood, M. J. A.; Biteen, J. S.; Atwater, H. A.; Polman, A. Quenching of Si nanocrystal photoluminescence by doping with gold or phosphorous. *Journal of Luminescence* **2005**, *114* (2), 137-144. DOI: 10.1016/j.jlumin.2004.12.014. Ruffino, F.; Romano, L.; Carria, E.; Miritello, M.; Grimaldi, M. G.; Privitera, V.; Marabelli, F. A Combined Ion Implantation/Nanosecond Laser Irradiation Approach towards Si Nanostructures Doping. *Journal of Nanotechnology* **2012**, *2012*, 635705. DOI: 10.1155/2012/635705.
(38) Byon, K.; Tham, D.; Fischer, J. E.; Johnson, A. T. Synthesis and postgrowth doping of silicon nanowires. *Applied Physics Letters* **2005**, *87* (19), 193104. DOI: 10.1063/1.2128070.
(39) Carroll, G. M.; Limpens, R.; Neale, N. R. Tuning Confinement in Colloidal Silicon Nanocrystals with Saturated Surface Ligands. *Nano Letters* **2018**, *18* (5), 3118-3124. DOI: 10.1021/acs.nanolett.8b00680.
(40) Robin, A.; Livache, C.; Ithurria, S.; Lacaze, E.; Dubertret, B.; Lhuillier, E. Surface Control of Doping in Self-Doped Nanocrystals. *ACS Applied Materials & Interfaces* **2016**, *8* (40), 27122-27128. DOI: 10.1021/acsami.6b09530.
(41) Lambrecht, W. Dopants and Defects in Semiconductors. *Materials Today* **2012**, *15* (7-8), 349. DOI: 10.1016/s1369-7021(12)70146-3.
(42) Wang, F. F. Y. *Impurity Doping Processes in Silicon*; Elsevier Science, 2012.
(43) Chen, R.; Bent, S. F. Highly Stable Monolayer Resists for Atomic Layer Deposition on Germanium and Silicon. *Chemistry of Materials* **2006**, *18* (16), 3733-3741. DOI: 10.1021/cm0607785.
(44) Thiessen, A. N.; Ha, M.; Hooper, R. W.; Yu, H.; Oliynyk, A. O.; Veinot, J. G. C.; Michaelis, V. K. Silicon Nanoparticles: Are They Crystalline from the Core to the Surface? *Chemistry of Materials* **2019**, *31* (3), 678-688. DOI: 10.1021/acs.chemmater.8b03074.
(45) Balcı, S.; Sezgi, N. A.; Eren, E. Boron Oxide Production Kinetics Using Boric Acid as Raw Material. *Industrial & Engineering Chemistry Research* **2012**, *51* (34), 11091-11096. DOI: 10.1021/ie300685x.
(46) Frésart, E. d.; Rhee, S. S.; Wang, K. L. Boron oxide interaction with silicon in silicon molecular beam epitaxy. *Applied Physics Letters* **1986**, *49* (14), 847-849. DOI: 10.1063/1.97513.
(47) Hessel, C. M.; Henderson, E. J.; Veinot, J. G. C. An Investigation of the Formation and Growth of Oxide-Embedded Silicon Nanocrystals in Hydrogen Silsesquioxane-Derived Nanocomposites. *The Journal of Physical Chemistry C* **2007**, *111* (19), 6956-6961. DOI: 10.1021/jp070908c.
(48) Carlson, D. E.; Smith, R. W.; Magee, C. W.; Zanzucchi, P. J. The role of hydrogen in heavily doped amorphous silicon. *Philosophical Magazine B* **1982**, *45* (1), 51-68. DOI: 10.1080/13642818208246388. Shacham-Diamand, Y. Y.; Oldham, W. G. The effect of hydrogen on boron diffusion in SiO2. *Journal of Electronic Materials* **1986**, *15*, 229-233.
(49) Nogami, M.; Quang, V. X.; Ohki, S.; Deguchi, K.; Shimizu, T. Reduction Mechanisms of Cu2+-Doped Na2O–Al2O3–SiO2 Glasses during Heating in H2 Gas. *The Journal of Physical Chemistry B* **2018**, *122* (3), 1315-1322. DOI: 10.1021/acs.jpcb.7b10913. Cao, J.; Li, X.; Wang, L.; Zhang, Z.; Xu, S.; Peng, M. New strategy to enhance the broadband near-infrared emission of bismuth-doped laser glasses. *Journal of the American Ceramic Society* **2018**, *101* (6), 2297-2304. DOI: https://doi.org/10.1111/jace.15412. Nogami, M. Reduction Mechanism for Eu Ions

in Al2O3-Containing Glasses by Heat Treatment in H2 Gas. *The Journal of Physical Chemistry B* **2015**, *119* (4), 1778-1784. DOI: 10.1021/jp511513n. Nogami, M.; Watanabe, K.; Ito, Y.; Ito, H.; Nakano, H. Hydrogen Gas Reaction with Eu3+-Doped Al2O3–SiO2 Glasses. *Journal of the American Ceramic Society* **2010**, *93* (6), 1663-1667. DOI: https://doi.org/10.1111/j.1551-2916.2010.03653.x.
(50) Dirkx, R. R.; Spear, K. E. Optimization of thermodynamic data for silicon borides. *Calphad* **1987**, *11* (2), 167-175. DOI: 10.1016/0364-5916(87)90011-3. Mostafa, A.; Medraj, M. Binary Phase Diagrams and Thermodynamic Properties of Silicon and Essential Doping Elements (Al, As, B, Bi, Ga, In, N, P, Sb and Tl). *Materials* **2017**, *10* (6), 676. DOI: 10.3390/ma10060676.
(51) Milliken, S.; Cui, K.; Klein, B. A.; Cheong, I. T.; Yu, H.; Michaelis, V. K.; Veinot, J. G. C. Tailoring B-doped silicon nanocrystal surface chemistry via phosphorus pentachloride – mediated surface alkoxylation. *Nanoscale* **2021**, *13* (43), 18281-18292, 10.1039/D1NR05255A. DOI: 10.1039/D1NR05255A.
(52) Belot, V.; Corriu, R.; Leclercq, D.; Mutin, P. H.; Vioux, A. Thermal reactivity of hydrogenosilsesquioxane gels. *Chemistry of Materials* **1991**, *3* (1), 127-131. DOI: 10.1021/cm00013a029.
(53) Wheeler, L. M.; Kramer, N. J.; Kortshagen, U. R. Thermodynamic Driving Force in the Spontaneous Formation of Inorganic Nanoparticle Solutions. *Nano Letters* **2018**, *18* (3), 1888-1895. DOI: 10.1021/acs.nanolett.7b05187.
(54) Yamauchi, J.; Yoshimoto, Y.; Suwa, Y. X-ray photoelectron spectroscopy analysis of boron defects in silicon crystal: A first-principles study. *Journal of Applied Physics* **2016**, *119* (17), 175704. DOI: 10.1063/1.4948572.
(55) Kazahaya, T.; Hirose, M. Coordination Number of Doped Boron Atoms in Photochemically-Deposited Amorphous Silicon Studied by X-Ray Photoelectron Spectroscopy. *Japanese Journal of Applied Physics* **1986**, *25* (Part 2, No. 1), L75-L77. DOI: 10.1143/jjap.25.l75. Li, L. H.; Xing, T.; Chen, Y.; Jones, R. Boron Nitride Nanosheets for Metal Protection. *Advanced Materials Interfaces* **2014**, *1* (8), 1300132. DOI: 10.1002/admi.201300132.
(56) Zhou, S.; Pi, X.; Ni, Z.; Luan, Q.; Jiang, Y.; Jin, C.; Nozaki, T.; Yang, D. Boron- and Phosphorus-Hyperdoped Silicon Nanocrystals. *Particle & Particle Systems Characterization* **2014**, *32* (2), 213-221. DOI: 10.1002/ppsc.201400103.
(57) Mirabella, S.; De Salvador, D.; Bruno, E.; Napolitani, E.; Pecora, E. F.; Boninelli, S.; Priolo, F. Mechanism of Boron Diffusion in Amorphous Silicon. *Physical Review Letters* **2008**, *100* (15). DOI: 10.1103/physrevlett.100.155901.
(58) Mirabella, S.; De Salvador, D.; Napolitani, E.; Bruno, E.; Priolo, F. Mechanisms of boron diffusion in silicon and germanium. *Journal of Applied Physics* **2013**, *113* (3), 031101. DOI: 10.1063/1.4763353.
(59) Sadigh, B.; Lenosky, T. J.; Caturla, M.-J.; Quong, A. A.; Benedict, L. X.; Diaz De La Rubia, T.; Giles, M. M.; Foad, M.; Spataru, C. D.; Louie, S. G. Large enhancement of boron solubility in silicon due to biaxial stress. *Applied Physics Letters* **2002**, *80* (25), 4738-4740. DOI: 10.1063/1.1484557.
(60) Yang, Z.; De Los Reyes, G. B.; Titova, L. V.; Sychugov, I.; Dasog, M.; Linnros, J.; Hegmann, F. A.; Veinot, J. G. C. Evolution of the Ultrafast Photoluminescence of Colloidal Silicon Nanocrystals with Changing Surface Chemistry. *ACS Photonics* **2015**, *2* (5), 595-605. DOI: 10.1021/acsphotonics.5b00143. Kelly, J. A.; Veinot, J. G. C. An Investigation into Near-UV Hydrosilylation of Freestanding Silicon Nanocrystals. *ACS Nano* **2010**, *4* (8), 4645-4656. DOI: 10.1021/nn101022b. Boukherroub, R.; Morin, S.; Wayner, D. D. M.; Bensebaa, F.;

Sproule, G. I.; Baribeau, J. M.; Lockwood, D. J. Ideal Passivation of Luminescent Porous Silicon by Thermal, Noncatalytic Reaction with Alkenes and Aldehydes†. *Chemistry of Materials* **2001**, *13* (6), 2002-2011. DOI: 10.1021/cm000790b. Jurbergs, D.; Rogojina, E.; Mangolini, L.; Kortshagen, U. Silicon nanocrystals with ensemble quantum yields exceeding 60%. *Appl. Phys. Lett.* **2006**, *88* (1), 233116. DOI: 10.1063/1.2210788. Islam, M. A.; Mobarok, M. H.; Sinelnikov, R.; Purkait, T. K.; Veinot, J. G. C. Phosphorus Pentachloride Initiated Functionalization of Silicon Nanocrystals. *Langmuir* **2017**, *33* (35), 8766-8773. DOI: 10.1021/acs.langmuir.7b00518. Rosso-Vasic, M.; Spruijt, E.; van Lagen, B.; De Cola, L.; Zuilhof, H. Alkyl-Functionalized Oxide-Free Silicon Nanoparticles: Synthesis and Optical Properties. *Small* **2008**, *4*, 1835-1841. DOI: 10.1002/smll.200800066. Li, Z. F.; Ruckenstein, E. Water-Soluble Poly(acrylic acid) Grafted Luminescent Silicon Nanoparticles and Their Use as Fluorescent Biological Staining Labels. *Nano Letters* **2004**, *4* (8), 1463-1467. DOI: 10.1021/nl0492436. Sato, S.; Swihart, M. T. Propionic-Acid-Terminated Silicon Nanoparticles: Synthesis and Optical Characterization. *Chemistry of Materials* **2006**, *18* (17), 4083-4088. DOI: 10.1021/cm060750t.
(61) Greenhagen, J. R.; Andaraarachchi, H. P.; Li, Z.; Kortshagen, U. R. Synthesis of PEG-grafted boron doped Si nanocrystals. *The Journal of chemical physics* **2019**, *151* (21), 211103-211103. DOI: 10.1063/1.5128608 PubMed.
(62) Fujii, M.; Sugimoto, H.; Imakita, K. All-inorganic colloidal silicon nanocrystals-surface modification by boron and phosphorus co-doping. *Nanotechnology* **2016**, *27* (26), 262001. DOI: 10.1088/0957-4484/27/26/262001 From NLM.
(63) Thiessen, A. N.; Zhang, L.; Oliynyk, A. O.; Yu, H.; O'Connor, K. M.; Meldrum, A.; Veinot, J. G. C. A Tale of Seemingly "Identical" Silicon Quantum Dot Families: Structural Insight into Silicon Quantum Dot Photoluminescence. *Chemistry of Materials* **2020**, *32* (16), 6838-6846. DOI: 10.1021/acs.chemmater.0c00650. Belyakov, V. A.; Burdov, V. A.; Lockwood, R.; Meldrum, A. Silicon Nanocrystals: Fundamental Theory and Implications for Stimulated Emission. *Advances in Optical Technologies* **2008**, *2008*, 279502. DOI: 10.1155/2008/279502.

Chapter 4:

(1) Oliva-Chatelain, B. L.; Ticich, T. M.; Barron, A. R. Doping silicon nanocrystals and quantum dots. *Nanoscale* **2016**, *8* (4), 1733-1745. DOI: 10.1039/c5nr04978d. Makkar, M.; Viswanatha, R. Frontier challenges in doping quantum dots: synthesis and characterization. *RSC Advances* **2018**, *8* (39), 22103-22112. DOI: 10.1039/c8ra03530j. Iori, F.; Ossicini, S. Effects of simultaneous doping with boron and phosphorous on the structural, electronic and optical properties of silicon nanostructures. *Physica E: Low-dimensional Systems and Nanostructures* **2009**, *41* (6), 939-946. DOI: https://doi.org/10.1016/j.physe.2008.08.010. Sugimoto, H.; Fujii, M.; Imakita, K.; Hayashi, S.; Akamatsu, K. All-Inorganic Near-Infrared Luminescent Colloidal Silicon Nanocrystals: High Dispersibility in Polar Liquid by Phosphorus and Boron Codoping. *The Journal of Physical Chemistry C* **2012**, *116* (33), 17969-17974. DOI: 10.1021/jp305832x. Sugimoto, H.; Okazaki, T.; Fujii, M. Mie Resonator Color Inks of Monodispersed and Perfectly Spherical Crystalline Silicon Nanoparticles. *Advanced Optical Materials* **2020**, *8* (12), 2000033. DOI: https://doi.org/10.1002/adom.202000033. Sugimoto, H.; Zhou, H.; Takada, M.; Fushimi, J.; Fujii, M. Visible-light driven photocatalytic hydrogen generation by water-soluble all-inorganic core–shell silicon quantum dots. *Journal of Materials Chemistry A* **2020**, *8* (31), 15789-15794, 10.1039/D0TA01071E. DOI: 10.1039/D0TA01071E.

(2) Wong, A. P. Y.; Sun, W.; Qian, C.; Jelle, A. A.; Jia, J.; Zheng, Z.; Dong, Y.; Ozin, G. A. Tailoring CO2 Reduction with Doped Silicon Nanocrystals. *Advanced Sustainable Systems* **2017**, *1* (11), 1700118. DOI: https://doi.org/10.1002/adsu.201700118.
(3) Rocks, C.; Svrcek, V.; Velusamy, T.; Macias-Montero, M.; Maguire, P.; Mariotti, D. Type-I alignment in MAPbI3 based solar devices with doped-silicon nanocrystals. *Nano Energy* **2018**, *50*, 245-255. DOI: https://doi.org/10.1016/j.nanoen.2018.05.036. Cho, E.-C.; Green, M. A.; Conibeer, G.; Song, D.; Cho, Y.-H.; Scardera, G.; Huang, S.; Park, S.; Hao, X. J.; Huang, Y.; et al. Silicon Quantum Dots in a Dielectric Matrix for All-Silicon Tandem Solar Cells. *Advances in OptoElectronics* **2007**, *2007*, 1-11. DOI: 10.1155/2007/69578.
(4) Ni, Z.; Ma, L.; Du, S.; Xu, Y.; Yuan, M.; Fang, H.; Wang, Z.; Xu, M.; Li, D.; Yang, J.; et al. Plasmonic Silicon Quantum Dots Enabled High-Sensitivity Ultrabroadband Photodetection of Graphene-Based Hybrid Phototransistors. *ACS Nano* **2017**, *11* (10), 9854-9862. DOI: 10.1021/acsnano.7b03569.
(5) Fujii, M.; Fujii, R.; Takada, M.; Sugimoto, H. Silicon Quantum Dot Supraparticles for Fluorescence Bioimaging. *ACS Applied Materials and Interfaces* **2020**, *3* (6), 6099-6107. DOI: 10.1021/acsanm.0c01295. McVey, B. F. P.; Tilley, R. D. Solution Synthesis, Optical Properties, and Bioimaging Applications of Silicon Nanocrystals. *Accounts of Chemical Research* **2014**, *47* (10), 3045-3051. DOI: 10.1021/ar500215v.
(6) Chen, J.; Rohani, P.; Karakalos, S. G.; Lance, M. J.; Toops, T. J.; Swihart, M. T.; Kyriakidou, E. A. Boron-hyperdoped silicon for the selective oxidative dehydrogenation of propane to propylene. *Chemical Communications* **2020**, *56* (68), 9882-9885, 10.1039/D0CC02822C. DOI: 10.1039/D0CC02822C.
(7) Ni, Z.; Pi, X.; Zhou, S.; Nozaki, T.; Grandidier, B.; Yang, D. Size-Dependent Structures and Optical Absorption of Boron-Hyperdoped Silicon Nanocrystals. *Advanced Optical Materials* **2016**, *4* (5), 700-707. DOI: 10.1002/adom.201500706. Zhou, S.; Pi, X.; Ni, Z.; Luan, Q.; Jiang, Y.; Jin, C.; Nozaki, T.; Yang, D. Boron- and Phosphorus-Hyperdoped Silicon Nanocrystals. *Particle & Particle Systems Characterization* **2014**, *32* (2), 213-221. DOI: 10.1002/ppsc.201400103. Zhou, S.; Pi, X.; Ni, Z.; Ding, Y.; Jiang, Y.; Jin, C.; Delerue, C.; Yang, D.; Nozaki, T. Comparative Study on the Localized Surface Plasmon Resonance of Boron- and Phosphorus-Doped Silicon Nanocrystals. *ACS Nano* **2015**, *9* (1), 378-386. DOI: 10.1021/nn505416r. Zhou, S.; Ni, Z.; Ding, Y.; Sugaya, M.; Pi, X.; Nozaki, T. Ligand-Free, Colloidal, and Plasmonic Silicon Nanocrystals Heavily Doped with Boron. *ACS Photonics* **2016**, *3* (3), 415-422. DOI: 10.1021/acsphotonics.5b00568. Rohani, P.; Banerjee, S.; Sharifi-Asl, S.; Malekzadeh, M.; Shahbazian-Yassar, R.; Billinge, S. J. L.; Swihart, M. T. Synthesis and Properties of Plasmonic Boron-Hyperdoped Silicon Nanoparticles. *Advanced Functional Materials* **2019**, *29* (8), 1807788. DOI: 10.1002/adfm.201807788.
(8) Fujii, M.; Sugimoto, H.; Imakita, K. All-inorganic colloidal silicon nanocrystals—surface modification by boron and phosphorus co-doping. *Nanotechnology* **2016**, *27* (26), 262001. DOI: 10.1088/0957-4484/27/26/262001.
(9) Ho, J. C.; Yerushalmi, R.; Smith, G.; Majhi, P.; Bennett, J.; Halim, J.; Faifer, V. N.; Javey, A. Wafer-Scale, Sub-5 nm Junction Formation by Monolayer Doping and Conventional Spike Annealing. *Nano Letters* **2009**, *9* (2), 725-730. DOI: 10.1021/nl8032526. Ho, J. C.; Yerushalmi, R.; Jacobson, Z. A.; Fan, Z.; Alley, R. L.; Javey, A. Controlled nanoscale doping of semiconductors via molecular monolayers. *Nature Materials* **2008**, *7* (1), 62-67. DOI: 10.1038/nmat2058.

(10) Ye, L.; de Jong, M. P.; Kudernac, T.; van der Wiel, W. G.; Huskens, J. Doping of semiconductors by molecular monolayers: monolayer formation, dopant diffusion and applications. *Materials Science in Semiconductor Processing* **2017**, *62*, 128-134. DOI: https://doi.org/10.1016/j.mssp.2016.12.018.
(11) Mathey, L.; Alphazan, T.; Valla, M.; Veyre, L.; Fontaine, H.; Enyedi, V.; Yckache, K.; Danielou, M.; Kerdiles, S.; Guerrero, J.; et al. Functionalization of Silica Nanoparticles and Native Silicon Oxide with Tailored Boron-Molecular Precursors for Efficient and Predictive p-Doping of Silicon. *The Journal of Physical Chemistry C* **2015**, *119* (24), 13750-13757. DOI: 10.1021/acs.jpcc.5b03408. Agarwala, A.; Subramani, T.; Goldbourt, A.; Danovich, D.; Yerushalmi, R. Facile Monolayer Formation on SiO2 Surfaces via Organoboron Functionalities. *Angewandte Chemie International Edition* **2013**, *52* (29), 7415-7418. DOI: https://doi.org/10.1002/anie.201302655.
(12) Alphazan, T.; Mathey, L.; Schwarzwälder, M.; Lin, T.-H.; Rossini, A. J.; Wischert, R.; Enyedi, V.; Fontaine, H.; Veillerot, M.; Lesage, A.; et al. Monolayer Doping of Silicon through Grafting a Tailored Molecular Phosphorus Precursor onto Oxide-Passivated Silicon Surfaces. *Chemistry of Materials* **2016**, *28* (11), 3634-3640. DOI: 10.1021/acs.chemmater.5b04291.
(13) Hessel, C. M.; Henderson, E. J.; Veinot, J. G. C. Hydrogen Silsesquioxane: A Molecular Precursor for Nanocrystalline Si−SiO2 Composites and Freestanding Hydride-Surface-Terminated Silicon Nanoparticles. *Chemistry of Materials* **2006**, *18* (26), 6139-6146. DOI: 10.1021/cm0602803.
(14) Feher, F. J.; Budzichowski, T. A. Heterosilsesquioxanes: synthesis and characterization of Group 15 containing polyhedral oligosilsesquioxanes. *Organometallics* **1991**, *10* (3), 812-815. DOI: 10.1021/om00049a051.
(15) Zeng, B.; He, K.; Wu, H.; Ye, J.; Zheng, X.; Luo, W.; Xu, Y.; Yuan, C.; Dai, L. Zirconium-Embedded Polyhedral Oligomeric Silsesquioxane Containing Phosphaphenanthrene-Substituent Group Used as Flame Retardants for Epoxy Resin Composites. *Macromolecular Materials and Engineering* **2021**, *306* (6), 2100012. DOI: https://doi.org/10.1002/mame.202100012.
(16) Owens, T. M.; Nicholson, K. T.; Fosnacht, D. R.; Orr, B. G.; Banaszak Holl, M. M. Formation of Mixed Monolayers of Silsesquioxanes and Alkylsilanes on Gold. *Langmuir* **2006**, *22* (23), 9619-9622. DOI: 10.1021/la061477c.
(17) Daasch, L.; Smith, D. Infrared Spectra of Phosphorus Compounds. *Analytical Chemistry* **1951**, *23* (6), 853-868. DOI: 10.1021/ac60054a008.
(18) Sherwood, P. M. A. Introduction to Studies of Phosphorus-Oxygen Compounds by XPS. *Surface Science Spectra* **2002**, *9* (1), 62-66. DOI: 10.1116/11.20030101.
(19) Hashemi, A.; Bahari, A. Structural and dielectric characteristic of povidone–silica nanocomposite films on the Si (n) substrate. *Applied Physics A* **2017**, *123* (8), 535. DOI: 10.1007/s00339-017-1152-6.
(20) Ciolacu, F. C. L.; Choudhury, N. R.; Dutta, N.; Kosior, E. Molecular Level Stabilization of Poly(ethylene terephthalate) with Nanostructured Open Cage Trisilanolisobutyl-POSS. *Macromolecules* **2007**, *40* (2), 265-272. DOI: 10.1021/ma061060d.
(21) Clark, R. J.; Aghajamali, M.; Gonzalez, C. M.; Hadidi, L.; Islam, M. A.; Javadi, M.; Mobarok, M. H.; Purkait, T. K.; Robidillo, C. J. T.; Sinelnikov, R.; et al. From hydrogen silsesquioxane to functionalized silicon nanocrystals. *Chemistry of Materials* **2017**, *29* (1), 80-89. DOI: 10.1021/acs.chemmater.6b02667.
(22) Dasog, M.; Yang, Z.; Veinot, J. G. C. Size-controlled solid state synthesis of luminescent silicon nanocrystals using Stöber silica particles. *CrystEngComm* **2012**, *14* (22), 7576-7578,

10.1039/C2CE25950H. DOI: 10.1039/C2CE25950H. Chan, T.-H.; Melnyk, A. Kinetics and mechanism of the sulfoxide-silane reaction. *Journal of the American Chemical Society* **1970**, *92* (12), 3718-3722. DOI: 10.1021/ja00715a030.
(23) Hayichelaeh, C.; Reuvekamp, L. A. E. M.; Dierkes, W. K.; Blume, A.; Noordermeer, J. W. M.; Sahakaro, K. Enhancing the Silanization Reaction of the Silica-Silane System by Different Amines in Model and Practical Silica-Filled Natural Rubber Compounds. *Polymers* **2018**, *10* (6), 584.
(24) Sápi, A.; Kéri, A.; Kálomista, I.; Dobó, D. G.; Ákos, S.; Juhász, K. L.; Ákos, K.; Kónya, Z.; Galbács, G. Determination of the platinum concentration of a Pt/silica nanocomposite decorated with ultra small Pt nanoparticles using single particle inductively coupled plasma mass spectrometry. *Journal of Analytical Atomic Spectrometry* **2017**, *32* (5), 996-1003, 10.1039/C7JA00039A. DOI: 10.1039/C7JA00039A. Gorham, J. M.; Murphy, K.; Liu, J.; Tselenchuk, D.; Stan, G.; Nguyen, T. M.; Holbrook, R. D.; Winchester, M.; Cook, R. F.; MacCuspie, R. I.; et al. *Preparation of silver nanoparticle loaded cotton threads to facilitate measurement development for textile applications*; National Institute of Standards and Technology, 2015. DOI: 10.6028/NIST.SP.1200-8.
(25) Caccamo, S.; Puglisi, R. A. Carbon-Free Solution-Based Doping for Silicon. *Nanomaterials* **2021**, *11* (8), 2006. Su, Y.; Wang, C.; Hong, Z.; Sun, W. Thermal Disproportionation for the Synthesis of Silicon Nanocrystals and Their Photoluminescent Properties. *Frontiers in Chemistry* **2021**, *9*, Review. DOI: 10.3389/fchem.2021.721454.
(26) Shimizu, Y.; Takamizawa, H.; Inoue, K.; Yano, F.; Nagai, Y.; Lamagna, L.; Mazzeo, G.; Perego, M.; Prati, E. Behavior of phosphorous and contaminants from molecular doping combined with a conventional spike annealing method. *Nanoscale* **2014**, *6* (2), 706-710, 10.1039/C3NR03605G. DOI: 10.1039/C3NR03605G.
(27) Widjonarko, D.; Jumina, J.; Kartini, I.; Nuryono, N. Phosphonate modified silica for adsorption of Co(II), Ni(II), Cu(II), and Zn(II). *Indonesian Journal of Chemistry* **2014**, *14*, 143-151.
(28) Kovalev, A. I.; Wainstein, D. L.; Tetelbaum, D. I.; Hornig, W.; Kucherehko, Y. N. Investigation of the electronic structure of the phosphorus-doped Si and SiO2:Si quantum dots by XPS and HREELS methods. *Surface and Interface Analysis* **2004**, *36* (8), 959-962. DOI: https://doi.org/10.1002/sia.1811.
(29) Hiller, D.; López-Vidrier, J.; Gutsch, S.; Zacharias, M.; Wahl, M.; Bock, W.; Brodyanski, A.; Kopnarski, M.; Nomoto, K.; Valenta, J.; et al. Boron-Incorporating Silicon Nanocrystals Embedded in SiO(2): Absence of Free Carriers vs. B-Induced Defects. *Scientific reports* **2017**, *7* (1), 8337-8337. DOI: 10.1038/s41598-017-08814-0 PubMed. He, W.; Li, Z.; Wen, C.; Liu, H.; Shen, W. Size dependence of phosphorus doping in silicon nanocrystals. *Nanotechnology* **2016**, *27* (42), 425710. DOI: 10.1088/0957-4484/27/42/425710. Limpens, R.; Neale, N. R. Free electron-driven photophysics in n-type doped silicon nanocrystals. *Nanoscale* **2018**, *10* (25), 12068-12077, 10.1039/C8NR02173B. DOI: 10.1039/C8NR02173B. Limpens, R.; Fujii, M.; Neale, N. R.; Gregorkiewicz, T. Negligible Electronic Interaction between Photoexcited Electron–Hole Pairs and Free Electrons in Phosphorus–Boron Co-Doped Silicon Nanocrystals. *The Journal of Physical Chemistry C* **2018**, *122* (11), 6397-6404. DOI: 10.1021/acs.jpcc.7b12313.

Chapter 5:

(1) Wheeler, L. M.; Kramer, N. J.; Kortshagen, U. R. Thermodynamic Driving Force in the Spontaneous Formation of Inorganic Nanoparticle Solutions. *Nano Letters* **2018**, *18* (3), 1888-1895. DOI: 10.1021/acs.nanolett.7b05187.
(2) Milliken, S.; Cui, K.; Klein, B. A.; Cheong, I. T.; Yu, H.; Michaelis, V. K.; Veinot, J. G. C. Tailoring B-doped silicon nanocrystal surface chemistry via phosphorus pentachloride – mediated surface alkoxylation. *Nanoscale* **2021**, *13* (43), 18281-18292, 10.1039/D1NR05255A. DOI: 10.1039/D1NR05255A.
(3) Lawson, J. R.; Melen, R. L. Recent developments and applications of Lewis acidic boron reagents. In *Organometallic Chemistry: Volume 41*, Vol. 41; The Royal Society of Chemistry, 2017; pp 1-27.
(4) Astruc, D. Introduction: Nanoparticles in Catalysis. *Chemical Reviews* **2020**, *120* (2), 461-463. DOI: 10.1021/acs.chemrev.8b00696.
(5) Luu, Q. S.; Kim, J.; Jo, D.; Jeong, J.; Lee, Y. Applications and perspective of silicon particles in hyperpolarized 29Si magnetic resonance imaging. *Applied Spectroscopy Reviews* **2020**, *55* (6), 476-490. DOI: 10.1080/05704928.2019.1676255. Kosaka, N.; Ogawa, M.; Choyke, P. L.; Kobayashi, H. Clinical implications of near-infrared fluorescence imaging in cancer. *Future Oncol* **2009**, *5* (9), 1501-1511. DOI: 10.2217/fon.09.109 PubMed.
(6) Wu, C.-Y.; Hsieh, H.-H.; Chang, T.-Y.; Lin, J.-J.; Wu, C.-C.; Hsu, M.-H.; Lin, M.-C.; Peng, S.-L. Development of MRI-Detectable Boron-Containing Gold Nanoparticle-Encapsulated Biodegradable Polymeric Matrix for Boron Neutron Capture Therapy (BNCT). *International Journal of Molecular Sciences* **2021**, *22* (15), 8050.
(7) Alauddin, M. M. Positron emission tomography (PET) imaging with (18)F-based radiotracers. *Am J Nucl Med Mol Imaging* **2012**, *2* (1), 55-76. PubMed.
(8) Jeon, M. H.; Kwon, Y.-D.; Kim, M. P.; Torres, G. B.; Seo, J. K.; Son, J.; Ryu, Y. H.; Hong, S. Y.; Chun, J.-H. Late-Stage 18F/19F Isotopic Exchange for the Synthesis of 18F-Labeled Sulfamoyl Fluorides. *Organic Letters* **2021**, *23* (7), 2766-2771. DOI: 10.1021/acs.orglett.1c00671.
(9) Iovkova-Berends, L.; Wängler, C.; Zöller, T.; Höfner, G.; Wanner, K. T.; Rensch, C.; Bartenstein, P.; Kostikov, A.; Schirrmacher, R.; Jurkschat, K.; et al. t-Bu2SiF-derivatized D2-receptor ligands: the first SiFA-containing small molecule radiotracers for target-specific PET-imaging. *Molecules* **2011**, *16* (9), 7458-7479. DOI: 10.3390/molecules16097458 From NLM.
(10) Hoppenz, P.; Els-Heindl, S.; Beck-Sickinger, A. G. Peptide-Drug Conjugates and Their Targets in Advanced Cancer Therapies. *Frontiers in Chemistry* **2020**, *8*, Review. DOI: 10.3389/fchem.2020.00571.
(11) Ehrhardt, K. M.; Radomsky, R. C.; Warren, S. C. Quantifying the Local Structure of Nanocrystals, Glasses, and Interfaces Using TEM-Based Diffraction. *Chemistry of Materials* **2021**, *33* (23), 8990-9011. DOI: 10.1021/acs.chemmater.1c03017.
(12) Hunter, K. I.; Bedford, N.; Schramke, K.; Kortshagen, U. R. Probing Dopant Locations in Silicon Nanocrystals via High Energy X-ray Diffraction and Reverse Monte Carlo Simulation. *Nano Letters* **2020**, *20* (2), 852-859. DOI: 10.1021/acs.nanolett.9b03025.
(13) Fleck, N.; Amli, H.; Dhanak, V.; Ahmed, W. Chapter 11 - Characterization techniques in energy generation and storage. In *Emerging Nanotechnologies for Renewable Energy*, Ahmed, W., Booth, M., Nourafkan, E. Eds.; Elsevier, 2021; pp 259-285.
(14) Mocatta, D.; Cohen, G.; Schattner, J.; Millo, O.; Rabani, E.; Banin, U. Heavily doped semiconductor nanocrystal quantum dots. *Science* **2011**, *332* (6025), 77-81. DOI:

10.1126/science.1196321 From NLM. Pablo-Pedro, R.; Magaña-Fuentes, M. A.; Videa, M.; Kong, J.; Li, M.; Mendoza-Cortes, J. L.; Van Voorhis, T. Understanding Disorder in 2D Materials: The Case of Carbon Doping of Silicene. *Nano Letters* **2020**, *20* (9), 6336-6343. DOI: 10.1021/acs.nanolett.0c01775.
(15) McCluskey, M. D.; Haller, E. E. *Dopants and Defects in Semiconductors*; Taylor & Francis, 2012.
(16) Albert, M. J. The Climate Crisis, Renewable Energy, and the Changing Landscape of Global Energy Politics. *Alternatives* **2021**, *46* (3), 89-98. DOI: 10.1177/03043754211040698.
(17) Nayak, P. K.; Mahesh, S.; Snaith, H. J.; Cahen, D. Photovoltaic solar cell technologies: analysing the state of the art. *Nature Reviews Materials* **2019**, *4* (4), 269-285. DOI: 10.1038/s41578-019-0097-0.
(18) Rühle, S. Tabulated values of the Shockley–Queisser limit for single junction solar cells. *Solar Energy* **2016**, *130*, 139-147. DOI: https://doi.org/10.1016/j.solener.2016.02.015.
(19) Li, H.; Zhang, W. Perovskite Tandem Solar Cells: From Fundamentals to Commercial Deployment. *Chemical Reviews* **2020**, *120* (18), 9835-9950. DOI: 10.1021/acs.chemrev.9b00780.
(20) Oliva-Chatelain, B. L.; Ticich, T. M.; Barron, A. R. Doping silicon nanocrystals and quantum dots. *Nanoscale* **2016**, *8* (4), 1733-1745. DOI: 10.1039/c5nr04978d.
(21) Rocks, C.; Svrcek, V.; Velusamy, T.; Macias-Montero, M.; Maguire, P.; Mariotti, D. Type-I alignment in MAPbI3 based solar devices with doped-silicon nanocrystals. *Nano Energy* **2018**, *50*, 245-255. DOI: https://doi.org/10.1016/j.nanoen.2018.05.036.
(22) Cho, E.-C.; Green, M. A.; Conibeer, G.; Song, D.; Cho, Y.-H.; Scardera, G.; Huang, S.; Park, S.; Hao, X. J.; Huang, Y.; et al. Silicon Quantum Dots in a Dielectric Matrix for All-Silicon Tandem Solar Cells. *Advances in OptoElectronics* **2007**, *2007*, 069578. DOI: 10.1155/2007/69578.

Appendix

Appendix A

Calculation of Surface Coverage from TGA

In Chapter 2 and 4 the surface coverage of silicon nanoparticles (SiNPs) was indirectly determined using thermogravimetric analysis (TGA).

The surface coverage from TGA weight-loss was calculated as follows:

$$\%\, Surface\ Coverage = \frac{\%\, Experimental\ weight\ loss}{\%\, Theoretical\ weight\ loss} \quad (1)$$

$$\%\, Theoretical\ weight\ loss = \frac{Ligands\ theoretical\ weight}{Ligands\ and\ SiNCs\ theoretical\ weight} x100 \quad (2)$$

$$SiNCs\ theoretical\ weight = \frac{N(Si)x\ M(Si)}{N_A} \quad (3)$$

$$Ligands\ theoretical\ weight = \frac{N(L)x\ M(L)}{N_A} \quad (4)$$

Where N(Si) = Total number of silicon atoms per nanocrystal

N(L) = Total number of ligands per nanocrystal surface

M(Si) = Molar mass of Si

M(L) = Molar mass of ligand

N_A = Avogadro's number

Substituting equation (3) and (4) into equation (2) simplifying results in equation (5)

$$\%Theoretical\ weight\ loss = \frac{N(L)\cdot M(L)}{N(L)\cdot M(L)+N(Si)\cdot M(Si)} x100 \quad (5)$$

The number of Si atoms in SiNPs was calculated using a density of 2.329 g/cm^3 and a volume of a 3 or 6 nm sphere for the SiNPS used in Chapter 2 and 4 respectively:

$V = \frac{4}{3}\,\pi\, {r_{NP}}^3$ (6)

$m = vd$ (7)

$n = \frac{m}{M}$ (8)

$N(Si) = n \times N_A$ (9)

The number of surface Si was calculated by subtracting the radius of Si from the radius of the of SiNP:

$r_{NP} - r_{Si} = r$ (10)

This radius is then substituted into equation 6 and using equation 7, 8, 9 the number of core atoms, N(C), is calculated. This can then be subtracted from the number of Si in the SiNP to calculate the number of surface atoms:

N(L)= N(Si) - N(C) (11)

Appendix B

Calculation of Surface Coverage from XPS

The calculated number of surface atoms determined in Appendix A can be estimated as the number of available surface sites for bonding with POSS-P from Chapter 4. The percentage of atoms on the surface of NP can be determined by dividing the number of surface atoms by the total number of atoms then multiplied by 100:

$$\%N(S) = \frac{N(L)}{N(Si)} \times 100 \quad (12)$$

Since each POSS-P unit would contain one P atom, we assume that the atomic percent P found in the survey spectrum represents the total POSS-P ligands interacting with the surface. This number is compared with the calculated percentage of available surface sites to determine the surface coverage.

$$\%Surface\ coverage = \frac{at.\%\ P}{\%N(S)} \quad (13)$$

Appendix C

Crystallite size calculations from PXRD

The average crystallite size was calculated from the FWHM of the Gaussian-Lorentzian fit for peaks corresponding to the cubic crystalline Si in the p-XRD patterns of the precursor and B-doped SiNPs using the following equation:

$$D = \frac{\kappa\lambda}{\beta cos\theta} \quad (14)$$

Where,

D = crystallite size (nm)

$\kappa = 0.9$ (Scherrer constant)

$\lambda = 0.15406$ nm (wavelength of x-ray source)

β = FWHM (radians)

θ = peak position (radians)